

# Plasma-Assisted Atomic Layer Deposition for Microelectronics Applications

**Dissertation**

zur Erlangung des akademischen Grades

**Doktoringenieur  
(Dr.-Ing.)**

von **MSc. Akinwumi Abimbola AMUSAN**

geb. am 2 October 1984 in Ibadan, Nigeria

genehmigt durch die Fakultät für Elektrotechnik und Informationstechnik  
der Otto-von-Guericke-Universität Magdeburg

Gutachter:

Prof. Dr.-Ing. Edmund P. Burte

Prof. Dr. rer. nat. habil. Frank T. Edelmann

Promotionskolloquium am: September 29, 2016

# Declaration by Candidate

I hereby declare that the dissertation entitled *Plasma-assisted atomic layer deposition for microelectronics applications* submitted to the Faculty of Electrical Engineering, Otto-von-Guericke-University Magdeburg, is my own work and effort under the guidance of Prof. Edmund P. Burte and Dr. Ing. Bodo Kalkofen, Institute for Micro and Sensor Systems, Otto-von-Guericke-University Magdeburg, Germany and that it has not been submitted anywhere as a whole for any award. Where other sources of information have been used, they have been properly referenced.

Akinwumi Abimbola AMUSAN

Magdeburg, September 29, 2016

# Zusammenfassung

Die Plasmaunterstützte Atomlagenabscheidung (PALD) ist ein bekanntes Verfahren für die Abscheidung hoch-konformer dünner Schichten durch sequentielle und selbst-beschränkte chemische Oberflächenreaktionen. Diese Abscheidemethode ist besonders für die Abscheidung von gleichförmigen Schichten auf Oberflächenstrukturen mit hohem Aspektverhältnis geeignet, wie sie für die Herstellung von mikroelektronischen Bauelementen benötigt werden. Silberschichten und Dotierstoff enthaltende Oxidschichten ( $\text{Sb}_2\text{O}_5$ ,  $\text{B}_2\text{O}_3$ ,  $\text{SiO}_2$  und  $\text{PO}_x/\text{SiO}_2$ ) wurden auf verschiedenen Substraten mittels Plasmaunterstützter Atomlagenabscheidung abgeschieden. Dabei wurden zwei unterschiedliche PALD-Anlagen eingesetzt, die mit verschiedenen neuartigen Prototypen-Plasmaquellen ausgestattet waren.

Die abgeschiedenen Schichten wurden mittels verschiedener Analyseverfahren charakterisiert. Zur Anwendung kamen dabei: Röntgenphotoelektronen-spektroskopie (XPS), Röntgenbeugung (XRD), Röntgenfluoreszenzanalyse (XRF), Atomkraftmikroskopie (AFM), Rasterelektronenmikroskopie (SEM), Transmissionselektronenmikroskopie (TEM) mit Energiedispersiver Röntgenspektroskopie (EDX), Sekundärionen-Massenspektrometrie (SIMS), Vierspitzenmessung und Ellipsometrie.

Silberschichten wurden mittels PALD auf verschiedenen Materialien, wie Silicium, Siliciumoxid, Titanitrid, Titan, Nickel, Cobalt und Wolfram, abgeschieden, wobei die Abscheidetemperaturen im Bereich von 70 °C bis 200 °C variiert wurden. Das größte Wachstum pro Zyklus wurde mit 0.03 nm bei einer Temperatur von 120 °C auf  $\text{SiO}_2$ -Oberflächen erzielt. Die Silberschichten waren polykristallin mit kubischer Kristallstruktur und enthielten nur geringe Kohlenstoff- und Sauerstoffkontaminationen. Ein 97 nm dicker Silberfilm, abgeschieden bei einer Temperatur von 120 °C, wies einen spezifischen Widerstand von  $5.7 \mu\Omega\text{cm}$  auf. Leitfähige Silberschichten, die mittels PALD auf Strukturen mit hohem Aspektverhältnis abgeschieden werden können, wären geeignet, als Keimschichten für die Herstellung von Leiterbahnen eingesetzt zu werden. Haftschichten mit hoher Oberflächenenergie, wie Cobalt und Nickel, können dabei benutzt werden, um gleichmäßiges Wachstum und schnellere Vereinigung von Silberinseln während des Wachstumsprozesses zu erzielen.

Dotierstoffhaltige Oxide, die mittels plasmaunterstützter Atomlagenabscheidung abgeschieden werden, können als Dotierstoffquelle für ultra-flache Dotierung von Silicium und Germanium eingesetzt werden.  $\text{B}_2\text{O}_3$  wurde als Quelle für p-Dotierung von Silicium eingesetzt. Phosphorhaltige Oxidschichten ( $\text{PO}_x/\text{SiO}_2$ ) sollten für die n-Dotierung von Silicium, Germanium sowie Silicium-Germanium und  $\text{Sb}_2\text{O}_5$ -Schichten sollten für die n-Dotierung von Silicium-Germanium- und Germaniumsubstraten geeignet sein.

# Abstract

Plasma-assisted atomic layer deposition (PALD) is a known technique for deposition of highly conformal thin films from sequential and self limiting surface chemical reactions. This deposition technique is particularly useful for conformal deposition on high aspect ratio structures which is applicable in microelectronics fabrication. Silver layers and dopant containing oxide thin films ( $\text{Sb}_2\text{O}_5$ ,  $\text{B}_2\text{O}_3$ ,  $\text{SiO}_2$  and  $\text{PO}_x/\text{SiO}_2$ ) have been deposited on different substrates by plasma-assisted atomic layer deposition using two PALD reactors with new prototype plasma sources.

The deposited layers were characterized by several techniques such as x-ray photoelectron spectroscopy (XPS), x-ray diffraction (XRD), x-ray fluorescence (XRF), atomic force microscopy (AFM), scanning electron microscopy (SEM), transmission electron microscopy (TEM) with energy dispersive x-ray spectroscopy (EDX), secondary ion mass spectrometry (SIMS), four point probe measurement and ellipsometric measurement.

Silver films were grown by PALD on different surfaces such as silicon, silicon oxide, titanium nitride, titanium, nickel, cobalt and tungsten in the deposition temperature range from 70 °C to 200 °C. A maximum silver growth per cycle of 0.03 nm was obtained at 120 °C on  $\text{SiO}_2$  surface. The silver layers had polycrystalline cubic crystal properties, low carbon and oxygen contamination, and a resistivity of  $5.7 \mu\Omega \cdot \text{cm}$  for 97 nm Ag layer on  $\text{SiO}_2$  substrate at 120 °C deposition temperature. Conducting silver layers deposited on high aspect ratio structures by PALD process are applicable for example as seed layers in multilevel interconnects. High surface energy adhesion layers such as cobalt and nickel can be used to promote smooth growth and faster coalescence of silver islands during deposition.

Plasma-assisted atomic layer deposited solid phase dopant containing oxide layers can be used as diffusion source layer for ultra shallow doping in silicon and germanium.  $\text{B}_2\text{O}_3$  were used as source layer for p-type doping in silicon while phosphorus containing oxide ( $\text{PO}_x/\text{SiO}_2$ ) may be suitable as source layer for n-type doping in silicon, germanium and silicon-germanium substrates.  $\text{Sb}_2\text{O}_5$  source layer may be suitable for n-type doping in silicon-germanium and germanium substrates.

# Acknowledgements

My profound gratitude goes to my supervisor, Professor Edmund P. Burte for the opportunity and all the support as a PhD student in his group.

Also, Dr Bodo Kalkofen, took time in explaining lot of things to me in the clean room especially from the beginning of my work.

I must also mention some of my colleagues and fellow students, like Kevin, Mahdav, Iman, Anand, Shoaib, Challa, and Soaib, who have always kept my company in the office and in the lab. They were all good friends.

A lot of other people contributed to this great achievement directly or indirectly.

I must mention my beautiful wife, Elizabeth and our little daughter, Precious for their patience while away from them.

My parent, Mr and Mrs Amusan; inlaws, Mr and Mrs Adewusi, Mr Adewusi Lana, Adeola, Tolu; and all my siblings, Taiwo, Kehinde, Yemisi and Muyiwa, were all very encouraging. Friends within and outside the university like Ola, David, Ahams, Yinka, Lekan, and Alaba, were all amazing for making my stay memorable during the study program.

Above all, I am grateful to God for keeping me all this while and making the work successfully completed.

Thank you all and God bless you!

# Contents

|   |          |
|---|----------|
| Declaration . . . . .                                     | ii       |
| Zusammenfassung . . . . .                                 | iii      |
| Abstract . . . . .  | iv       |
| Acknowledgements . . . . .                                | v        |
| Contents . . . . .  | vi       |
| List of Figures . . . . .                                 | vii      |
| List of Tables . . . . .                                  | viii     |
| Abbreviations . . . . .                                   | ix       |
| <b>Introduction</b>                                       | <b>1</b> |
| 1.1 Material layers and their applications . . . . .      | 1        |
| 1.2 Motivation . . . . .                                  | 2        |
| 1.3 Aim of the dissertation . . . . .                     | 5        |
| 1.4 Objectives of the dissertation . . . . .              | 5        |
| 1.5 Structure of the dissertation . . . . .               | 5        |
| <b>Atomic Layer Deposition (ALD)</b>                      | <b>7</b> |
| 2.1 Basis of atomic layer deposition . . . . .            | 7        |
| 2.2 Description of ALD processes . . . . .                | 8        |
| 2.3 Growth per cycle . . . . .                            | 10       |
| 2.4 Ideal ALD and other non ALD processes . . . . .       | 10       |
| 2.5 Requirements for ideal ALD precursors . . . . .       | 12       |
| 2.6 Overview of ALD precursors types . . . . .            | 14       |
| 2.6.1 Metal precursors . . . . .                          | 14       |
| 2.6.2 Non-metal precursors . . . . .                      | 16       |
| 2.7 Applications of thin films deposited by ALD . . . . . | 17       |
| 2.8 Hardware requirements for ALD processes . . . . .     | 22       |
| 2.9 ALD reactor categories . . . . .                      | 23       |
| 2.9.1 Reactor flow scheme . . . . .                       | 23       |
| 2.9.2 Precursor separation scheme . . . . .               | 24       |
| 2.9.3 Other special reactor design . . . . .              | 25       |
| 2.10 Precursor dosage scheme . . . . .                    | 25       |
| 2.10.1 Direct vapor draw . . . . .                        | 26       |

|        |   |    |
|--------|---|----|
| 2.10.2 | Direct vapor draw with booster . . . . .                                | 26 |
| 2.10.3 | Precursor bubbling system . . . . .                                     | 28 |
| 2.10.4 | Inert gas valving . . . . .   | 28 |
| 2.11   | Plasma-assisted atomic layer deposition . . . . .                       | 29 |
| 2.11.1 | Physics of plasma . . . . .   | 29 |
| 2.11.2 | Classification of plasma ALD sources . . . . .                          | 32 |
| 2.11.3 | Advantages and limitation of plasma ALD . . . . .                       | 34 |
| 2.12   | Review of previous Ag PALD and CVD processes . . . . .                  | 35 |
| 2.13   | Review of previous PALD processes on the selected oxide films . . . . . | 38 |
| 2.13.1 | Sb <sub>2</sub> O <sub>5</sub> film . . . . .                           | 38 |
| 2.13.2 | B <sub>2</sub> O <sub>3</sub> film . . . . .                            | 39 |
| 2.13.3 | SiO <sub>2</sub> film . . . . .   | 40 |
| 2.13.4 | PO <sub>x</sub> /SiO <sub>2</sub> film . . . . .                        | 42 |

**Film Characterization Principles 43**

|       |   |    |
|-------|---|----|
| 3.1   | Ellipsometry . . . . .  | 43 |
| 3.1.1 | Polarization of light . . . . .                                       | 43 |
| 3.1.2 | Principle of operation of ellipsometer . . . . .                      | 45 |
| 3.1.3 | Ellipsometer configurations . . . . .                                 | 46 |
| 3.1.4 | Ellipsometric modelling and data analysis . . . . .                   | 47 |
| 3.1.5 | SENTECH SE 850 ellipsometer . . . . .                                 | 48 |
| 3.2   | Four point probe measurement . . . . .                                | 50 |
| 3.2.1 | Equivalent circuit of two and four point probe measurements . . . . . | 50 |
| 3.2.2 | Four point probe configurations . . . . .                             | 52 |
| 3.2.3 | Probe types . . . . .   | 53 |
| 3.2.4 | CDE Resmap 168 . . . . .  | 53 |
| 3.3   | Scanning probe microscopy . . . . .                                   | 55 |
| 3.3.1 | Scanning tunneling microscopy . . . . .                               | 55 |
| 3.3.2 | Atomic force microscopy . . . . .                                     | 56 |
| 3.4   | X-ray photoelectron spectroscopy (XPS) . . . . .                      | 59 |
| 3.4.1 | Operating principle . . . . .   | 59 |
| 3.4.2 | Conservation of energy in XPS . . . . .                               | 59 |
| 3.4.3 | XPS instrumentation . . . . .   | 62 |
| 3.5   | Introduction to x-ray fluorescence (XRF) . . . . .                    | 63 |
| 3.6   | Introduction to x-ray diffraction (XRD) . . . . .                     | 64 |
| 3.7   | Introduction to electron microscopy . . . . .                         | 65 |
| 3.7.1 | Scanning electron microscopy . . . . .                                | 65 |
| 3.7.2 | Transmission electron microscopy . . . . .                            | 66 |
| 3.8   | Introduction to secondary ion mass spectrometry (SIMS) . . . . .      | 66 |

|  |            |
|--|------------|
| <b>Plasma-Assisted Atomic Layer Deposition Reactors used</b>                                   | <b>68</b>  |
| 4.1 The ‘SENTECH’ PALD system . . . . .  | 68         |
| 4.2 The ‘HFO’ PALD system . . . . .  | 71         |
| <b>Results and Discussions</b>   | <b>74</b>  |
| 5.1 Plasma distribution monitoring with a silver coated silicon wafer . . . . .                | 74         |
| 5.1.1 Plasma monitoring on the ‘SENTECH’ PALD system . . . . .                                 | 75         |
| 5.1.2 Plasma monitoring on the ‘HFO’ PALD system . . . . .                                     | 79         |
| 5.1.3 Improved ‘EPILOGOS’ ICP source with stub tuner on the ‘SEN-<br>TECH’ system . . . . .    | 82         |
| 5.1.4 Other comments on the ‘EPILOGOS’ ICP source . . . . .                                    | 83         |
| 5.2 Plasma-assisted ALD of silver (Ag) layers . . . . .  | 85         |
| 5.2.1 Silver precursor used . . . . .  | 85         |
| 5.2.2 Ag films deposited by PALD with the first ICP source (30 W maxi-<br>mum power) . . . . . | 86         |
| 5.2.3 Ag PALD film investigation with spectroscopic ellipsometry . . . . .                     | 91         |
| 5.2.4 Ag films deposited by PALD with the improved ICP source (50W<br>maximum power) . . . . . | 94         |
| 5.3 Plasma-assisted ALD of dielectric oxide and dopant layers . . . . .                        | 110        |
| 5.3.1 PALD of antimony oxide ( $\text{Sb}_2\text{O}_5$ ) film . . . . .                        | 110        |
| 5.3.2 PALD of boron oxide film . . . . .   | 116        |
| 5.3.3 PALD of silicon oxide film . . . . .   | 122        |
| 5.3.4 PALD of phosphorus containing oxide film . . . . .                                       | 126        |
| 5.4 Doping from PALD source layer . . . . .  | 133        |
| 5.4.1 Silicon (Si) doping . . . . .  | 133        |
| 5.4.2 Germanium (Ge) doping . . . . .  | 140        |
| 5.4.3 Silicon-Germanium (Si-Ge) doping . . . . .   | 141        |
| <b>Conclusion and Future Prospects</b>   | <b>143</b> |
| 6.1 Summary and conclusion . . . . .   | 143        |
| 6.1.1 Plasma monitoring . . . . .  | 143        |
| 6.1.2 Silver layers plasma-assisted ALD . . . . .  | 143        |
| 6.1.3 Oxide dopant layers plasma-assisted ALD . . . . .  | 144        |
| 6.1.4 Doping from plasma-assisted ALD source layer . . . . .                                   | 145        |
| 6.2 Future work and recommendation . . . . .   | 145        |
| 6.2.1 Silver layers plasma-assisted ALD . . . . .  | 145        |
| 6.2.2 Oxide dopant layers plasma-assisted ALD . . . . .  | 146        |
| 6.2.3 Doping from plasma-assisted ALD source layer . . . . .                                   | 146        |



|   |            |
|---|------------|
| <b>Appendices</b>   | <b>147</b> |
| A.1 Snell's law . . . . .   | 147        |
| A.2 Figure of merit for ellipsometric fit . . . . .                           | 147        |
| A.3 Calculation of sheet resistance in four point probe measurement . . . . . | 148        |
| A.4 Periodic table of the elements . . . . .                                  | 150        |
| <b>Resume</b>   | <b>151</b> |
| <b>Related Publications</b>   | <b>152</b> |
| <b>References</b>   | <b>153</b> |

# List of Figures

|      |  |    |
|------|--|----|
| 1.1  | Cross section of an IC chip showing multiple interconnect levels . . . . .                   | 3  |
| 1.2  | Plot of $I_d$ vs $V_{gs}$ in MOSFET as $L_g$ decreases . . . . .                             | 4  |
| 1.3  | FinFET variations . . . . .  | 4  |
| 2.1  | ALD process sequence . . . . .   | 9  |
| 2.2  | Ideal ALD and other non ALD behaviour . . . . .  | 11 |
| 2.3  | Organometallic precursors . . . . .  | 15 |
| 2.4  | Oxygen coordinated metal-organic precursors . . . . .  | 15 |
| 2.5  | Nitrogen coordinated metal-organic precursors . . . . .                                      | 15 |
| 2.6  | Silicon coordinated metal-organic precursors: Metal alkylsilyl . . . . .                     | 16 |
| 2.7  | Application of ALD in IC fabrication . . . . .   | 17 |
| 2.8  | Solar cell passivation . . . . .   | 19 |
| 2.9  | ALD $Al_2O_3$ for thin film magnetic head fabrication used in hard disk drives               | 20 |
| 2.10 | Thin film electroluminescence display . . . . .  | 21 |
| 2.11 | ALD reactor types based on flow scheme . . . . .   | 23 |
| 2.12 | Temporal atomic layer deposition . . . . .   | 24 |
| 2.13 | Spatial atomic layer deposition . . . . .  | 24 |
| 2.14 | Flow-through reactor design for porous substrates . . . . .                                  | 25 |
| 2.15 | Direct vapor draw . . . . .  | 26 |
| 2.16 | Vertical electropolished stainless steel bubbler . . . . .                                   | 27 |
| 2.17 | Direct draw with booster . . . . .   | 27 |
| 2.18 | Bubbling system . . . . .  | 28 |
| 2.19 | Illustration of inert gas valving . . . . .  | 28 |
| 2.20 | Plasma-assisted and thermal atomic layer deposition processes . . . . .                      | 29 |
| 2.21 | Plasma generation principles . . . . .   | 30 |
| 2.22 | Different plasma processes with their corresponding ion flux density and<br>energy . . . . . | 31 |
| 2.23 | Radical enhanced plasma ALD . . . . .  | 33 |
| 2.24 | Direct plasma ALD . . . . .  | 33 |
| 2.25 | Remote plasma ALD . . . . .  | 34 |
| 2.26 | TGA curves of selected Ag precursors . . . . .   | 37 |
| 3.1  | Elliptical polarization. . . . .   | 44 |
| 3.2  | Basic setup of an ellipsometer. . . . .  | 45 |

|      |  |    |
|------|--|----|
| 3.3  | Ellipsometry model . . . . .   | 48 |
| 3.4  | Ellipsometry measurement and data processing . . . . .   | 48 |
| 3.5  | SE 850 ellipsometer in the clean room, Semiconductor Technology group,<br>University of Magdeburg . . . . .  | 49 |
| 3.6  | Two Point Probe Set up . . . . .   | 50 |
| 3.7  | Four point probe . . . . .   | 51 |
| 3.8  | Four point probe configurations . . . . .  | 52 |
| 3.9  | CDE Resmap 168 in the clean room, Semiconductor Technology group,<br>University of Magdeburg . . . . .   | 54 |
| 3.10 | Scanning Probe Microscopy . . . . .  | 55 |
| 3.11 | Basic components of scanning probe microscopy . . . . .  | 56 |
| 3.12 | Atomic force microscopy operation principles . . . . .   | 57 |
| 3.13 | Atomic force microscope setup from Veeco Instruments in the measurement<br>laboratory, Semiconductor Technology group, University of Magdeburg . . | 58 |
| 3.14 | Band energy diagram for a conducting sample and spectrometer . . . . .   | 60 |
| 3.15 | Band energy diagram for an insulating sample and spectrometer . . . . .  | 61 |
| 3.16 | Basic components of x-ray photoelectron spectroscopy instrument . . . . .  | 62 |
| 3.17 | Basic principles of x-ray fluorescence (XRF) and / Particle induced x-ray<br>emission (PIXE) . . . . .   | 63 |
| 3.18 | Illustration of x-ray beam incident on planes of crystal lattice . . . . .   | 64 |
| 3.19 | Basic components of electron microscopes . . . . .   | 65 |
| 3.20 | Illustration of ion beam sputtering process in secondary ion mass spec-<br>trometry (SIMS) . . . . .   | 66 |
| 4.1  | Schematic diagram of ‘EPILOGOS’ ICP plasma source . . . . .  | 68 |
| 4.2  | The ‘SENTECH’ PALD system . . . . .  | 69 |
| 4.3  | Software user interface for the ‘SENTECH’ PALD reactor control and data<br>logging . . . . .   | 70 |
| 4.4  | The ‘HFO’ PALD system . . . . .  | 72 |
| 4.5  | Software interface for the ‘HFO’ PALD system . . . . .   | 73 |
| 5.1  | Ellipsometric model for the layer stack with silver oxide on top . . . . .   | 75 |
| 5.2  | Oxygen plasma monitoring on ICP with 200 sccm O <sub>2</sub> flow at room tem-<br>perature . . . . .   | 76 |
| 5.3  | Hydrogen plasma monitoring on ICP with 200 sccm H <sub>2</sub> flow and substrate<br>at room temperature . . . . .                                 | 77 |
| 5.4  | Hydrogen plasma monitoring on ICP with 70 sccm H <sub>2</sub> flow and substrate<br>at 250 °C temperature . . . . .                                | 77 |
| 5.5  | Oxygen plasma monitoring on CCP with 100 sccm O <sub>2</sub> flow at room tem-<br>perature . . . . .   | 79 |
| 5.6  | Final wafer map of Figure 5.5g . . . . .   | 80 |

|      |  |     |
|------|--|-----|
| 5.7  | Hydrogen plasma monitoring on CCP with 250 sccm H <sub>2</sub> flow at room temperature . . . . .  | 81  |
| 5.8  | Oxygen plasma monitoring on upgraded ICP source with 250 sccm O <sub>2</sub> flow, 50 W plasma power, 10 s plasma exposure and substrate at room temperature . . . . .   | 82  |
| 5.9  | Hydrogen plasma monitoring on upgraded ICP source with 200 sccm H <sub>2</sub> flow, 200 sccm / 70 sccm Ar flow ( during ignition / plasma burning), 50 W plasma power and 70 °C substrate temperature . . . . . | 83  |
| 5.10 | Coatings inside the dual plasma tubes after several ALD processes . . . . .  | 83  |
| 5.11 | Ag(fod)(PEt <sub>3</sub> ) (fod = 2,2-dimethyl- 6,6,7,7,8,8,8-heptafluorooctane-3,5-dionato) . . . . .   | 85  |
| 5.12 | Initial process sequence . . . . .   | 86  |
| 5.13 | Ellipsometric wafer map of 100 cycles Ag PALD compared with 100 cycles H <sub>2</sub> plasma only as well as 100 cycles Ag precursor only at 120 °C deposition temperature on 150 mm wafer . . . . .             | 87  |
| 5.14 | XPS before and after 30 s argon sputtering of the deposited Ag film at 120 °C deposition temperature with 30 W plasma power . . . . .  | 88  |
| 5.15 | XPS result of Ag film deposited at 250 °C temperature . . . . .  | 89  |
| 5.16 | Morphology of Ag film for 1500 cycles deposited at 250 °C temperature . . . . .  | 89  |
| 5.17 | XRD result of Ag film for 1500 cycles deposited at 250 °C temperature . . . . .  | 90  |
| 5.18 | Ellipsometric spectra of Ag film showing resonance absorption . . . . .  | 91  |
| 5.19 | Ellipsometric spectra of Ag films on SiO <sub>2</sub> /Si substrate taken after different PALD cycles . . . . .  | 92  |
| 5.20 | Light energy dependent optical properties of Ag films on SiO <sub>2</sub> /Si substrate . . . . .  | 93  |
| 5.21 | Optimized process sequence for Ag film plasma-assisted atomic layer deposition . . . . .   | 94  |
| 5.22 | Comparison of $\Delta$ spectra for varying Ag precursor pulse times . . . . .  | 95  |
| 5.23 | Comparison of $\Delta$ spectra for varying Ag precursor purge times . . . . .  | 96  |
| 5.24 | Comparison of $\Delta$ spectra for varying chamber wall temperatures . . . . .   | 96  |
| 5.25 | Investigation of Ag precursor saturation for PALD Ag growth . . . . .  | 97  |
| 5.26 | Investigation of H <sub>2</sub> plasma saturation for PALD Ag growth . . . . .   | 97  |
| 5.27 | Chemical composition by XPS of PALD Ag films (a, b, c) at different deposition temperatures compared with PVD Ag film (d) . . . . .  | 99  |
| 5.28 | Crystallinity of PALD Ag films compared with PVD Ag film . . . . .   | 100 |
| 5.29 | Distribution of particle sizes for PALD Ag films grown at 120 °C deposition temperature on different substrates . . . . .  | 101 |
| 5.30 | Morphology of PALD Ag films grown on TiN surface at 120 °C deposition temperature . . . . .  | 102 |

|      |   |     |
|------|---|-----|
| 5.31 | Surface roughness of PALD Ag films grown on different substrates at 120 °C deposition temperature for varying PALD cycles . . . . .   | 102 |
| 5.32 | SEM morphology of PALD Ag films grown on Co surface at 120 °C deposition temperature for 3068 PALD cycles . . . . .   | 104 |
| 5.33 | SEM morphology of PALD Ag films grown on Ni surface at 120 °C deposition temperature for 3068 PALD cycles . . . . .   | 104 |
| 5.34 | SEM morphology of PALD Ag films grown on W surface at 120 °C deposition temperature for 3068 PALD cycles . . . . .  | 105 |
| 5.35 | SEM morphology of PALD Ag films grown on TiN surface at 120 °C deposition temperature for 3068 PALD cycles . . . . .  | 105 |
| 5.36 | SEM morphology of PALD Ag films grown on SiO <sub>2</sub> surface at 120 °C deposition temperature for 3068 PALD cycles . . . . .   | 106 |
| 5.37 | SEM and TEM cross sectional image of PALD Ag film deposited at 120 °C on Ti/TiN/SiO <sub>2</sub> /Si trenches of 2 μm width and 1 μm depth . . . . .  | 106 |
| 5.38 | SEM images of conducting PALD Ag film on silicon oxide . . . . .  | 107 |
| 5.39 | Resistivity and AFM morphology of evaporated Ag PVD films . . . . .   | 108 |
| 5.40 | Investigation of Sb precursor saturation for Sb <sub>2</sub> O <sub>5</sub> PALD growth . . . . .   | 110 |
| 5.41 | Investigation of O <sub>2</sub> plasma saturation for Sb <sub>2</sub> O <sub>5</sub> PALD growth . . . . .  | 111 |
| 5.42 | Variation of total purge times for Sb precursor and O <sub>2</sub> plasma . . . . .   | 111 |
| 5.43 | Variation of PALD cycles (a) and repeatability of the process (b) for Sb <sub>2</sub> O <sub>5</sub> PALD growth . . . . .  | 112 |
| 5.44 | Variation of deposition temperatures for Sb <sub>2</sub> O <sub>5</sub> PALD growth . . . . .   | 112 |
| 5.45 | TEM (a) and SEM (b) after Sb <sub>2</sub> O <sub>5</sub> PALD deposition on high aspect ratio structures and AFM measurements of 73 nm Sb <sub>2</sub> O <sub>5</sub> film (c) . . . . .  | 114 |
| 5.46 | Stability of Sb <sub>2</sub> O <sub>5</sub> film . . . . .  | 115 |
| 5.47 | Investigation of B <sub>2</sub> O <sub>3</sub> deposition and film stability in air from tris-dimethyl-amido borane (TDMAB or B(N(CH <sub>3</sub> ) <sub>2</sub> ) <sub>3</sub> ) with O <sub>2</sub> plasma and O <sub>3</sub> as oxidizing source . . . . . | 116 |
| 5.48 | Investigation of saturation for TDMAB and O radicals at room temperature and 100 °C deposition . . . . .  | 117 |
| 5.49 | In-situ process monitoring with Quadrupole Mass Spectrometry using MID (multiple ion detection) scan of some specific masses . . . . .  | 118 |
| 5.50 | Investigation of B <sub>2</sub> O <sub>3</sub> growth depending on deposition temperature . . . . .   | 119 |
| 5.51 | Variation of PALD cycles for B <sub>2</sub> O <sub>3</sub> PALD deposition at 20 °C and 100 °C deposition temperature . . . . .   | 119 |
| 5.52 | Stabilizing B <sub>2</sub> O <sub>3</sub> films with Sb <sub>2</sub> O <sub>5</sub> capping . . . . .   | 120 |
| 5.53 | Stabilizing B <sub>2</sub> O <sub>3</sub> films with Al <sub>2</sub> O <sub>3</sub> capping . . . . .   | 120 |
| 5.54 | B <sub>2</sub> O <sub>3</sub> film (50 cycles) capped with in-situ Sb <sub>2</sub> O <sub>5</sub> film (50 cycles) at 100 °C on BHF cleaned patterned Si high aspect ratio structure . . . . .  | 121 |

|      |   |     |
|------|---|-----|
| 5.55 | Investigation of saturation for TDMAS pulse . . . . .   | 122 |
| 5.56 | Wafer maps of PALD SiO <sub>2</sub> for varying TDMAS pulse times . . . . .   | 123 |
| 5.57 | Investigation of O <sub>2</sub> plasma saturation for PALD SiO <sub>2</sub> growth . . . . .  | 124 |
| 5.58 | Wafer maps of PALD SiO <sub>2</sub> for varying O <sub>2</sub> plasma pulse times . . . . .   | 125 |
| 5.59 | Investigation of PALD cycle variation for SiO <sub>2</sub> PALD deposition at 150 °C  | 126 |
| 5.60 | PO <sub>x</sub> PALD deposition from TEOP and O <sub>2</sub> plasma at different temperatures   | 127 |
| 5.61 | Illustration of PALD PO <sub>x</sub> /SiO <sub>2</sub> mixed oxide deposition . . . . .   | 128 |
| 5.62 | Deposition of PO <sub>x</sub> /SiO <sub>2</sub> mixed oxide by PALD . . . . .   | 129 |
| 5.63 | Stability of uncapped PO <sub>x</sub> /SiO <sub>2</sub> mixed oxide film compared with PO <sub>x</sub> /SiO <sub>2</sub><br>capped with SiO <sub>2</sub> layer in-situ . . . . .  | 130 |
| 5.64 | Stability of uncapped PO <sub>x</sub> /SiO <sub>2</sub> mixed oxide film compared with PO <sub>x</sub> /SiO <sub>2</sub><br>capped with Sb <sub>2</sub> O <sub>5</sub> layer ex-situ . . . . .  | 130 |
| 5.65 | PO <sub>x</sub> /SiO <sub>2</sub> mixed oxide film (20 super cycles, (M=5,N=1)) capped with<br>in-situ SiO <sub>2</sub> film (100 cycles) at 150 °C on BHF cleaned patterned Si high<br>aspect ratio structure . . . . .  | 131 |
| 5.66 | PO <sub>x</sub> /SiO <sub>2</sub> mixed oxide film (40 super cycles, (M=5,N=1)) at 150 °C capped<br>ex-situ with Sb <sub>2</sub> O <sub>5</sub> film (100 cycles) at 100 °C on BHF cleaned patterned<br>Si high aspect ratio structure . . . . .  | 132 |
| 5.67 | Illustration of diffusion doping process from PALD source layers . . . . .  | 133 |
| 5.68 | SIMS measured boron concentration profiles in silicon of different sam-<br>ples with PALD B <sub>2</sub> O <sub>3</sub> source layers after rapid thermal annealing (RTA)<br>treatments . . . . .   | 133 |
| 5.69 | Comparison of SIMS measured B and Sb profiles in silicon for rapid<br>thermal annealed and unannealed samples with same thickness of PALD<br>B <sub>2</sub> O <sub>3</sub> capped with Sb <sub>2</sub> O <sub>5</sub> source layers . . . . .   | 134 |
| 5.70 | Comparison of SIMS measured B and Sb profiles in silicon for sample with<br>only PALD Sb <sub>2</sub> O <sub>5</sub> source layer and sample with PALD B <sub>2</sub> O <sub>3</sub> capped with<br>Sb <sub>2</sub> O <sub>5</sub> source layer after same flash annealing conditions . . . . . | 135 |
| 5.71 | Comparison of SIMS measured B and Sb profiles in silicon for samples<br>with same PALD B <sub>2</sub> O <sub>3</sub> thickness but different PALD Sb <sub>2</sub> O <sub>5</sub> capping (50<br>cycles and 100 cycles capping) after same rapid thermal annealing conditions                    | 135 |
| 5.72 | Comparison of SIMS measured B and Sb profiles in silicon for samples<br>with different types of annealing treatment . . . . .   | 136 |
| 5.73 | Comparison of SIMS measured P and Sb profiles in Si for uncapped<br>PO <sub>x</sub> /SiO <sub>2</sub> source layers after varying flash anneal treatment time . . . . .   | 136 |
| 5.74 | Comparison of SIMS measured P and Sb profiles in Si for uncapped<br>PO <sub>x</sub> /SiO <sub>2</sub> source layer after varying flash anneal energy density . . . . .  | 137 |
| 5.75 | Comparison of SIMS measured P and Sb profiles in Si for uncapped<br>PO <sub>x</sub> /SiO <sub>2</sub> source layer after varying flash anneal pre-heat temperature . .  | 137 |

|      |  |     |
|------|--|-----|
| 5.76 | Comparison of SIMS measured P and Sb profiles in Si for uncapped PO <sub>x</sub> /SiO <sub>2</sub> and SiO <sub>2</sub> capped PO <sub>x</sub> /SiO <sub>2</sub> source layer after increasing flash anneal runs . . . . . | 138 |
| 5.77 | Comparison of SIMS measured P and Sb profiles in Si for PO <sub>x</sub> /SiO <sub>2</sub> source layer capped with different material layers after similar flash anneal treatment  | 139 |
| 5.78 | Comparison of SIMS measured P and Sb profiles in Si for PO <sub>x</sub> /SiO <sub>2</sub> capped with Sb <sub>2</sub> O <sub>5</sub> source layer after 10 ms and 20 ms flash times . . . . .                              | 139 |
| 5.79 | SIMS profile in epitaxial Ge (1μm) for uncapped PO <sub>x</sub> /SiO <sub>2</sub> source layer after flash anneal . . . . .  | 140 |
| 5.80 | SIMS profile in epitaxial Ge (1μm) for PO <sub>x</sub> /SiO <sub>2</sub> capped with Sb <sub>2</sub> O <sub>5</sub> source layer after flash anneal . . . . .  | 140 |
| 5.81 | SIMS profile in epitaxial Ge (1μm) for Sb <sub>2</sub> O <sub>5</sub> source layer after flash anneal  | 141 |
| 5.82 | SIMS profile in epitaxial SiGe (50 nm) for uncapped PO <sub>x</sub> /SiO <sub>2</sub> source layer after flash anneal . . . . .  | 142 |
| 5.83 | SIMS profile in epitaxial SiGe (50 nm) for PO <sub>x</sub> /SiO <sub>2</sub> capped with Sb <sub>2</sub> O <sub>5</sub> source layer after flash anneal . . . . .  | 142 |
| 5.84 | SIMS profile in epitaxial SiGe (50 nm) for Sb <sub>2</sub> O <sub>5</sub> source layer after flash anneal . . . . .  | 142 |
| A.1  | Four point probe measurement. . . . .  | 148 |

# List of Tables

|      |  |     |
|------|--|-----|
| 2.1  | Other names given to ALD method . . . . .  | 8   |
| 2.2  | Categories of thin films deposited by ALD . . . . .  | 18  |
| 2.3  | Previous Ag PALD and CVD processes . . . . .   | 36  |
| 2.4  | Precursors for SiO <sub>2</sub> ALD and PALD processes . . . . .   | 41  |
| 3.5  | Probe types . . . . .  | 54  |
| 3.6  | Probe applications . . . . .   | 54  |
| 5.7  | Comparing the resistivity obtained with the previous Ag PALD reported .  | 109 |
| 5.8  | Cauchy dispersion coefficients of PALD Sb <sub>2</sub> O <sub>5</sub> film deposited at 100 °C<br>temperature . . . . .    | 114 |
| 5.9  | Deposition parameters for TDMAB saturation investigation . . . . .   | 117 |
| 5.10 | Deposition parameters for O radicals saturation investigation . . . . .  | 117 |
| 5.11 | PALD cycle variation for PO <sub>x</sub> deposition at 200 °C . . . . .  | 127 |
| 5.12 | PALD super cycle variation for PO <sub>x</sub> /SiO <sub>2</sub> (M=5,N=1) mixed oxide deposi-<br>tion at 150 °C . . . . . | 131 |



# Abbreviations

$\Omega$  Ohms

AFM Atomic Force Microscopy

ALD Atomic Layer Deposition

BEOL Back End of Line

CCP Capacitively coupled plasma

CMOS Complementary Metal Oxide Semiconductor

CVD Chemical Vapor Deposition

DNA Deoxyribonucleic acid

DRAM Dynamic Random Access Memories

EDX Energy Dispersive X-ray Spectroscopy

FEOL Front End of Line

FET Field Effect Transistor

FPP Four Point Probe

IC Integrated Circuit

ICP Inductively coupled plasma

MOSFET Metal Oxide Semiconductor Field Effect Transistor

PALD Plasma-Assisted Atomic Layer Deposition

PCSA Polarizer Compensator Sample Analyser

PIXE Particle Induced X-ray Emission

PSA Polarizer Sample Analyser

PSCA Polarizer Sample Compensator Analyser

PVD Physical Vapor Deposition  
RAE Rotating Analyser Ellipsometry  
RCE Rotating Compensator Ellipsometry  
RNA Ribonucleic acid  
RPE Rotating Polarizer Ellipsometry  
SEM Scanning Electron Microscope  
SIMS Secondary Ion Mass Spectrometry  
SPM Scanning Probe Microscopy  
STM Scanning Tunneling Microscopy  
TEM Transmission Electron Microscope  
XPS X-ray Photoelectron Spectroscopy  
XRD X-ray Diffraction  
XRF X-ray Fluorescence

# Introduction

## 1.1 Material layers and their applications

Semiconductor integrated circuit (IC) fabrication processes involve several fabrication steps on a wafer which broadly fall into four processing categories, namely, material deposition, material removal (etching and chemical mechanical planarization), patterning by lithography and electrical properties modification (doping and annealing). These IC processing steps in modern terms are further classified as front end of line and back end of line processes. Front end of line (FEOL) starts and ends directly on the wafer substrate involving processes as obtained in CMOS fabrication such as wafer selection, wafer chemical mechanical planarization and wafer cleaning, growth of dielectric on the wafer (typically silicon oxide), patterning of the transistor active regions, shallow trench isolation, well formation, gate module formation, as well as source and drain module formation [1]. Back end of line (BEOL) processes on the other hand involve interconnection of all transistor nodes on the wafer which include formation of contacts, insulating layers (dielectrics), metal levels interconnects, and bonding sites for chip-to-package connections. All these processes (both FEOL and BEOL) may require deposition of thin films of various materials from thicknesses of few angstroms to few micrometers for different applications, for instance gate oxides are usually made of oxides of dielectric typically silicon oxide, hafnium oxide, and zirconium oxide. Also contacts and interconnects are electrically conductive materials like metals (for instance Cu and Al), while diffusion barriers can be metal nitride such as TiN. These materials can be deposited by various methods such as physical vapor deposition and chemical vapor deposition. Physical vapor deposition (PVD) converts the required physical material to vapor and transfer the material in vapor or plasma phase to the substrates usually under high vacuum. Physical vapor deposition can be electron beam evaporation, electrical thermal evaporation, pulsed laser deposition and sputter deposition. However, physical vapor deposition techniques are usually limited by directionality of the flux of material. And as a result, deposition by PVD with good step coverage on advanced structures such as three-dimensional structures, trenches and fin shaped structures might be challenging. On the other hand, chemical vapor deposition requires gas and surface reactions of two or more precursors leaving the required material on the substrate and purging the reaction by-products. Deposition of thin films by chemical reactions are in general more uniform than physical deposition

but sometimes with slightly lower film quality. Moreover, there are some applications which requires extremely conformal thin film of materials and this needs some special form of chemical vapor deposition which is called atomic layer deposition. Atomic layer deposition involves surface self limiting reactions and has the ability to deposit materials with excellent step and surface coverage, pin hole free and even with excellent physical properties sometimes close to the bulk material. Some specific applications of atomic layer deposited films include solar cell passivation [2] (aluminum oxide and silicon oxide back and front side coating reduces surface recombination velocity of charge carriers), dopant layers for shallow pn junctions [3], deposition of high - k dielectric in CMOS transistors, metal electrode deposition in high aspect ratio structures for memory devices and interconnects, optical coatings [4] and coating of arbitrary shaped structures and fragile materials such as polymers and papers [5].

## 1.2 Motivation

Atomic layer deposition has the advantage of extreme film conformality on planar and three-dimensional structures with controllable thickness from a fraction of monolayer and as such efficient atomic layer deposition processes for different materials would be necessary. Silver will be deposited as an example of metal PALD process while dielectric oxide layers such as boron oxide, antimony oxide, phosphorus containing oxide and silicon oxide will as well be deposited by PALD. Two proposed applications of these deposited layers in microelectronics fabrication are:

- metallization application for silver layers
  - silicon and germanium doping from PALD oxide films as dopant source
- (i) Some of the requirements for future metallization and interconnects as identified by ITRS (International Technology Roadmap for Semiconductor) is the use of lower permittivity insulation medium as well as lower resistivity contact materials.

Low resistivity contact material would imply low heat dissipation ( $I^2R$ ) and low signal propagation delay ( $RC$ ) within the IC. Silver has the lowest resistivity ( $\approx 1.6 \mu\Omega\cdot\text{cm}$ ), low residual stress compared to copper [7] and can also be scaled down to sub 100 nm without substantial increase in resistivity as compared to copper [8]. Silver is therefore considered as a potential replacement to copper in interconnects and contact formation for integrated circuit fabrication. Typical back end of line process in IC metallization requires multiple metal levels (Figure 1.1) for interconnecting all nodes within the IC as well as to the external lead terminal. These multilevel interconnects usually requires etching of deep trenches (vias) in insulating medium which will be filled with the conducting interconnecting materials such as aluminum, copper,

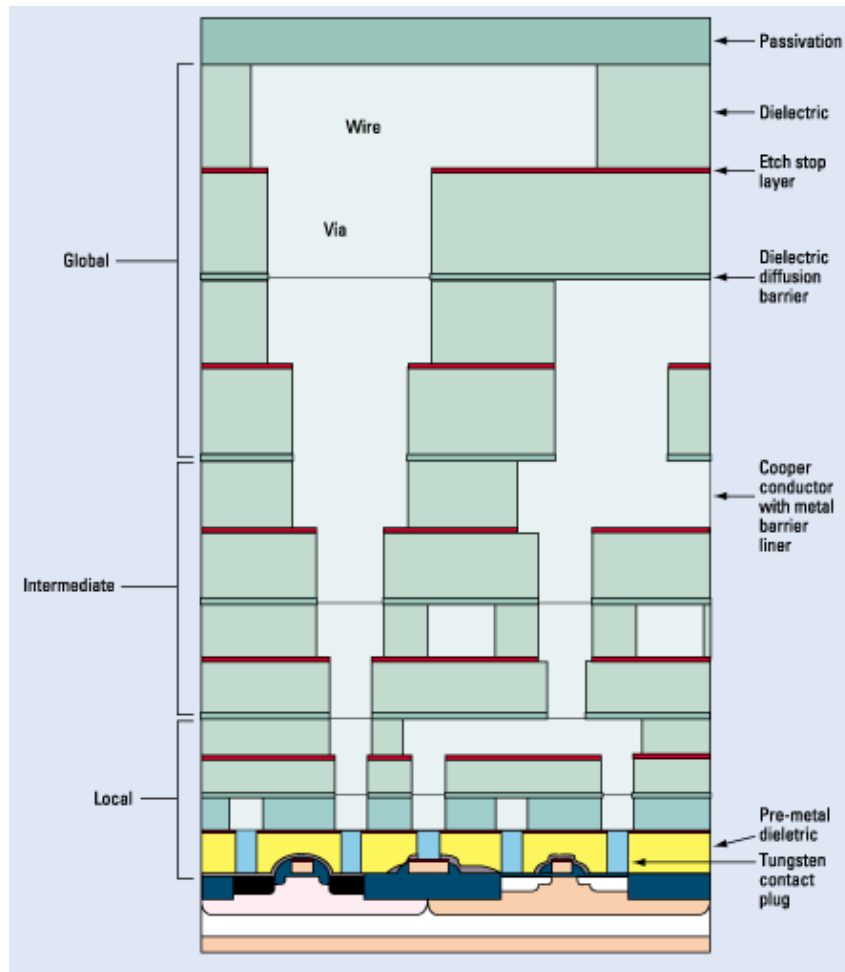


Figure 1.1: Cross section of an IC chip showing multiple interconnect levels [6]

tungsten or silver. Some conventional methods of silver thin film deposition include electroplating [9], physical vapor deposition [10], chemical vapor deposition [11] and atomic layer deposition [12,13]. Atomic layer deposition has potential advantage of excellent step coverage on three-dimensional structures, possible low temperature processes and it is also compatible with silicon microfabrication. Plasma-assisted atomic layer deposited silver layers can be useful for example as seed layers for silver electroplating in vias and holes required for multi-level interconnect in integrated circuits.

- (ii) Gordon Moore made an observation reported in 1965 that the number of transistors on a chip doubles every 18 months. Continuation of Moore's scaling is reaching a limit (below 100 nm gate length) where the gate voltage can no longer effectively control the drain current in conventional two dimensional MOSFET because of short channel effects.

Figure 1.2 illustrates the undesirable typical MOSFET scaling effect showing an increase in drain current at zero gate voltage as the gate length becomes smaller. As a result, new three-dimensional transistor structures such as ultra-thin-body FET,

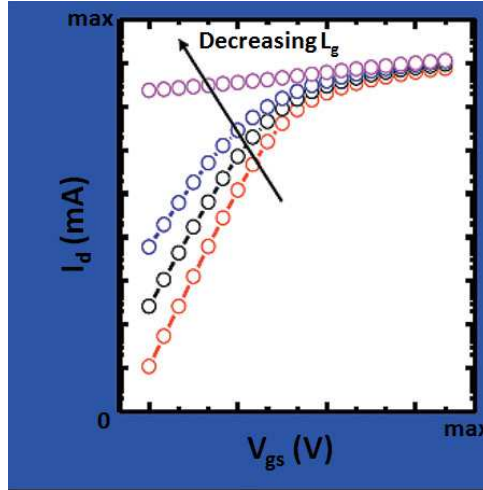


Figure 1.2: Plot of  $I_d$  vs  $V_{gs}$  in MOSFET as  $L_g$  decreases, where  $I_d$  is the drain current in milliamperes (mA),  $V_{gs}$  is the gate to source voltage in volts (V),  $L_g$  is the gate length. Both scales (x and y) are shown from 0 to maximum (max). Adapted from [14]

FinFET and nanowire transistors (Figure 1.3) are being proposed as possible solutions to overcome this scaling limitation from short channel effects [14, 15]. Fabrication of high density three-dimensional transistors circuits on a chip will require production of ultra-shallow pn junctions with high activation levels ( $\geq 10^{20} \text{ cm}^{-3}$  [16]), abrupt junctions ( $\leq 2 \text{ nm/decade}$  [16]), as well as conformal doping of the three-dimensional structures.

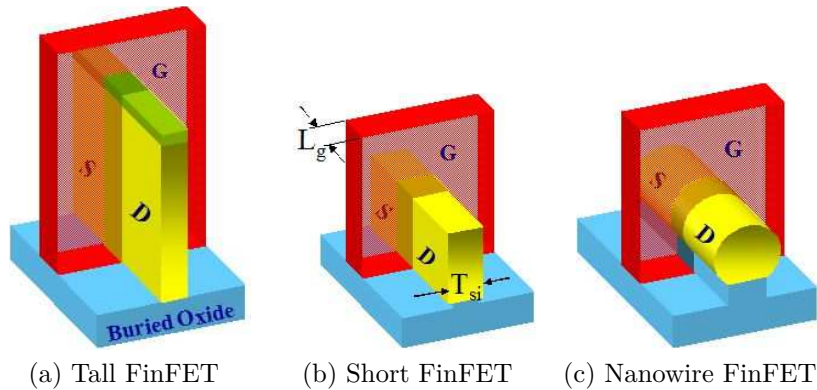


Figure 1.3: FinFET variations [15]

Current doping technologies such as ion implantation and plasma doping [17] suffer severe limitation from crystal damage resulting to undesired deep diffusion of dopants (transient enhanced diffusion), dopants channeling in crystalline materials and dopants shadowing at three-dimensional surface. While diffusion from spin on dopant source [18], gas phase dopants [19, 20] and molecular layer source [21] do not have radiative damage, it may also be challenging to carefully control the dose. The thickness of dopant layers fabricated by PALD can be easily controlled layer

by layer and deposition can as well be conformal on planar and three-dimensional structures. Therefore, dopant layers deposited by PALD on silicon and germanium substrates can be applied for shallow and conformal doping from solid phase diffusion of pre-deposited PALD sources.

### **1.3 Aim of the dissertation**

Selected material films which are silver (Ag), boron oxide ( $B_2O_3$ ), antimony oxide ( $Sb_2O_5$ ), silicon oxide ( $SiO_2$ ) and phosphorus containing films ( $PO_x/SiO_2$ ) will be deposited on different substrates using two remote plasma-assisted atomic layer deposition reactors ('SENTECH' PALD system and 'HFO' PALD system) with new prototype plasma sources ('EPILOGOS' ICP plasma source in 'SENTECH' PALD system and 'EPILOGOS' CCP plasma source in 'HFO' PALD system). Some specific applications of the deposited materials will also be demonstrated.

### **1.4 Objectives of the dissertation**

- (i) To deposit conducting silver layers by plasma-assisted atomic layer deposition in three-dimensional structures suitable for integrated circuit multilevel interconnects with a new prototype ICP plasma source.
- (ii) To develop plasma-assisted atomic layer deposition processes for dielectric oxide layers and dopants layers of antimony oxide, boron oxide, phosphorus oxide and silicon oxide.
- (iii) To characterize the deposited layers by various techniques such as ellipsometry, four point probe (FPP), AFM measurements, SEM / TEM measurements, XRD measurements, XPS measurements, EDX measurements, and XRF measurements.
- (iv) To evaluate the plasma sources in both PALD systems.
- (v) To demonstrate application of plasma-assisted atomic layer deposited films of boron oxide, phosphorus containing layers and antimony oxide film for silicon and or germanium doping.

### **1.5 Structure of the dissertation**

The first chapter introduces the dissertation leading to motivation, aim and objectives. Chapter two describes the general background, review of atomic layer deposition and plasma-assisted atomic layer deposition. Chapter three describes some principles of film

characterization techniques used in this work. Chapter four gives the description of the plasma assisted atomic layer deposition reactors used in this work. Chapter five discusses the results of each sections of the experiments. Chapter six gives the summary, conclusion and future work.



# Atomic Layer Deposition (ALD)

## 2.1 Basis of atomic layer deposition

Thin solid films can be deposited by chemical reaction and or thermal decomposition of one or more reactants over heated substrates. This technique, also known as chemical vapor deposition (CVD), usually involves gas phase and surface reactions of one or more reactants leaving the required film on the substrate. Usually for CVD processes, all reactants (precursors) are supplied to the reaction chamber simultaneously, without necessarily purging previous reactants. ALD is a variation of CVD whereby the reactants are supplied separately into the reaction chamber, with an intermediate purge step of earlier reactant and by-products, before supplying the next precursor thereby preventing mixing of two reactants in gas phase. Each precursor saturates the surface and in an ideal case reacts with the next precursor only at the surface, resulting to less than monolayer of the grown film. ALD processes have the ability to precisely control the film thickness (due to the so called self limiting reaction properties), as well as to grow high quality film with excellent conformality. Therefore, with continued aggressive Moore's scaling and increasing aspect ratio structures, the need for ALD grown films becomes more and more important. ALD was first demonstrated as molecular layering by a set of Russian scientist in 1960 [22], later Tuomo Suntola (Finnish scientist) and co-workers developed it further in 1970 and also patented it [23] with the original goal of developing a production process for thin film electroluminescent (TFEL) displays [24]. However, ALD has been adopted for wider applications and the International Technology Roadmap for Semiconductors (ITRS) has included ALD processes for producing high-k dielectric gate oxides as well as copper diffusion barriers in interconnects [25,26]. ALD was named atomic layer epitaxy at the time of its invention [23] because the emphasis was on sequential controlled surface reactions resulting to layer by layer growth [27]. However epitaxial growth is commonly referred to as growth of single crystal films on top of single crystal substrates, with well defined structural relationship between the two. And so, to avoid confusion, the name atomic layer epitaxy (ALE) is only reserved for epitaxial films. Over the years, the ALD method has been given several other names [27] and this is summarized in Table 2.1. Atomic layer deposition is the general accepted name for all kind of films (crystalline and amorphous).

Table 2.1: Other names given to ALD method [27]

| Accronym | Name  | Comments                          |
|----------|---|-----------------------------------|
| ALD      | Atomic Layer Deposition                     | for all kinds of film             |
| ALE      | Atomic Layer Epitaxy                        | only epitaxial film               |
| ALG      | Atomic Layer Growth                         | similar to ALD but seldom used    |
| ALCVD    | Atomic Layer Chemical Vapor Deposition      | related to CVD                    |
| MLE      | Molecular Layer Epitaxy                     | molecular compound precursor used |
| DLE      | Digital Layer Epitaxy                       | digital thickness control         |
| ML       | Molecular Layering                          | mostly Russian literature         |
|          | Successive Layerwise Chemisorption          |                                   |
|          | Sequential Surface Chemical Reaction Growth |                                   |
|          | Pulsed Beam Chemical Vapor Deposition       |                                   |

## 2.2 Description of ALD processes

ALD is a deposition process which involves alternating, sequential, saturating precursor dosage with intermediate purge steps and self limiting surface reactions. This can be separated into four basic step as shown in Figure 2.1.

- (i) The surface is exposed to precursor A, the precursor is adsorbed on the surface until it completely saturates the surface. Excess precursor would not have any effect on the surface after saturation.
- (ii) The excess precursor A and reaction by-products are purged away with an inert gas or simply pumped away from the chamber.
- (iii) The surface is again exposed to precursor B until it completely saturates the surface. Exchange reaction takes place.
- (iv) Reaction by-products and excess precursor are purged. The surface is left with usually less than a monolayer of the grown film.

The four steps above is actually one ALD cycle, and the cycle is repeated until the desired film thickness is obtained. Some salient features of ideal ALD process are as described below:

- (i) The growth is initiated due to the presence of reactive surface groups or chemisorption sites on the surface. There is usually finite number of active sites (reactive surface groups or chemisorption sites) on the surface.
- (ii) Self limiting reactions implies that the growth is self controlled and depends on the number of active sites on the surface. Precursor chemisorbs or reacts with all

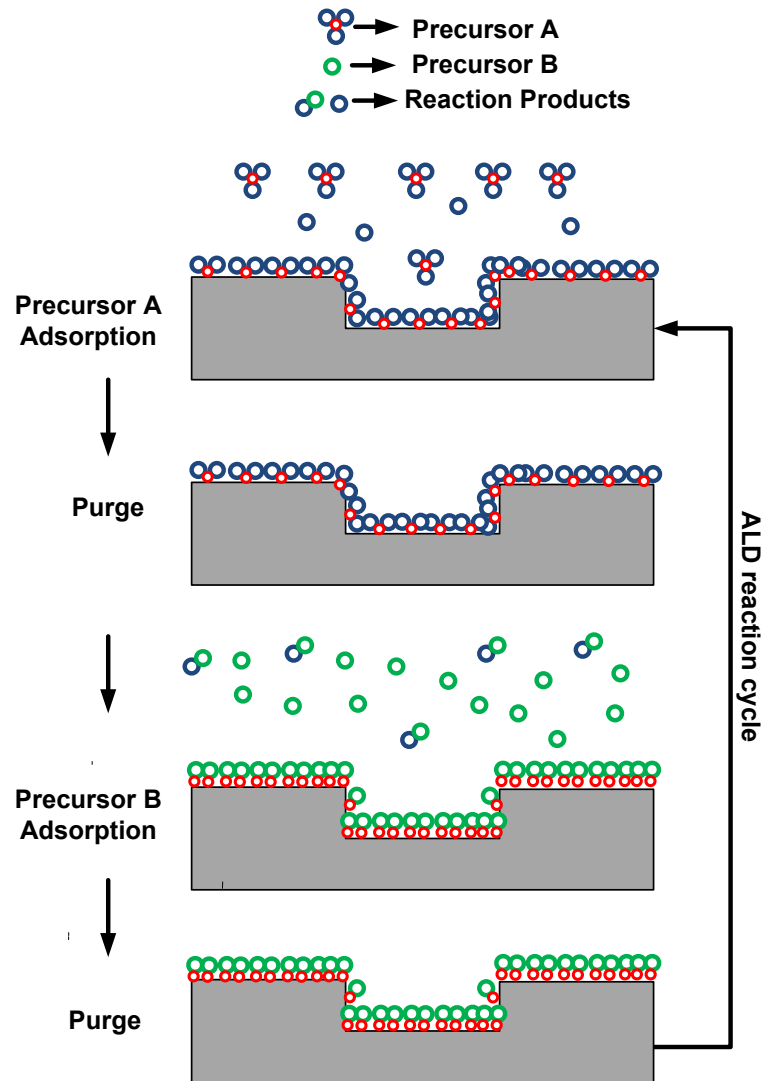


Figure 2.1: ALD process sequence

available active sites irreversibly (that is without desorption of the adsorbed species during purge time). Once the active sites are completely covered by the precursor, the growth process should stop. Growth process should not depend on precursor flux homogeneity if enough precursor is supplied to saturate the surface. This allows precise thickness control on atomic level and also gives conformal deposition. In addition, film properties (stoichiometry) can be controlled from atomic level and dense, uniform, and pin hole free film can also be produced. It also allows deposition on large surfaces and batch deposition on multiple wafers.

- (iii) Alternating precursor dosing implies that there will be no gas phase reactions, rather there are surface exchange reactions. This allows the use of highly reactive precursor and as a result reactions can as well take place at lower temperatures compared to CVD processes. Besides, film and reactor contamination can also be reduced by eliminating gas phase reactions, and as a result high quality films are produced at

lower deposition temperatures.

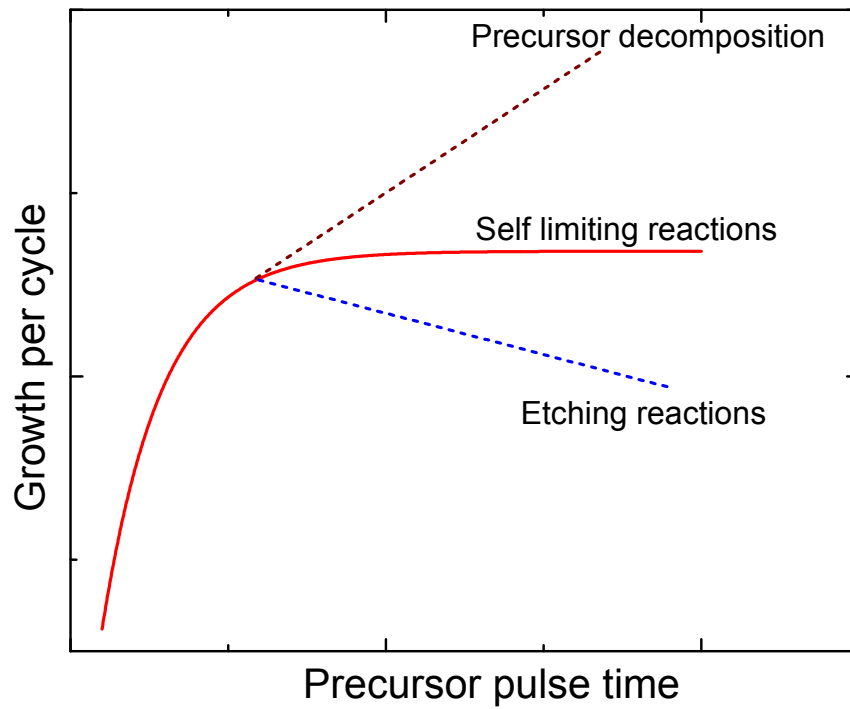
- (iv) ALD processes can be extremely slow, and the film thickness in one cycle is usually less than a monolayer. But with continuous Moore's scaling, the required film thickness has also decreased sufficiently to the point where low growth rate becomes a non-limiting factor.

## 2.3 Growth per cycle

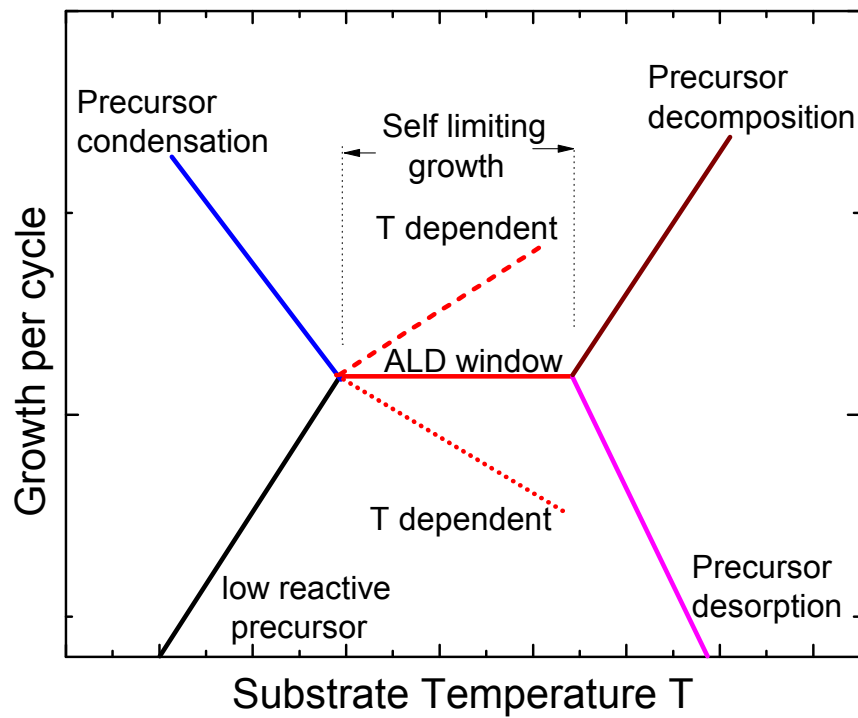
Growth per cycle is the thickness of the deposited material in one cycle. The growth per cycle depends on the reaction mechanism, number of active sites and steric hindrance of ligands [28]. Usually growth per cycle is less than a monolayer of the film because of steric hindrance effect. Steric hindrance is an effect where the ligands of the chemisorbed (adsorbed) precursor on the surface shield the active sites from the next available precursor molecule. In most cases, the larger the precursor ligands, the lower the growth per cycle. Maximum growth per cycle is obtained when highest number of active sites react through ligand exchange, releasing the highest number of ligands before being limited by steric hinderance.

## 2.4 Ideal ALD and other non ALD processes

Figure 2.2 shows the growth behaviour of an ideal ALD process and other non ALD processes as a function of precursor pulse and substrate temperature. It is important to note that for an ideal ALD process, the reaction is self limiting thus allowing accurate thickness control with the number of cycles (Figure 2.2a). It also deposits a monolayer of the material within a reasonable temperature window with excellent film conformality and releases by-products that can easily be purged. Usually growth of less than a monolayer is observed as a result of steric hindrance and reduction in surface reaction sites. A temperature window which gives a constant self limiting growth per cycle over a given temperature range is called the **ALD window**. However, the growth per cycle in the self limiting region (ALD) could also vary with temperature in some cases. ALD growth per cycle can be dependent on the deposition temperature due to temperature dependent number of surface reaction groups or precursor adsorption. This is often observed in deposition of oxide films, in which the surface hydroxyl group decompose at higher temperature into oxygen and water. In this case, the ALD growth per cycle decreases as deposition temperature is increased. The other case of increased ALD growth with temperature has been observed in deposition of some metals such as cobalt and copper (transition metals) [29] where metal precursor and hydrogen gas were used as reactants, noble metals such as ruthenium and irridium where metal precursor and oxygen gas were



(a) Growth per cycle against pulse time



(b) Growth per cycle against deposition temperature

Figure 2.2: Ideal ALD and other non ALD behaviour

used as reactant [30,31], as well as dielectrics such as antimony oxide [32,33] and antimony sulphide [32] where antimony precursor, ozone and hydrogen sulphide were used as reactant. For noble metal processes, the noble metal surface catalyses the oxygen gas molecule into oxygen atoms at higher temperature, thereby increasing the density of surface oxygen atoms and this explains the increase in ALD growth per cycle of noble metals with increased temperature. It might be that the reaction also need some other temperature activation in remaining cases of increased ALD growth per cycle with temperature. Non ideal ALD reactions such as precursor decomposition, etching reaction, precursor condensation, low reactive precursor, and precursor desorption are illustrated in Figure 2.2. In the case of a low reactive precursor, the reaction rate is temperature dependent, which means the precursor exposure is not long enough to achieve saturation. An excessively long precursor pulse time might achieve saturation for a low reactive precursor. A non ideal ALD process involving condensation of precursor would have higher growth per cycle at lower deposition temperature. While indication of precursor decomposition would be, when the growth per cycle increases indefinitely (non self limiting), as the precursor pulse time is increased without reaching saturation, at a particular temperature and also at elevated temperatures, because precursors can thermally decompose into the grown film adding to the expected ALD growth. Again, for etching reaction, the growth per cycle initially increases and then decreases with increase in precursor supply, indicating that the precursor is etching the film.

## 2.5 Requirements for ideal ALD precursors

Precursors are chemical reactants used to deposit materials by ALD processes. Usually, these precursors should meet some specific requirements to be suitable for ALD processes and the right choice of ALD precursors is quite important. These requirements are discussed below [34].

- (i) **Sufficient volatility:** ALD processes mostly require precursors to be in vapor phase when fed in to the reaction chamber. Gases and high vapor pressure liquids are preferred as ALD and CVD precursors because they can be easily contained in large volume and can be drawn in high fluxes into the reaction chamber. Although low vapor pressure solid sources can also be used, they can only be loaded into small volume and might need frequent reloading after usage, which is often inconvenient. In addition, there could also be particle transportation by the carrier gas to the substrate if fine powders are used, which can introduce particulate defect in the film.
- (ii) **Thermal stability without self decomposition:** Precursor should not decompose on the substrate upon adsorption at the deposition temperature in order to keep the self limiting property of ALD. It should also not decompose in the lines and

in the precursor bubbler as well, therefore a knowledge of precursor decomposition temperature is useful to decide all the chamber temperatures (lines, container and substrate). Metal halides are best choices with respect to thermal stability while metal organic compounds are often limited to temperature below 300 °C [34]. In some cases, thermal decomposition of precursor can result in the same film as the ALD grown film. In such cases, little precursor thermal decomposition might be tolerated. However it should be noted that thermal decomposition can also introduce impurities into the grown film, and as such precursor decomposition should be minimized.

- (iii) **Quick and complete chemical reactions:** Unlike CVD, precursors are dosed one at a time in ALD with an intermediate purge step, thereby eliminating gas phase chemical reactions. This allows the use of highly reactive precursors in ALD and it becomes beneficial to use aggressive precursors since chemical reactions can reach completion within short time. Also, ALD precursors should have complete reactions such that no impurities are incorporated into the film.
- (iv) **No etching reactions:** Ideal ALD precursors should not etch the film or the substrate because this can reduce the film uniformity and might destroy the whole process.
- (v) **No precursor dissolving in the film or the substrate:** Precursor should chemisorb and not dissolve in the substrate or the film.
- (vi) **Unreactive and volatile by – products:** Ideal ALD precursors should also produce a mild by-product which can be easily purged from the chamber. The by-products can in some cases be re-adsorbed onto the film or block the reaction sites if not efficiently purged. In worst case, it can also etch the film. Therefore the by-products of ideal precursors should be mild and volatile.
- (vii) **Other desirable requirements:** Some other requirements are purity, low cost, easy to handle and synthesize, non toxic and environmental friendly. Some of these specific requirements depend on applications, for instance semiconductor applications will require high purity precursors, while coating applications may not need high purity precursors. Cost of precursor depends on its demand which change over time. Also, in some cases dangerous chemicals cannot be fully avoided, for example pyrophoric precursors which are highly reactive, and as such special care and safety precaution must be taken in handling them.

## 2.6 Overview of ALD precursors types

On general basis, ALD precursors can either be a metal precursor or non metal precursor.

### 2.6.1 Metal precursors

Metal precursors are further sub classified as pure elements, metal halides, metal-organic and organometallic compounds.

#### Elemental precursors

The first ALD processes used either volatile elements such as zinc and sulfur, [24, 34] and non metal halides. Pure elements are less volatile and are therefore limited in usage or might require the use of very high deposition temperatures. Only cadmium, mercury and zinc have reasonable vapor pressure at low temperature. However, growth per cycle may be quite high because there is no steric hindrance limitation with elemental precursor.

#### Metal-halides

These precursors contain direct bond between metal and halogen such as metal-chloride, metal-bromide, metal-iodide and metal-fluoride. They are usually reactive precursors and thermally stable at high temperature but with the disadvantage of yielding corrosive reaction products such as acids, which could possibly etch the film, chamber lines and walls. Example is  $\text{TiCl}_4$  which has been used in deposition of titanium [35]. In some cases, metal halide can also have oxygen coordination atom, for instance tungsten oxyfluoride,  $\text{WOF}_4$  was used instead of  $\text{WF}_4$  for the deposition of  $\text{WO}_3$  because  $\text{WF}_4$  gives more problematic corrosive products than  $\text{WOF}_4$  [36].

#### Organometallic precursors

Organometallic precursor do have at least one direct carbon to metal bond. Two common examples are metal alkyl (Figure 2.3a) and metal cyclopentadienyl (Figure 2.3b). Metal alkyls of the periodic table from group 12 to 14 have been widely studied. The group 12 to 14 metal alkyls are highly reactive, pyrophoric and volatile. A popular example is trimethylaluminum, which has been successfully used together with water, ozone and oxygen radicals for the deposition of aluminum oxide.  $\text{Al}_2\text{O}_3$  deposition from trimethylaluminum and water is usually taken as the ideal ALD process, because the surface reaction mechanism is well understood [28]. Metal cyclopentadienyl is another choice of organometallic precursor, for example hafnium and zirconium cyclopentadienyl together with water or ozone have been used for the deposition of high-k oxides [37, 38].



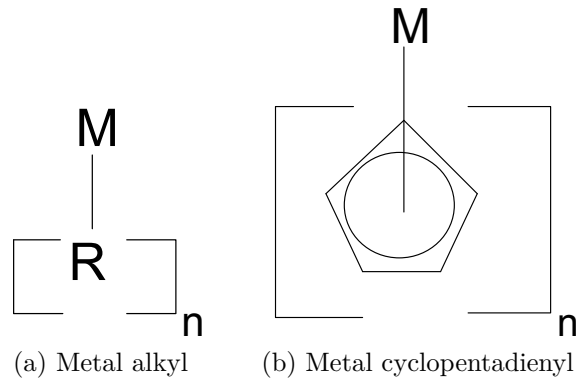


Figure 2.3: Organometallic precursors

### Metal-organic precursors

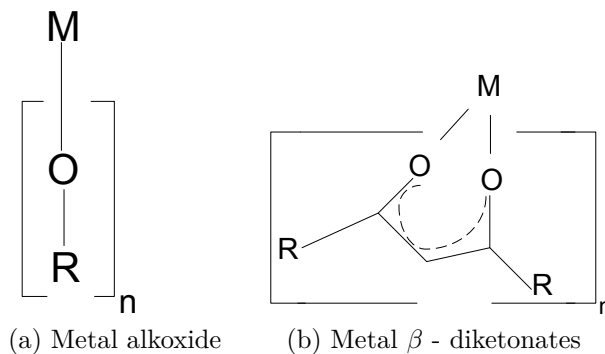


Figure 2.4: Oxygen coordinated metal-organic precursors

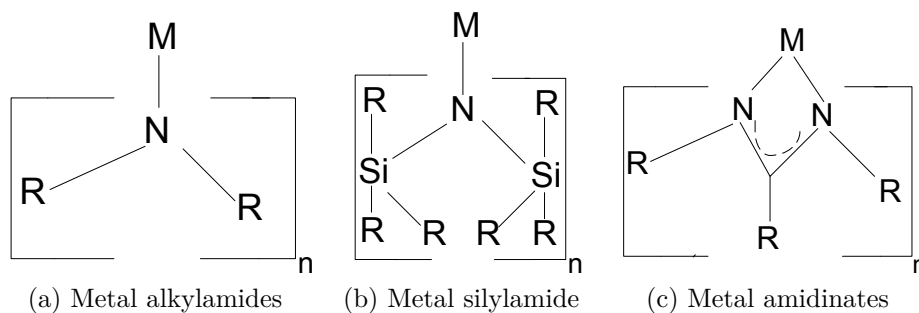


Figure 2.5: Nitrogen coordinated metal-organic precursors

Metal-organic precursors contain metal and some organic compounds. Usually in this case, there is no direct metal to carbon bond, rather the compound is coordinated by some other elements such as oxygen or nitrogen. Common examples of oxygen coordinated metal organic precursors are metal alkoxide (Figure 2.4a) and metal  $\beta$ -diketonates (Figure 2.4b). Metal alkoxides are moderately reactive and thermally stable up to 250 °C [34] and have been used for deposition of some metal oxides, for instance  $\text{Ti}(\text{OMe})_4$  [39,40] and  $\text{Al}(\text{OEt})_3$  [40,41] were used for  $\text{TiO}_2$  and  $\text{Al}_2\text{O}_3$  deposition respectively. Besides

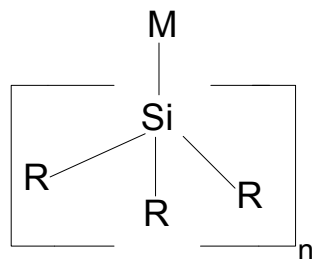


Figure 2.6: Silicon coordinated metal-organic precursors: Metal alkylsilyl

silicon alkoxide,  $\text{Si}(\text{OEt})_4$  has been used for growing mixed oxides or incorporating silicon atom into another film.  $\text{AlSi}_x\text{O}_y$  was grown from  $\text{Al}(\text{Me})_3$ ,  $\text{Si}(\text{OEt})_4$  and  $\text{O}_2$  plasma [42]. Volatile metal  $\beta$ -diketonates can be found for nearly all metals [43] and have been used for deposition of metal oxides [44], metal sulphides [45] and pure noble metals [13]. Some categories of nitrogen coordinated metal organic precursors are metal alkylamide, metal silylamide and metal amidinates (Figure 2.5). Metal alkylamide has wide range of precursors available for different elements but with limited thermal stability as required for ALD precursors. Alkylamides have been widely used for deposition of oxides with ozone, water and oxygen radicals as reactants. Metal acetamidinates with molecular hydrogen as reducing agent have been used for the deposition of transition metals such as Fe, Co, Ni and Cu [29]. There could also be coordination from other elements such as silicon, as shown in Figure 2.6, which gives metal alkylsilyl. Alkylsilyl of tellurium and selenium with a metal halide as the second precursor was used for the deposition of corresponding metal selenides and tellurides [46].

## 2.6.2 Non-metal precursors

Common non-metal precursors are hydrogen, nitrogen, chalcogenide and oxygen sources.

### Hydrogen sources

Hydrogen is used as reducing agent for depositing metals. Molecular hydrogen is less reactive at low temperature and can only be used as reducing agent on catalytic surfaces or in form of hydrogen plasma radicals. In addition, some other reducing agents have also been used in ALD such as Zn vapor [47], silanes [48], trimethyl aluminum [49] and borane [50].

### Nitrogen sources

Nitrogen itself is usually inert and often used as carrier gas and for purging.  $\text{NH}_3$  is often the nitrogen source and reducing agent used for deposition of nitride films. In addition, plasma activated  $\text{NH}_3$  or nitrogen can also improve the reactivity. Some other nitrogen sources are  $\text{N}_2\text{H}_4$ ,  $(\text{CH}_3)_2\text{NNH}_2$ ,  $^t\text{BuNH}_2$  and  $\text{CH}_2\text{CHCH}_2\text{NH}$  [51].

## Chalcogenide sources

Elemental chalcogens such as Te, Se and S are less reactive and they can only be used in ALD process provided the other precursor is volatile and reactive enough [51,52]. Hydrides of these chalcogens such as  $H_2S$ ,  $H_2Se$  and  $H_2Te$  are found to be more reactive but they are extremely toxic and their alkyl compound derivative is usually found as substitute [27].  $H_2S$  has also been generated in-situ during the ALD process from decomposition of thioacetamide [53].

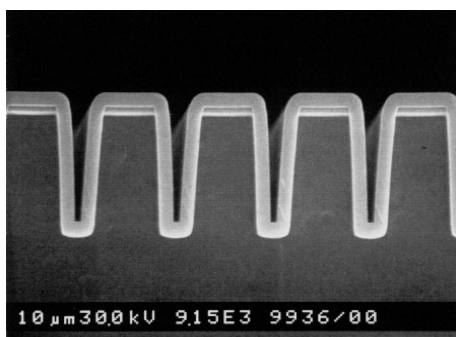
## Oxygen sources

Molecular oxygen is also quite inert unless in some exceptional cases where a catalytic surface breaks down the molecular oxygen into atomic oxygen. Ozone and oxygen plasma (atomic oxygen or oxygen radical) are the common pure oxygen sources used in ALD. Some other oxidizing source are water ( $H_2O$ ), hydrogen peroxide ( $H_2O_2$ ), nitrogen oxide ( $N_2O$ ) and in some cases alcohol [54].

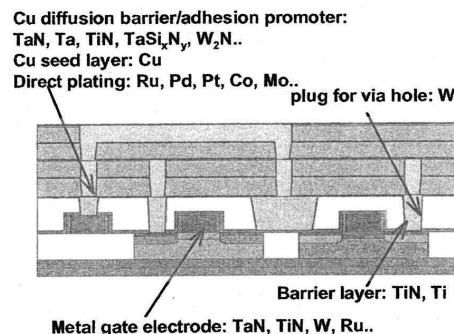
## 2.7 Applications of thin films deposited by ALD

Atomic layer deposited films of different categories with examples are shown in Table 2.2. Detailed references of the possible precursor combination to give those films can be found in [40] and [27]. Some applications of atomic layer deposited films are discussed below.

- (i) **Integrated circuits fabrication** : Some application areas of films deposited by ALD in IC fabrication include the use of high-k dielectric oxides such as  $HfO_2$ ,  $ZrO_2$  and  $Al_2O_3$  as gate oxides in MOSFETs and as capacitor dielectric in dynamic random access memories (DRAM) in order to obtain higher capacitances with thicker oxide thicknesses thereby reducing electron tunneling leakage current through the oxide.



(a)  $Al_2O_3$  ALD on high aspect ratio [26,55], a potential high-k dielectric material for gate oxide in MOSFETs



(b) Applications of metal and metal nitrides ALD [56]

Figure 2.7: Application of ALD in IC fabrication

Table 2.2: Categories of thin films deposited by ALD [34]

| Categories                      | Examples   |
|---------------------------------|--|
| Oxides                          |  |
| Dielectric                      | $\text{Al}_2\text{O}_3$ , $\text{Sb}_2\text{O}_5$ , $\text{B}_2\text{O}_3$ , $\text{HfO}_2$ , $\text{Ta}_2\text{O}_5$ , $\text{Nb}_2\text{O}_5$ ,<br>$\text{SiO}_2$ , $\text{Y}_2\text{O}_3$ , $\text{MgO}$ , $\text{GeO}_2$ , $\text{La}_2\text{O}_3$ , $\text{CeO}_2$ ,<br>$\text{PrO}_x$ , $\text{Nd}_2\text{O}_3$ , $\text{Sm}_2\text{O}_3$ , $\text{EuO}_x$ , $\text{Gd}_2\text{O}_3$ , $\text{Dy}_2\text{O}_3$ ,<br>$\text{Ho}_2\text{O}_3$ , $\text{Er}_2\text{O}_3$ , $\text{Tm}_2\text{O}_3$ , $\text{Yb}_2\text{O}_3$ , $\text{Lu}_2\text{O}_3$ , $\text{SrTiO}_3$ ,<br>$\text{BaTiO}_3$ , $\text{PbTiO}_3$ , $\text{PbZrO}_3$ , $\text{Bi}_x\text{Ti}_y\text{O}$ , $\text{Bi}_x\text{Si}_y\text{O}$ , $\text{SrTa}_2\text{O}_6$ ,<br>$\text{SrBi}_2\text{Ta}_2\text{O}_9$ , $\text{YScO}_3$ , $\text{LaAlO}_3$ , $\text{NdAlO}_3$ , $\text{GdScO}_3$ , $\text{LaScO}_3$ ,<br>$\text{LaLuO}_3$ , $\text{Er}_3\text{Ga}_5\text{O}_{13}$ |
| Conducting and / semiconducting | $\text{Ga}_2\text{O}_3$ , $\text{In}_2\text{O}_3$ , $\text{In:ZnO}$ , $\text{In}_2\text{O}_3:\text{Sn}$ , $\text{In}_2\text{O}_3:\text{F}$ , $\text{In}_2\text{O}_3:\text{Zr}$ ,<br>$\text{SnO}_2$ , $\text{SnO}_2:\text{Sb}$ , $\text{ZnO}$ , $\text{ZnO:Al}$ , $\text{ZnO:B}$ , $\text{ZnO:Ga}$ ,<br>$\text{RuO}_2$ , $\text{RhO}_2$ , $\text{IrO}_2$ , $\text{V}_2\text{O}_5$ , $\text{WO}_3$ , $\text{W}_2\text{O}_3$ ,<br>$\text{NiO}$ , $\text{FeO}_x$ , $\text{CrO}_x$ , $\text{CoO}_x$ , $\text{MnO}_x$  |
| Other ternaries                 | $\text{LaCoO}_3$ , $\text{LaNiO}_3$ , $\text{LaMnO}_3$ , $\text{La}_{1-x}\text{Ca}_x\text{MnO}_3$  |
| Nitrides                        |  |
| Semiconductor/dielectric        | $\text{AlN}$ , $\text{GaN}$ , $\text{InN}$ , $\text{BN}$ , $\text{Cu}_3\text{N}$ ,<br>$\text{Zr}_3\text{N}_4$ , $\text{Hf}_3\text{N}_4$ , $\text{SiN}_x$ , $\text{Ta}_3\text{N}_5$   |
| Metallic                        | $\text{TiN}$ , $\text{Ti-Si-N}$ , $\text{Ti-Al-N}$ , $\text{TaN}$ , $\text{NbN}$ ,<br>$\text{MoN}$ , $\text{WN}_x$ , $\text{WN}_x\text{C}_y$   |
| Element                         | $\text{Ag}$ , $\text{Cu}$ , $\text{W}$ , $\text{Si}$ , $\text{Ge}$ , $\text{Ru}$ , $\text{Pt}$ , $\text{Ir}$ ,<br>$\text{Pd}$ , $\text{Rh}$ , $\text{Co}$ , $\text{Fe}$ , $\text{Ni}$ , $\text{Mo}$ , $\text{Ta}$ , $\text{Ti}$ , $\text{Al}$  |
| II-VI compounds                 | $\text{ZnS}$ , $\text{ZnSe}$ , $\text{ZnTe}$ ; $\text{CaS}$ , $\text{SrS}$ , $\text{BaS}$<br>$\text{CdS}$ , $\text{CdTe}$ , $\text{MnTe}$ , $\text{HgTe}$  |
| II-VI based TFEL phosphors      | $\text{ZnS:M}$ ( $\text{M}=\text{Mn,Tb,Tm}$ ), $\text{CaS:M}$ ( $\text{M}=\text{Eu,Ce,Tb,Pb}$ ),<br>$\text{SrS:M}$ ( $\text{M}=\text{Ce,Tb,Pb}$ )  |
| III-V compounds                 | $\text{GaAs}$ , $\text{AlAs}$ , $\text{AlP}$ , $\text{InP}$ , $\text{GaP}$ , $\text{InAs}$   |
| Fluorides                       | $\text{CaF}_2$ , $\text{SrF}_2$ , $\text{MgF}_2$ , $\text{LaF}_3$ , $\text{ZnF}_2$   |
| Others                          | $\text{La}_2\text{S}_3$ , $\text{PbS}$ , $\text{In}_2\text{S}_3$ , $\text{Cu}_x\text{S}$ , $\text{CuGaS}_2$ , $\text{Y}_2\text{O}_2\text{S}$ ,<br>$\text{WS}_2$ , $\text{TiS}_2$ , $\text{SiC}$ , $\text{TiC}_x$ , $\text{TaC}_x$ ,<br>$\text{WC}_x$ , $\text{Ca}_x(\text{PO}_4)_y$ , $\text{CaCO}_3$ , $\text{Ge}_2\text{Sb}_2\text{Te}_5$  |

In addition, deposition on high aspect ratio structures may be necessary to increase the capacitance cross sectional area. ALD can be extremely conformal and this favours the deposition of high-k dielectrics on high aspect ratio structures (see Figure 2.7a). Metallic nitrides films by ALD such as TiN and  $\text{W}_2\text{N}$  are used as diffusion barrier and adhesion promoter (see Figure 2.7b) in interconnects while

ALD of metal seed layers such as Cu seed layer is used for Cu electroplating in high aspect ratio structures required for IC metallization in Cu damascene process. ALD of low k dielectric such as  $\text{SiO}_2$  is also required in multi-level interconnects for electrode insulation and reduction of inter-electrode capacitances. Recently, ALD of ZnO [57] and GaN [58] has been used as active material for the fabrication of thin film phototransistors. ALD has also been proposed for fabrication dopant layers suitable for solid state diffusion doping in high aspect ratio structures [3], [59].

(ii) **Solar cells :**

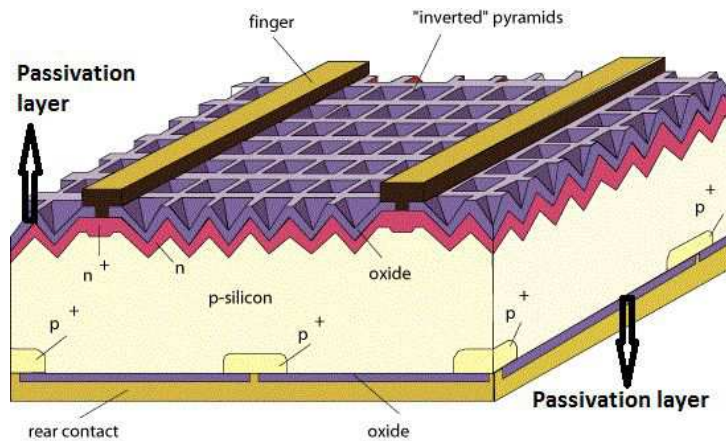
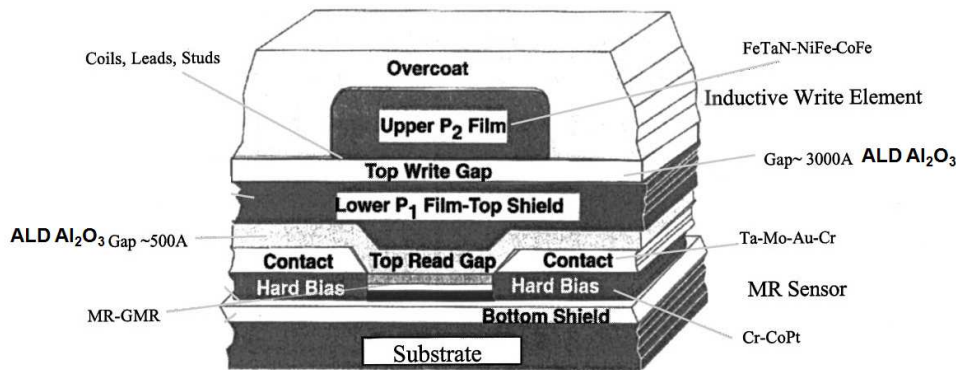


Figure 2.8: Solar cell passivation [60]

One critical limitation of solar cells is recombination of charge carriers at the interfaces due to high surface defects density. Films deposited by ALD are being used for surface passivation in solar cells to reduce carrier recombination (Figure 2.8). ALD of  $\text{Al}_2\text{O}_3$  and recently  $\text{Ga}_2\text{O}_3$  [61] can effectively field - passivate highly doped p-type Si emitter mainly because it has high density of negative oxide charges. Where as  $\text{SiO}_2$  can passivate both n and p type Si mainly because it reduces its interface defects. ALD of  $\text{SiN}_y$  can effectively passivate highly doped n-type Si because of high density of positive oxide interface charges. Besides, ALD of  $\text{SiN}_y$  can serve as anti-reflection coatings in solar cells. In addition, transparent and conducting oxides such as  $\text{InO}_2:\text{Sn}$  and  $\text{In}:\text{ZnO}$  [62] are used for coating the front side of solar cells. II-VI materials deposited by ALD such as CdTe and CdS [63] can be used as buffer layer material in solar cell fabrication.



(a) Hard disk drive [64]



(b) Cross section of a thin film magnetic head [65]

Figure 2.9: ALD  $\text{Al}_2\text{O}_3$  for thin film magnetic head fabrication used in hard disk drives

(iii) **Magnetic devices** : ALD of  $\text{Al}_2\text{O}_3$  meet all the essential dielectric requirements for magnetic heads which are perfect conformality, high breakdown strength (9 - 10 MV/cm), low leakage current and low compressive film stress ( $< 200$  MPa) [65]. Atomic layer deposited  $\text{Al}_2\text{O}_3$  is therefore used for insulating dielectric gaps in magnetic thin film heads (Figure 2.9b) required to read and write data in modern hard disk drives (Figure 2.9a).

(iv) **Thin film electroluminescent displays** :

The birth of ALD in the mid 70's was because of the need for production of dense and pinhole-free thin film electroluminescent coating on large surface areas. This is because pinhole and low density film makes electroluminescent displays more susceptible to breakdown at higher electric fields. The thin film materials deposited by ALD required for fabrication of electroluminescent displays (Figure 2.10) are  $\text{ZnS:Mn}$  as the electroluminescent layer,  $\text{Al}_2\text{O}_3$  or  $\text{Al}_x\text{Ti}_y\text{O}$  as insulators and  $\text{Al}_2\text{O}_3$  as passivation and protective layers [34].



Figure 2.10: Thin film electroluminescence display [66]

- (v) **Optical coatings** : Thanks to its perfect conformality, the ALD method can be used for interference coatings in optics such as anti-reflection coating and highly reflective coatings. One application already mentioned is in solar cells, where anti-reflection coatings are usually required on the front side for perfect light absorption into the solar cell. ALD of multi-layer interference coatings have been applied for optical wavelength from infra-red, through visible to soft and hard x-ray region [34,67–70]. However, lack of general commercial adoption of ALD in optical coatings may be due to slow ALD deposition speed as well as high equipment costs.
- (vi) **Protective coatings** : Atomic layer deposited films can be used as a protective coatings against corrosion or chemical attack. Some materials such as silver and stainless steel do not lose their appearance when coated with thin  $\text{Al}_2\text{O}_3$  (less than 10nm) layer and this will prevent the materials from tarnishing.
- (vii) **Heterogenous catalysts and photo – catalysts** : Heterogenous catalysts are made from high surface area templates for instance silica or alumina spheres coated with some other additives to achieve the desired catalytic property. Deposition of catalytic additives by ALD could give conformal growth on the high surface area templates resulting in homogeneous particle sizes. Some metal oxides such as  $\text{TiO}_2$ ,  $\text{Al}_2\text{O}_3$ ,  $\text{ZrO}_2$  and  $\text{CeO}_2$  (cerium oxide) as well as noble metals such as Pt, Rh, Ru, Ir and Ag do have catalytic properties [71].  $\text{TiO}_2$  is photocatalytic.
- (viii) **Coating of temperature – sensitive and arbitrary – shaped substrates** : Substrates of different shapes can be coated by ALD. Industrial ALD for coating porous powders (particles) requires special reactor design such as fluidized bed reactor design having a particle - holding porous cylinder with a particle filter [71]. The use of plasma radicals and some other highly reactive precursors in ALD processes also makes it possible to develop low temperature ALD processes which is suitable for coating temperature sensitive substrates such as polymers. Cotton fibers and

paper substrates were coated with atomic layer deposited ZnO film with effective conductivity up to  $24 \text{ S} \cdot \text{cm}^{-1}$  obtained for the deposited films [5]. Low temperature ALD of oxide films such as  $\text{Al}_2\text{O}_3$  can also be used to passivate organic (temperature sensitive) light emitting diode (OLED) displays.

- (ix) **Micro electro – mechanical system (MEMS)** : Reliability of silicon based MEMS devices can be degraded because of mechanical wear, stiction, fatigue, shock as well as oxidation and impurity diffusion. ALD coating of  $\text{Al}_2\text{O}_3$  has been used as wear resistant [72] and as insulating dielectric to prevent short circuit [73],  $\text{WS}_2$  as solid lubricant [74] and  $\text{Al}_2\text{O}_3/\text{ZnO}$  alloy for charge dissipation [75] in MEMS devices.

## 2.8 Hardware requirements for ALD processes

Atomic layer deposition system hardwares for semiconductor technology should generally include the following:

- (i) **Loadlock, handling and transfer system** : The substrate to be coated is inserted in the loadlock. This can be a silicon wafer with certain diameter size. In some cases sample substrates could also be placed on a carrier wafer. Modern ALD systems have an automated handling system for transfer of wafer back and forth from the loadlock into the reaction chamber.
- (ii) **ALD reactor or reaction chamber** : The reaction and deposition takes place in the ALD reactor. It is usually a vacuum chamber with heated substrate holder (susceptor), on which the substrate is placed. The temperature of the substrate is controlled automatically. ALD reactor walls are also sometimes heated up to certain temperature to avoid precursor condensation on the walls.
- (iii) **Precursor source, delivery and purge lines** : ALD is a chemical process and thus there are precursor sources, which can be held in heated precursor bottles or simply gas lines. There is also heated delivery line from the precursor bottle to the reactor. Precursor dosage is controlled by opening and closing of fast acting valves (ALD valves) from the delivery line to the ALD reactor. Precursor lines are also purged with an inert carrier gas.
- (iv) **Exhaust system** : The ALD reactor has an exhaust path in which reaction products are evacuated using a vacuum pump. The vacuum pump also maintains the reactor at low pressure. Loadlock and transfer systems are usually evacuated with a vacuum pump.
- (v) **Automation and control system** : Processes are controlled using computers or microcontrollers through an automation software interface which controls opening of



all valves and all other process parameters.

## 2.9 ALD reactor categories

ALD reactors could be categorized based on some criteria such as the reactor flow scheme, the precursor separation scheme and the substrate type.

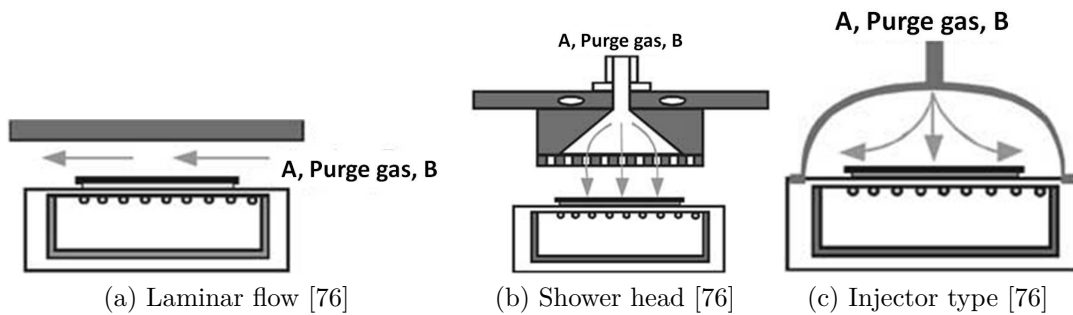


Figure 2.11: ALD reactor types based on flow scheme. A and B are precursors.

### 2.9.1 Reactor flow scheme

#### Laminar flow type

Laminar flow is shown in Figure 2.11a. Gas inlet is from the sides and flows across the wafer. The reaction volume is also quite small, which allows better purge. This scheme usually allows good precursor utilization efficiency. However, there could be thickness non-uniformity because of precursor depletion at the source inlet, making it less suitable for large area deposition.

#### Shower head type

Shower head type (Figure 2.11b) has gas inlet perpendicular to the substrate, through a shower head for uniform precursor flux distribution. The thickness non-uniformity is excellent but the purge is inefficient because of relatively large reactor volume and low conductance of the shower head holes, making it difficult to achieve a pure ALD process.

#### Injector type

This also has gas inlet perpendicular to the substrate but no shower head (Figure 2.11c). The structure is simple, maintenance is easier, there is no precursor depletion over large area substrate and uniformity is also good. However the chamber volume has to be minimized for better precursor utilization efficiency and lower purge times.

## 2.9.2 Precursor separation scheme

ALD reactor classification in this regard can be based on temporal or spatial separation of the precursors.

### Temporal ALD

This is the most common precursor separation scheme. The substrate location remain the same during ALD cycle but precursors are separated in time with an evacuation or purge step in between (Figure 2.12). The ALD reactor has to be connected to a vacuum pump for evacuation and purge. Precursor dose and process gases require accurate control and should be sufficient to saturate the surface. In addition, purge times should also be long enough to remove the remaining unreacted precursor and half reaction by-products. There is usually material deposition onto the chamber walls with this scheme.

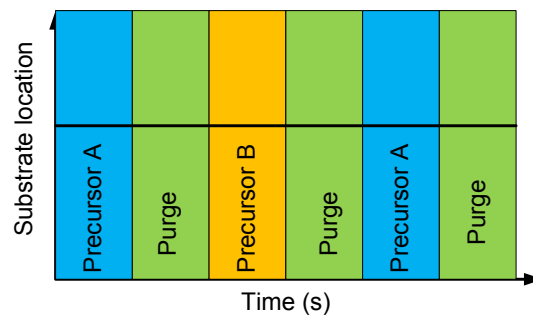


Figure 2.12: Temporal atomic layer deposition

### Spatial ALD

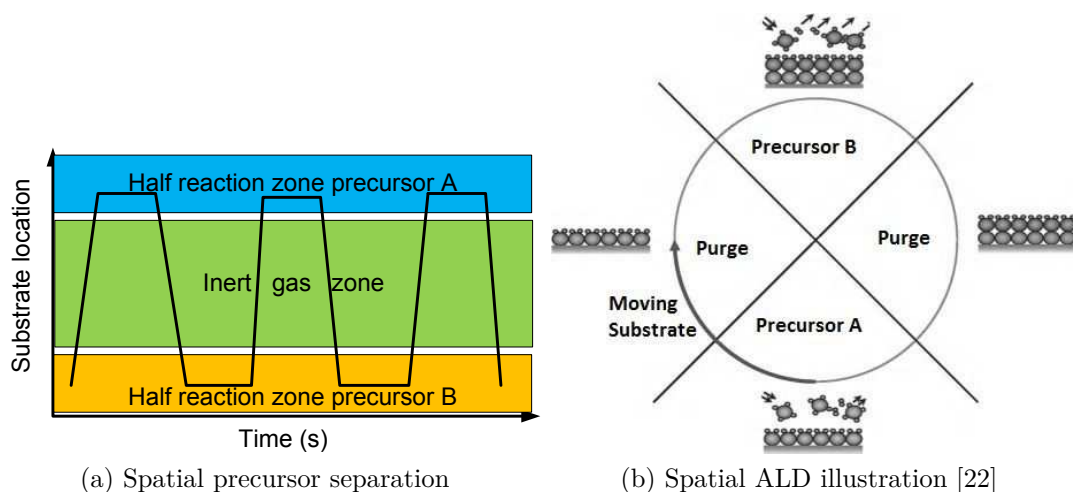


Figure 2.13: Spatial atomic layer deposition

The earlier reactor used for ALD was based on spatial ALD [23]. In this scheme, substrate position moves within different spatially separated zones during the reaction

cycle. There are four zones (Figure 2.13); half reaction zone for precursor A, inert gas zone for precursor A purge, half reaction zone for precursor B and inert gas zone for precursor B purge. Gas flows are static in each zone, which means there is no time spent in filling and purging of the chamber. The process speed is limited by the speed at which the substrate moves and the reaction speed (kinetics). The precursors are physically separated and deposition will only take place on the substrate and not on the reactor chamber walls. In this way, precursors are also better utilized and there should be no particulate film contamination through redeposition from the chamber walls.

### 2.9.3 Other special reactor design

Porous particles need special reactor design to hold and uniformly coat the particles.

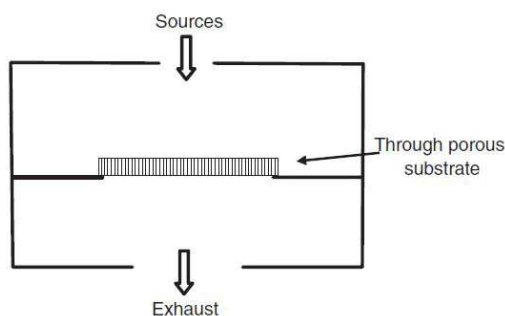


Figure 2.14: Flow-through reactor design for porous substrates [34]

Flow-through reactor design (Figure 2.14) can be used for samples that have pores. Precursor can flow through the sample allowing improved conformality. A form of flow-through reactor is the fluidized bed reactor design used for coating particles (powder) [71]. In this case, particles are held in a porous cylinder with a mesh filter and stirrer. The precursor flows through the porous cylinder while the stirrer prevents the particles from fusing together during the coating process. A rotating substrate can also be used for stirring. Flow-through reactor may consume a lot of precursor during the ALD process. A modified version is static flow [77] where precursor is filled into the chamber and “hold”, before pump down. Coating of non porous powder may be very difficult in terms of reactor design [34].

## 2.10 Precursor dosage scheme

ALD processes require efficient control of precursor dosage into the reactor. The source of precursor can be external, so it is placed in a bottle or bubbler outside the reaction chamber. In some cases precursor sources can also be internal, then it is placed in the same vacuum chamber as the substrate. Precursors can be solid, liquid or gas. Usually, liquid and gas precursor sources are preferred in ALD processes because of efficient transport in

vapor phase. Precursor vapor inlet into the chamber is usually controlled by opening and closing of fast solenoid or pneumatic mechanical valve valves in which the vapor can also be transported by an inert carrier gas. The opening time for the ALD valves can be as short as 10 ms for millions to tens of millions of cycles. For efficient gas transport cold traps are usually avoided by setting the line temperature higher than the bottle temperature. It is therefore necessary that the ALD valve can be operated at higher temperature, up to 150 °C at least. Special pneumatic valves can be operated at 200 °C to 250 °C which is considered to be the operation temperature limit [34]. There are several schemes of precursor dosage and the ultimate choice depends on the precursor vapor pressure. These are direct vapor draw, direct vapor draw with booster, bubbler system, and inert gas valving system.

### 2.10.1 Direct vapor draw

Precursors with sufficient vapor pressure (practically 10 mbar higher than reactor pressure) can be dosed with direct vapor draw system. Precursor can be filled in a simple bottle of a type shown in Figure 2.15b. Direct vapor draw scheme is shown in Figure 2.15a. ALD valves are indicated in the figure, in black color for opened valve and white for closed valve.

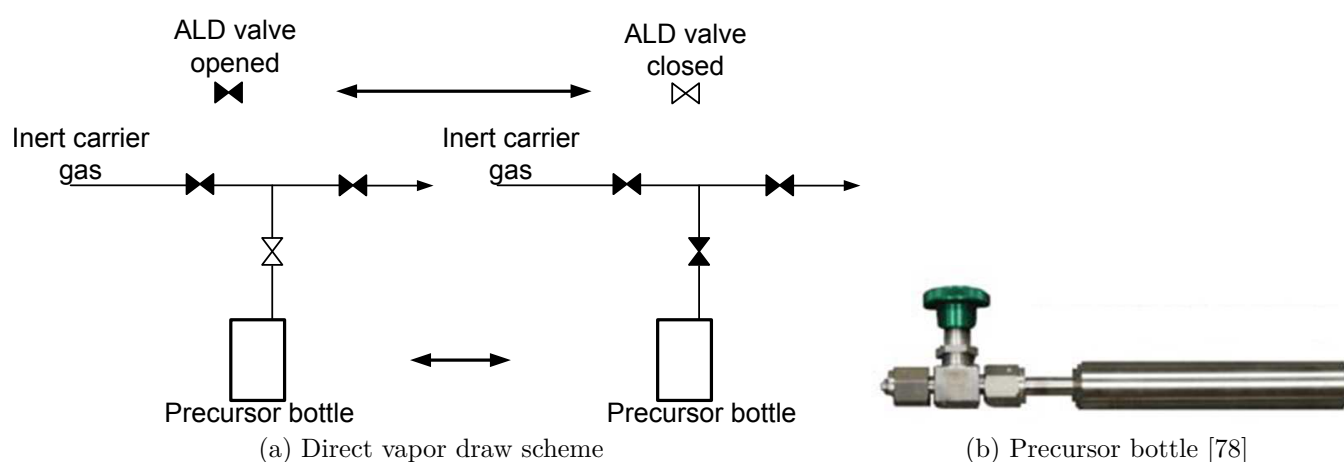


Figure 2.15: Direct vapor draw

The valves in line with arrow direction that lead to the reaction chamber (chamber not shown) must be opened first, with a preset inert carrier gas flow in the arrow direction as shown in Figure 2.15a. The ALD valve next to the bottle is simply opened during “ON” precursor pulse time and closed during “OFF” precursor pulse time.

### 2.10.2 Direct vapor draw with booster

When the precursor vapor pressure is lower or approximately equal to the chamber pressure, then it is not possible to use a simple direct draw scheme. Instead a direct vapor draw with



Figure 2.16: Vertical electropolished stainless steel bubbler [78]

booster can be used in such situation (precursor vapor pressure  $\leq$  reactor pressure). The key point in this scheme is that the precursor bottle has to be filled with inert carrier gas to boost its total pressure before drawing like a direct vapor draw. Suppose the precursor is filled in a bubbler of a type shown in Figure 2.16, with one inlet port and one outlet port, direct vapor draw with booster is illustrated in Figure 2.17.

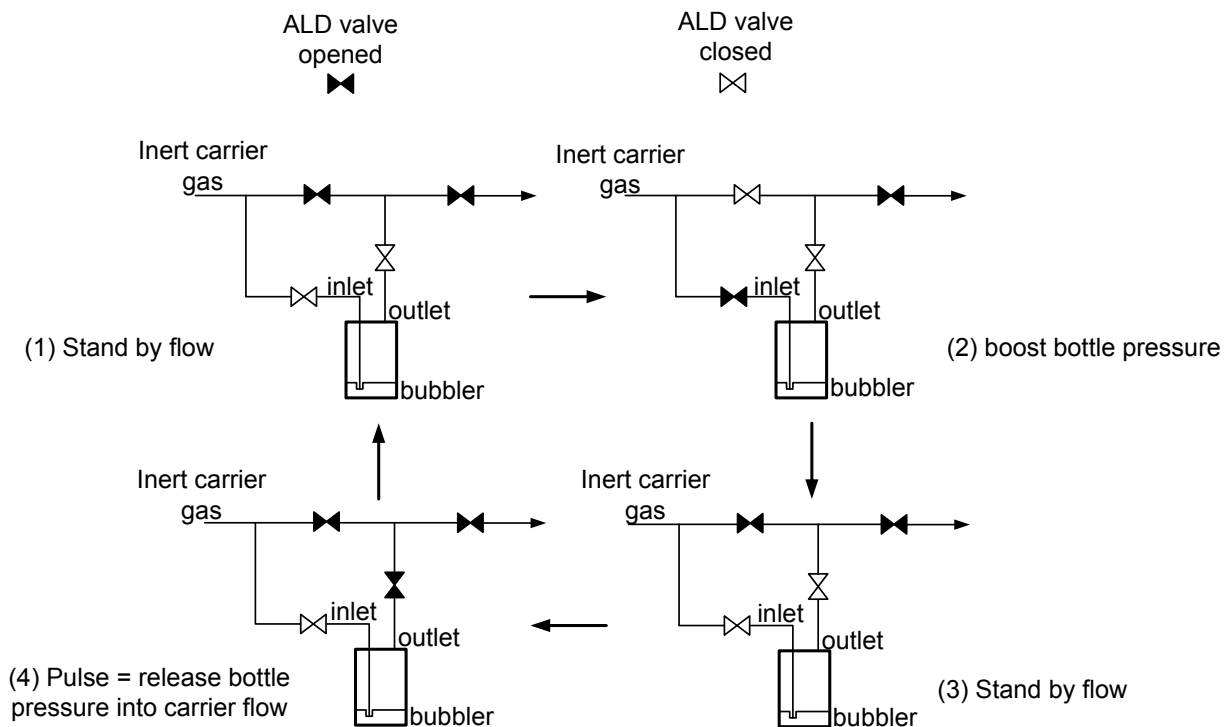


Figure 2.17: Direct draw with booster

The first step is to set an inert carrier gas flow into the chamber (valves in line with arrow direction in Figure 2.17 opened), then the bubbler is filled with inert carrier gas for short time (1 s to 2 s) through the bubbler inlet to boost the bottle pressure, after which the bubbler inlet valve is closed while the inert carrier gas is directed back to the chamber, and finally the mixture of vapor and inert booster gas is drawn by opening the outlet (ALD) valve.

### 2.10.3 Precursor bubbling system

A bubbling system can be used for very low vapor pressure precursor when the precursor vapor pressure is smaller than the reactor pressure. Also, a bubbler of a type shown in Figure 2.16 can be used for precursor bubbling. There is an inlet port with a dip tube going inside the bubbler and an outlet port. Precursor bubbling system is shown in Figure 2.18, the inert carrier gas flow is set into the chamber in the first step, and next the inlet and the outlet ALD valves are simultaneously opened during precursor “ON” times. This allows the carrier gas to flow through the bubbler and mix with the precursor into the chamber. In other words the direction of carrier flow is switched through the precursor bubbler during precursor “ON” times.

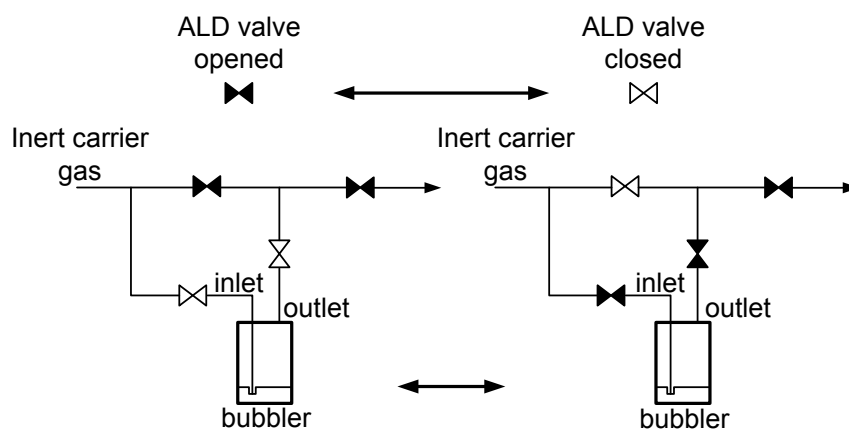


Figure 2.18: Bubbling system

### 2.10.4 Inert gas valving

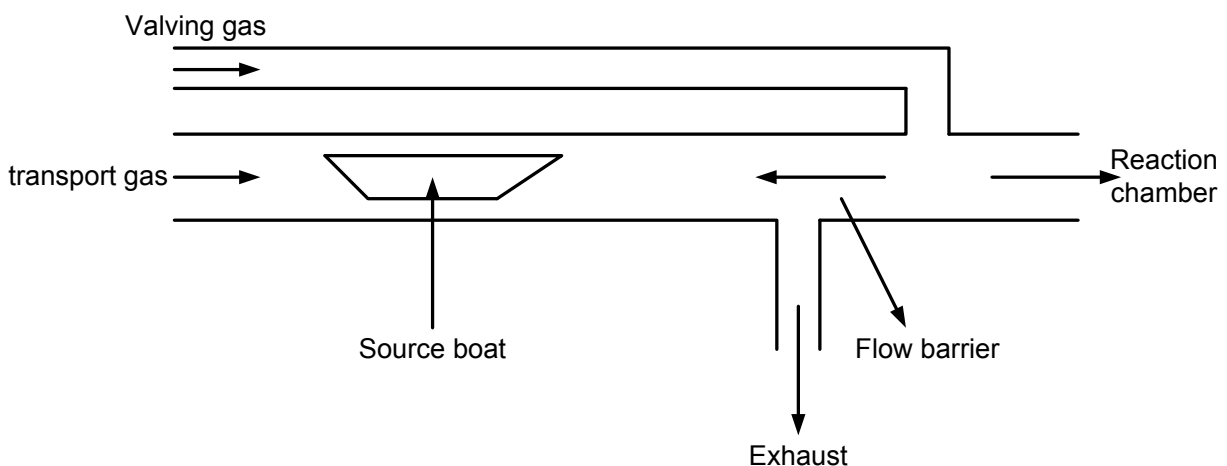


Figure 2.19: Illustration of inert gas valving [34]

Inert gas valving system (Figure 2.19) can be used as well for low vapor pressure precursor typically less than 1 mbar. In such case, the precursor source is placed in an

open boat in the same vacuum as the substrate (internal precursor source). The valving system as the name suggests does not require a mechanical valve, but an inert gas flow is used to control the flow of the precursor. There is a transport gas over the precursor and a valving gas in between the chamber and the precursor. During precursor “ON” time, transport gas is “ON” while valving gas is “OFF”. While during precursor “OFF” time, transport gas is “OFF” while valving gas is “ON”.

## 2.11 Plasma-assisted atomic layer deposition

As earlier described in section 2.2, ALD is a modification of chemical vapor deposition processes where the surface is exposed to individual reactants (precursors) separately with an intermediate purge step in between. A plasma-assisted ALD process is an energy-enhanced process in which the second half ALD cycle utilizes energetic particles and radicals in the reaction process (Figure 2.20). The common plasma gases used in ALD processes are hydrogen, oxygen, ammonia and nitrogen.

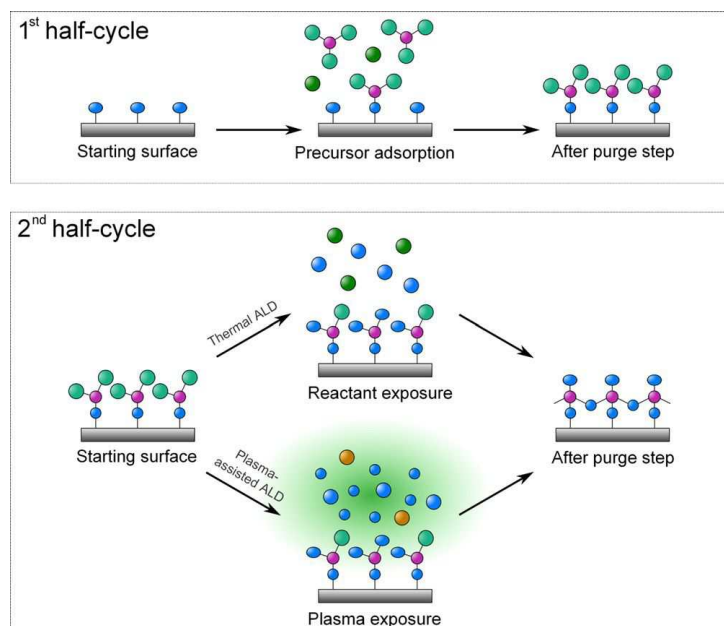


Figure 2.20: Plasma-assisted and thermal atomic layer deposition processes [79]

The plasma radicals typically replace thermal ALD precursors such as  $\text{H}_2\text{O}$ ,  $\text{O}_3$  and  $\text{NO}_2$  in ligand exchange reactions.

### 2.11.1 Physics of plasma

In physics, plasma is often taken as the fourth state of matter because it is created by supplying some form of energy to neutral gas molecules. A plasma is a partially ionized gas which contains electrons, ions (positive and negative) as well as neutral atoms and molecules. On the average plasma is electrically neutral, that is the total density

of electrons and negative ions is equal to density of positive ions [79, 80]. Methods of supplying energy to gas molecules for plasma generation are shown in Figure 2.21. One way is to supply thermal energy, for example in flames where the gas molecules undergo exothermic chemical reaction. Another method is thermal heating of gas into plasma through adiabatic compression of gas molecules. Gas molecules can also be ionized into plasma when bombarded with energetic particles such as electrons, photons, neutrons and ions. While charged particles can be affected by surrounding electric field, neutral particles have the advantage of not being perturbed by electric and magnetic fields.

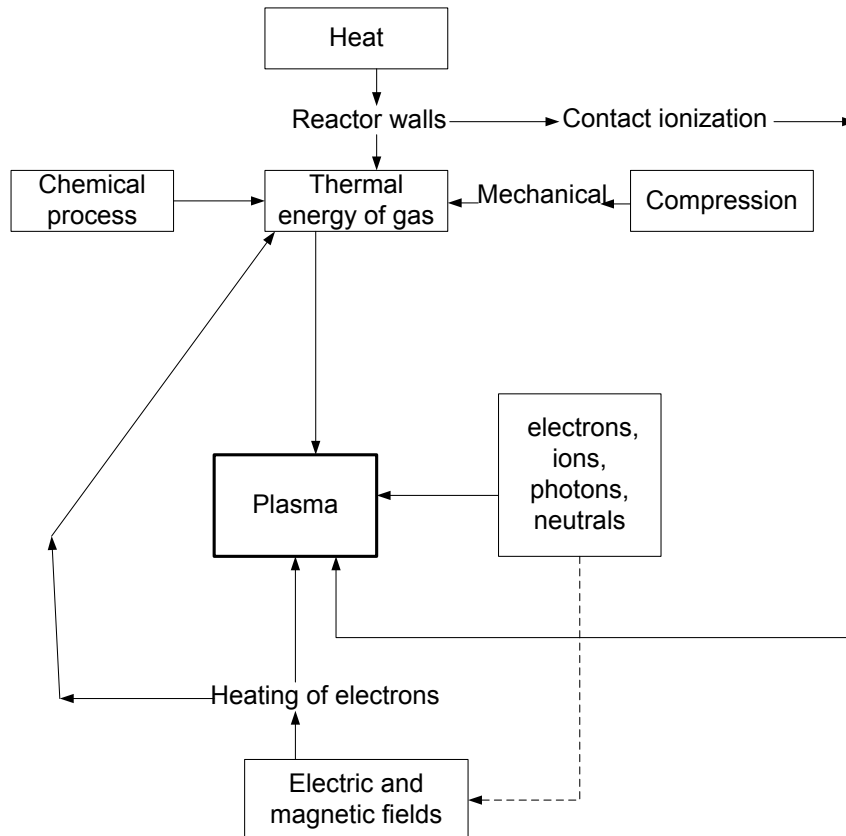


Figure 2.21: Plasma generation principles: Adapted from [81]

Plasma can also be generated by supplying electric or magnetic field directly to neutral gas. Plasma can be categorized into hot plasma and cold plasma.

### Hot plasma

Hot plasma has electrons, ions and neutrals at the same equilibrium energy (temperature). Nearly all the gas molecules are fully ionized in hot plasma.

### Cold plasma

In cold plasma, only a fraction of the gas is ionized. The most common way of generating cold plasma is by using electric or magnetic fields as the energy source. Any volume of



neutral gas will have some few electrons and ions present in it, and these electrons and ions are accelerated in the presence of electric or magnetic field. Electrons will usually have higher kinetic energy than heavier ions. The accelerated electrons will gain sufficient kinetic energy to ionize more neutrals through collision with the neutral gases creating avalanche of charge carriers. The avalanche of charge carriers is also balanced by loss of charge carriers and resulting in a steady state plasma. The hot electrons do not only ionize, they can also dissociate and excite neutrals through impact collision. This result in formation of highly reactive plasma radicals (atomic and molecular neutral), ions and photons. The degree of ionization is usually very low in typical processing plasma (in the range of  $10^{-6}$  to  $10^{-3}$ ) and as a result most of the ions and electrons are lost before reaching the surface. Flux of radicals is much higher than flux of ions and electrons to the surface. However, ions arriving at the surface have higher energy than electrons due to acceleration of ions in the plasma sheath. The plasma sheath is the potential between the plasma and the substrate defined as [79]:

$$V_p - V_f = \frac{T_e}{2e} + \frac{T_e}{2e} \ln \left( \frac{m_i}{2\pi m_e} \right) \quad (2.1)$$

where  $V_p$  is the plasma potential,  $V_f$  is the substrate potential,  $T_e$  is the electron energy in eV,  $e$  is the electron charge,  $m_e$  is the electron mass and  $m_i$  is the ion mass.

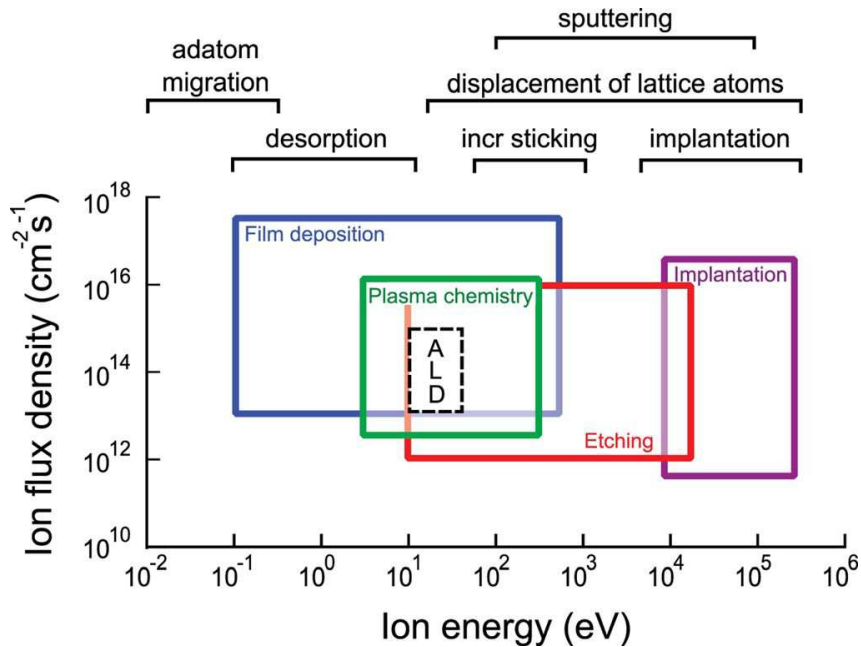


Figure 2.22: Different plasma processes with their corresponding ion flux density and energy [79, 82]

The energy of the ions arriving at the substrate also depend on the collision mean free path of the ions and the thickness of the plasma sheath. At higher plasma pressure, collision

mean free path of ions could be smaller than the plasma sheath thickness resulting in low ion energy at the substrate. On the other hand, low plasma pressure would allow large ion mean free path, which means that ions can be accelerated over the entire plasma sheath thickness resulting in ion bombardment at the substrate (high energy ions). For typical processing plasma, the plasma sheath potential is  $< 50$  V. However, the plasma sheath potential can also be much higher depending on the plasma gas, reactor geometry, grounding or biasing of the electrode (substrate). In fact, for certain plasma processing such as etching and ion implantation, high ions energy would be desired (Figure 2.22). Figure 2.22 shows the different plasma processes with their corresponding ion flux density and ion energy.

### **Key features during plasma sequence in ALD processes**

- (i) Highly reactive radicals are generated during the plasma step. The reactivity of the radicals can also be tuned from the plasma parameters such as power, gases, flows and pressure.
- (ii) The plasma does not heat the substrate within short time since only electrons have high energy and not the whole gas phase species.
- (iii) Reaction surfaces are also bombarded with energetic ions which can also promote the surface reaction rates.
- (iv) Some gas phase species are excited into higher energy level by electron impact collision. Thus emitting electromagnetic radiation from visible to vacuum ultraviolet region upon radiative decay of excited species to lower energy level.
- (v) Plasma can also undergo other reactions such as recombination into non reactive species. High recombination rate can affect the deposition uniformity especially in deep trenches.
- (vi) Volatile reaction products can also be excited, ionized or dissociated by the plasma.

### **2.11.2 Classification of plasma ALD sources**

There are three basic equipment configurations

#### **Radical enhanced plasma ALD**

The plasma source is placed at a distance from the reactor in this case. Only plasma radicals will reach the substrate. Most of the charge carriers (electrons and ions) would have recombined along the line and would not be able to reach the substrate. Flux density of plasma radicals is also lower due to recombination.

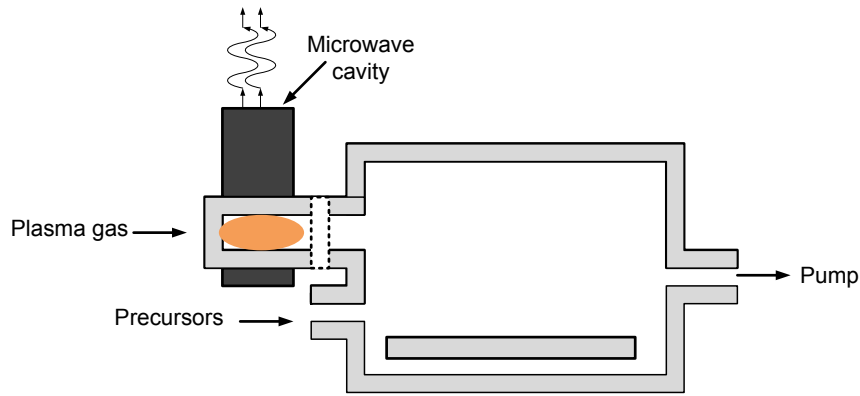


Figure 2.23: Radical enhanced plasma ALD

### Direct plasma ALD

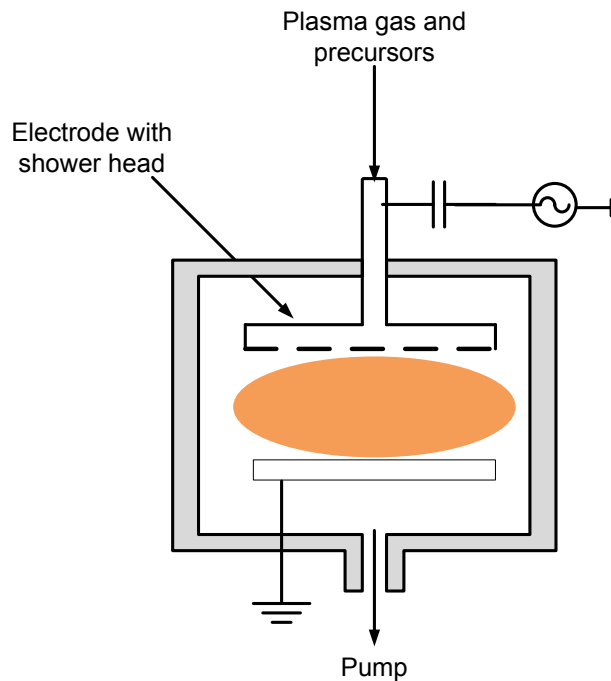


Figure 2.24: Direct plasma ALD

In direct plasma ALD, plasma is generated between an electrode plate and the substrate directly inside the reactor. One electrode is above the substrate and connected to RF power while the substrate is grounded. Gases are introduced to the reactor from the powered electrode through a shower head or with laminar flow. The flux density of plasma radicals is much higher together with ions, electrons, and photons on the substrate in direct plasma compared to radical enhanced and remote plasma configurations. The deposition can be very uniform with short plasma time in this configuration, however, the ions, electrons and photons could also damage the substrate in some cases.

## Remote plasma ALD

The substrate is not involved in plasma generation here and the plasma is generated remotely in a region above the substrate. Radical flux density is also quite high but the density of electrons and ions would have decreased to zero before reaching the substrate. Examples are RF driven remote inductively coupled plasma, microwave driven remote inductively coupled plasma (ICP) and electron cyclotron resonance plasma. Another approach for remote plasma ALD is to place an additional electrode grid in between the top electrode and the substrate in a direct plasma system. This can be seen as a sort of remote capacitively coupled plasma (CCP) source in which the active plasma is confined between the top electrode and the grid (Figure 2.25b). Flux of ions, electrons and photons is also reduced to the substrate.

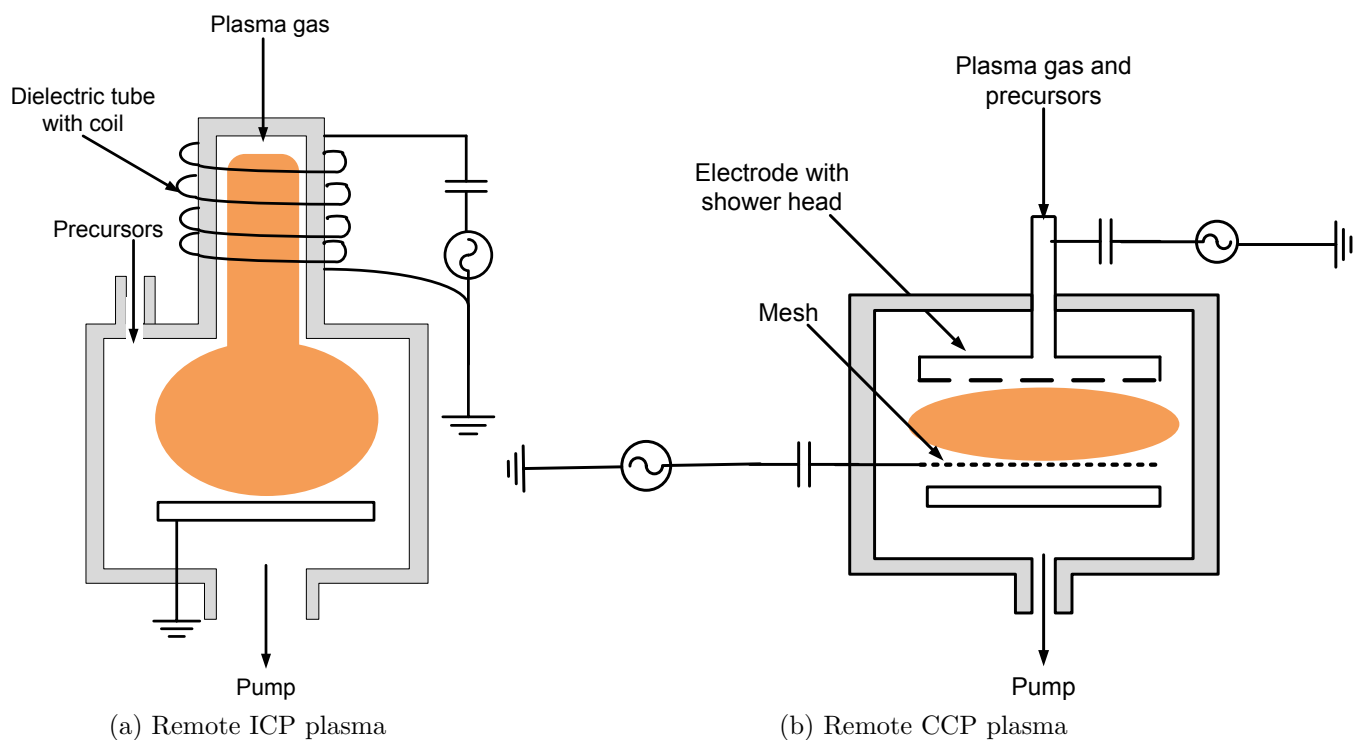


Figure 2.25: Remote plasma ALD

### 2.11.3 Advantages and limitation of plasma ALD

#### Advantages

- (i) Deposition can be carried out at low temperature.
- (ii) Growth per cycle is generally increased.
- (iii) Film stoichiometry can be controlled easily.
- (iv) Other processing can be done such as plasma pre and post-treatment.

- (v) Material properties are improved such as film density.
- (vi) Choices of precursors are increased.

### **Limitation**

- (i) Reduced conformality on high aspect ratio structures because of radical recombination on the side walls.
- (ii) Exposure of the surface to ions and especially vacuum ultra-violet radiation can cause high interfacial defects. Carrier lifetime was found to reduce with plasma exposure due to vacuum ultra-violet radiation exposure [79].
- (iii) Complex plasma hardware would be required for industrial batch process.

## **2.12 Review of previous Ag PALD and CVD processes**

Silver is a future interconnect material because of its low bulk resistivity ( $\approx 1.6 \mu\Omega \cdot \text{cm}$ ). Other applications of silver films are plasmonics [83], highly reflective mirror coating [84], anti-microbial coating [85], gas sensors [86], catalyst [87] and decorations.

A summary of Ag PALD and MOCVD processes found in literature are given in Table 2.3. The reference work for the Ag deposition was the article reported by Kariniemi et al. [13], where Ag layers were deposited in a Beneq TFS-200 ALD-reactor, with a remote plasma source configuration. The plasma was generated using a 13.56 MHz radio frequency, 100 Watts power source, and capacitively coupled between a top electrode and a grid electrode placed at about 4 cm distance from the substrate. Mixture of hydrogen and argon was used to generate hydrogen plasma discharge as a reducing agent for the Ag precursor. The choice of Ag precursor was determined through a thermogravimetric measurements (TGA) of some available Ag precursors in literature (Figure 2.26).  $\text{Ag}(\text{fod})(\text{PEt}_3)$  was the best choice because the weight remaining after decomposition was the lowest compared to the percentage of Ag in the precursor, which means that a significant amount of the precursor vaporized before decomposition. The Ag depositions were carried out on silicon and glass substrates. The precursor dosage was done by inert gas valving (Figure 2.19) and Ag ALD type growth were obtained in temperature range from 120 °C - 140 °C with 0.03 nm growth per cycle, while slight additional CVD decomposition was observed above 140 °C (150 °C and 200 °C).

Table 2.3: Previous Ag PALD and CVD processes

| Ag deposition method | Ag prec.   | other prec. or gases           | Dep. temp. (°C) | GPC                         | $\rho$ ( $\mu\Omega \cdot \text{cm}$ ), film thickness | Substrates                             | Ref. and year |
|----------------------|--|--------------------------------|-----------------|-----------------------------|--|--|---------------|
| Plasma-enhanced ALD  | Ag(fod)(PEt <sub>3</sub> )   | H <sub>2</sub> plasma          | 100 - 120       | 0.8 nm/min                  | 18, 50 nm  | SiO <sub>2</sub> (native)/Si           | [12], 2015    |
| Plasma-enhanced ALD  | Ag(fod)(PEt <sub>3</sub> )   | H <sub>2</sub> plasma          | 120 - 150       | 0.03 nm/cycle               | 6 - 8, 20 nm   | Si, glass                              | [13], 2011    |
| Liquid injection ALD | (hfac)Ag(1,5-COD) in toluene   | propanol                       | 110 - 150       | -                           | -  | glass, SiN                             | [88], 2010    |
| MOCVD                | ((Ag(OOCCH <sub>2</sub> <sup>t</sup> Bu)(PEt <sub>3</sub> )) <sub>n</sub> ) in toluene | N <sub>2</sub>                 | 300 - 500       | -                           | $\infty$   | TiO <sub>2</sub> /SiO <sub>2</sub> /Si | [11], 2009    |
| Radical-enhanced ALD | Ag(O <sub>2</sub> C <sup>t</sup> Bu)(PEt <sub>3</sub> )                                | H radicals                     | 140             | 0.12 nm/cycle               | 6, 40 nm   | Si, glass                              | [89], 2007    |
| MOCVD                | (hfac)Ag(VTES)   | Argon                          | > 180           | -                           | 1.83, >500 nm  | TiN/Si, SiO <sub>2</sub> /Si,          | [90], 2005    |
|                      | Ag(fod)(PEt <sub>3</sub> )   | Argon                          | > 230           | -                           | 1.92, >500 nm  | TiN/Si, SiO <sub>2</sub> /Si           |               |
| MOCVD                | ((tfac)AgP(OEt) <sub>3</sub> )   | Argon                          | 330             | > 23 nm/min                 | 1.61, bulk thickness                                   | Si and glass                           | [91], 2005    |
| MOCVD                | (hfac)Ag(BTMSA)  | H <sub>2</sub> /N <sub>2</sub> | 150 - 250       | 4 - 8 nm/min                | 6.5, unknown   | Si, SiO <sub>2</sub> /Si               | [92], 2001    |
| MOCVD                | Ag(fod)(PR <sub>3</sub> )  | H <sub>2</sub>                 | 300             | -                           | 2.5 - 3, 2000 nm                                       | glass, Si, Cu, Ag                      | [93], 1995    |
|                      | Ag(hfac)(PR <sub>3</sub> )   | H <sub>2</sub>                 | 350             | 2 $\mu\text{m}/\text{hour}$ | 6.5, 1100 nm   | glass, Si, Cu, Ag                      |               |

Ag prec. = Ag precursor, Dep. temp. = Deposition temperature, GPC = Growth per cycle,  $\rho$  = resistivity, Ag(fod)(PEt<sub>3</sub>) = (2,2-dimethyl-6,6,7,7,8,8-heptafluorooctane-3,5-dionato)silver(I)triethylphosphine, (hfac)Ag(1,5-COD) = (hexafluoroacetylacetonato)silver(I)(1,5-cyclooctadiene), ((Ag(OOCCH<sub>2</sub><sup>t</sup>Bu)(PEt<sub>3</sub>))<sub>n</sub>) = (tertbutylcarboxylate)(triethylphosphine)silver, Ag(O<sub>2</sub>C<sup>t</sup>Bu)(PEt<sub>3</sub>) = (2,2-dimethylpropionato)silver(I)triethylphosphine, (hfac)Ag(VTES) = vinyltriethylsilane(hexafluoroacetylacetonato)silver(I), ((tfac)AgP(OEt)<sub>3</sub>) = silver (I) 1,1,1-trifluoro-2,4-pentanedionate triethyl phosphite adduct, (hfac)Ag(BTMSA) = (1,1,1,5,5,5-hexafluoro-2,4-pentanedionato)-silver[bis(trimethylsilyl)acetylene] complex, hfac = hexafluoroacetylacetonato, fod = 2,2-dimethyl-6,6,7,7,8,8-heptafluorooctane-3,5-dionato, R = CH<sub>3</sub>, C<sub>2</sub>H<sub>5</sub>

The Ag films grown were polycrystalline with a resistivity of 6 - 8  $\mu\Omega \cdot \text{cm}$  for 22 nm thick layer. Spatial plasma enhanced atomic layer deposition of Ag films at atmospheric pressure using Ag(fod)(PEt<sub>3</sub>) and hydrogen plasma is reported in reference [12]. The plasma source design was derived from a surface dielectric barrier discharge [12], with typical power density of 5 - 10 W/cm<sup>2</sup>. Mixture of hydrogen and nitrogen was used for plasma generation. Ag films were grown on silicon substrate (with native oxide) in the temperature range from 100 °C - 120 °C. It was shown that film morphology can be controlled by substrate temperature through Ag surface diffusion and concluded that both high growth rate and low deposition temperatures may promote smooth Ag film growth by spatial ALD. The Ag growth rate was 0.8 nm/min and with resistivity of 18  $\mu\Omega \cdot \text{cm}$  for 50 nm thick Ag layer. The film thickness was measured by profilometry in this case.

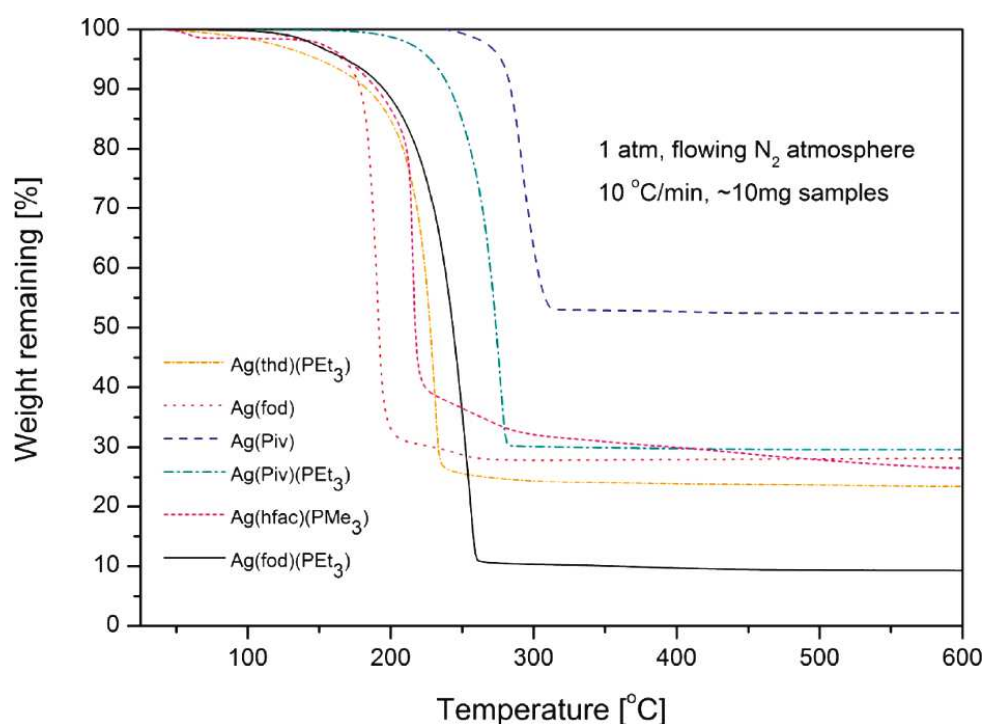


Figure 2.26: TGA curves of selected Ag precursors. (thd = 2,2,6,6-tetramethyl- 3,5-heptanedionato, piv = 2,2-dimethylpropionato, fod = 2,2-dimethyl-6,6,7,7,8,8-heptafluorooctane-3,5-dionato, and hfac = 1,1,1,5,5-hexafluoroacetylacetonato. [13]

Silver nanoparticles were grown by liquid injection atomic layer deposition on glass and amorphous silicon nitride membranes substrates, using (hfac)Ag(1,5-COD) dissolved in a 0.1 M toluene solution and propanol as reducing agent in the temperature range from 110 °C - 150 °C [88]. Transmission electron microscopy shows that the nanoparticles were face centered cubic, faceted silver crystallites. Nucleation density and size of Ag nanoparticles depends on deposition temperature and it was reported that the nucleation density increases from  $7 \times 10^9$  to  $1.5 \times 10^{11}$  particles . cm<sup>-2</sup> as the deposition temperature is reduced from 150 °C to 110 °C [88].

Metallic silver films were grown using radical-enhanced atomic layer deposition technique with (2,2-dimethylpropionato)silver(I)triethylphosphine ( $\text{Ag}(\text{O}_2\text{C}^t\text{Bu})(\text{PEt}_3)$ ) precursor and hydrogen radicals [89]. Deposition were carried out on silicon and glass substrates. The ALD growth per cycle obtained was 0.12 nm at 140 °C deposition temperature on silicon substrate. Conformal deposition was obtained on patterned silicon high aspect ratio of 9:1. A film resistivity of  $6 \mu\Omega \cdot \text{cm}$  was obtained for 40 nm thick Ag layer. The film thicknesses were computed from the relative concentrations obtained from the EDX measurements using the bulk density for silver [89].

MOCVD of silver films are reported in references [11,90–93]. Approximately bulk resistivity of silver ( $1.61 \mu\Omega \cdot \text{cm}$ ) was obtained for relatively thick silver films (500 nm and above), as the best result for the MOCVD experiments. MOCVD processes may be faster than ALD processes but with lower film conformality on high aspect ratio structures. Silver PALD processes thus require optimized process conditions and better film properties which is part of the goal of this dissertation.

## 2.13 Review of previous PALD processes on the selected oxide films

### 2.13.1 $\text{Sb}_2\text{O}_5$ film

Antimony oxide films have broad range of applications. It can be used for gas sensing, where the film conductance depends on gas exposure, and sensitivity to hydrogen [94], ethanol [95] and methane [96] have been reported in literature. It can possibly be used as sensor for temperature measurement since its electrical conductivity linearly depends on temperature [97]. They have also been used as catalyst, for example in the selective oxidation and ammoxidation of aromatics and alkenes [98] as well as the selective oxidation of ethanol [99]. It can as well be used as flame retardant synergist in combination with halogenated materials [100]. Antimony oxide is a high refractive index material (2.087 - 2.35), which is required for fabrication of low loss high reflecting mirrors used for high power lasers and Fabry-Perot interferometric applications [33].  $\text{Sb}_2\text{O}_3$  glasses have been shown to allow extended infrared transmission [101]. Antimony oxide can also be used as moisture barrier layer capping, sacrificial layer and etch stop layer in CMOS process, since it can tolerate harsh conditions such as resistance to buffered HF and  $\text{HNO}_3$  at temperature up to 40 °C [102]. Antimony is also a dopant in silicon and germanium.  $\text{Sb}_2\text{O}_5$  film can be a source of n-type doping in silicon or germanium, which is the application area of interest in this work.

To date, the  $\text{Sb}_2\text{O}_5$  film deposition reported in literature were all based on thermal atomic layer deposition. Plasma-assisted processes have not been reported, and it will be beneficial to have a plasma-assisted  $\text{Sb}_2\text{O}_5$  ALD process because of the possibility to obtain a



relatively high growth per cycle at reduced deposition temperature compare to thermal ALD process.

Antimony-doped tin dioxide film with low resistivity and high transparency was deposited on glass substrate by atomic layer deposition from  $\text{SnCl}_4$ ,  $\text{SbCl}_5$  and  $\text{H}_2\text{O}$  at 500 °C [103]. However, the precursor used here can give undesirable corrosive chloride by-products.

Furthermore,  $\text{Sb}_2\text{O}_5$  film was deposited on hydrogen terminated silicon substrates using triisopropylantimony as precursor and water or ozone as oxidizing source [102]. The deposited film with water consists of small crystallites, while the film deposited with ozone was continuous. Growth per cycle obtained was 0.06 nm at 200 °C deposition temperature and 0.16 nm at 300 °C deposition temperature [102].

Antimony oxide ( $\text{Sb}_2\text{O}_5$ ) and antimony sulphide ( $\text{Sb}_2\text{S}_3$ ) film were grown on silicon substrate and nanoporous alumina substrate at 120 °C deposition temperature using tris(dimethylamido)antimony, ozone and hydrogen sulphide [32]. The growth per cycle obtained at 120 °C deposition temperature was 0.185 nm for  $\text{Sb}_2\text{O}_5$  and 0.058 nm for  $\text{Sb}_2\text{S}_3$ .

$\text{Sb}_2\text{O}_5$  film was also deposited on hydrogen terminated silicon substrates using triethylantimony and ozone in the temperature range between 50 °C and 250 °C [33]. The deposited film thickness was very small at temperatures below 100 °C and the growth per cycle increased approximately linearly with increase in deposition temperature between 100 °C and 250 °C. The growth per cycle was about 0.01 nm at 100 °C and 0.075 nm at 250 °C. Very smooth  $\text{Sb}_2\text{O}_5$  films were grown with ozone as the oxidizing source. The surface roughness of 72 nm  $\text{Sb}_2\text{O}_5$  film as measured by atomic force microscopy was 0.159 nm on a  $2 \times 2 \mu\text{m}^2$  area. Investigation of thermal stability of  $\text{Sb}_2\text{O}_5$  film deposited on silicon substrate suggests that  $\text{Sb}_2\text{O}_5$  film may be thermally stable at temperatures below 600 °C. Small decrease in layer thickness was observed after rapid thermal annealing in oxygen at 500 °C due to desorption of surface contaminants and beginning of film densification [33]. There was a large decrease in layer thickness as the annealing temperature rises above 700 °C, and complete evaporation of about 20 nm  $\text{Sb}_2\text{O}_5$  film was observed at annealing temperatures from 900 °C [33].  $\text{Sb}_2\text{O}_5$  failed to act as a dopant source in silicon. There was little or no diffusion of Sb into Si from  $\text{Sb}_2\text{O}_5$  source after rapid thermal annealing process as observed in the SIMS result and the measured sheet resistance [33].

### 2.13.2 $\text{B}_2\text{O}_3$ film

Boron is a key dopant for semiconductor material such as silicon or germanium.  $\text{B}_2\text{O}_3$  layer can therefore be used as a boron source for diffusion doping. Other application areas of  $\text{B}_2\text{O}_3$  film are limited because of its instability in ambient air, since moisture transforms  $\text{B}_2\text{O}_3$  film into boric acid ( $\text{H}_3\text{BO}_3$ ) [104]. Boric acid is effective as a solid lubricant [105].

There have been only few reports on  $B_2O_3$  atomic layer deposition. Atomic layer deposition of  $B_2O_3$  films on soda lime glass and silicon substrates at room temperature using  $BBr_2$  and  $H_2O$  have been reported [104], but it is usually necessary to avoid halide precursors due to problematic corrosive by-products. Growth per cycle obtained was 0.076 nm at 20 °C, which decreased to 0.005 nm at 50 °C deposition temperature [104].

$B_2O_3$  ALD using a halogen-free precursor was first demonstrated in [59], where  $B_2O_3$  film was deposited on silicon substrate from tris(dimethylamido)borane and ozone as precursors. A growth per cycle of 0.03 nm was obtained at 50 °C deposition temperature [59]. Recently, Kim et al. reported the atomic layer deposition of  $B_2O_3$  film on silicon substrates at 150 °C deposition temperature using trimethyl borate (TMB) as the boron precursor and ozone or oxygen plasma as oxidizing source [106]. The film growth per cycle obtained at 150 °C deposition temperature was 0.04 nm with oxygen plasma oxidizing source and 0.035 nm with ozone oxidizing source. It was shown that mixture of  $B_2O_3/SiO_2$  film can be grown by alternating atomic layer deposition sequence of  $B_2O_3$  and  $SiO_2$ , in which the layers were used for efficient p-type doping in silicon [106].

### 2.13.3 $SiO_2$ film

$SiO_2$  is an important material with wide application areas. It is a common gate dielectric of MOS, CMOS, or thin film transistors. It can serve as thin film light absorption layer in amorphous silicon solar cell to improve light absorption efficiency. It is also used as a passivation layer to minimize interface defect densities in solar cells [107] as well as passivation of OLEDs and polymers [108].  $SiO_2$  is an important material for passive optical components [109, 110] such as waveguides, splitters, combiners, and active optical components such as optical modulators and optical amplifiers [110]. An interest in  $SiO_2$  PALD in this work is to use it as a capping layer for other films, as well as for the growth of mixed oxide of  $SiO_2/PO_x$  film by PALD. There have been quite a number of publications on atomic layer deposition of  $SiO_2$  films, and the possible precursor combination used is summarized in Table 2.4. ALD of  $SiO_2$  using several chloride-based silicon precursor with  $H_2O$  [111–120] and  $O_3$  [121–123] as oxidizing source have been well reported. The  $SiO_2$  film growth per cycle decreased as the deposition temperature was increased while using  $SiCl_4$  and  $H_2O$  precursor combination [111, 112]. Depositions were carried out at lower temperature (room temperature or near room temperature) using  $SiCl_4$  and  $H_2O$  as precursor with pyridine or pyridinium chloride salt [112, 116–119] and ammonia as catalyst [115]. The growth per cycle reported was higher (0.21 - 0.216 nm [112, 115] and 0.08 nm [118]) with the catalyzed  $SiO_2$  ALD, compare to uncatalyzed ALD using  $SiCl_4$  and  $H_2O$  as precursor. A maximum film growth per cycle of 0.35 nm was obtained at 300 °C deposition temperature using  $SiCl_2H_2$  and  $O_3$  as precursor [122]. However,  $SiO_2$  ALD using chloride-based silicon precursor has some serious drawbacks such as high reaction

temperature required in the case of uncatalyzed  $\text{SiCl}_4$  and  $\text{H}_2\text{O}$  (600 - 800 K substrate temperature), problematic corrosive by-products, and reactivity of catalyst (such as  $\text{NH}_3$ ) with  $\text{HCl}$  by-products to form ammonium salts [124].

Table 2.4: Precursors for  $\text{SiO}_2$  ALD and PALD processes [40]

| Reactant A  | Reactant B                                      | Growth Temp. | GPC              | References          |
|---|---|--------------|------------------|---------------------|
| $\text{SiCl}_4$   | $\text{H}_2\text{O}$                            | 600 - 800 K  | 0.075 - 0.11 nm  | [111–114]           |
| $\text{SiCl}_4$   | $\text{H}_2\text{O} + \text{cat}^{\text{a}}$    | 300 K        | 0.08 - 0.216 nm  | [112, 115–119]      |
| $\text{Si}_2\text{Cl}_6$  | $\text{O}_3$                                    | 403 - 453 °C | 0.32 nm          | [121]               |
| $\text{SiCl}_3\text{H}$   | $\text{H}_2\text{O}$                            | 180 °C       | -                | [120]               |
| $\text{SiCl}_2\text{H}_2$                                       | $\text{O}_3$                                    | 250 - 450 °C | 0.25 - 0.35 nm   | [122, 123]          |
| $\text{SiH}_4$  | $\text{N}_2\text{O}^{\text{b}}$                 | 100 - 400 °C | 0.13 nm          | [125]               |
| $\text{Si}(\text{OMe})_4$                                       | $\text{H}_2\text{O}$                            | 150 °C       | -                | [126]               |
| $\text{Si}(\text{OMe})_4$                                       | $\text{H}_2\text{O} + \text{NH}_3 \text{ cat.}$ | room - 80 °C | 0.2 - 0.3 nm     | [127]               |
| $\text{Si}(\text{OEt})_4$                                       | $\text{H}_2\text{O} + \text{cat.}$              | room - 70 °C | 0.07 - 0.08 nm   | [124, 128]          |
| $\text{Si}(\text{OEt})_4$                                       | $\text{O}_2^{\text{b}}$                         | 150 - 250 °C | 0.03 nm          | [42, 129, 130]      |
| $\text{Si}(\text{OEt})_3((\text{CH}_2)_3\text{NH}_2)$           | $\text{H}_2\text{O} + \text{O}_3$               | 120 - 200 °C | 0.06±0.01 nm     | [131–136]           |
| $\text{Si}(\text{O}^t\text{Pe})_3\text{OH}$                     | $\text{AlMe}_3$                                 | 225 - 250 °C | 12 nm            | [137]               |
|   |   | 175 °C       | 1.8 nm           | [138]               |
| $(\text{Me}_3\text{Si})_2\text{NH}$                             | $\text{O}_2$                                    | 500 - 550 °C | 1 wt-%           | [139]               |
| $\text{SiH}_2(\text{N}(\text{CH}_3)_2)_2$                       | $\text{O}_3$                                    | 275 °C       | 0.031 - 0.118 nm | [140, 141]          |
| $\text{SiH}_2(\text{NH}^t\text{Bu})_2$                          | $\text{O}_2^{\text{b}}$                         | 110 °C       | 0.16±0.003 nm    | [142]               |
| $\text{SiH}_2(\text{NEt}_2)_2$                                  | $\text{O}_2^{\text{b}}$                         | 280 °C       | 0.076 nm         | [143]               |
|   |   | 200 °C       | 0.13 nm          | [144]               |
| $\text{SiH}_2(\text{NEt}_2)_2$                                  | $\text{O}_3$                                    | 100 °C       | 0.0085 nm        | [145]               |
| $\text{SiH}(\text{N}(\text{CH}_3)_2)_3$                         | $\text{O}_3$                                    | 275 °C       | 0.021 - 0.077 nm | [140, 141, 146–148] |
| $[(\text{CH}_3)_2\text{CH}]_3\text{SiH} + \text{Ar}^{\text{b}}$ | $\text{O}_2^{\text{b}}$                         | 50 °C        | 0.65 - 3.59 nm   | [149]               |
| $\text{SiH}(\text{N}(\text{CH}_3)_2)_3$                         | $\text{O}_2^{\text{b}}$                         | 150-300 °C   | 0.09 - 0.115 nm  | [150]               |
| $\text{SiH}(\text{N}(\text{CH}_3)_2)_3$                         | $\text{H}_2\text{O}_2$                          | 150-550 °C   | 0.08 - 0.18 nm   | [151, 152]          |
| $\text{Si}(\text{NCO})_4$                                       | $\text{H}_2\text{O}$                            | room         | 0.17 nm          | [153]               |
| $\text{Si}(\text{NCO})_4$                                       | $\text{NEt}_3$                                  | 150 °C       | 0.12 nm          | [154]               |
| $\text{MeOSi}(\text{NCO})_3$                                    | $\text{H}_2\text{O}_2$                          | room         | 0.2 nm           | [155, 156]          |

a = catalyst, b = plasma, Et = ethyl, Me = methyl,  $\text{O}^t\text{Pe}$  = tertiary-pentoxy,  $^t\text{Bu}$  = tertiary-butyl, wt-%=weight-percent.

As a result, several chlorine-free silicon precursors have been reported in literature for  $\text{SiO}_2$  ALD such as silane ( $\text{SiH}_4$ ) [125], silicon alkoxide [42, 124, 126–130], alkyl-aminosilane [140–148, 150–152], and some other metal-organic precursors [131–139, 153–156].  $\text{SiO}$  films were deposited by ALD from  $\text{SiH}_4$  and  $\text{N}_2\text{O}$  plasma in the temperature range from 100 - 400 °C with a maximum growth per cycle of 0.13 nm. These films were used as offset spacer in high-k/metal gate stacks [125]. ALD of  $\text{SiO}_2$  from tetramethyl orthosilicate ( $\text{Si}(\text{OMe})_4$ ) and water vapour as precursor at 150 °C deposition temperature deposited on  $\text{Au}/\text{TiO}_2$  could modify the catalytic property of  $\text{Au}/\text{TiO}_2$  nanoparticles [126]. Hatton et

al. demonstrated the ALD of SiO<sub>2</sub> films onto SiO<sub>2</sub> colloidal crystal and polymer spheres, with tetramethyl orthosilicate (Si(OMe)<sub>4</sub>) and NH<sub>4</sub>OH as precursor (H<sub>2</sub>O) and catalyst (NH<sub>3</sub>), at room and 80 °C deposition temperature, using a simple test tube for precursor dosage and obtained an estimated ALD growth per cycle of 0.2 - 0.3 nm [127]. ALD of SiO<sub>2</sub> was also reported at room [124] and 70 °C [128] deposition temperature using tetraethyl orthosilicate (Si(OEt)<sub>4</sub>) as silicon precursor with water as oxidizing source and a catalyst (such as ammonia NH<sub>3</sub> [124] or C<sub>2</sub>H<sub>5</sub>N [128]) with growth per cycle of 0.07 - 0.08 nm. Some other reported SiO<sub>2</sub> ALD using amino-silane and metal-organic Si precursors are given in Table 2.4 with the maximum growth per cycle and the deposition temperature range.

#### 2.13.4 PO<sub>x</sub>/SiO<sub>2</sub> film

Phosphorus belongs to n-type dopant class for silicon and germanium, therefore phosphorus containing film can be a source layer for n-type doping in silicon and germanium. Other applications of phosphorus and phosphorus compounds include the use of phosphates as fertilizers [157], application of organophosphorus compounds for plasticizers, flame retardants, pesticides, extraction agents, and water treatment [158], fabrication of safety matches [159], production of less brittle oxygen-free copper-phosphorus alloy [160], as well as biological applications [161]. There are limited reports on deposition of phosphorus containing films and there are no reports of PO<sub>x</sub>/SiO<sub>2</sub> PALD film deposition in literature. Trifonov et al. studied the reactivity of phenol-formaldehyde towards PCl<sub>3</sub>, in which the reactive group (OH) in the polymer (phenol-formaldehyde) could react through ligand exchange with towards PCl<sub>3</sub> [162], resulting to modification of the polymer surface. Deposition of boron phosphate on silica surface by molecular layering from trimethyl borate B(OCH<sub>3</sub>)<sub>3</sub> and phosphorus oxychloride (POCl<sub>3</sub>) have been reported [163].

# Film Characterization Principles

After deposition of thin films, it is usually necessary to characterize the layers in order to know its properties. Specifically, properties such as film thickness, refractive index, resistivity, elemental composition, film morphology, film topography (surface roughness) and crystallinity are often determined with some various techniques. Some of the characterization methods used in the experiments are ellipsometry, four point probe, scanning electron microscopy, transmission electron microscopy, atomic force microscopy, secondary ion mass spectrometry, x-ray photoelectron spectroscopy, x-ray fluorescence and x-ray diffraction.

## 3.1 Ellipsometry

Ellipsometry is a technique used to measure the optical properties of films. Optical properties such as thickness and refractive index of films can be measured to high degree of accuracy, by detecting a change in polarization of light reflected from a sample. The technique is not sensitive to intensity fluctuations because, it only measures amplitude ratio and phase change between the s and p components of the reflected wave. It is also non destructive and repeatable with high accuracy.

### 3.1.1 Polarization of light

Light wave in general normally have elliptic polarization. This means the electric field vector form a trajectory of an ellipse in a plane perpendicular to the direction of propagation. One revolution is completed in the time interval  $\frac{2\pi}{\omega}$ . Moreover, the polarization can also be described with two harmonic components each along perpendicular axes x and y. If the two components on x and y are phase shifted, then the resulting path is an ellipse (Figure 3.1).

The amplitude of the wave along x and y axes are  $E_{ox}$  and  $E_{oy}$  respectively. The time dependence electric field vector  $\vec{E}(t)$  can be written in complex form as:

$$\vec{E}(t) = \text{Re} \begin{bmatrix} E_{ox}e^{i\Delta} \\ E_{oy} \end{bmatrix} e^{i\omega(t-t_0)} \quad (3.1)$$

where  $\Delta$  is the relative phase change between  $E_{ox}$  and  $E_{oy}$  components,  $\omega$  is the angular

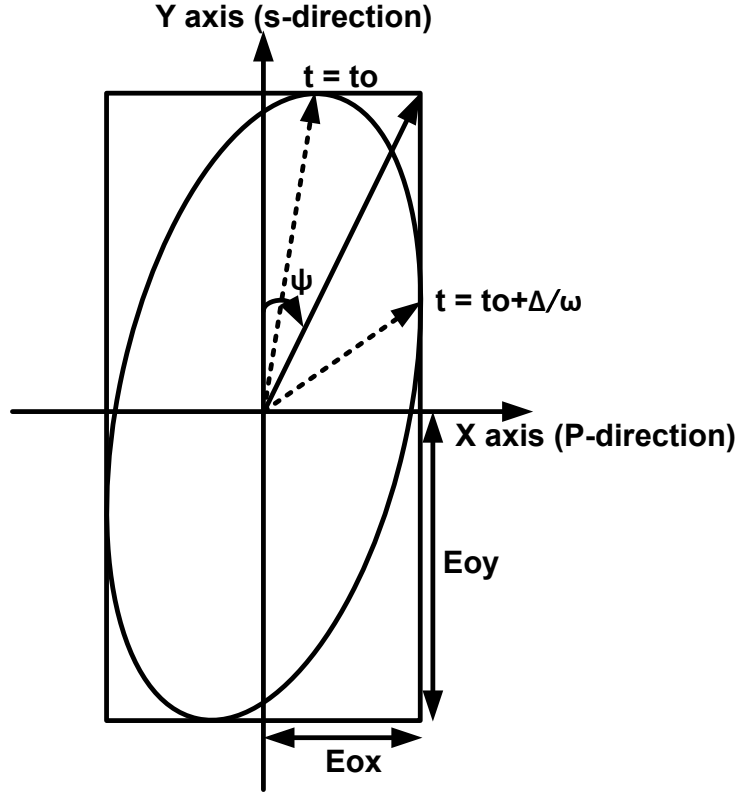


Figure 3.1: Elliptical polarization.

frequency and  $t_o$  is the initial time. The electric field component is maximum at  $t = t_o + \frac{\Delta}{\omega}$  and  $t = t_o$  along the x axis and y axis respectively, as shown in the dotted line in Figure 3.1. The angle  $\Psi$  determines the relative amplitude ratio between  $E_{ox}$  and  $E_{oy}$  components. From Figure 3.1,

$$\tan \Psi = \frac{E_{ox}}{E_{oy}} \quad (3.2)$$

Therefore the Jones vector for the elliptic polarization can be written as [164]:

$$\begin{bmatrix} \sin \Psi e^{i\Delta} \\ \cos \Psi \end{bmatrix}$$

Two special cases of elliptic polarization are linear and circular polarization. For linear polarization the phase change  $\Delta = 0$  or  $\pi$ . The electric field forms a linear trajectory and has an angle  $\Psi$  between the plane of oscillation and the x-axis. This angle is called the azimuth. Moreover, electric field has only one components oscillating either along x or y direction. Linearly polarized light are produced by linear polarizer. These devices only allow light polarized along its axis to propagate, while it rejects all other polarization directions. The angular setting of the polarizer is the azimuth of the resulting polarized light.

For circular polarization, the phase change  $\Delta = \pm \frac{\pi}{2}$  and the angle  $\Psi = \frac{\pi}{4}$ . Circularly polarized light can be formed when a linearly polarized light pass through a retarder. A quarter wave plate gives a retardation of  $\frac{\pi}{2}$ . In other words, the electric field components

on x and y axis have equal amplitude but a phase change of  $\frac{\pi}{2}$ . Therefore, if the relative angle  $\Psi$  between a polarizer axis and the fast axis of the quarter wave plate is set to be  $\frac{\pi}{4}$ , the resulting polarization will definitely be circular.

### 3.1.2 Principle of operation of ellipsometer

An ellipsometer is used to measure the thickness and the optical parameters of films. The basic setup is as shown in Figure 3.2. When linearly polarized light is incident on a sample at an oblique angle, the reflected light will have an elliptical polarization. The basic set-up comprises of the light source, polarizer, analyzer and detector. The two compensators are optional components. The light source, polarizer and analyzer produce an incident light of known polarization on to the sample. Upon reflection, the polarization of the light changes, and the goal is to detect that change with the analyzer and the detector. The compensators can introduce some retardation to the propagating light to suite the detection scheme. For example in null ellipsometry, the compensators are adjusted such that the reflected light is linearly polarized just before the analyzer.

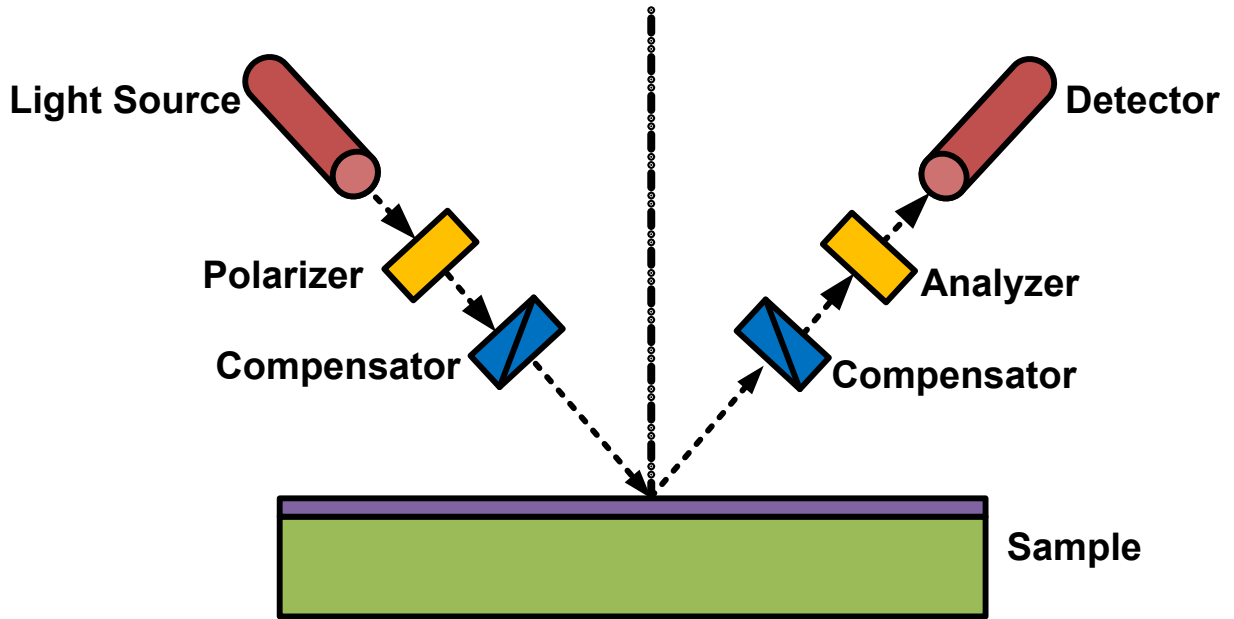


Figure 3.2: Basic setup of an ellipsometer.

The two important parameters in ellipsometry are the  $\Psi$  and  $\Delta$  values.  $\Psi$  is related to the amplitude ratio between the s and p components of the reflected light, while  $\Delta$  is related to the phase change between the s and p components of the reflected light. This is given from the relation in equation 3.3 [164]:

$$\frac{R_p}{R_s} = \tan \Psi e^{i\Delta} \quad (3.3)$$

where  $R_p$  and  $R_s$  are the reflectance of the p and s polarized light. Assuming the

measurement is done in air,  $R_p$  and  $R_s$  can be determined from Fresnel equation [165].

$$R_s = \frac{\cos \theta_i - n \cos \theta_t}{\cos \theta_i + n \cos \theta_t} \quad R_p = \frac{n \cos \theta_i - \cos \theta_t}{n \cos \theta_i + \cos \theta_t} \quad (3.4)$$

where  $n$  is the complex index of refraction of the sample;  $n = n_r - ik$ ,  $n_r$  is the real part of the refractive index and  $k$  is the imaginary part of the refractive index,  $\theta_i$  and  $\theta_t$  are the angles of incidence and refraction respectively, which are related by snell's law (appendix A.1).

$$\cos \theta_t = \sqrt{1 - \frac{1}{n^2} \sin^2 \theta_i} \quad (3.5)$$

By substituting equation 3.5 and 3.4 in equation 3.3, it can be observed that for a known angle of incidence, the reflectance ratio depends on the real part of refractive index, imaginary part and thickness of the sample. The phase change also depends on the sample thickness. Finally, the reflectance ratio  $\rho$  is given as [166]:

$$\rho = \frac{R_p}{R_s} = \tan \Psi e^{i\Delta} = f(n_j, k_j, t_j) \quad (3.6)$$

### 3.1.3 Ellipsometer configurations

The two important ellipsometric angle  $\Psi$  and  $\Delta$  are determined from the measurements, and this can be done using some configurations.

- (i) Null ellipsometry (PCSA or PSCA): The configuration used can be polarizer, compensator, sample and analyser (PCSA) or polarizer, sample, compensator and analyser (PSCA). The source, polarizer and compensator prepares a known polarization state of light incident on a sample, while the analyser and detector are used to determine the change in polarization produced by the sample. In null ellipsometry, the axis of the polarizer and analyser are adjusted until the light polarization just before the analyser is linear, and analyser is simply rotated until no light is detected by the detector. The angular setting of the polarizer (P) and the analyser (A) at null directly relates to  $\Psi$  and  $\Delta$  as [164]:

$$\Psi = A \quad \Delta = 2P + \frac{\pi}{2} \quad (3.7)$$

This technique has a high precision but very slow and needs high intensity of light for proper measurement.

- (ii) Rotating polarizer or rotating analyser system (RPE or RAE): Rotating analyser and rotating polarizer are both referred to as photometry system. Unlike null



ellipsometry, photometry system does not require having a zero signal at the detector. It measures intensities of the reflected light at different azimuth angles. The system set up can just be polarizer, sample and analyser (PSA) and may not necessarily require a compensator. Different intensities measurement can be taken at varying azimuth angles, by keeping the polarizer fixed and rotating the analyser (RAE), or vice versa (RPE). And the ellipsometry data  $\Psi$  and  $\Delta$ , are calculated from these measured intensities. RPE generally requires sources that are unpolarized while RAE requires photodetectors that are not sensitive to polarization for more accurate measurements.

- (iii) Rotating compensator system(RCE): A method of eliminating the polarization sensitivity of the source and detector is to use PCSA or PSCA photometry configuration instead of PSA. In both cases, the polarizer and analyser axis are kept fixed while the compensator azimuth (retarder) is rotated and corresponding intensities are measured at different rotation angles. In this case, the photodetector sees constant polarization [167] and polarization dependency of photodetector is removed.
- (iv) Phase modulated ellipsometer: Phase modulators ellipsometer may not have moving parts, rather it will introduce a phase change along its optical path by some mechanism. The ellipsometer configuration can be polarizer, modulator, sample and analyzer. In addition, the two common modulation scheme used are photoelastic modulator and liquid crystal modulator ellipsometry. In photoelastic modulators, a periodic birefringence is induced in a silica bar by a piezoelectrically generated standing acoustic wave, thus modulating the polarization of emerging light [168]. While for liquid crystal modulators, birefringence is induced by applying an electrical voltage which controls the orientation and alignment of the liquid crystal molecule. Both ellipsometer configurations are widely used in in-situ ellipsometric measurements.

### 3.1.4 Ellipsometric modelling and data analysis

Ellipsometry is a powerful technique, but it can only measure directly the angles  $\Psi$  and  $\Delta$ , and there is need for further extraction of the interesting parameters such as refractive index  $n$ , extinction coefficient  $k$  and thickness, from the measurements. In the case of sample thickness measurement, it is important to know the layer stack in the sample as shown in Figure 3.3. In addition, each layer is also given the right optical model.

As shown in Figure 3.4, at first the measurement  $\Psi$  and  $\Delta$  as a function of wavelength, is taken. Again  $\Psi$  and  $\Delta$  are also computed from the optical models and layer stack. The computed values and the measured values are compared until an error limit is reached. In other words, the model is fitted to the measurement until there is a good fit, defined by least mean squared error,  $MSE \approx 0$  or chi squared error,  $\chi^2 \approx 1$  (appendix A.2). The

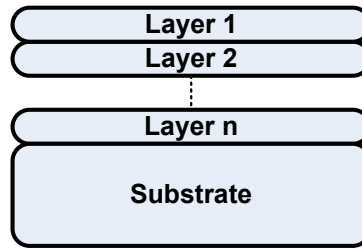


Figure 3.3: Ellipsometry model

value of the thickness, refractive index or extinction ratio that gives a good fit will be the final measurement results.

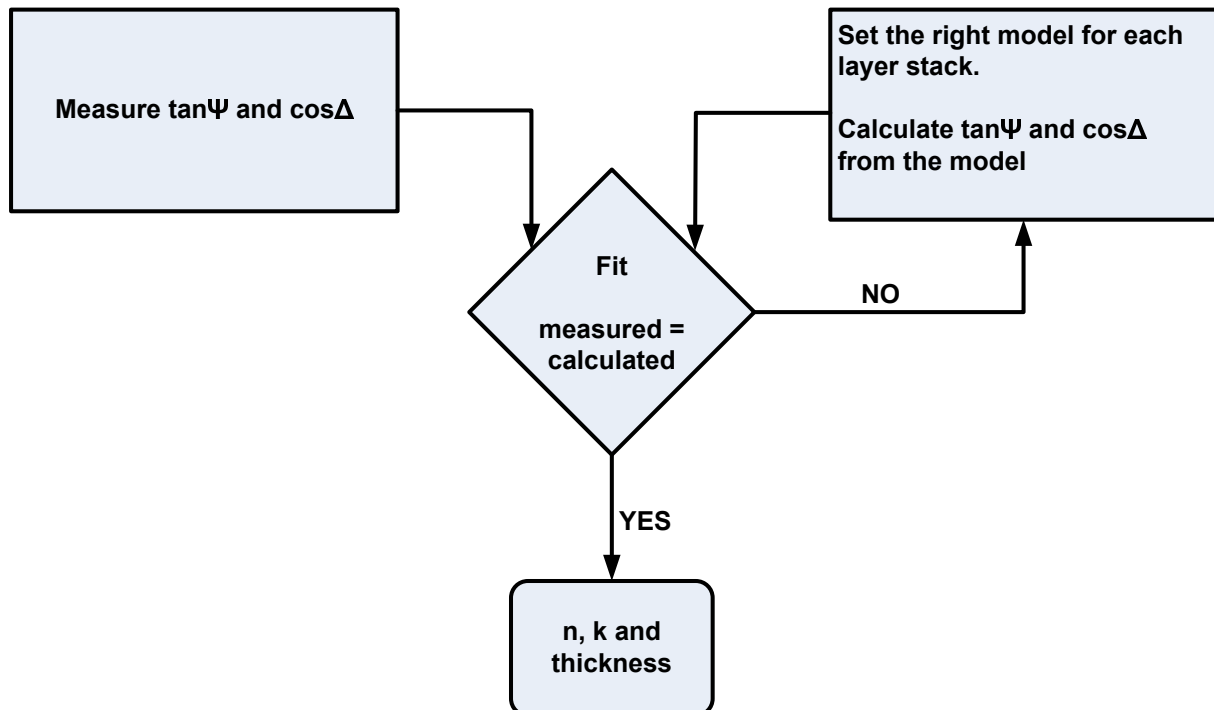


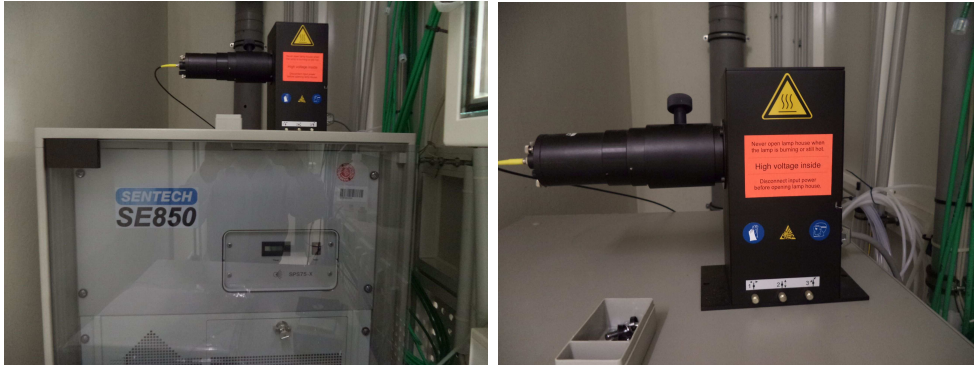
Figure 3.4: Ellipsometry measurement and data processing

### 3.1.5 SENTECH SE 850 ellipsometer

SE 850 by SENTECH Instruments Berlin, was used for all ellipsometric measurements in the wavelength range 280 nm to 850 nm. It combines both PSA and PCSA photometric rotating analyser ellipsometric setup. Its major components are (Figure 3.5):

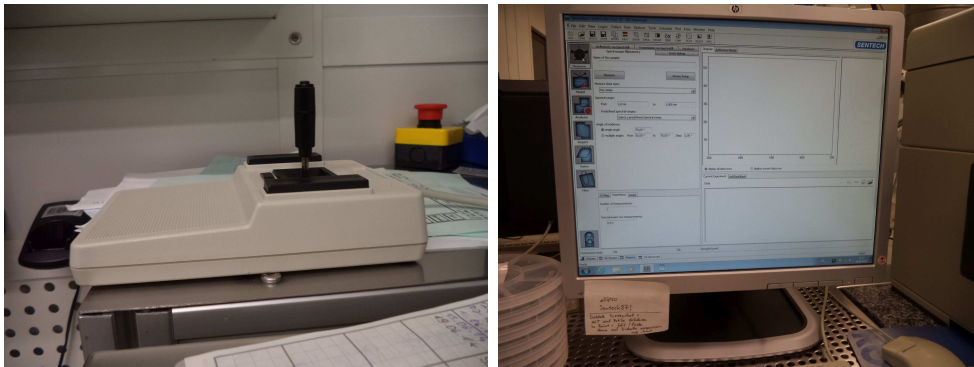
- (i) Xenon lamp: usually from UV/VIS/IR
- (ii) Polarizer, analyzer, compensator and detector
- (iii) Sample stage
- (iv) Optical camera for adjusting sample height and tilt

- (v) Goniometer for setting incidence and reflection angles
- (vi) Computer system, computer screen and joy stick
- (vii) SpectraRay\3 software for measurement, data acquisition and fitting.



(a) Computer system

(b) Xenon lamp (UV-VIS)



(c) Joy stick for sample stage control

(d) Computer screen



(e) Goniometer, sample stage, optical camera, polarizer, analyzer and detector

Figure 3.5: SE 850 ellipsometer in the clean room, Semiconductor Technology group, University of Magdeburg

## 3.2 Four point probe measurement

Resistivity is an important parameter in semiconductor materials, which tells us how strong the material opposes flow of electric current. In general, resistivity can be uniform for epitaxially grown semiconductor compared to doped semiconductor. This is because the segregation coefficient is usually less than unity in doped semiconductor. Resistivity affects other device parameters such as series resistance, capacitance, and threshold voltage. For a doped semiconductor, resistivity is inversely proportional to free electron and hole concentrations, as well as the electron and hole mobilities. Four point probe is a setup that can be used to measure resistivities of conductive materials.

### 3.2.1 Equivalent circuit of two and four point probe measurements

Consider two point probe placed on a sample under test, with a current source applied along, and voltage drop measured across the same probes. The electrical equivalent circuit for this set up is shown in Figure 3.6.

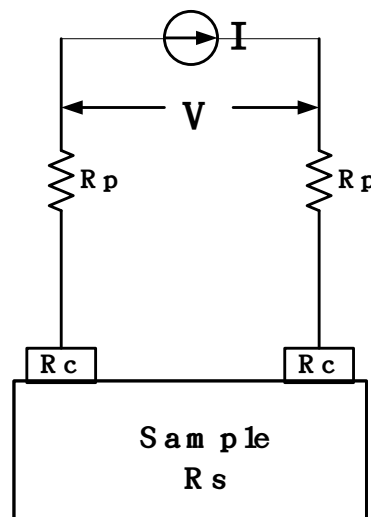


Figure 3.6: Two Point Probe Set up

The total resistance is given as:

$$\frac{V}{I} = 2R_p + 2R_c + R_s \quad (3.8)$$

where  $R_p$ ,  $R_c$  and  $R_s$  are probe, contact and sample resistance respectively. Clearly, it is difficult to unambiguously determine the sample resistance, because of the influence of probe and contact resistance. To correct this, four probes are placed on the sample separated at equal distance (Figure 3.7).

Electric current source is applied across the two outer probes, while voltage drop is measured between the inner probes. The current path is similar to that of the two probe measurement. However, negligible current flows inside the inner probes, because of the

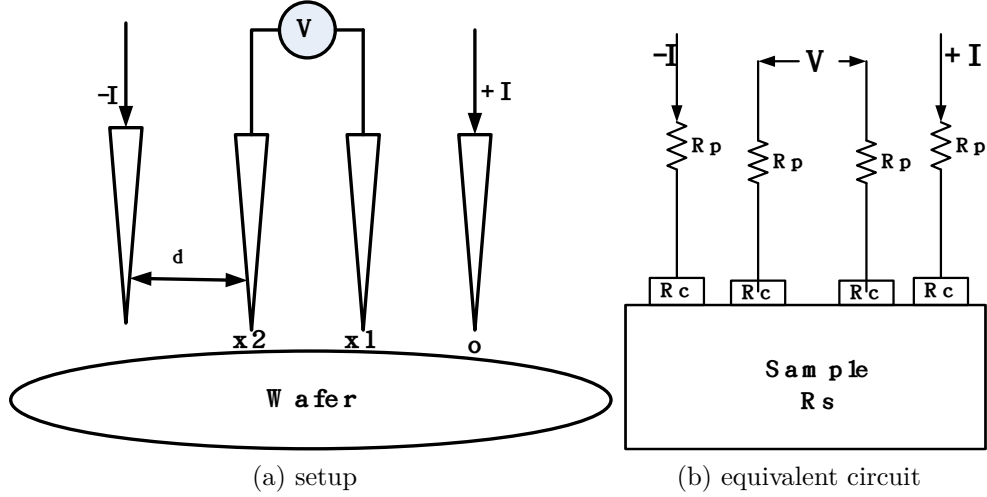


Figure 3.7: Four point probe

voltmeter high input impedance. Therefore, the sample resistance can be derived from the two parameters,  $V$  and  $I$ . For bulk materials, where the sample thickness ( $t$ ) is much greater than the probe spacing ( $d$ ), resistivity ( $\rho$ ) is given as (see appendix A.3):

$$\rho = 2\pi d \left( \frac{V}{I} \right) (\Omega m) \quad (3.9)$$

A more generalized expression for the resistivity that takes into account of arbitrary wafer shape is:

$$\rho = 2\pi d F \left( \frac{V}{I} \right) (\Omega m) \quad (3.10)$$

where  $F$  is a correction factor that corrects for probe location near sample edges, sample thickness, sample diameter, probe placement, and sample temperature [169].

The sample thickness should be known in order to calculate the sheet resistance, assuming the resistivity is uniform in the bulk sample. Sheet resistance is defined as the resistivity per sample thickness. The sheet resistance for bulk sample is therefore given as:

$$R_s = \frac{2\pi d F}{t} \left( \frac{V}{I} \right) (\Omega/\text{square}) \quad (3.11)$$

On the other hand, for thin films the probe spacing ( $d$ ), is much greater than the sample thickness ( $t$ ). Sheet resistance ( $R_s$ ) in this case, does not depend on the sample thickness, and can be calculated as (details in appendix A.3):

$$R_s = 4.534 \left( \frac{V}{I} \right) (\Omega/\text{square}) \quad (3.12)$$

The term  $\frac{2\pi d F}{t}$  in the expression for bulk samples reduces to 4.534 [169] for sufficiently thin layers where  $t \ll d$ .

### 3.2.2 Four point probe configurations

As earlier shown in equation 3.10, the correction factors must be determined to obtain accurate resistivity measurement. The correction factor reduces to 4.534 only for a colinear and equally spaced probe, with sample thickness much less than probe separation. It is therefore necessary to reduce the dependence of the resistivity measurements on correction factors due to sample geometries and probe location. And as a result, there are two different probe configurations used:

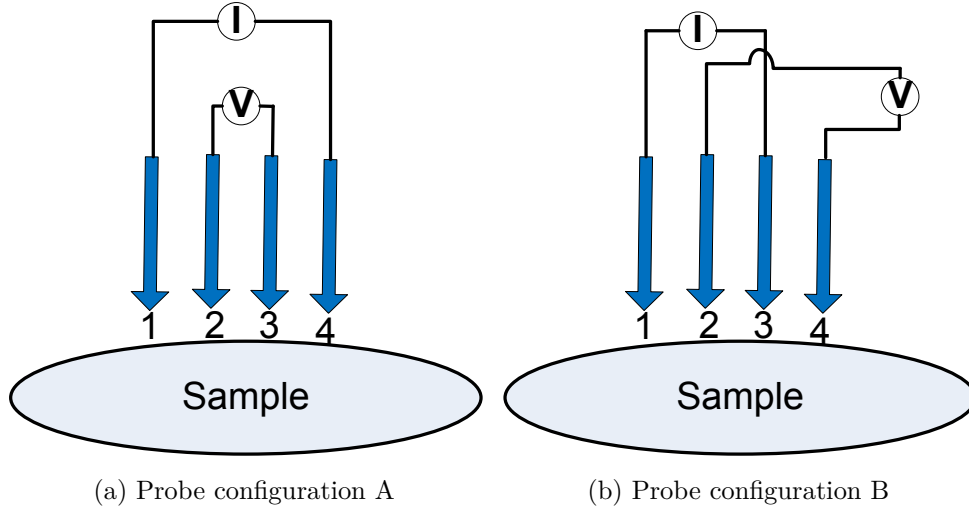


Figure 3.8: Four point probe configurations

- (i) Probe configuration A: Electric current is applied between pins 1 and 4, while voltage drop on the sample is measured between pins 2 and 3. Therefore, the average of forward voltage to current ratio and the reverse voltage to current ratio is obtained as [169, 170]:

$$R_a = \frac{1}{2} \left( \frac{V_{f23}}{I_{f14}} + \frac{V_{r23}}{I_{r14}} \right) \quad (3.13)$$

- (ii) Probe configuration B: Electric current is applied between pins 1 and 3, while voltage drop on the sample is measured between pins 2 and 4. Therefore, the average of forward voltage to current ratio and the reverse voltage to current ratio can be calculated as [169, 170]:

$$R_b = \frac{1}{2} \left( \frac{V_{f24}}{I_{f13}} + \frac{V_{r24}}{I_{r13}} \right) \quad (3.14)$$

Moreover, one probe configuration measurement (single configuration) or combination of measurements from both probe configurations (dual configuration) can be used to measure the sample sheet resistance.

### Single configuration

Single configuration takes measurement in probe configuration A alone and this is used to calculate the sheet resistance. This is generally fast and has better signal to noise ratio. The sheet resistance for single configuration is given as:

$$R_s[1] = 4.534 (R_a) \quad (3.15)$$

### Dual configuration

Dual configuration takes measurements from both probe configurations A and B and calculates the sheet resistance from this two measurements. This is more accurate than single configuration because it minimizes the effect of probe placement and sample geometry. The advantages of dual configuration are:

- (i) It does not require high symmetry orientation of the probe. It corrects for pin wobbling.
- (ii) The lateral dimension of the sample do not have to be known. The two different measurement actually include the geometric correction factors.
- (iii) The two measurements also correct for probe spacing by itself.

The sheet resistance for dual configuration is given as [169,170]:

$$R_s[2] = -14.696 + 25.173 \left( \frac{Ra}{Rb} \right) - 7.872 \left( \frac{Ra}{Rb} \right)^2 \quad (3.16)$$

### 3.2.3 Probe types

Probe types are categorized based on four specification namely; pin material (which is typically made from tungsten carbide), pin spacing (typically 1 mm), pin tip radius (typically 40  $\mu\text{m}$  to 500  $\mu\text{m}$ ), and compressive force (typically 70 g to 200 g). Choice of probe depends on properties of materials to be measured such as film thickness and conductivity. This is categorized in Tables 3.5 and 3.6.

### 3.2.4 CDE Resmap 168

The four point probe used was made by creative design engineering with the model CDE Resmap 168 as shown in Figure 3.9. It has the capability to transfer wafer automatically from the cassette slot to the chuck. It can also measure in both single and dual configurations.

Table 3.5: Probe types

| Type   | Tip radius ( $\mu m$ ) | Force (g) | Spacing (mm) |
|--------|------------------------|-----------|--------------|
| A      | 40                     | 100       | 1            |
| B      | 100                    | 100       | 1            |
| C      | 200                    | 100       | 1            |
| D(/70) | 500                    | 70        | 1            |
| E      | 40                     | 200       | 1.58         |
| F      | 40                     | 100       | 0.635        |
| G      | 100                    | 100       | 0.635        |
| H      | 200                    | 100       | 0.635        |
| FC     | 100                    | 100       | 0.5          |
| GC     | 200                    | 100       | 0.5          |

Table 3.6: Probe applications

| Type   | Applications   |
|--------|--|
| A      | Metal film   |
| B      | General metal, high dose implant                           |
| C      | Medium dose implant ( $R_s \approx 1000 \Omega/sqr$ )      |
| D(/70) | Low dose implant, very thin metal film                     |
| E      | Thick substrates, doped silicon wafers, diffusion          |
| F      | Similar to A probe but for smaller (2 mm) edge exclusion   |
| G      | Similar to B probe but for smaller (2 mm) edge exclusion   |
| H      | Similar to C probe but for smaller (2 mm) edge exclusion   |
| FC     | Similar to A probe but for smaller (1.5 mm) edge exclusion |
| GC     | Similar to C probe but for smaller (1.5 mm) edge exclusion |



Figure 3.9: CDE Resmap 168 in the clean room, Semiconductor Technology group, University of Magdeburg



### 3.3 Scanning probe microscopy

In scanning probe microscopy, the image of a surface is measured by scanning a physical sharp probe across a sample surface and monitoring the interaction between the probe and the surface. Unlike some other microscopy method (for example scanning electron microscopy), samples do not have to be placed in ultrahigh vacuum before taking measurements. The primary categories of scanning probe microscopy is as shown in Figure 3.10.

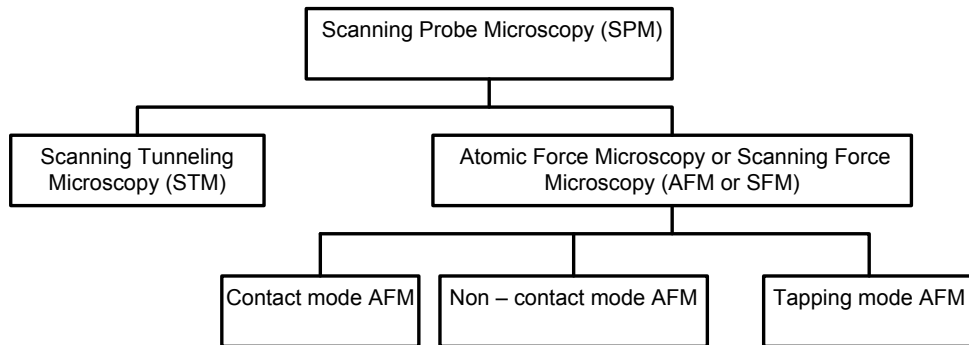


Figure 3.10: Scanning Probe Microscopy

Most of the family of scanning probe microscopy have common basic components which are illustrated in Figure 3.11. The basic components are:

- (i) Microscope; which consist of scanner, probe and detector
- (ii) Controller analog electronics
- (iii) Vibration isolation
- (iv) Computer
- (v) Two graphics monitors; one for control panel display and the other for image display

#### 3.3.1 Scanning tunneling microscopy

If a voltage  $V$  is applied between a probe and the sample surface, separated at a close distance  $d$ , a tunneling current  $I$  flows through the sample. This tunneling current decreases exponentially as the distance between the sample and the probe increases. That is  $I \approx Ve^{-cd}$ , where  $c$  is constant. First, the device chooses a “setpoint” tunneling current, and then a feedback controller loop is used to keep this “setpoint” constant (at each  $x,y$  data point) during scanning, by vertically moving the scanner along  $z$  axis until the “setpoint” is reached. The computer stores the vertical position of the scanner at “setpoint” for each  $x,y$  data point. The scanner will have to move vertically higher for a bump and closer to the surface for a deep, to keep the same “setpoint”. The stored vertical position

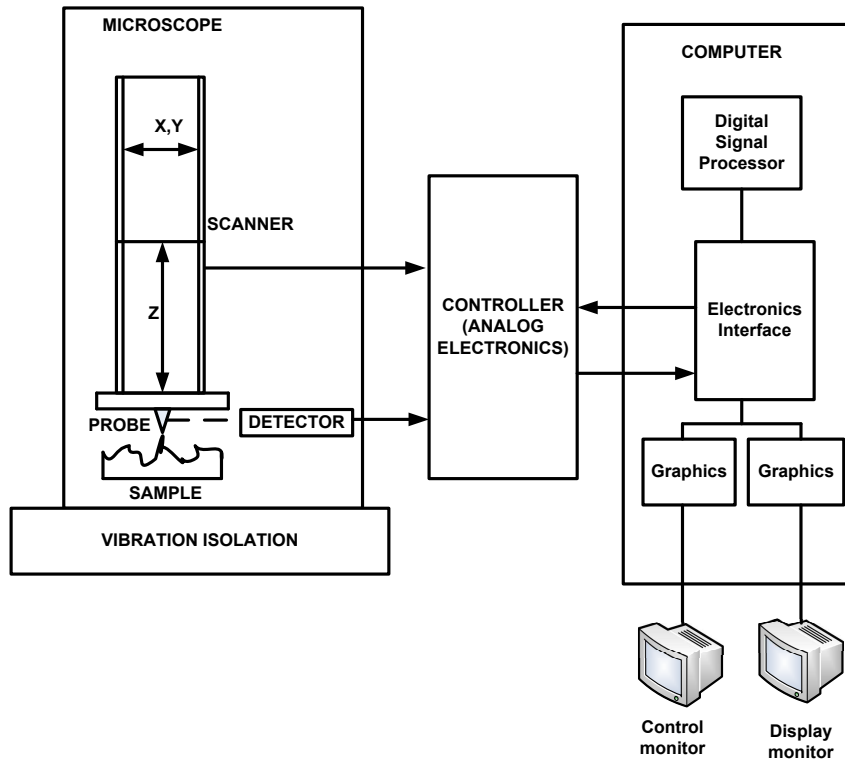


Figure 3.11: Basic components of scanning probe microscopy: Adapted from [171]

of the scanner at each x,y data point gives the topographic image of the sample. STM can only be used to measure conducting and semiconducting surfaces.

### 3.3.2 Atomic force microscopy

There are three modes of operation of AFM. These are contact mode, tapping mode and non-contact mode.

#### Contact mode

When a scanning probe attached to a cantilever physically touches a surface, there exists an interactive force (attractive or repulsive) between the probe and the surface. This interactive force is converted into elastic force using a cantilever with certain spring constant. As a result, the interactive force makes the cantilever to deflect which gives the surface topography. Hookes law is given as  $f = -kx$ , where  $f$  is the force,  $k$  is the spring constant and  $x$  is the deflection. For every scan point in the (x,y) plane (refer to Figure 3.12), a feedback loop maintains a constant “setpoint” deflection (force) between the surface and the probe by moving the scanner vertically along the z direction. The vertical position of the scanner at “setpoint” maps the surface topography. Electric signal information of cantilever deflection is obtained by using beam deflection method (Figure 3.12), where the cantilever deflects an illuminated laser beam towards a split photo diode. Typical probes used in contact mode measurements are made of silicon nitride with 20 nm

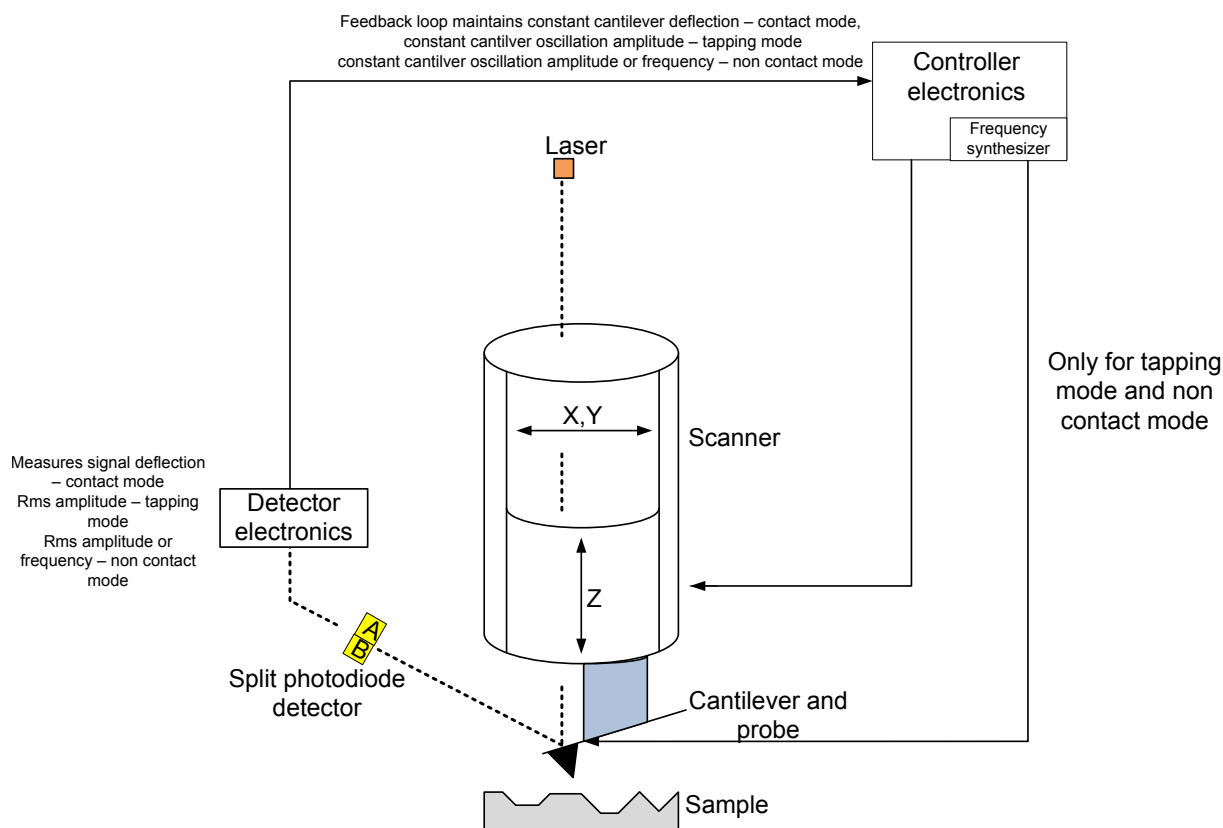


Figure 3.12: Atomic force microscopy operation principles: Adapted from [171]

to 60 nm tip radius, 100  $\mu\text{m}$  and 200  $\mu\text{m}$  cantilever length and 0.01 to 1.0 N/m spring constant. Some advantages of contact mode measurements are high speed measurements and atomic resolution in the lateral direction while some disadvantages are image distortion from lateral shear force and damage to soft samples.

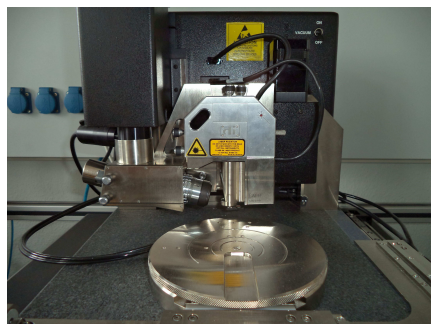
### Tapping mode

Here, the cantilever oscillates at or slightly below its resonance frequency with an amplitude ranging typically from 20 nm to 100 nm [171]. The probe lightly “taps” on the sample surface while scanning and touches the surface at the bottom of its oscillation swing. A constant “setpoint” cantilever oscillation amplitude is also maintained during scanning by a feedback loop which moves the scanner vertically until the “setpoint” oscillation signal is obtained at the photodetector. The vertical position of the scanner at “setpoint” oscillation amplitude gives the surface topography. Typical probes are made of silicon with 20 - 100 N/m spring constant, 200 - 400 kHz resonant frequency, 5 - 10 nm tip radius and 125  $\mu\text{m}$  cantilever length. Lateral resolution can be as high as 1 nm to 5 nm on most samples and there is no lateral shear force exerted on the samples but tapping mode measurement is slightly slower compared to contact mode. The atomic force microscope setup used for all measurements in this work is shown in Figure 3.13. It is usually operated in tapping mode and made from Veeco Instruments. It comprises of microscope (Figure

3.13a), dimension controller (Figure 3.13c), scanning probe microscope controller (Figure 3.13b), computer system (Figure 3.13e) and two computer screens (Figure 3.13d).

### Non-contact mode

Non contact mode is quite similar to tapping mode but the tip does not touch the surface during oscillation. The “setpoint” can be either cantilever oscillation amplitude or frequency. Non contact mode is suitable for measuring images of soft samples or fluid because there will be no damage to sample or tip since the tip does not touch the sample. Lateral resolution is however poor because it depends on tip to sample separation. The measurement speed is also slower compare to contact and tapping mode.



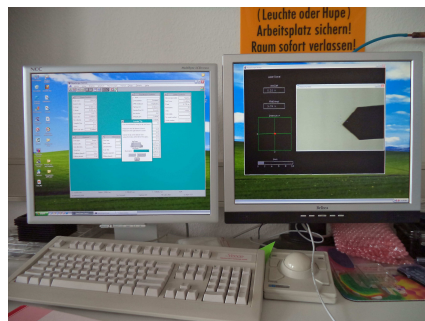
(a) Atomic force microscope



(b) Scanning probe microscope controller



(c) Dimension Controller



(d) Two computer monitors



(e) Computer system

Figure 3.13: Atomic force microscope setup from Veeco Instruments in the measurement laboratory, Semiconductor Technology group, University of Magdeburg

## 3.4 X-ray photoelectron spectroscopy (XPS)

X-ray photoelectron spectroscopy is an atomic spectroscopic technique which is used for probing the chemical composition (atomic and molecular composition) of the surface of a material. This technique is also known as electron spectroscopy for chemical analysis because it is capable of providing the quantitative analysis of a material surface.

### 3.4.1 Operating principle

XPS is based on photoelectric effect which is the ejection of electrons from the surface of a material due to impinging photons of sufficient energy. The material to be analysed is bombarded with soft x-rays of about 200 - 2000 eV (usually at ultra high vacuum conditions) which penetrates into the bulk of the material. This results in the ejection of electrons (photoionization) from the tightly bound core levels in the atom or from weakly bound valence levels. Some fraction of the electrons especially close to the surface (about 2 - 20 atomic layers (less than 100 Å) depth) will be collected in the vacuum system, while the deeply generated photoelectrons will lose their energy due to inelastic collision in the material. The collected electrons are energy analysed and a spectrum of electron intensity as a function of energy is obtained. For photoionization to take place in a solid at a particular atomic orbital, the incident photon energy must be greater than the sample binding energy associated with the atomic orbital and the work function of the solid. Each element has a unique binding energy associated with each core atomic orbital, and as a result XPS spectra give the fingerprint of the elements in the sample in which the intensity of the peaks also gives the percentage of each element. In addition, the shape of the peak can be slightly altered depending on the chemical bonding of the element, therefore XPS also gives information about the chemical state of the elements.

### 3.4.2 Conservation of energy in XPS

For a conducting sample, the band energy diagram of the sample and spectrometer is shown in Figure 3.14.

When the sample is electrically connected to the spectrometer, charge flows from one to another until the two Fermi levels coincide. In addition, the binding energy  $E_{bf}$  for the sample is obtained with reference to the Fermi level. Therefore the kinetic energy of the photo-generated electrons leaving the surface of the sample is given as:

$$KE_1 = h\nu - E_{bf} - \phi_s \quad (3.17)$$

where  $E_{bf}$  is the binding energy of the electron with respect to the Fermi level,  $\phi_s$  is the work function of the sample, and  $h\nu$  is the energy of the impinging photons (x-rays). Since

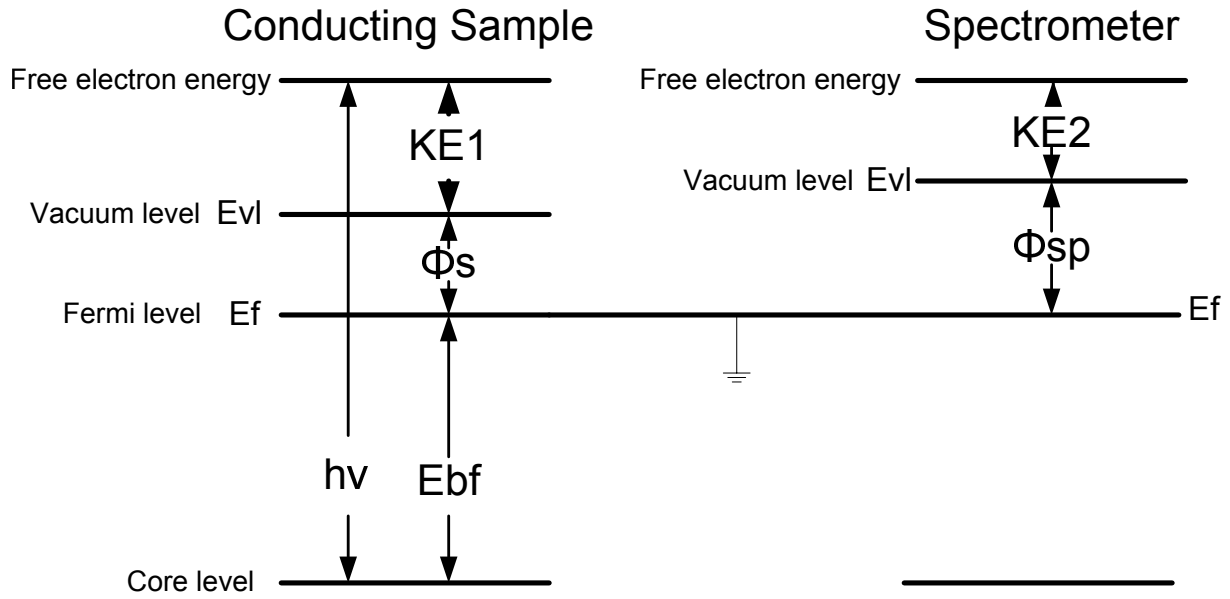


Figure 3.14: Band energy diagram for a conducting sample and spectrometer

the conducting sample is charged with respect to the spectrometer, there is a potential difference  $\phi_s - \phi_{sp}$ , called the contact potential which accelerates or decelerates the photo-emitted electrons. Therefore the kinetic energy of the electrons reaching the spectrometer for a conducting sample is given as:

$$KE2 = hv - Ebf - \phi_s + \phi_s - \phi_{sp} \quad (3.18a)$$

$$KE2 = hv - Ebf - \phi_{sp} \quad (3.18b)$$

where  $\phi_{sp}$  is the work function of the spectrometer. Which means for a conducting sample, the kinetic energy of the electrons reaching the spectrometer is independent on the sample work function but depends on the work function of the spectrometer. In XPS, the total energy  $E_{total}$  (electron kinetic energy and potential) is usually measured with respect to the fermi level of the spectrometer and for a conducting sample this is given as:

$$E_{total} = hv - Ebf - \phi_{sp} + \phi_{sp} \quad (3.19a)$$

$$E_{total} = hv - Ebf \quad (3.19b)$$

Hence, for a conducting sample, an absolute measurement of the binding energy is also possible without knowing the sample work function.

On the other hand, for an insulating sample the fermi levels of the sample and the spectrometer do not coincide because no conduction mechanism exists rather equilibrium exists between the flooding electrons and the sample vacuum potential (Figure 3.15) [172]. This occur when the energy of the flooding electron and the surface vacuum potential of

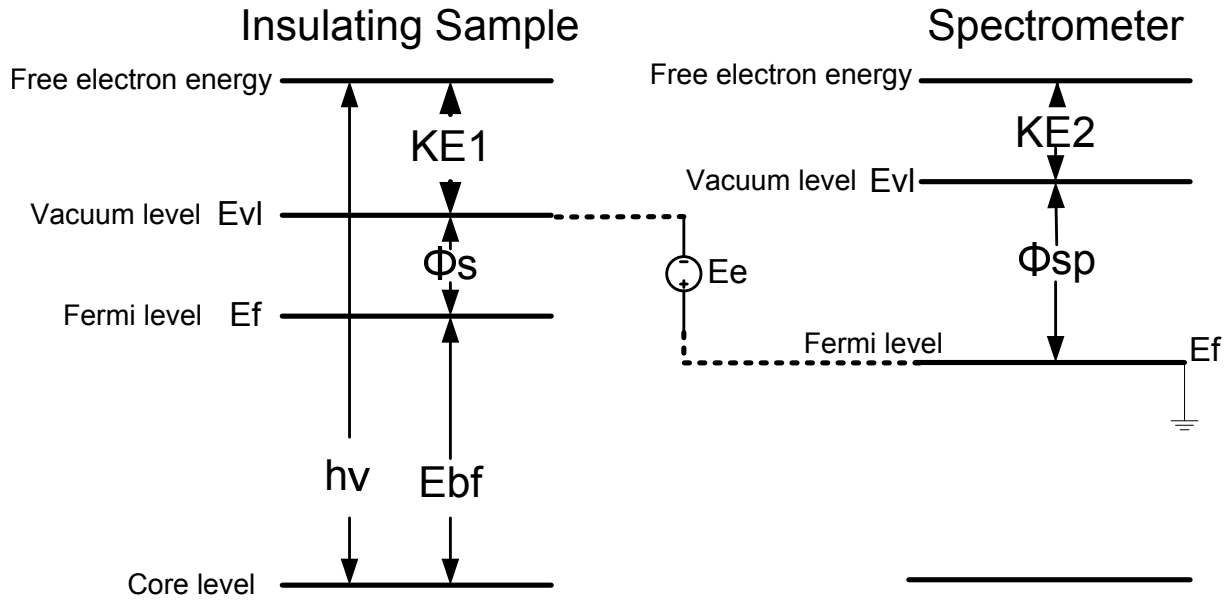


Figure 3.15: Band energy diagram for an insulating sample and spectrometer

the sample are equal. In this case, the electrons leaving the surface as measured by the instrument has a total energy given as:

$$E_{total} = hv - E_{bf} - \phi_s + E_e \quad (3.20)$$

where  $E_e$  is the effective energy of the flooding electrons relative to the spectrometer fermi level.

Therefore if  $E_e$  is known, the binding energy for an insulating sample depends on the sample work function. Which means, we need to also know the sample work function in order to absolutely determine the binding energy for an insulating sample. Thus the conservation of energy in XPS is given for conducting and insulating sample as:

$$\text{Conducting sample } KE2 = hv - E_{bf} - \phi_{sp} \quad (3.21a)$$

$$\text{Insulating sample } KE2 = hv - E_{bf} - \phi_s + E_e - \phi_{sp} \quad (3.21b)$$

where KE2 is the kinetic energy of the electrons at the spectrometer,  $E_{bf}$  is the binding energy relative to the fermi level and  $\phi_{sp}$  and  $\phi_s$  are the spectrometer and sample work function,  $E_e$  is the effective energy of the flooding electrons relative to the spectrometer fermi level,  $h\nu$  is the photon energy.

### 3.4.3 XPS instrumentation

A schematic of XPS equipment parts is given in Figure 3.16. This consists of source of fixed energy radiation, electron energy analyser, ultrahigh vacuum environment, and electron detector. The source of fixed energy radiation can be x-ray source or synchrotron.

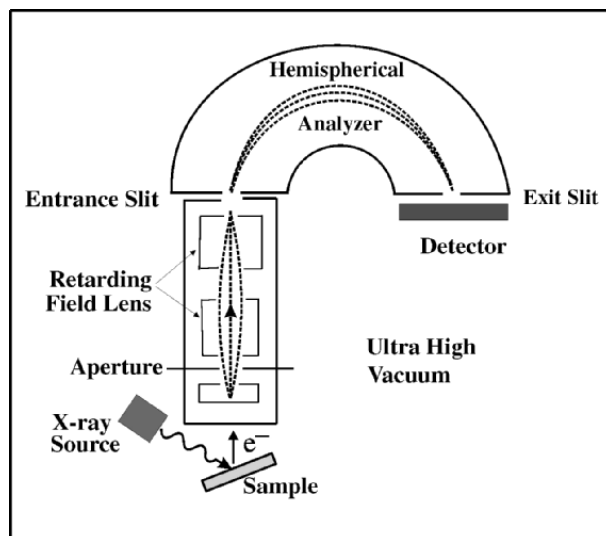


Figure 3.16: Basic components of x-ray photoelectron spectroscopy instrument [173]

An electron energy analyser separates the emitted electrons according to their kinetic energy and thereby measure the flux of emitted electrons of a particular energy. An ultrahigh vacuum is required to enable the emitted photoelectrons to be analyzed without interference from gas phase collisions. The excitation x-ray source must be monochromatic because the energy of the photogenerated electrons depends on it. As the x-rays illuminate an area of a sample, electrons are ejected with a range of energies and directions. The electrostatic and/or magnetic lens units (electron optics) collect part of these emitted electrons defined by those rays that can be transferred through the apertures and focused them to the analyzer entrance slit. Electrostatic fields within the concentric hemispherical analyzer are used to filter electrons of only a specific energy (the so called pass energy) to reach the detector. Specific initial kinetic energy of electrons are measured by setting voltages for the lens system such that the required initial energy is focussed onto the entrance slit and also that the electron velocity is retarded to have same energy as the pass energy of the hemispherical analyzer. A scan of the voltages applied to these transfer lenses is required to record a spectrum over a range of initial excitation energies.



### 3.5 Introduction to x-ray fluorescence (XRF)

X-ray fluorescence is a non-destructive chemical analytical technique which is used to identify the elements present in a sample from the emitted x-rays energies. This technique is both qualitative and quantitative. The principle of operation is illustrated in Figure 3.17. The sample is bombarded with energetic x-ray beam or accelerated particles. Photoionization takes place by the incident x-ray beam resulting to emission of core electrons from the sample (for example K-shell in Figure 3.17b). Ionization can also take place through impact of accelerated particles such as electrons, protons or ions and in such case the technique is referred to as particle induced x-ray emission (PIXE).

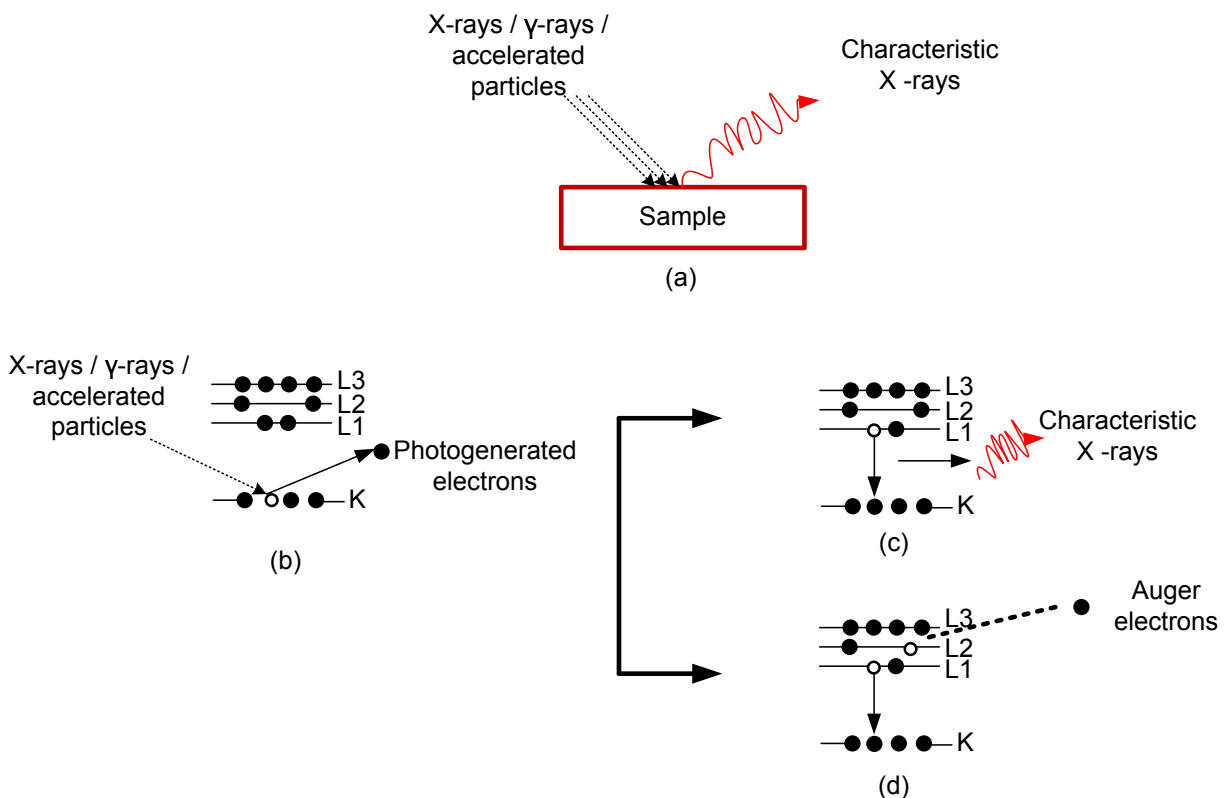


Figure 3.17: Basic principles of x-ray fluorescence (XRF) and / Particle induced x-ray emission (PIXE)

An vacant hole is left in the core shell after photoionization and as a result there is a transition of electron from a higher energy level (for instance L-shell in Figure 3.17c) into this vacant hole which results to emission of photons (x-rays) with energy  $E_{L1} - E_K$ , where  $E_{L1}$  is the energy of electron in L-shell 1 and  $E_K$  is the energy of electron in K-shell. In some other case the emitted x-ray can be reabsorbed in the sample (the so called Auger effect), leading to photoionization of a higher energy level electron (L2 level in Figure 3.17d). The emitted x-rays can be detected through energy dispersion or wavelength dispersion. Energy dispersive x-ray fluorescence separates and detects x-rays of specific energies and displays them on histograms. Wavelength dispersive x-ray fluorescence on

the other hand uses the reflection of x-rays off a crystal at a characteristic angle to detect x-rays of specific wavelength.

### 3.6 Introduction to x-ray diffraction (XRD)

X-ray diffraction is primarily used to identify crystalline structure of materials. An incident x-ray beam on a material surface is scattered (diffracted) into many directions by electrons present in the atoms of the material. Information about the arrangement of atoms in the material can be extracted from the measurement of intensities of the diffracted x-rays in specific directions.

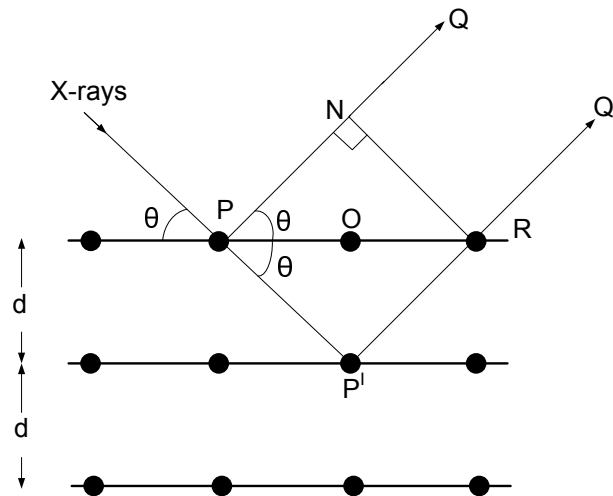


Figure 3.18: Illustration of x-ray beam incident on planes of crystal lattice

Suppose an x-ray beam is incident on a crystal lattice (as shown in Figure 3.18), this x-ray beam will be diffracted in different directions. However most of the diffracted beam will interfere destructively, thus cancelling out. While some of the beam will constructively interfere in some specific directions defined by the so called Bragg's law. Consider two reflected x-ray beam along path PQ and P<sup>I</sup>Q<sup>I</sup> in Figure 3.18, the phase difference between these two reflected x-ray beam is given as:

$$PP^I + P^I R - PN \tag{3.22}$$

But

$$PP^I = P^I R = \frac{d}{\sin \theta}, \quad PR = \frac{2d}{\tan \theta}, \quad PN = PR \cos \theta = \frac{2d \cos^2 \theta}{\sin \theta} \tag{3.23}$$

Which implies

$$PP^I + P^I R - PN = \frac{2d}{\sin \theta} - \frac{2d \cos^2 \theta}{\sin \theta} = 2d \sin \theta \tag{3.24}$$

For condition of constructive interference, Bragg's law states that the phase difference

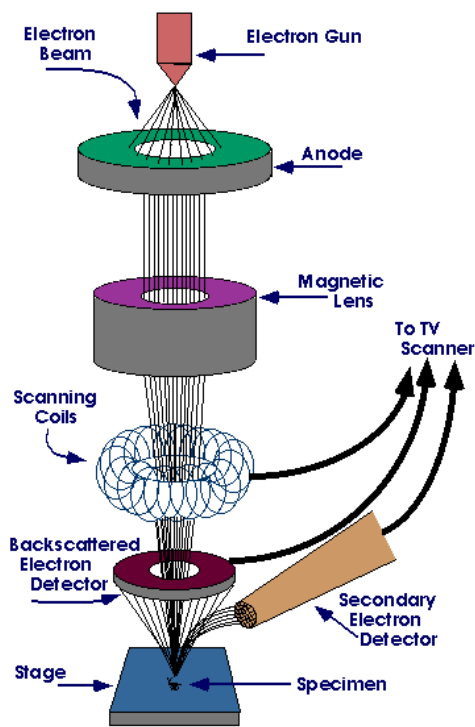
between these reflected rays must be integral multiple of incident x-ray wavelength. Which means:

$$2d \sin \theta = m\lambda \quad (3.25)$$

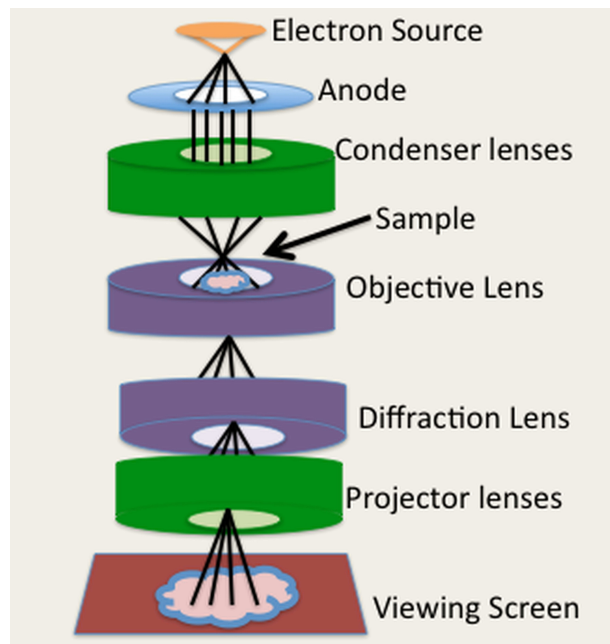
Thus, for any crystalline material we will obtain strong intensities of reflected (diffracted) x-ray beam at different incident angles by sweeping the x-ray incident angle until the Bragg condition is fulfilled. A plot of these intensities against twice of the incident angle ( $2\theta$ ) gives the XRD pattern of the crystalline material.

### 3.7 Introduction to electron microscopy

Electron microscopy is an imaging technique that uses incident electron beam as the probe. The surface is bombarded with energetic electron while the interaction between the surface and the incident electron is monitored and used to construct the image. Two common ones and especially used in this work are the scanning electron microscopy and transmission electron microscopy.



(a) Scanning electron microscope [174]



(b) Transmission electron microscope [175]

Figure 3.19: Basic components of electron microscopes

#### 3.7.1 Scanning electron microscopy

The basic components of scanning electron microscope are shown in Figure 3.19a. An electron beam generated by electron gun on top of the microscope follows a vertical

path through the microscope which is held under vacuum. These beams of electrons are collimated and focused downwards by electromagnetic fields and lenses towards the sample. Incident electron impact collision on the sample generates secondary electrons, backscattered electrons and x-rays. These x-rays, backscattered electrons, and secondary electrons are received by a detector and converted into a signal that is sent to a screen which produces the final image.

### 3.7.2 Transmission electron microscopy

The basic components of transmission electron microscope are shown in Figure 3.19b. In this case, the transmitted electrons through the sample are used to construct the image. Sample should be thin enough to allow some electrons to be transmitted through it. As a result, this technique requires careful specimen preparation such as ultrasonic disk cutting, dimpling, and ion-milling.

## 3.8 Introduction to secondary ion mass spectrometry (SIMS)

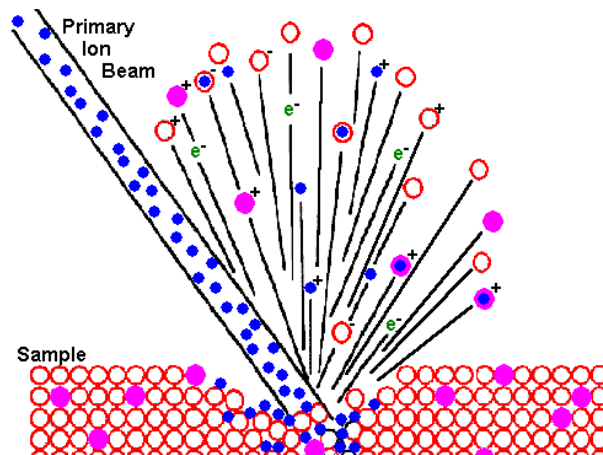


Figure 3.20: Illustration of ion beam sputtering process in secondary ion mass spectrometry (SIMS) [176]

Secondary ion mass spectrometry (SIMS) is used to detect and analyze trace elements in solid materials, especially semiconductors and thin films. SIMS is particularly useful for analysis of dopant impurities depth profile in semiconductors. The working principle of SIMS is bombardment of sample surface with primary ion beam before mass spectrometry of the emitted secondary ions from the surface. Figure 3.20 illustrates ion beam sputtering process in SIMS. A beam of primary ions (usually from Oxygen or Caesium) in the energy range 1 to 30 keV is focussed on small portion of the sample surface (typically less than 1  $\mu\text{m}$  diameter) which sputters about 1 to 10 nm depth of the sample producing sputtered

secondary ions. A mass analyser and detector is then used to analyse and measure the mass to charge ratio and ion counts of the sputtered secondary ions. SIMS normally produce qualitative measurement of trace elements. However quantitative analysis can be done with calibration from relative sensitivity factors of the desired elements and a matrix element. Basically, calibration can be done using the two equations [176],  $C_e = RSF \times \frac{I_e}{I_m}$  and  $RSF = C_m \times RSF_e$ , where  $C_e$  and  $C_m$  is the concentration of the desired element and the matrix element,  $RSF$  is the relative sensitivity factor of the desired element with respect to the matrix element,  $I_e$  and  $I_m$  is the ion current of desired element and the matrix element.

# Plasma-Assisted Atomic Layer Deposition Reactors used

## 4.1 The ‘SENTECH’ PALD system

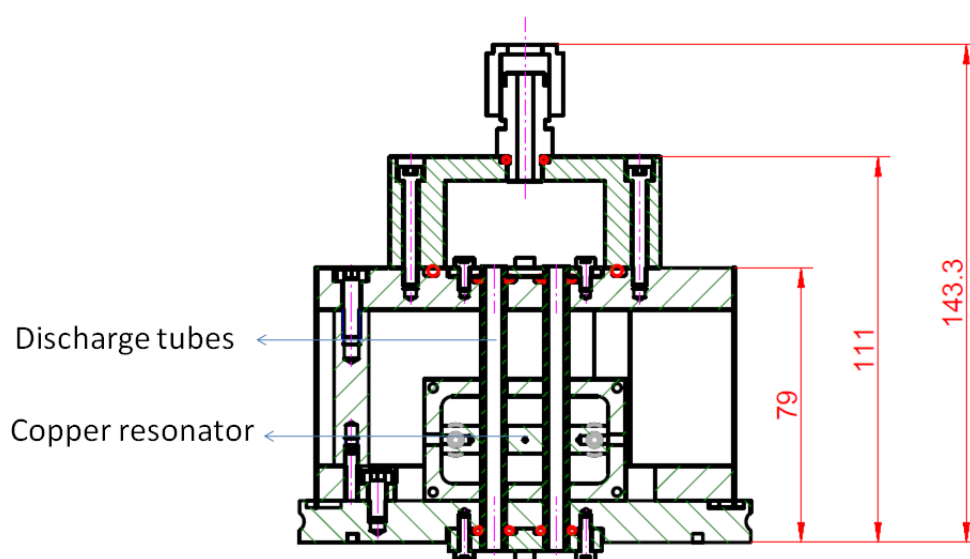
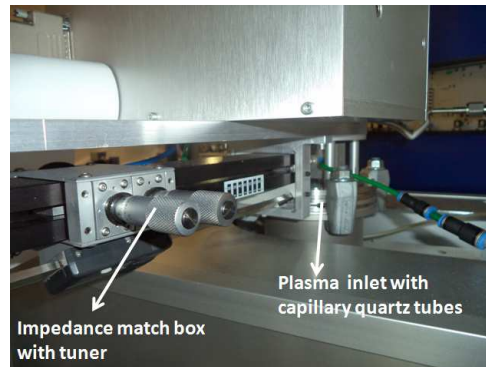


Figure 4.1: Schematic diagram of ‘EPILOGOS’ ICP plasma source [177]

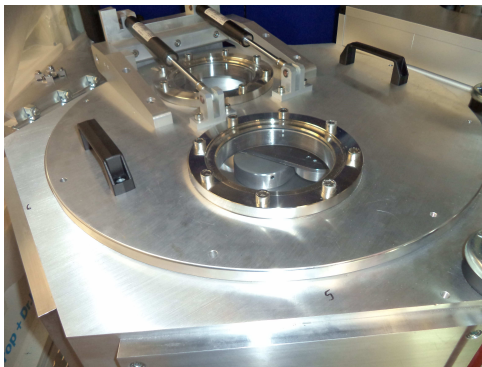
The ‘SENTECH’ plasma assisted ALD system (Figure 4.2) is developed by SENTECH Instruments Inc, Berlin. It is a single wafer ALD reactor with two precursor lines. One precursor line is capable of dosing the precursor using bubbler and booster configuration (described in section 2.10), while the other precursor line uses direct vapor draw scheme. The substrate can be heated up to 400 °C temperature while reactor walls and precursor lines can be heated up to 150 °C (but typically operated at 120 °C). Wafers are loaded in the loadlock (Figure 4.2d) and can be transferred automatically to the reaction chamber using a software-controlled robot arm. A prototype plasma source, called ‘EPILOGOS’ ICP plasma source, is mounted on top of the PALD reactor which generates the plasma radicals. The ‘EPILOGOS’ ICP plasma source is made of copper resonator that excites plasma simultaneously in twin quartz discharge tubes of 5 mm internal diameter (Figure 4.1). A microwave power is generated by GaAs oscillator at about 2.45 GHz frequency and maximum output power of 50 W. This generated microwave power is inductively coupled by the copper resonator into the discharge tubes which generates plasma. Usually, a low



(a) 'SENTECH' PALD cluster system



(b) 'EPILOGOS' ICP plasma source



(c) Fully automated transfer chamber

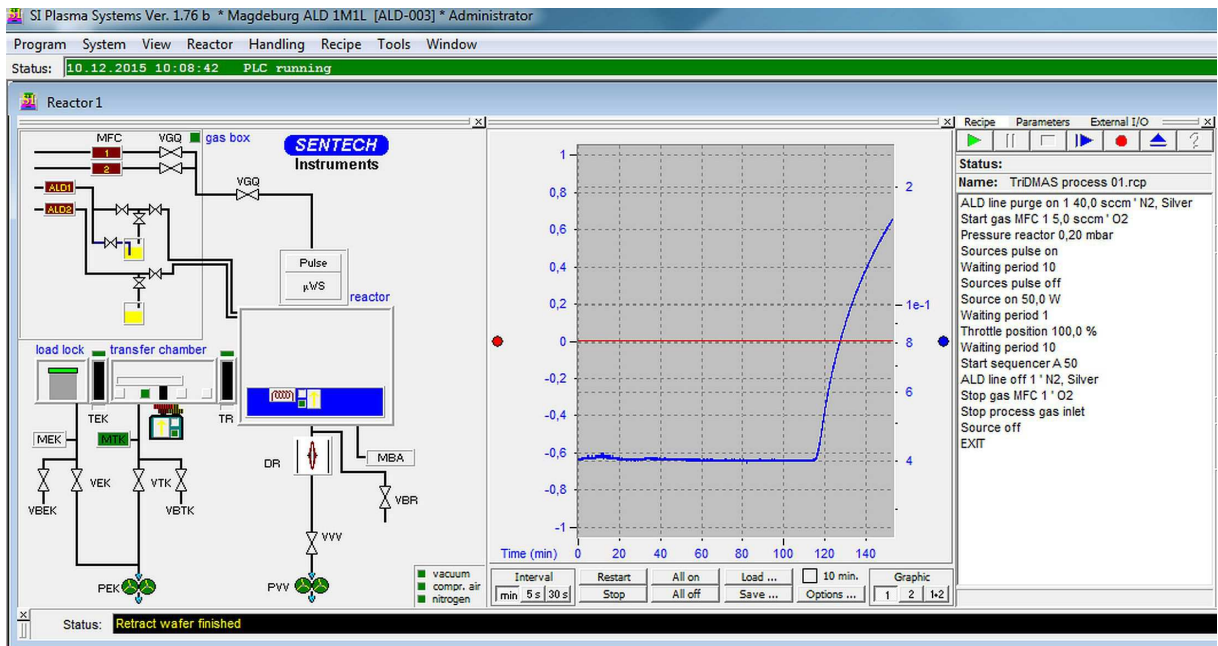


(d) Single wafer loadlock

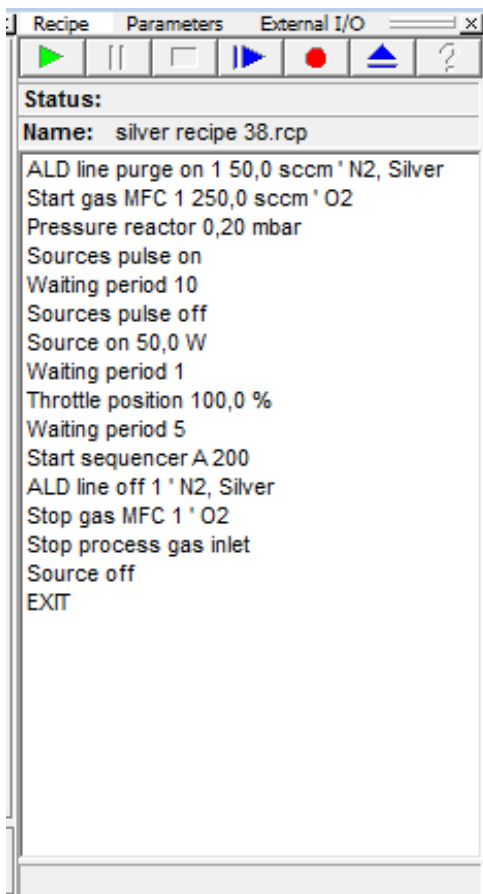
Figure 4.2: The 'SENTECH' PALD system

frequency ignition of 5 kV is required to generate a seed plasma that is then sustained through the inductively coupled microwave power. The electric field is mostly parallel to the discharge tubes capillary walls in the ICP source and thus there is negligible etching of the capillary walls that could lead to film contamination. Besides, the plasma parameters such as plasma power and frequency can be controlled independently of substrate parameters in the ICP source. Atomic O, N and H radicals can be generated with flux densities greater than  $2 \times 10^{16} \text{ cm}^{-2} \text{ s}^{-1}$  using gas flows of 100 to 300 sccm.

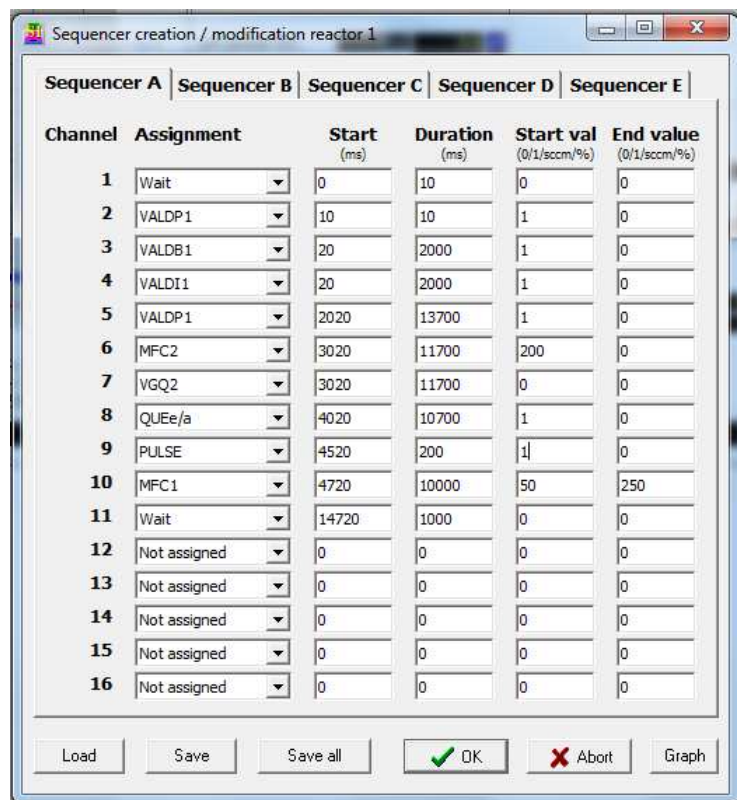
The PALD system is controlled using a modern client-server architecture. The server software is installed on a computer system that controls the PALD system via programmable



(a) Graphical user interface for the 'SENTECH' PALD system



(b) Recipe function



(c) Sequencer function

Figure 4.3: Software user interface for the 'SENTECH' PALD reactor control and data logging



logic controller (PLC) circuit. The PLC can be connected to the computer system using ethernet or RS232 cable. The client software can be installed on the same or a different computer and communicates with the server over a LAN, WAN or Internet. A graphical user interface is provided through which the user can operate the PALD system. This is shown in Figure 4.3. This software has two important inbuilt functions for process control which are “recipe” (Figure 4.3b) and “sequencer” (Figure 4.3c) functions. The “recipe” can be used to set some major process steps while “sequencer” can be used to set the ALD step such as opening and closing of ALD valves. In addition, the “sequencer” function can be used inside the “recipe” to develop full ALD processes. These features (“recipe” and “sequencer”) give the user flexible control over the process in simple algorithm (programming) steps.

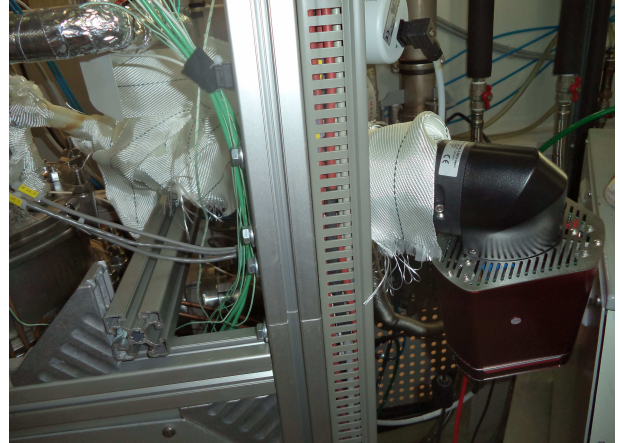
## 4.2 The ‘HFO’ PALD system

The ‘HFO’ PALD system was developed and build by the IMOS group, University of Magdeburg. It is a single wafer ALD reactor operated at low pressure and with three precursor lines. The reactor is a cold-wall system which is equipped with an inner liner that is heated by the susceptor plate. The precursor lines can be heated up to 250 °C temperature (although typically operated at 120 °C) while the substrate can be heated to 650 °C. Precursor dosing is achieved by direct vapor draw in all the three lines with nitrogen as carrier gas. The plasma radicals are generated by a capacitively coupled plasma source (‘EPILOGOS’ CCP) also developed by SENTECH Instruments GmbH and Ferdinand-Braun-Institut, Berlin.

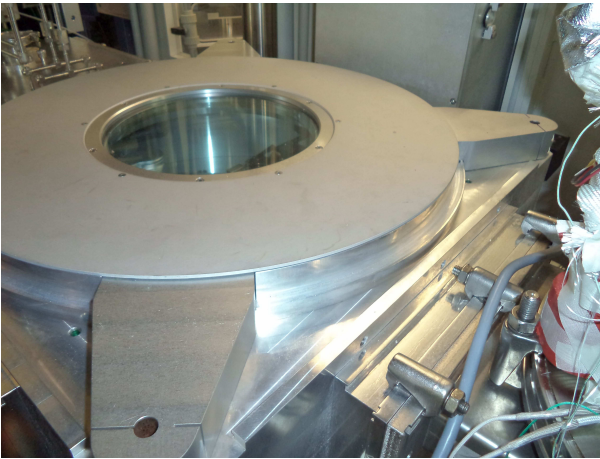
The ‘EPILOGOS’ CCP prototype is made up of 2 by 2 array (4 in total) of ceramic capillary tubes where plasma generation takes place and this was mounted as a module on top of the ALD reactor. There is no valve between the reactor and the plasma because small plasma gas can block undesired back flow of unwanted species into the plasma. Each discharge tube is powered by individual GaN microwave power oscillator at 2.45 GHz. All the microwave power oscillators are powered by a common 28 V dc supply with an input power of 112 W. The power delivered into the plasma is more than 10 W for each discharge tube. Plasma ignition is set by simply switching on the oscillators using a digital signal pulse from the control system. Fast and reproducible ignition is obtained for the gas flow of 50 sccm of pure oxygen. The flow density of atomic oxygen measured by a nickel probe for 200 and 300 sccm gas flow was  $5 \times 10^{15} \text{ cm}^{-2}\text{s}^{-1}$  and  $8 \times 10^{16} \text{ cm}^{-2}\text{s}^{-1}$ , respectively. The ALD system (Figure 4.4a) is equipped with loadlock having cassette capabilities as shown in Figure 4.4d, and dealer transfer system (Figure 4.4c) for wafer transfer under vacuum conditions. In addition, a rapid thermal processing system is attached to the same loadlock-dealer transfer system as the ALD reactor. The ALD system also has in-situ quadrupole mass spectrometry capability shown in Figure 4.4b. The ALD system



(a) 'HFO' PALD system (single wafer reactor) with 'EPILOGOS' CCP plasma source



(b) In-situ Quadrupole Mass Spectrometer attached to the 'HFO' system



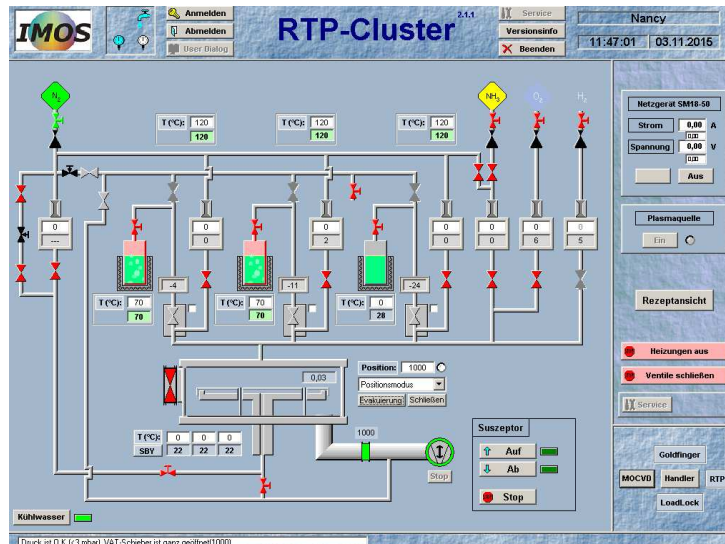
(c) Transfer chamber



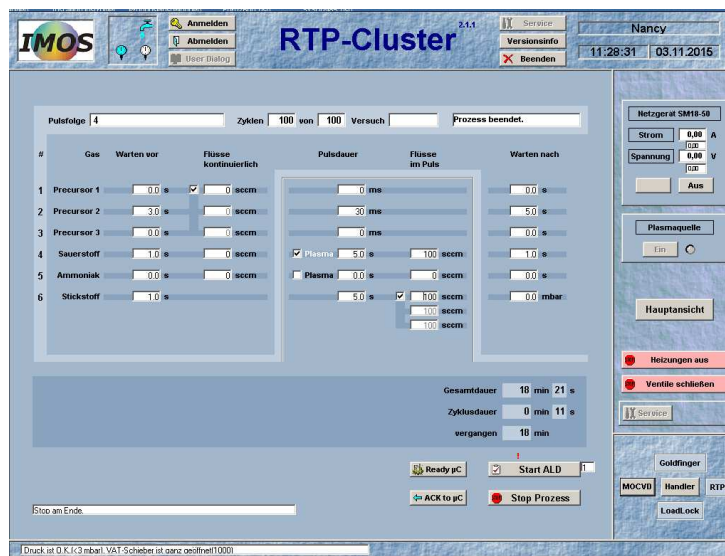
(d) Multiple wafer cassette inside loadlock

Figure 4.4: The 'HFO' PALD system

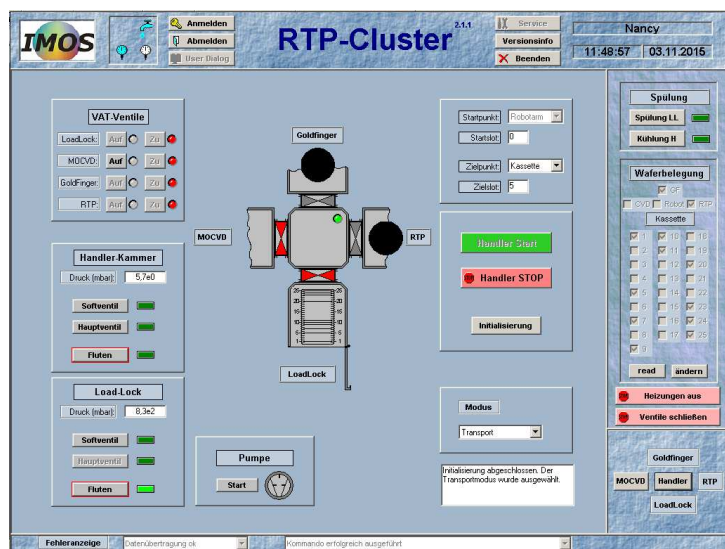
is programmed and controlled via a microcontroller using a software called VAC-NT from AIS Automation GmbH. The user interface of the ALD system is shown in Figure 4.5. Figure 4.5a is the chamber view showing the ALD chamber, valves, temperature controllers, precursor and gas lines. The process recipe is designed in the process view (Figure 4.5b) in which a process flow template is already given in the software fields. Also, transfer of wafer into the ALD chamber can be done under vacuum using the handler system (Figure 4.5c) in two steps, first from loadlock to the handler and then from handler to the ALD chamber.



(a) 'HFO' PALD system - chamber view



(b) 'HFO' PALD system - process view



(c) Handler system for wafer transfer

Figure 4.5: Software interface for the 'HFO' PALD system

# Results and Discussions

## 5.1 Plasma distribution monitoring with a silver coated silicon wafer

Plasma radicals can recombine inside the chamber when they collide with the walls and on the surface of the wafer. It might be necessary to know whether the plasma radicals are reaching the surface of the wafer as well as the radical distribution at the surface of the wafer. Efficient ALD process requires saturation of precursor on the surface. ALD processes can be limited by one of the precursor supply, which can be the plasma radicals, and this can prevent uniform and saturated deposition or give unnecessary long precursor times to achieve conformal ALD deposition. We can qualitatively know the oxygen and hydrogen plasma radical distribution without the need to make a deposition process, by using a silver coated silicon wafer. This gives useful information about the plasma source and helps hardware modifications where necessary. Silver can be oxidized with atomic oxygen at room temperature and molecular oxygen at elevated temperatures. Silver has been reported to be oxidized with atomic oxygen [178, 179]. Similarly, silver oxide can be reduced with molecular and atomic hydrogen [180, 181]. Reduction of silver oxide to silver with atomic hydrogen is more efficient as compared to silver oxide reduction with molecular hydrogen at room temperature. At elevated temperature, silver oxide can also be reduced to silver with molecular hydrogen.

For oxygen plasma monitoring, silver coated silicon wafer is oxidized with oxygen plasma and the effect can be directly seen on the wafer. Also, for hydrogen plasma monitoring, uniformly oxidized silver (silver oxide) is reduced to silver with hydrogen plasma. The silver surface becomes shining again, and the effect of hydrogen plasma can also be seen on the wafer. The basic chemical equations behind the two processes are:



The two processes are reversible and the wafer can be re-used for some time until the surface roughness due to plasma etching becomes sufficiently large.

Thick silver layers (about 100 nm) were deposited by physical vapor deposition (electron beam evaporation) on top of different substrates. One substrate was 150 mm silicon

wafer oxidized by thermal oxidation to silicon oxide. Another substrate was also titanium deposited on 150 mm silicon wafer. The silver layers could stick on both silicon oxide and titanium substrates. The deposited silver film was used to monitor the distribution of the plasma source by oxidation to silver oxide and subsequent reduction to silver. Two plasma sources were monitored, one is capacitive coupled plasma source installed on the ‘HFO’ PALD system. The other is inductively coupled plasma installed on the ‘SENTECH’ PALD system. The silver layer was oxidized to silver oxide with oxygen plasma exposure in both plasma sources, and again reduced with hydrogen plasma exposure. Ellipsometric model was created with a dielectric layer to account for the silver oxide as shown in Figure 5.1. And this was used to measure the silver oxide thickness map of the 150 mm wafer.

|                                 |
|---------------------------------|
| AgO (fit)                       |
| Ag PVD                          |
| Titanium                        |
| Cauchy SiO <sub>2</sub> (therm) |
| Silicon (100) Jellison          |

Figure 5.1: Ellipsometric model for the layer stack with silver oxide on top

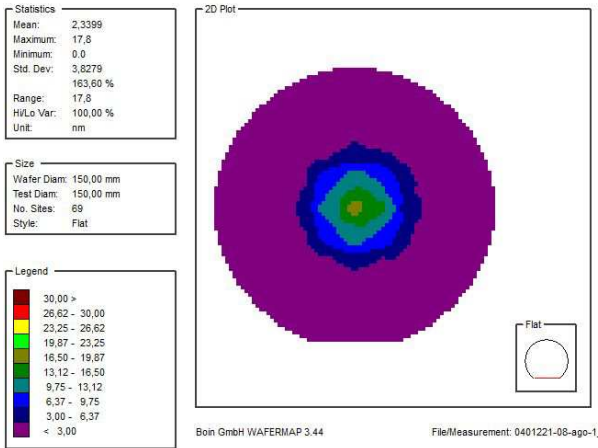
### 5.1.1 Plasma monitoring on the ‘SENTECH’ PALD system

#### ‘EPILOGOS’ ICP source oxygen plasma monitoring

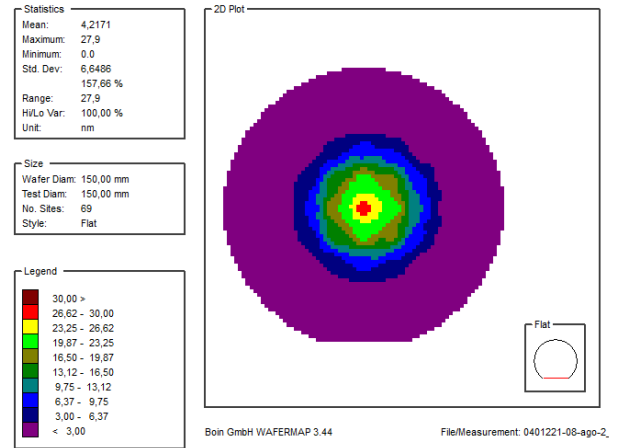
Oxidation was performed with the ICP source on the ‘SENTECH’ PALD system for three successive 30 s exposure respectively. The oxygen flow was 200 sccm while the plasma power was 30 watts. The wafer was exposed to oxygen plasma for the first 30 s and then the same wafer was exposed to oxygen plasma for the next 30 s as well as the last 30 s oxygen plasma exposure. Wafer maps were taken after each oxidation as shown in Figures 5.2a, 5.2b and 5.2c.

For the first 30 s oxidation, silver oxide was only around the middle of the wafer (Figure 5.2a). The oxygen plasma radicals from the ICP appear to be only localized in the middle. This can also be due to high oxygen radical recombination rates on metallic surface. Oxygen radicals recombine almost immediately after reaching the surface and this makes it more difficult to have uniform oxidation on the entire silver surface. Silver oxide is in the middle of the wafer because the two plasma source tube outlets are placed over the centre of the wafer. After subsequent oxidation, silver oxide increases significantly in the middle and much lower at the edges of the wafer (Figures 5.2b and 5.2c).

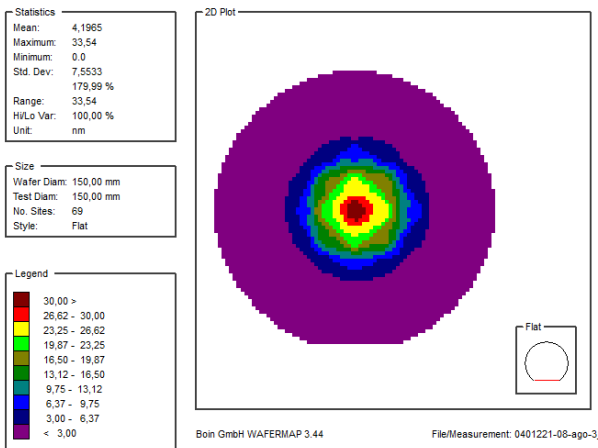
The wafer has a small brown spot in the middle after 90 s oxidation as shown in Figure



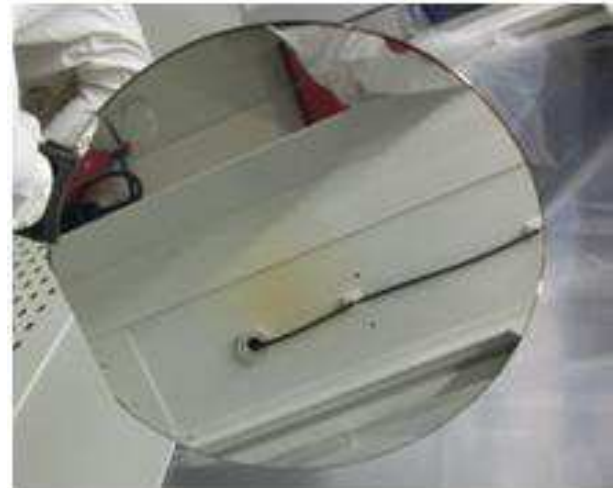
(a) First 30 s Ag oxidation



(b) Additional 30 s (60 s) Ag oxidation



(c) Additional 30 s (90 s) Ag oxidation



(d) Silver wafer image after 90 s oxidation on ICP

Figure 5.2: Oxygen plasma monitoring on ICP with 200 sccm  $O_2$  flow at room temperature

5.2d. In certain cases, this ICP source might have faster saturation plasma exposure times for deposition of materials on surfaces with lower oxygen radical recombination rates. However, it may need remarkably long plasma time for material deposition on metallic surfaces. Recombination rates of oxygen radicals on different substrates are given in [79]. Oxygen radicals have lower recombination rates on pyrex and silicon oxide surfaces. Therefore we might need lesser plasma time for deposition using oxygen radicals on such surfaces as compared to metallic surfaces.

## 'EPILOGOS' ICP source hydrogen plasma monitoring

The oxidized silver layer (silver oxide in Figures 5.2d and 5.2c) was reduced to silver by hydrogen plasma exposure after two successive 30 s exposure time (Figure 5.3) in the 'SENTECH' PALD system. The plasma power was 30 watts and the hydrogen flow was 200 sccm. 100 sccm argon was used for igniting the hydrogen plasma and substrate was held at room temperature. The wafer appears shining again immediately after the first 30 s hydrogen plasma exposure.

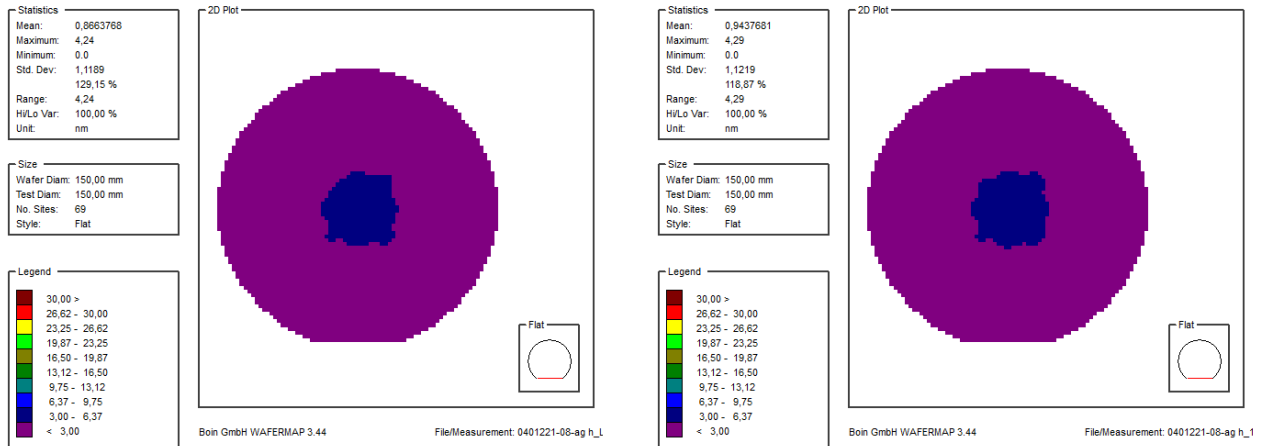


Figure 5.3: Hydrogen plasma monitoring on ICP with 200 sccm H<sub>2</sub> flow and substrate at room temperature

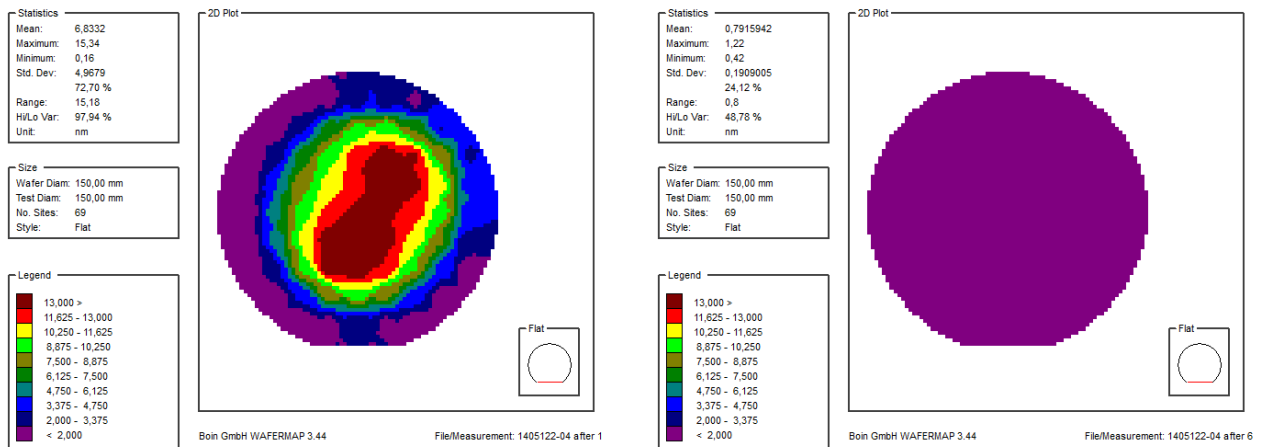


Figure 5.4: Hydrogen plasma monitoring on ICP with 70 sccm H<sub>2</sub> flow and substrate at 250 °C temperature

The next 30 s reduction (Figure 5.3b) did not give a significant change, but rather surface roughness. The silver oxide layer was quite thin and could be reduced back to

silver again. The maximum silver oxide thickness after 30 s hydrogen plasma exposure reduced from 33.54 nm to 4.29 nm with the model used, and only in the wafer middle position. Hydrogen plasma might also be localized in the middle as it was for oxygen plasma.

Another hydrogen plasma experiment was performed at higher substrate temperature (Figure 5.4) and hydrogen plasma reduction seems to be improved at higher temperature such as 250 °C and above, even hydrogen gas could reduce silver oxide at such elevated temperature. An improvement in hydrogen plasma reduction at higher temperature might be due to additional contribution from molecular hydrogen reduction at such temperature. However, thicker silver oxide layer could not be completely reduced back to silver again even after 20 minutes of hydrogen plasma exposure at 250 °C temperature with this ICP source. The ICP source can only reduce thin oxides and will take remarkably longer time to reduce thicker oxides. In order to deposit metals, it may also need long plasma exposure time to completely remove the ligands.



## 5.1.2 Plasma monitoring on the 'HFO' PALD system

### 'EPILOGOS' CCP source oxygen plasma monitoring

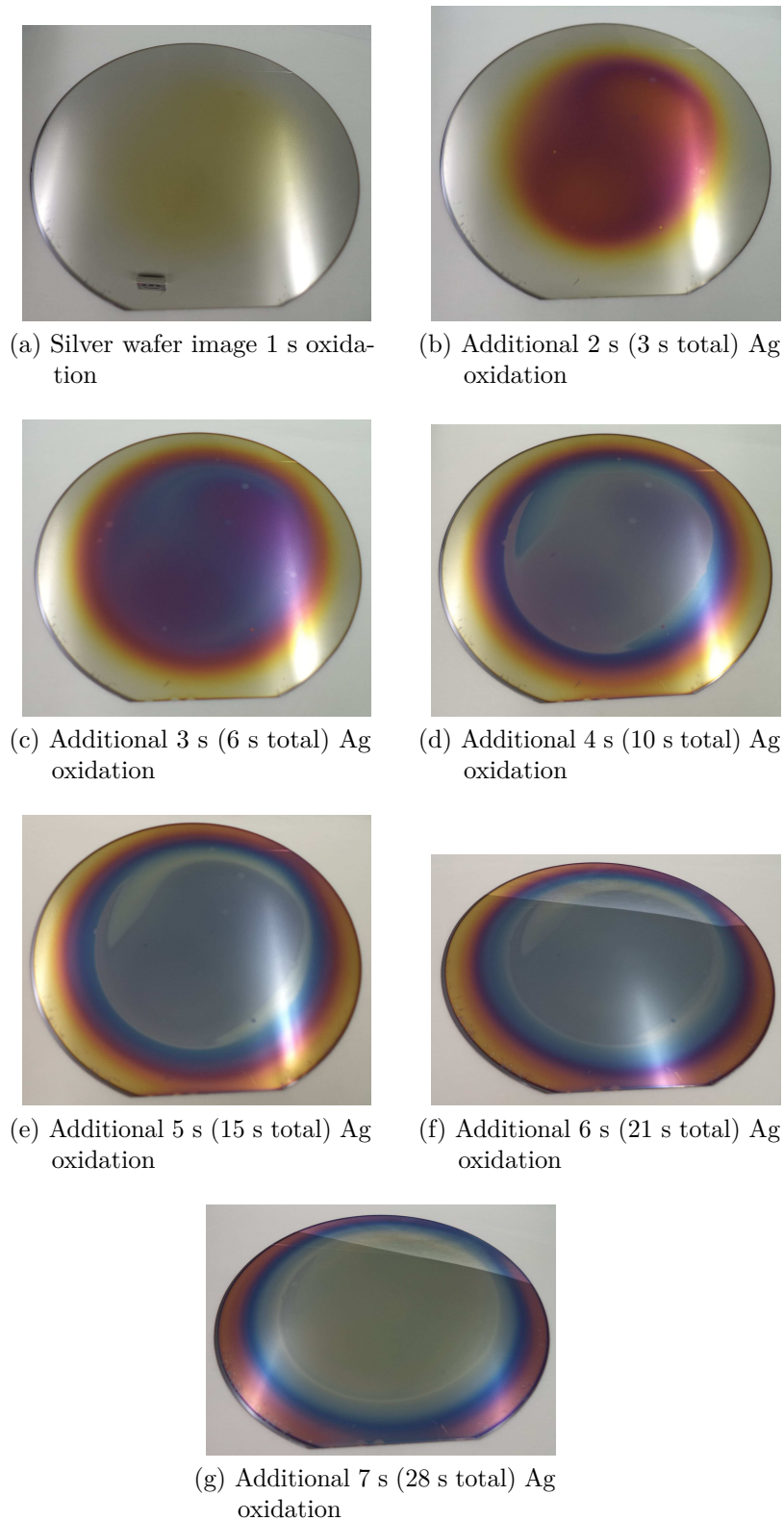


Figure 5.5: Oxygen plasma monitoring on CCP with 100 sccm  $O_2$  flow at room temperature

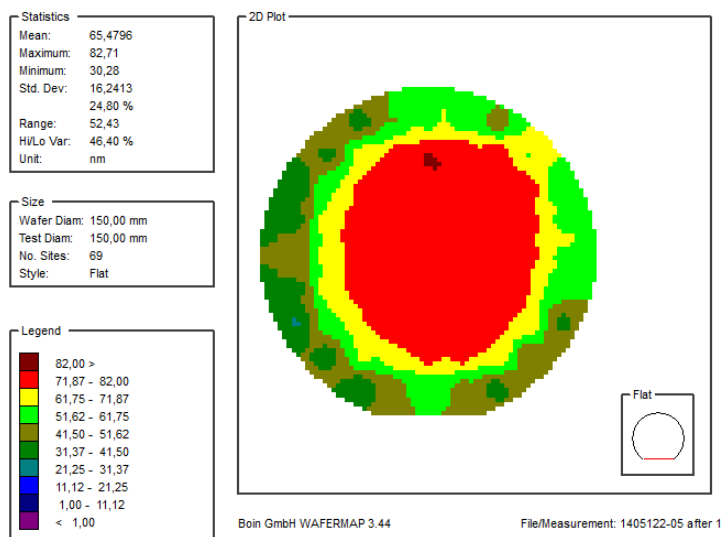
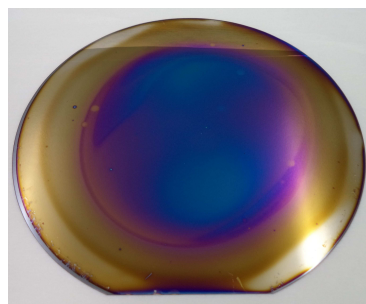


Figure 5.6: Final wafer map of Figure 5.5g

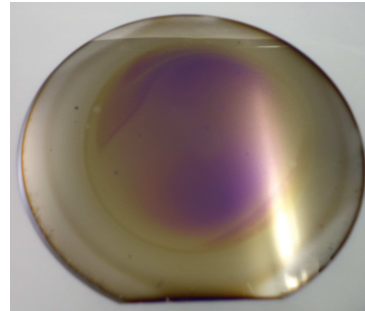
A fresh silver film was exposed to oxygen radicals produced by the CCP source on the ‘HFO’ PALD system with oxygen flow of 100 sccm. The exposure time was varied from 1 s to 7 s and oxidation was made on top of the previous one. That is, after 1 s plasma exposure, additional 2 s exposure was made on same wafer, and then increased up to 7 s. Wafer pictures were taken after each oxidation and the final ellipsometric measurement gave a maximum of 82 nm with the model used after a total time of 28 s oxygen plasma. The oxidation of the silver films appears more effective and has broader distribution as shown in Figure 5.5. For dielectric deposition, with lower plasma recombination rates, wide plasma distribution may not be necessary, since the plasma radicals will be able to saturate the surface within short time without being consumed. However it is necessary to make the plasma distribution broad for conformal deposition on metallic substrates since the plasma radicals are immediately consumed on reaching the metal surface. Moreover broad plasma distribution may be achieved by increasing the plasma power, using a shower head distribution and array of plasma inlets. In general, the CCP plasma source produced denser oxygen radicals as compared to the ‘EPILOGOS’ ICP source used, probably as a result of higher plasma power up to 50 to 60 W for the CCP, compared to 30 W for the ICP source. Another reason for better CCP efficiency is the different hardware configuration, since the CCP source has four inlet tubes (2 by 2) generating the plasma, whereas the ICP source has only two tubes placed over the centre of the wafer. Already 6 s oxygen plasma was sufficient to achieve a sufficiently wide oxidation of the silver surface over 150 mm wafer as compared to 90 s used for the ICP source. This can be seen in the wafer image in Figure 5.5 and the wafer map of Figure 5.6.

## 'EPILOGOS' CCP source hydrogen plasma monitoring

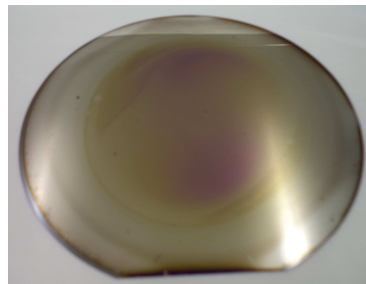
The oxidized silver layer (silver oxide wafer map in Figure 5.6) was again reduced to silver by hydrogen plasma exposure with the CCP source. The hydrogen flow was 250 sccm and after 20 s hydrogen plasma exposure, the silver oxide was completely reduced (Figure 5.7).



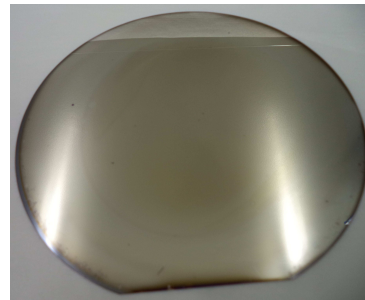
(a) 5 s H<sub>2</sub> plasma



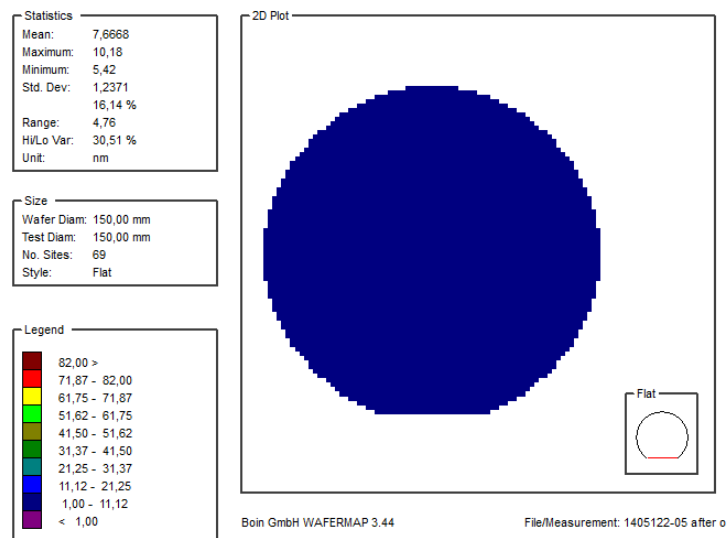
(b) Additional 5 s (10 s in total) H<sub>2</sub> plasma



(c) Additional 5s (15s in total) H<sub>2</sub> plasma



(d) After 30 s (in total) H<sub>2</sub> plasma



(e) Final wafer map after 30 s H<sub>2</sub> plasma

Figure 5.7: Hydrogen plasma monitoring on CCP with 250 sccm H<sub>2</sub> flow at room temperature

The maximum silver oxide thickness reduced from 80 nm to 10 nm with the model used and with broad radical distribution on substrate. The CCP source seems to be more effective for reduction and this type of source will be suitable for metal deposition. It takes only 20 s to completely reduce the silver oxide with the CCP source, while it will need more than 20 minutes exposure time to reduce silver oxide of same thickness with the ICP source. It can therefore be concluded that both the hydrogen and oxygen plasma radicals were more denser on the CCP source than the ICP source used.

### 5.1.3 Improved 'EPILOGOS' ICP source with stub tuner on the 'SENTECH' system

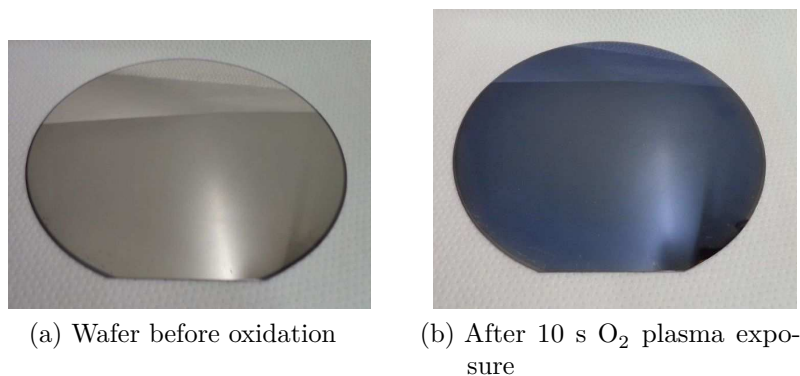


Figure 5.8: Oxygen plasma monitoring on upgraded ICP source with 250 sccm O<sub>2</sub> flow, 50 W plasma power, 10 s plasma exposure and substrate at room temperature

The 'EPILOGOS' ICP source power on the 'SENTECH' PALD system was increased up to 50 watts maximum output power, as compared to 30 watts with the old ICP source. In addition, the microwave source impedance was also matched with the plasma impedance using a stub tuner to reduce the reflected power. The stub tuner was set to obtain reflected power less than 2 W for 250 sccm O<sub>2</sub> flow and 50 W output power. The plasma source was again monitored with a silver coated wafer.

Ag coated wafer was clearly oxidized completely after 10 s O<sub>2</sub> plasma exposure (Figure 5.8). The middle of the wafer had a dark brown colour while the edge of the wafer was bluish, which means oxidation is still higher in the middle than the edges as expected, since the plasma outlet is over the centre of the wafer. However, the oxygen radical supply reached the edge of the wafer this time, as compared to the earlier ICP source with 30 W input power in Figure 5.2.

Similarly, hydrogen plasma was also monitored on the improved ICP source using the oxidized Ag coated wafer in the Figure 5.8b. Reduction of AgO to Ag is already visible with 5 s H<sub>2</sub> plasma exposure (Figure 5.9b) and the silver films starts to become shining after 15 s H<sub>2</sub> plasma exposure in total. The silver oxide on the wafer seems to be completely

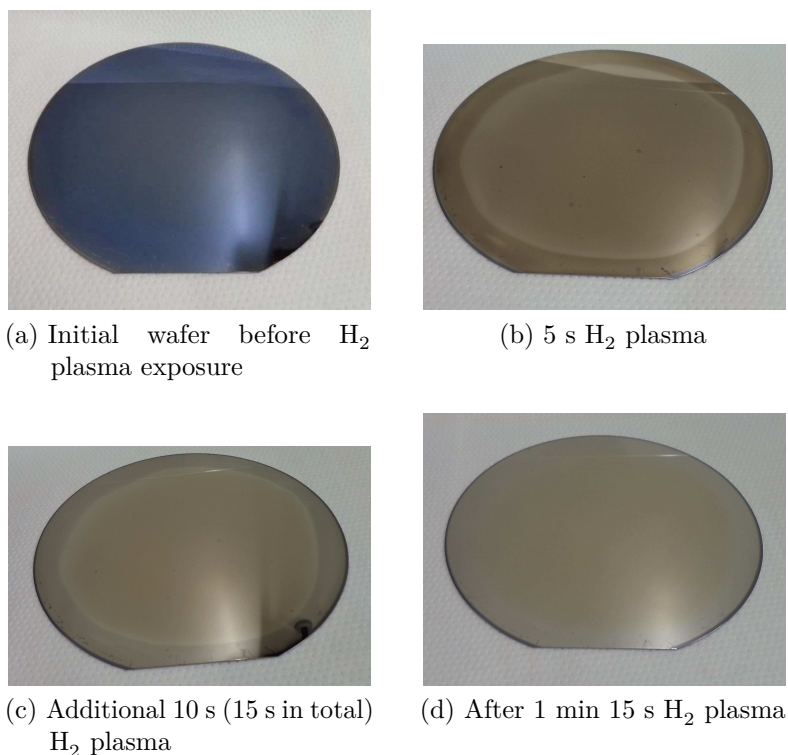


Figure 5.9: Hydrogen plasma monitoring on upgraded ICP source with 200 sccm H<sub>2</sub> flow, 200 sccm / 70 sccm Ar flow ( during ignition / plasma burning), 50 W plasma power and 70 °C substrate temperature

reduced to silver after more than 1 min hydrogen plasma exposure. The oxygen and hydrogen radicals generation on the improved ICP source is about comparable with that of the ‘EPILOGOS’ CCP source in section 5.1.2.

#### 5.1.4 Other comments on the ‘EPILOGOS’ ICP source



Figure 5.10: Coatings inside the dual plasma tubes after several ALD processes

The first ICP source was contaminated from accumulated Ag ALD experiments due to depositions inside the plasma tubes (Figure 5.10), which led to loss of efficiency of the plasma source over time. Continuous blocking gas of 200 - 300 sccm hydrogen was always flowing during the Ag pulse time for most of the experiments that led to contamination

inside the plasma tubes. However, this seems to be insufficient to completely prevent back diffusion into the tubes and hence problematic for the Ag ALD experiments. The blocking gas was then changed to argon with 250 sccm flow for other Ag processes, since argon is in principle denser than hydrogen and hence should minimize contamination in the plasma tubes. A valve between the plasma source and the chamber may be necessary for metal ALD process and there should be continuous check of performance and or contamination where necessary.

## 5.2 Plasma-assisted ALD of silver (Ag) layers

Silver films were deposited by plasma-assisted ALD using a silver precursor and hydrogen radicals on the 'SENTECH' PALD system with prototype 'EPILOGOS' ICP plasma source.

### 5.2.1 Silver precursor used

The silver precursor used is shown in Figure 5.11. The precursor class is silver  $\beta$ -diketonate, which is  $\text{Ag}(\text{fod})(\text{PEt}_3)$  (fod = 2,2-dimethyl-6,6,7,7,8,8,8-heptafluorooctane-3,5-dionato,  $\text{PEt}_3$  = triethyl phosphine). This silver precursor is the best choice found in literature suggested to be thermally stable up to 230 °C by thermogravimetric measurements [13] and is also commercially available (obtained from Strem Chemicals Inc).

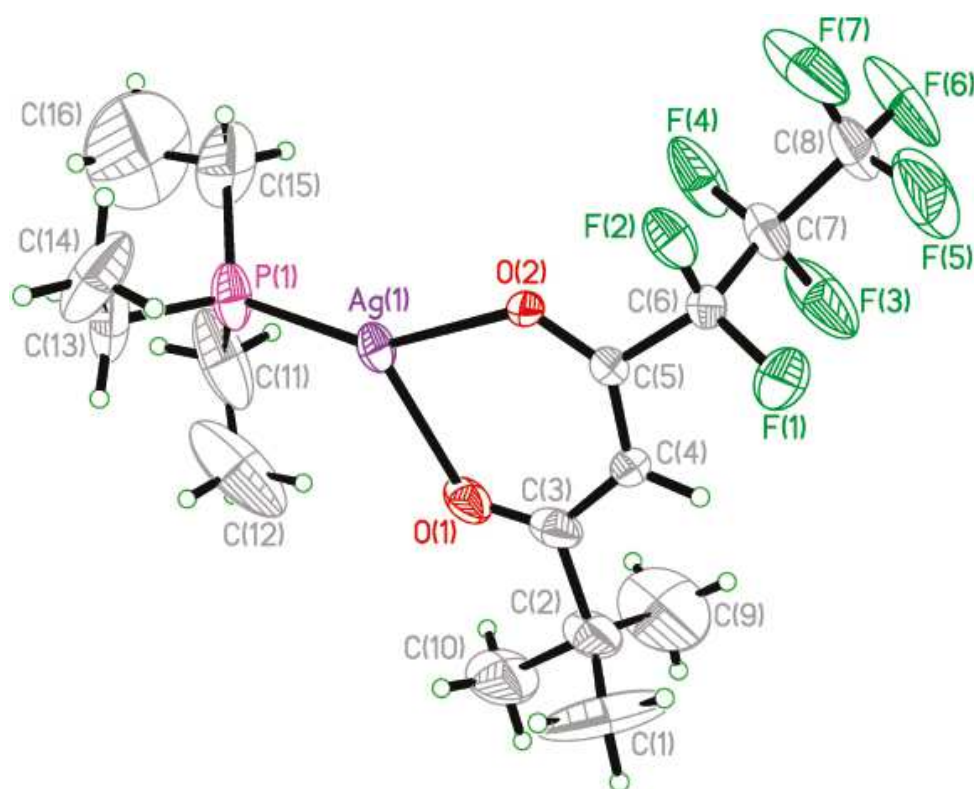


Figure 5.11:  $\text{Ag}(\text{fod})(\text{PEt}_3)$  (fod = 2,2-dimethyl- 6,6,7,7,8,8,8-heptafluorooctane-3,5-dionato) [13], Ag  $\beta$ -diketonates (see Figure 2.4b in section 2.6)  
Note: Vapor pressure equation was not found in literature

## 5.2.2 Ag films deposited by PALD with the first ICP source (30 W maximum power)

### 120 °C substrate temperature

Silver films were successfully deposited using the initial ICP plasma source with a maximum plasma power of 30 W.

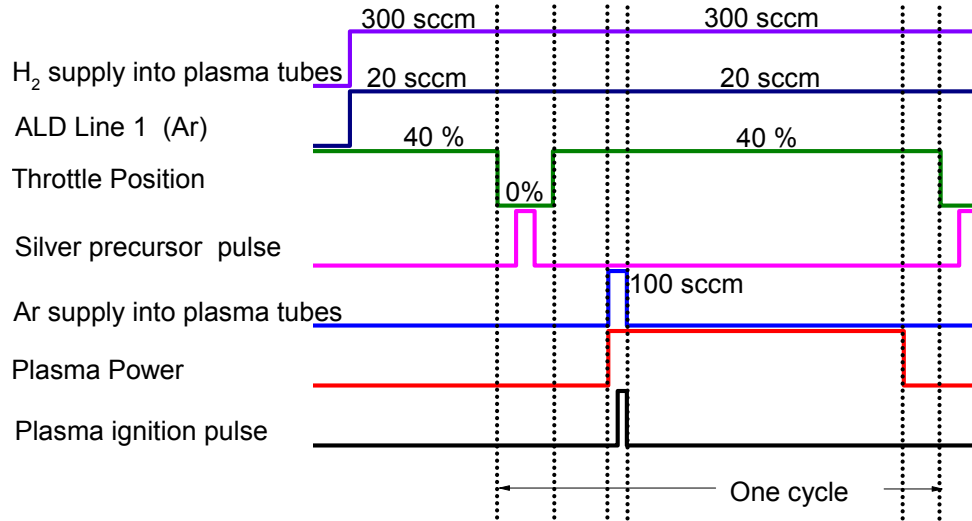
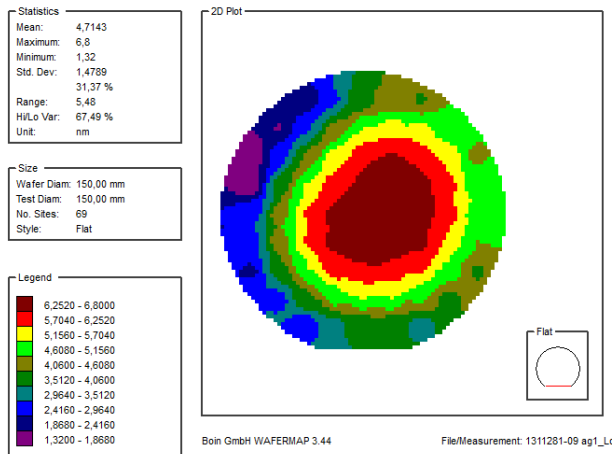


Figure 5.12: Initial process sequence

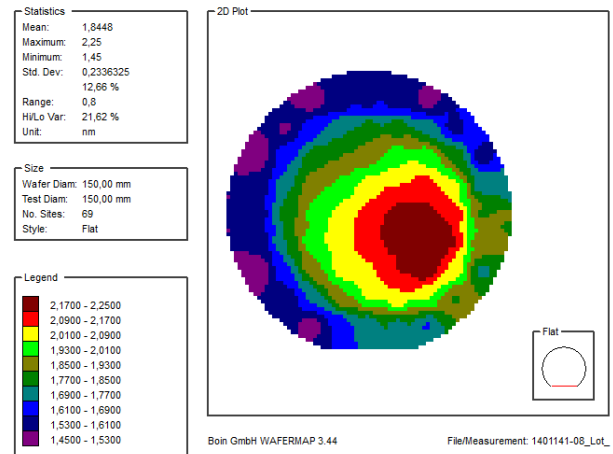
The process sequence is shown in Figure 5.12. Hydrogen gas is supplied continuously through the plasma head at 300 sccm gas flow. The hydrogen radicals are activated by using a short ignition pulse to create a seed plasma after which the plasma is sustained with the plasma power during the plasma exposure time. 100 sccm argon is supplied into the plasma head for hydrogen plasma ignition and discharge. 20 sccm argon is used as carrier gas for the Ag precursor. The silver precursor has a very low vapor pressure and, therefore, it can only be efficiently dosed using the bubbler configuration (illustrated in subsection 2.10.3, Figure 2.18). The throttle valve is closed during silver precursor dosage for optimal precursor usage. Deposition was done on Si / SiO<sub>2</sub> substrate at 120 °C substrate temperature.

A brendel oscillator model for silver was created by fitting all the parameters to obtain the least mean squared error between the measured ellipsometric spectra and the modelled spectra. This was used to take the wafer map for the deposited Ag film. Usually only the layer thickness is fitted during the wafer map measurements. Figure 5.13 shows the wafer map of Ag layer deposited on 150 mm Si wafer with native oxide at 120 °C temperature. A mean thickness of 4.7 nm (Figure 5.13a) was obtained for 100 cycles of Ag deposition with the model used. Silicon wafer was also exposed to only hydrogen plasma by running the same process sequence but keeping the metal precursor bottle closed. Some etching of the surface and surface roughness was measured with the ellipsometer using SiO<sub>2</sub> model

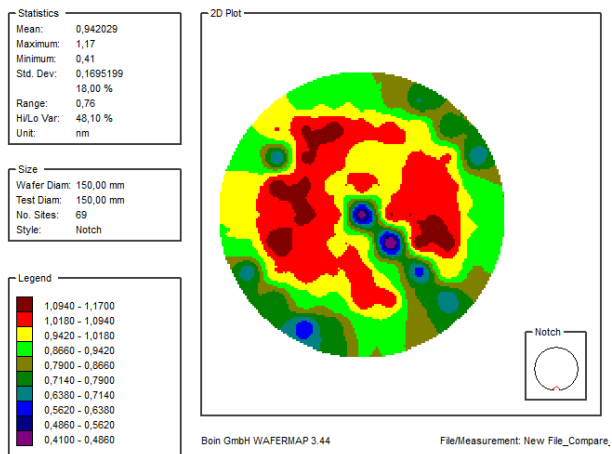




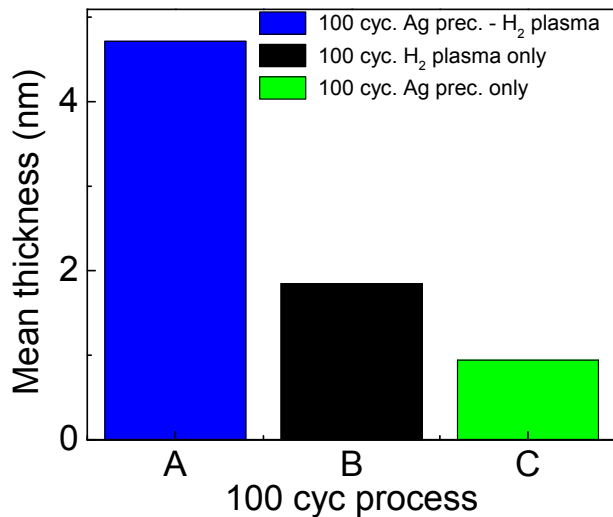
(a) 100 cycles Ag PALD at 120 °C (Ag model used for measurement)



(b) 100 cycles H<sub>2</sub> plasma only at 120 °C (SiO<sub>2</sub> model used for measurement)



(c) 100 cycles Ag precursor only with continuous H<sub>2</sub> gas flow at 120 °C (SiO<sub>2</sub> model used for measurement)



(d) Mean thickness on 150 mm wafer

Figure 5.13: Ellipsometric wafer map of 100 cycles Ag PALD compared with 100 cycles H<sub>2</sub> plasma only as well as 100 cycles Ag precursor only at 120 °C deposition temperature on 150 mm wafer.

Process parameter for Ag deposition: Ag precursor (pulse / purge) = 7.5 s / 6 s, H radicals (pulse / purge) = 5 s / 2 s, 70 °C chamber walls temperature, 120 °C substrate temperature, 30 W plasma power, 100 cycles

(Figure 5.13b). Hydrogen plasma is capable of etching the silicon surface if the metal precursor supply is insufficient on the surface. In addition, the silver precursor is not highly reactive with hydrogen gas. The maximum growth was about 1 nm for 100 cycles after dosing only Ag precursor without plasma activation, as shown in the wafer map of Figure 5.13c.

Chemical analysis by XPS (Figure 5.14) of the deposited Ag film at 120 °C indicates the presence of silver with carbon and fluorine contamination at the surface which reduced after

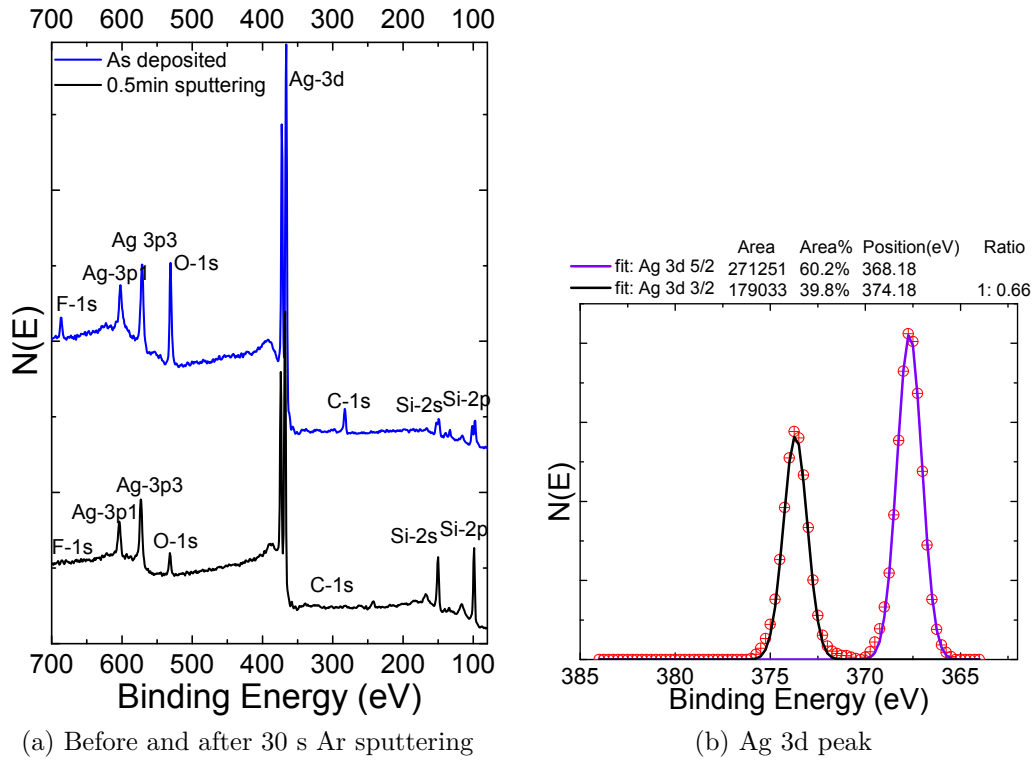


Figure 5.14: XPS before and after 30 s argon sputtering of the deposited Ag film at 120 °C deposition temperature with 30 W plasma power

argon sputtering. The shape and the measured binding energy of silver is as expected [182]. For pure Ag, the  $3d$  spectra region is asymmetrically splitted into two spin orbit components which are  $3d_{3/2}$  (374.2 eV) and  $3d_{5/2}$  (368.2 eV). There is also some oxygen contamination which could be partly from the native oxide of silicon.

### 250 °C substrate temperature

The growth per cycle decreased sufficiently after some further experiments due to degradation of the plasma source and deposition inside the plasma tubes (see Figure 5.10 in section 5.1.4). As a result, the deposition temperature was increased to 250 °C to increase the Ag growth. However, the silver precursor might not be that stable at such a high temperature and the Ag PALD film might have some parasitic CVD decomposition at this temperature. Deposition was made on thermal silicon oxide, titanium oxide and silicon substrates (with native oxide) at 250 °C with a plasma power of 25 W for 1500 cycles. XPS result of Ag film deposited at 250 °C temperature had high carbon contamination (more than 20 %) after 60 s argon sputtering (Figure 5.15) probably due to insufficient hydrogen radical supply as well as contamination from precursor decomposition at higher temperature.

In addition, film morphology by AFM and SEM (Figure 5.16) of the same Ag film (1500 PALD cycles at 250 °C deposition temperature) indicates that the film is made up of small Ag particles which are closely packed with a grain size of approximately 25 nm and

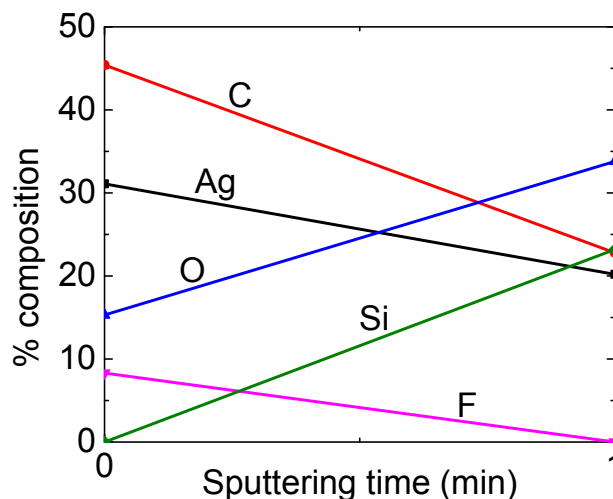
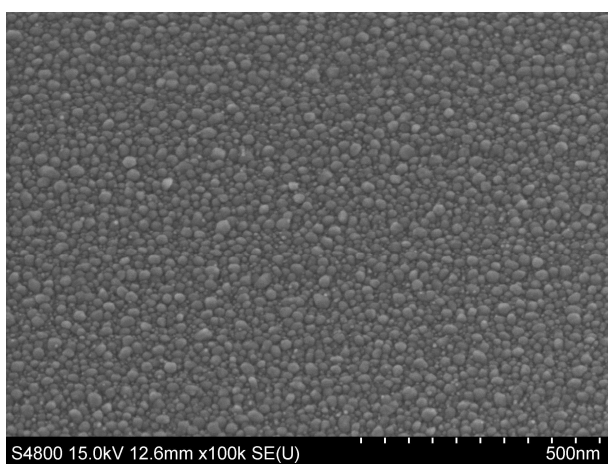
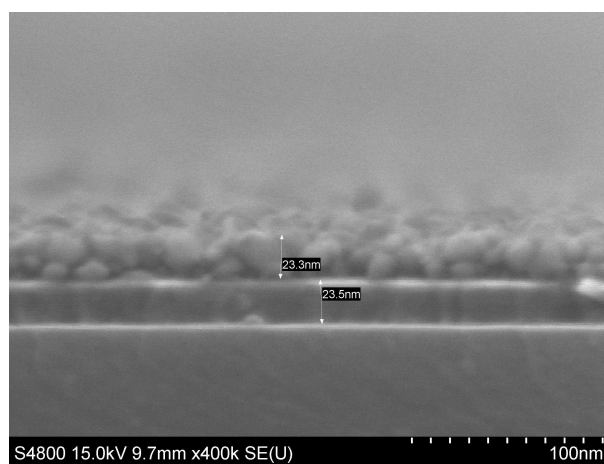


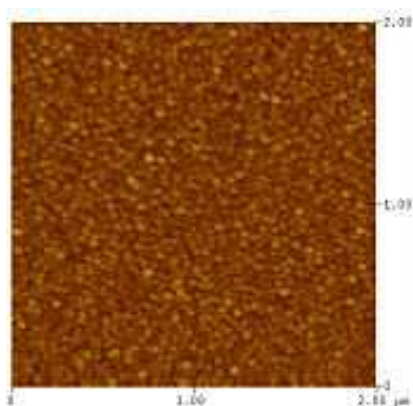
Figure 5.15: XPS result of Ag film deposited at 250 °C temperature



(a) SEM morphology of Ag PALD for 1500 cycles at 250 °C



(b) SEM crosssection of Ag PALD for 1500 cycles at 250 °C on SiO<sub>2</sub> substrate



(c) AFM morphology of Ag PALD for 1500 cycles at 250 °C

#### Image Statistics

|               |              |
|---------------|--------------|
| Img. Z range  | 26.181 nm    |
| Img. Mean     | -0.000000 nm |
| Img. Raw mean | 544.70 nm    |
| Img. Rms (Rq) | 3.248 nm     |
| Img. Ra       | 2.575 nm     |
| Img. Rmax     | 26.181 nm    |

Figure 5.16: Morphology of Ag film for 1500 cycles deposited at 250 °C temperature

mean square roughness of 3.25 nm. The Ag film thickness as determined from SEM cross section (Figure 5.16b) was 25.8nm for 1500 PALD cycles which corresponds to a maximum

growth per cycle of 0.16 Å at 250 °C substrate temperature on SiO<sub>2</sub> / Si substrate. This is lower than the growth per cycle obtained in literature with the same precursor which was approximately maximum 0.4 Å at 120 °C substrate temperature [13]. The low growth per cycle obtained here can be attributed to insufficient hydrogen radical supply due to degradation in the plasma source and low plasma power (25 W) used in the experiment compared to 100 W plasma power used in [13]. Sheet resistance of the deposited film in Figure 5.16 as measured with the four point probe was remarkably high as a result of non continuous Ag layer with smaller grains as well as some contamination in the film. The measured sheet resistance of this film was about 200 kΩ . sq<sup>r</sup><sup>-1</sup>.

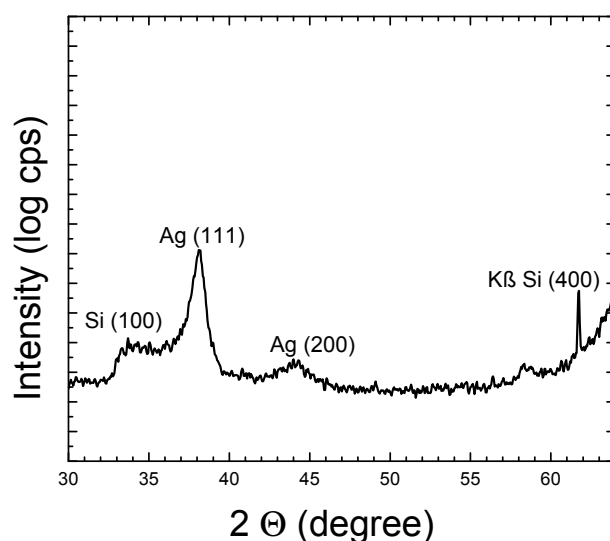


Figure 5.17: XRD result of Ag film for 1500 cycles deposited at 250 °C temperature

Analysis of this film by XRD (Figure 5.17) revealed cubic silver with reflection 38.12 ° for Ag (111), 44.28 ° for Ag (200) and 64.43 ° for Ag (220).

### 5.2.3 Ag PALD film investigation with spectroscopic ellipsometry

Spectroscopic ellipsometry spectra of plasma-assisted atomic layer deposited Ag film shown in Figure 5.18 indicate a resonance absorption around ultra violet region of the spectra.

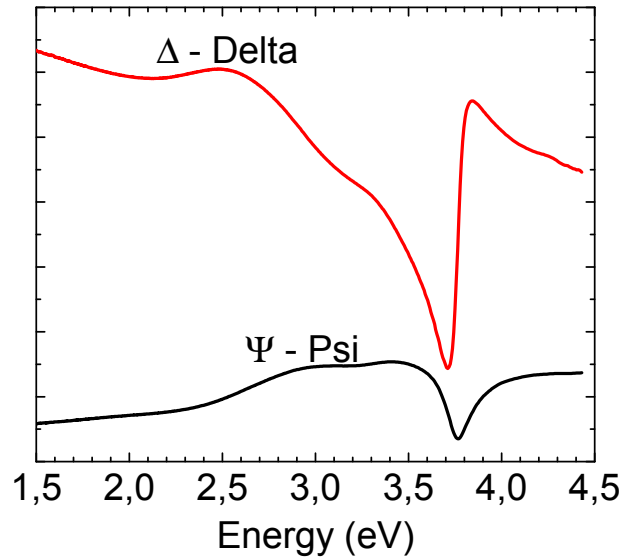


Figure 5.18: Ellipsometric spectra of Ag film showing resonance absorption

Silver is a plasmonic material, which means the surface electrons oscillate collectively in response to the electric field from the optical excitation. Moreover, at certain frequencies, the so called plasma frequency, the surface electron cannot oscillate as fast as the optical excitation. And as a result light with frequency below the plasma frequency is reflected, while above is transmitted. The ellipsometric spectra were taken between 280 nm to 850 nm (1.46 eV to 4.43 eV), below the plasma frequency of silver (9.6 eV, 129 nm [183]). This is why almost the light in the ellipsometer wavelength range were reflected as indicated from the  $\Psi$  spectra. In addition, the resonance absorption peak in the spectra was due to interband transition of bound electrons in silver from optical absorption. The lowest energy interband transition for silver occurs at 3.8 eV from 4d to 5s [184] which corresponds to the resonance wavelength that was observed in the ellipsometric spectra. Changes of the optical properties of Ag PALD layers grown on  $\text{SiO}_2(26\text{nm})/\text{Si}$  substrate were studied with spectroscopic ellipsometry ex situ for different PALD cycles. Ellipsometric measurements (Figure 5.19) show predominant increase in the angle  $\Psi$ , in the energy range from 2.3 to 3 eV as the number of deposition cycles is increased, while  $\Delta$  decreases as the deposition cycle is increased.  $\Psi$  is an indication of reflectivity of the film, while  $\Delta$  is the phase difference between the two orthogonal S and P reflected polarizations. The Ag film therefore becomes more reflective for thicker layers. In Ag PVD film, the ellipsometric angle  $\Psi$  is constant at  $45^\circ$  between 1.5 and 3.5 eV for a continuous and thick silver layer [184]. For comparison, 40 - 50 nm silver layers were deposited with electron beam evaporation, and the  $\Psi$  value for this PVD layer is almost constant at  $44^\circ$  for photon energy below 3.7 eV. On the other

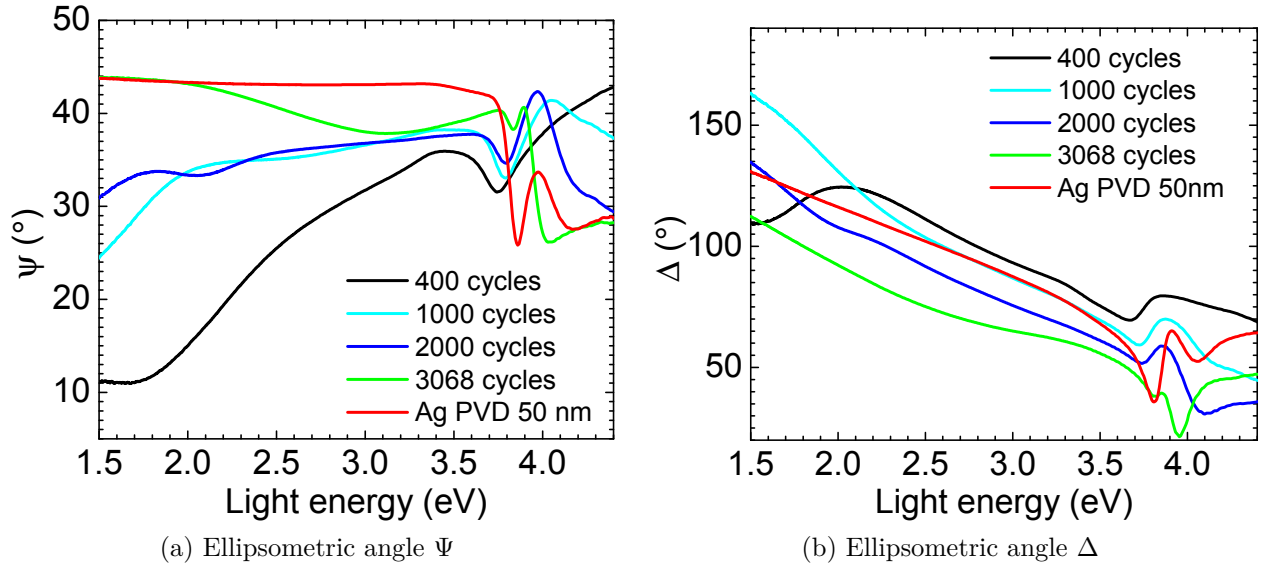
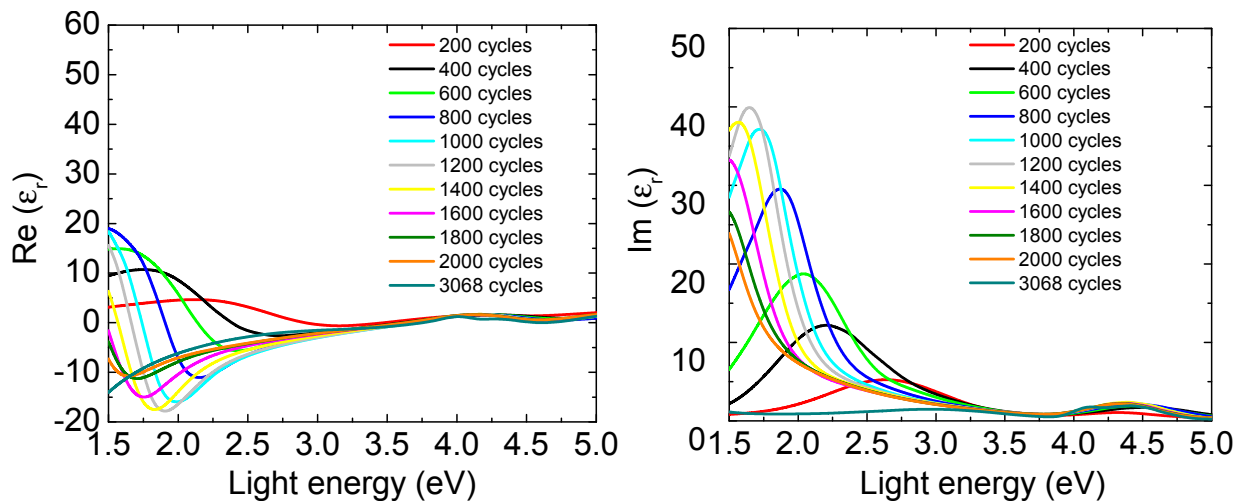


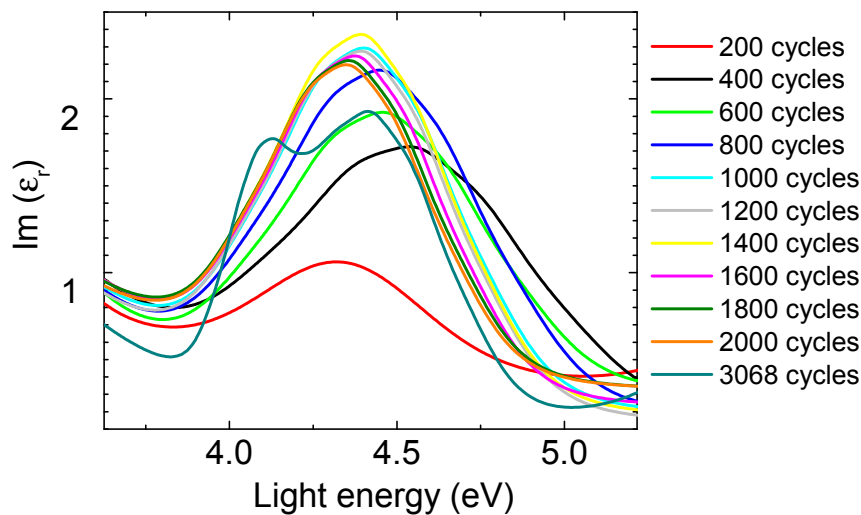
Figure 5.19: Ellipsometric spectra of Ag films on  $\text{SiO}_2/\text{Si}$  substrate taken after different PALD cycles

hand, for 3068 cycles (about 97 nm) Ag PALD grown film, the  $\Psi$  value is not constant below 3.7 eV, rather it was higher below 2 eV and lower between 2 eV and 3.75 eV. This could be an indication that the Ag PALD may not give perfectly continuous layers even with larger number of PALD cycles.

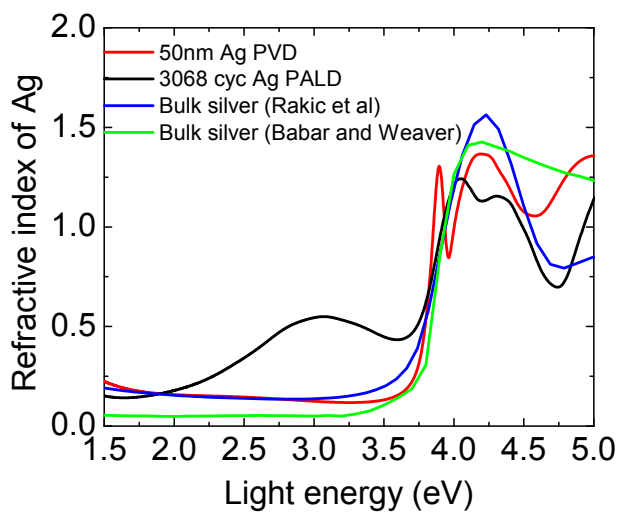
Relative permittivity and refractive index depending on incident light energy (Figure 5.20) were obtained from the ellipsometric spectrum by fitting the optical parameters and film thickness for the transparent layers using Brendel Oscillator model in the ellipsometer data base. The film thickness for the thick layers (3068 cycles) were determined from x-ray fluorescence (XRF) and SEM cross section. For transparent Ag layers, all the parameters in the oscillator model were fitted to obtain the lowest mean squared error. While for thick (non-transparent) Ag layers, the film thickness was kept almost at the measured value by SEM and XRF during fitting of other oscillator parameters to obtain the lowest mean squared error. In addition, the maximum mean square error obtained between the measured data and the fit was about 1. That is, the mean of squared deviation between the measured  $\Psi$  and  $\Delta$  and the calculated (fitted)  $\Psi$  and  $\Delta$  taken for all wavelengths is about 1 (See appendix A.2). Refractive index of PALD silver (about 97 nm for 3068 cycles) was compared with that of Ag PVD and bulk values (Figure 5.20d) found in the literature [185, 186]. From Figure 5.20d, refractive index of PVD Ag layers were approximately close to the bulk values in literature. However, Ag PALD had slightly different optical properties in the energy range 1.5 to 3.5 eV. Generally, Ag PVD layers should generally have less film contamination and also closer film morphology than PALD Ag layers which will affect the optical properties to a large extent. Figure 5.20a and 5.20b shows the real part and imaginary part of relative permittivity of Ag PALD layers obtained for varying PALD cycles.



(a) Real part of relative permittivity of PALD Ag (b) Imaginary part of relative permittivity of PALD Ag



(c)  $\text{Im}(\epsilon_r)$  of PALD Ag showing interband transition



(d) Refractive index of PALD Ag compared with PVD Ag and values found in literature

Figure 5.20: Light energy dependent optical properties of Ag films on  $\text{SiO}_2/\text{Si}$  substrate

The imaginary part and real part of relative permittivity obtained is similar to one found in literature [184, 187, 188]. Marsillac et al. [188] described in detail three types of plasmon resonances found in silver layers in the broadband range from 0.75 eV to 6.5 eV, which are intraband transitions (far infrared region), particle plasmon polariton (mid energy region) and interband transitions (ultraviolet region). Two features can be clearly seen in the dielectric functions obtained from the fit from 1.5 eV to 5 eV, which are the particle plasmon polariton (1.5 eV to 3 eV) and interband transition (just above 3.8 eV). From the imaginary part of the dielectric function in Figure 5.20b, one can see that the amplitude of the particle plasmon polariton (PPP) increases and also red shifted as the number of PALD cycles increases from 200 cycles until 1200 cycles, while just above 1200 cycles the amplitude of PPP decreases, a trend which was also observed in [188]. It can be concluded that the silver layers were initially unconnected islands as also observed in the AFM images, until after 1200 cycles (percolation threshold), the growth tends to move towards bulk regime (island are getting connected). In addition, the amplitude of interband transition mostly increases as the silver grows into bulk regime (Figure 5.20c). The infrared response of the real part of the dielectric function (Figure 5.20a) also falls to below zero when the film begins to conduct [187], which starts above 1500 PALD cycles.

#### 5.2.4 Ag films deposited by PALD with the improved ICP source (50W maximum power)

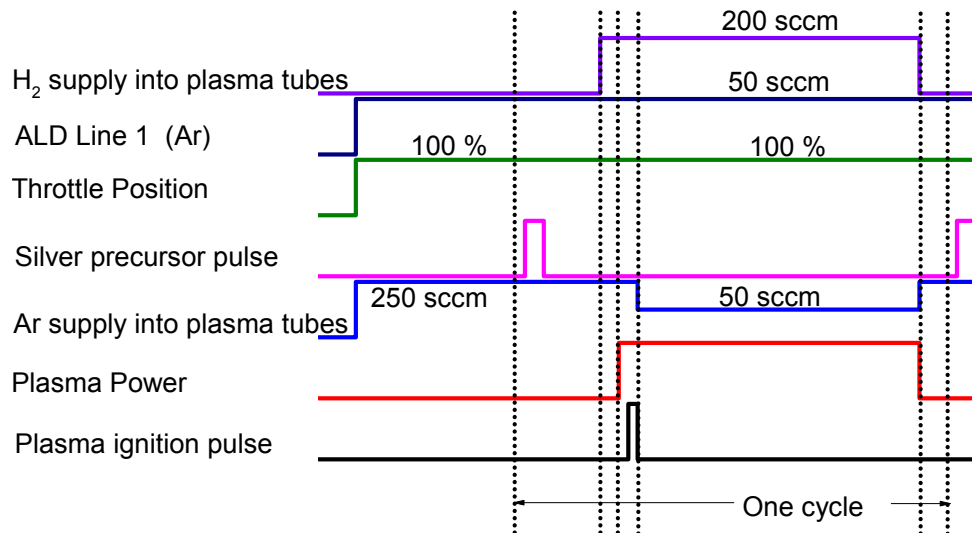


Figure 5.21: Optimized process sequence for Ag film plasma-assisted atomic layer deposition

In the improved ICP source, the maximum output power of the plasma source was increased to 50 W and a stub tuner was used to match the plasma impedance with the microwave input supply thus reducing the reflected power. It was earlier observed that there was always deposition in the plasma tubes due to back flow of precursor while



hydrogen was used as blocking gas (in earlier process sequence of Figure 5.12). As a result, the process sequence was modified such that there is higher argon flow (250 sccm) during the silver pulse, in order to prevent back diffusion of silver precursor into the plasma tubes, while hydrogen gas will be switched on only during plasma pulse. 50 sccm argon should in principle block precursor back flow into the plasma tubes based on the plasma design specifications. In addition, possible CVD reaction of silver precursor and hydrogen gas can be avoided when hydrogen gas is off during Ag precursor supply. Mixture of 50 sccm argon and 200 sccm hydrogen seems to give a better plasma discharge because the reflected power was much lower. The optimized process sequence is illustrated in Figure 5.21.

### Saturation investigation

The film thickness for varying pulse time (Ag precursor and H radicals) should be measured in order to investigate the self limiting condition of the process. However ellipsometric fit can sometimes be ambiguous especially for thicker Ag films and it might be faster to just compare the spectra. It has been shown earlier from the ellipsometric measurements in section 5.2.3 that the ellipsometric angle  $\Delta$  decreases as the Ag film thickness increases. For saturation investigation, depositions were made with varying Ag pulse time and H<sub>2</sub> plasma time on silicon substrates with native oxide of about 2 nm and the  $\Delta$  spectra were compared.

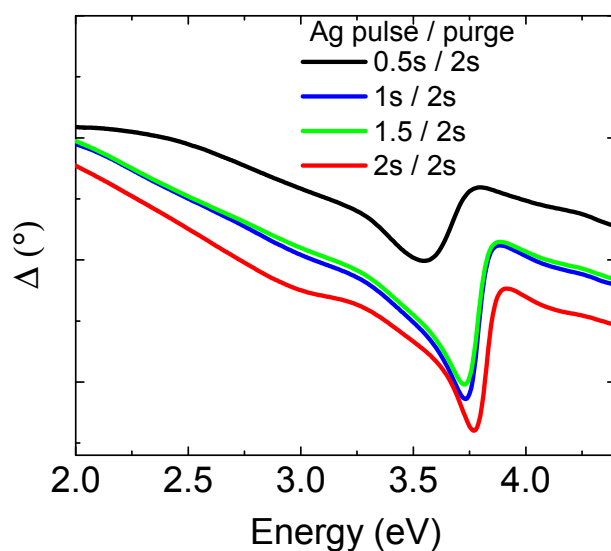


Figure 5.22: Comparison of  $\Delta$  spectra for varying Ag precursor pulse time. 500 PALD cycles, 10 s H<sub>2</sub> plasma, 120 °C deposition temperature and 70 °C chamber wall temperature

At first, the chamber walls was 70 °C and the pulse time was increased from 0.5 s to 2 s, with purge time of 2 s. Film thickness increases ( $\Delta$  goes down) as Ag precursor pulse time is increased (Figure 5.22).  $\Delta$  spectra for 1 s and 1.5 s Ag precursor pulse is identical but film thickness still increased ( $\Delta$  goes down) at 2 s Ag precursor pulse as a result of

increased parasitic CVD component due to excess precursor and insufficient purge time.

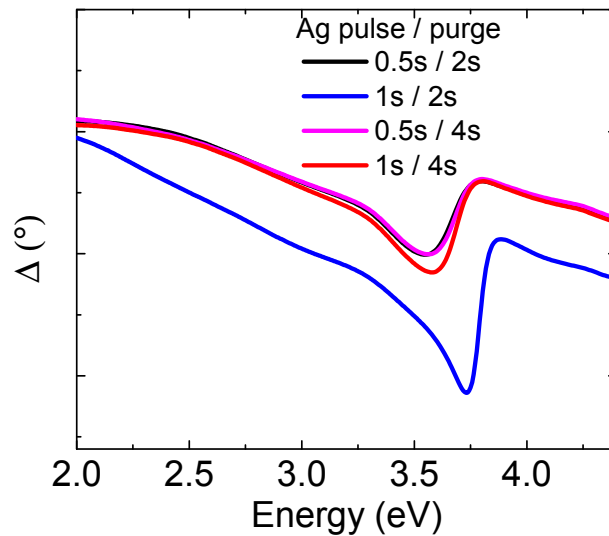


Figure 5.23: Comparison of  $\Delta$  spectra for varying Ag precursor purge times. 500 PALD cycles, 10 s  $H_2$  plasma, 120 °C deposition temperature and 70 °C chamber wall temperature

By increasing the Ag precursor purge time to 4 s (Figure 5.23),  $\Delta$  spectra for 0.5 s Ag pulse remained almost unchanged as with 2 s purge, while the Ag film thickness obtained for 1 s Ag pulse time even decreased further ( $\Delta$  increases) as the purge time is increased. Which means, 2 s purge time is only sufficient for 0.5 s Ag precursor pulse but already insufficient for 1 s Ag precursor pulse. Therefore with cold chamber walls (70 °C), there may be precursor condensation around the walls which will require excessive long purge to obtain a pure ALD process. As a result the chamber wall temperature was increased to 120 °C to achieve efficient purge and hence obtain a pure ALD process.

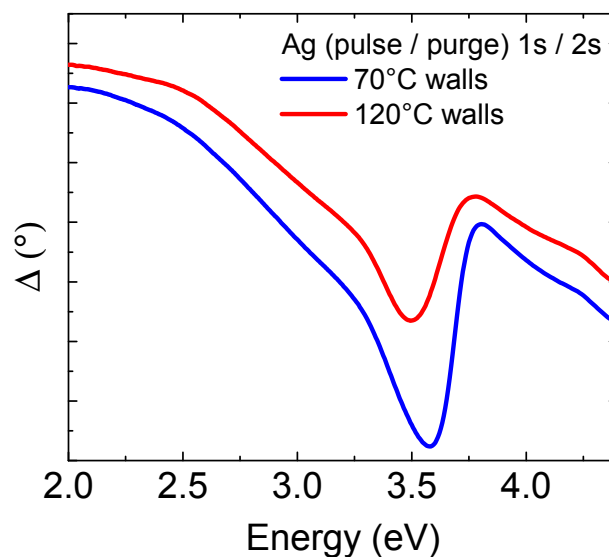


Figure 5.24: Comparison of  $\Delta$  spectra for varying chamber wall temperatures. 500 PALD cycles, 10 s  $H_2$  plasma, 120 °C deposition temperature

By repeating two processes of same parameters (Figure 5.24) at 70 °C and 120 °C wall temperatures, film thickness was lower with 120 °C wall temperature compared to 70 °C wall temperature, which implies that the purge will be efficient at higher temperature.

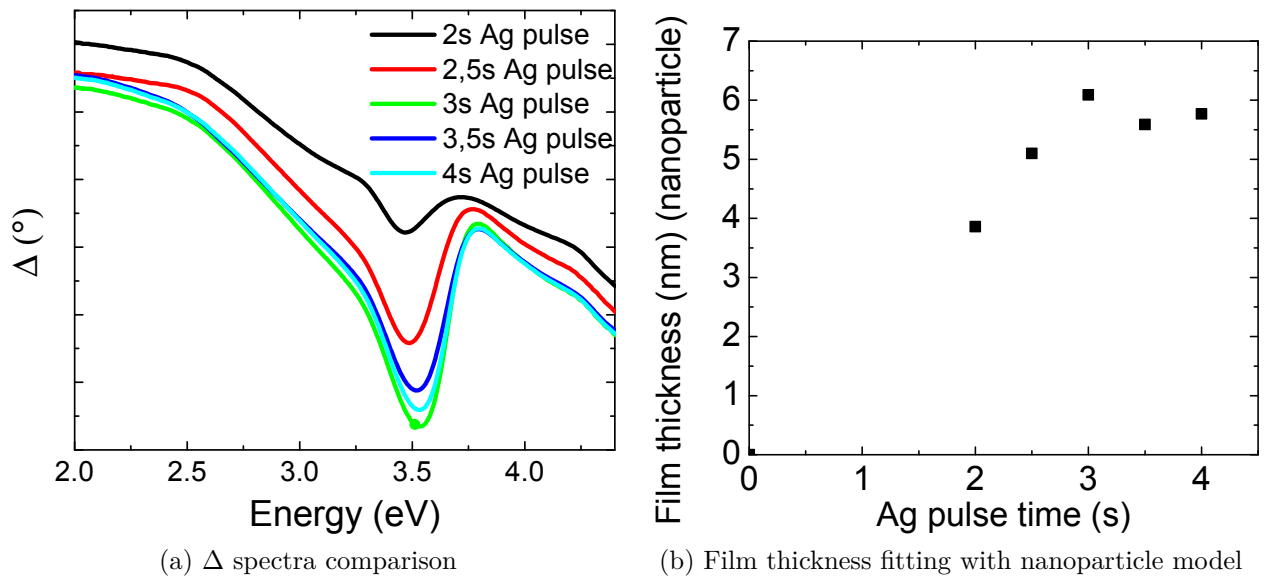


Figure 5.25: Investigation of Ag precursor saturation for PALD Ag growth.  
 Ag precursor (pulse / purge): varied / 10 s, H<sub>2</sub> plasma (pulse / purge): 10 s / 10 s, 200 PALD cycles, 120 °C substrate temperature, 120 °C chamber walls

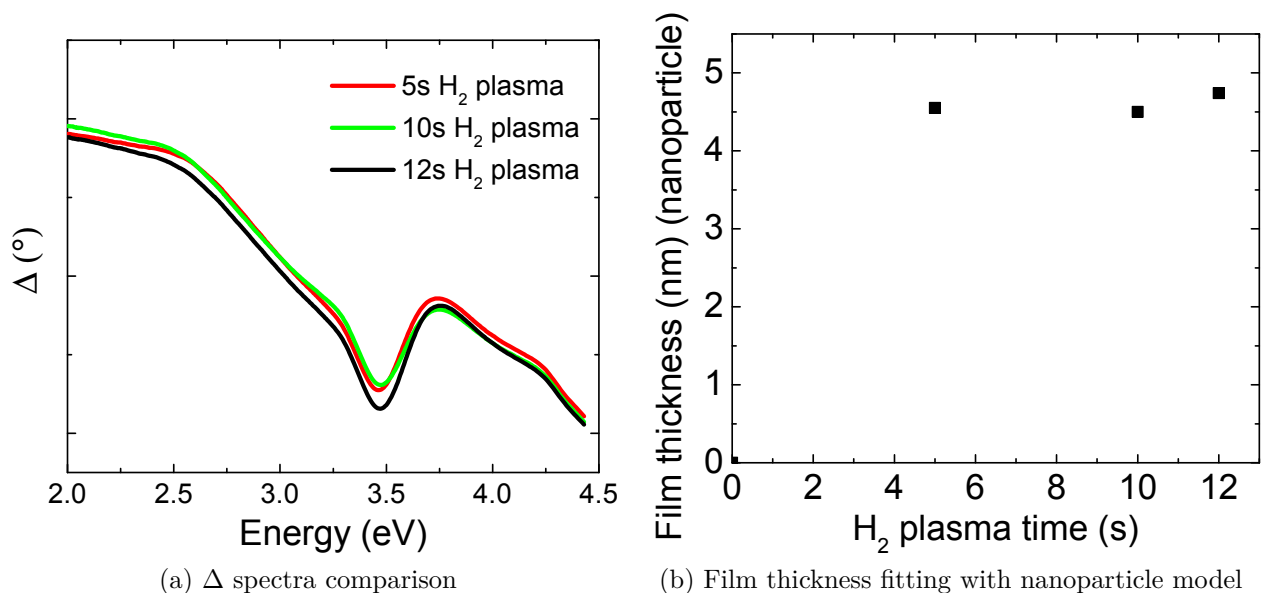


Figure 5.26: Investigation of H<sub>2</sub> plasma saturation for PALD Ag growth.  
 Ag precursor (pulse / purge): 3 s / 10 s, H<sub>2</sub> plasma (pulse / purge): varied / 10 s, 200 PALD cycles, 120 °C substrate temperature, 120 °C chamber walls

The purge time was increased to 10 s at 120 °C chamber wall temperature to completely purge the Ag precursor and the Ag pulse time was varied from 2 s to 4 s. Self saturating

process was observed at 3 s to 3.5 s Ag precursor pulse time (Figure 5.25) and 5s plasma time (Figure 5.26) with this condition for 200 PALD cycles. Film thicknesses for this transparent layers were determined by fitting the spectra using the nanoparticle model which gave comparable thickness.

Optimal process parameters are given below:

Silver precursor (Pulse / Purge) = 2 s / 2 s in bubbler mode

Hydrogen plasma (Pulse / Purge) = 10 s / 1 s

Argon carrier gas = 50 sccm

Bubbler temperature = 110 °C

Bubbler inlet line = 110 °C

Bubbler outlet line = 120 °C

Chamber walls = 120 °C

Substrate temperatures = 120 °C

Plasma gas:

Hydrogen (plasma off / plasma on) = 0 / 200 sccm

Argon (plasma off / plasma on) = 250 / 50 sccm

Plasma power = 50 W

Hydrogen plasma pretreatment = 3 min

PALD cycle time = 15 s

## Film characterization

Ag film deposition were carried out on small sample sizes (less than 10 mm by 10 mm) of different metallic substrates such as trenches of silicon covered with Ti/TiN layers as well as planar silicon surface covered with thin layers of SiO<sub>2</sub>, TiN, Co (cobalt), Ni (nickel) and W (tungsten) layers. The SiO<sub>2</sub> thin layer was prepared by thermal oxidation of Si in a furnace while Ti, TiN, Co and Ni thin films were deposited by physical vapor deposition (sputter deposition). W films were deposited by chemical vapor deposition followed by chemical mechanical polishing to obtain a starting rms roughness of 2 nm. The samples were always placed around the center of the susceptor just beneath the outlet of the plasma discharge tubes in all experiments for efficient plasma radical supply. PALD depositions were carried out at 70 °C, 120 °C and 200 °C substrate temperatures. A maximum growth per cycle of approximately 0.03 nm was obtained from Ag film thickness of more than 500 PALD cycles at all the three deposition temperatures. Samples of Ag layers on TiN surface were analyzed by XPS in order to eliminate the effect of oxygen contamination from an oxide surface. Pure Ag was obtained from the XPS measurement with carbon and oxygen contamination close to the detection limit (Figure 5.27) after 30 s argon sputtering for deposition made at 120 °C and 200 °C temperature, which indicate complete ligand

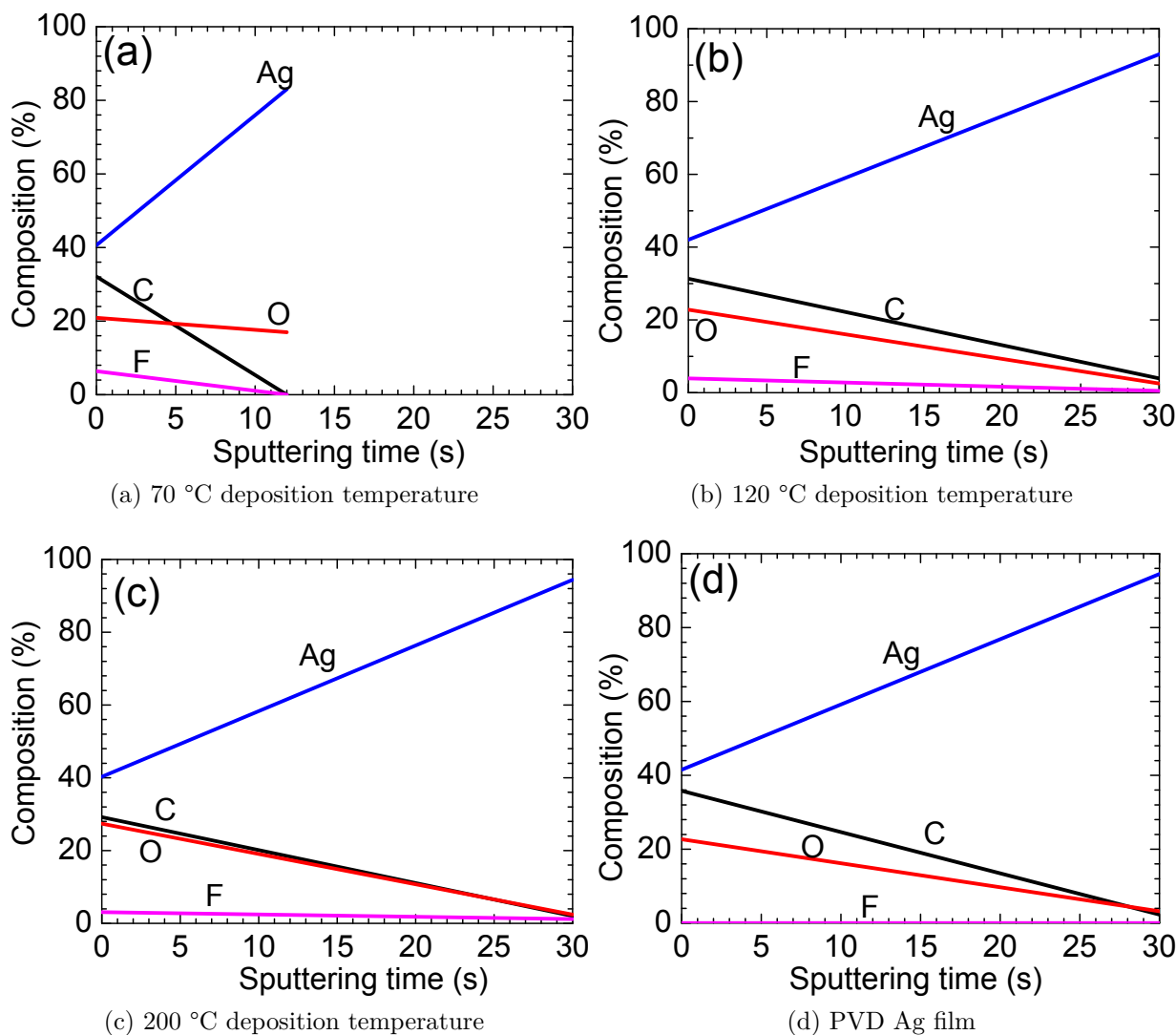


Figure 5.27: Chemical composition by XPS of PALD Ag films (a, b, c) at different deposition temperatures compared with PVD Ag film (d): (a) 70 °C deposition temperature (b) 120 °C deposition temperature (c) 200 °C deposition temperature (d) PVD Ag film

removal by the hydrogen plasma.

A large oxygen contamination was detected in the film for deposition carried out at 70 °C, which means there could be incomplete ligand removal or possible precursor condensation at this low temperature. For all the Ag PALD samples, oxygen and carbon were detected in the as deposited state due to adsorption of organic molecules on the surface. XPS analysis of PVD Ag (Figure 5.27d) layers grown by electron beam evaporation for comparison also had carbon and oxygen contamination on the surface, which reduced to detection limit after argon sputtering. XRD measurements of PALD silver layers (Figure 5.28) grown at 120 °C and 200 °C deposition temperature as well as of PVD silver layers both reveal polycrystalline cubic silver. Silver PALD grown at 70 °C deposition temperature also shows appearance of Ag[111] peak in the spectra for a much lower film thickness.

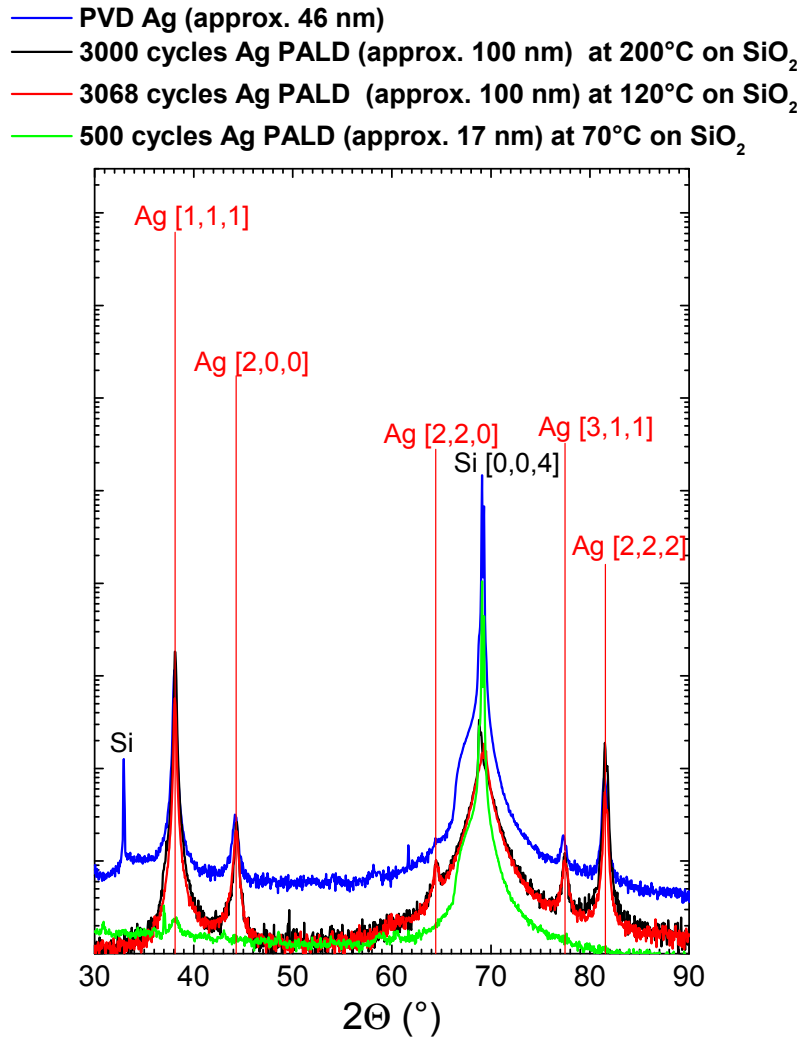


Figure 5.28: Crystallinity of PALD Ag films compared with PVD Ag film

### Deposition on different substrates

Analysis of Ag film morphology by AFM shows that Ag grew on all the substrates and the particle sizes increases with the number of cycles. The Ag particle distribution statistics (Figure 5.29) were determined from the AFM images using an imaging software called SPIP from Image Metrology A/S. The distributions were fitted into lognormal function as supposed in literature [12] using the Origin software. The Ag growth starts from appearance of islands on all the substrates which tends to coalescence as the number cycles is increased. The diameter of silver particles (Figure 5.29) increases with the number of PALD cycles which shows that the Ag film grows in Volmer Weber mode on all the substrates, where the growth starts from appearing of isolated silver islands to percolation and then bulk regime. The particle size distributions on SiO<sub>2</sub> and TiN surface were identical, which means that growth and coalescence of Ag islands could be identical on both surfaces. The average particle sizes and distributions on the metal surfaces (Co, Ni, W) were slightly larger at 1500 cycles, which indicates that wetting and coalescence of Ag

islands might be faster on metal surfaces.

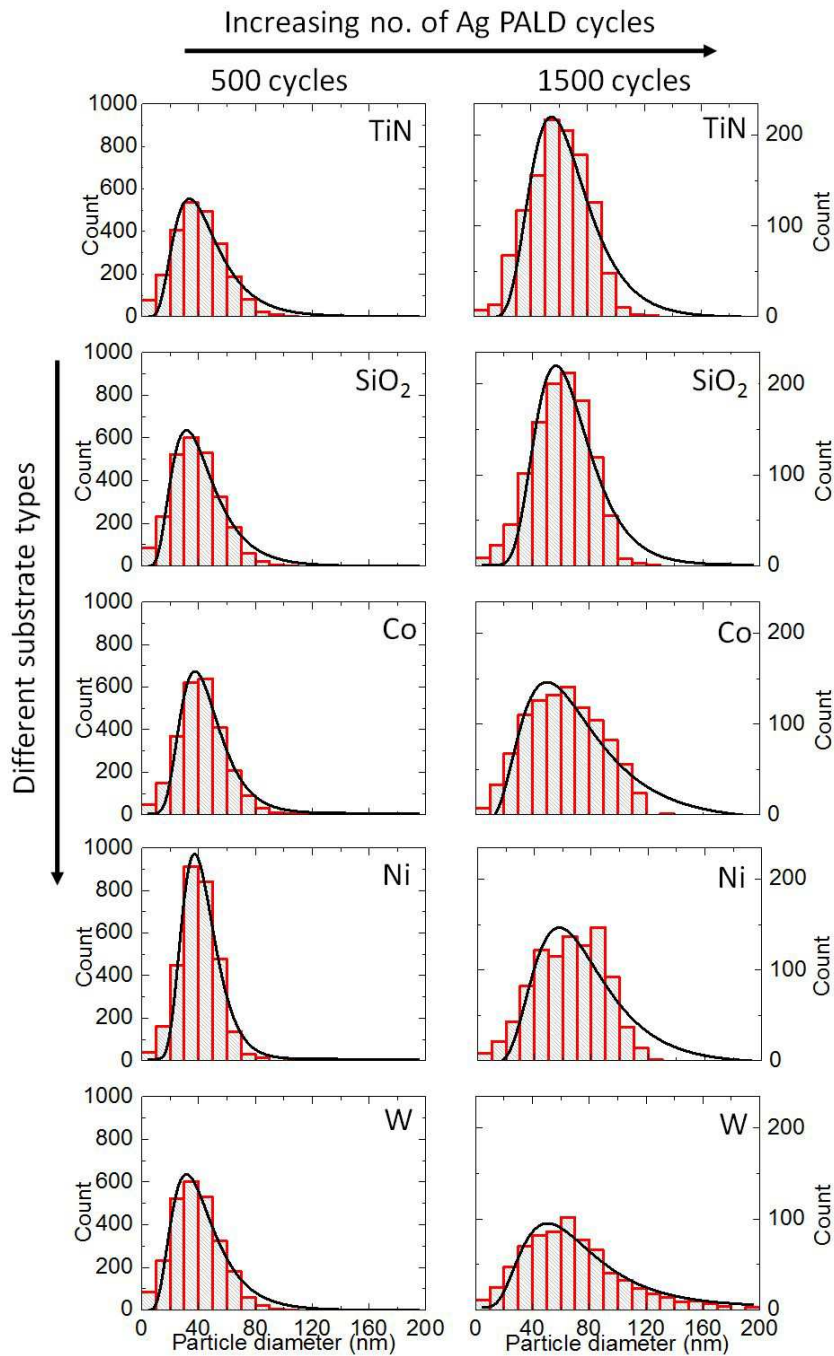


Figure 5.29: Distribution of particle sizes for PALD Ag films grown at 120 °C deposition temperature on different substrates. Black line curves are lognormal fit.

In addition, the rms roughness  $R_q$  (Figure 5.30) increased as the Ag film gets thicker. Silver on cobalt surface had the lowest roughness followed by titanium nitride, silicon oxide and nickel surfaces at 3068 Ag PALD cycles (Figure 5.31). Silver grew on tungsten surface with the highest surface roughness ( $R_q$ ) as revealed by AFM measurements. Wetting of film on a substrate during growth depends on the surface energy of the system. For an oxide substrate, a metal film will wet the substrate only when when at equilibrium [189]:

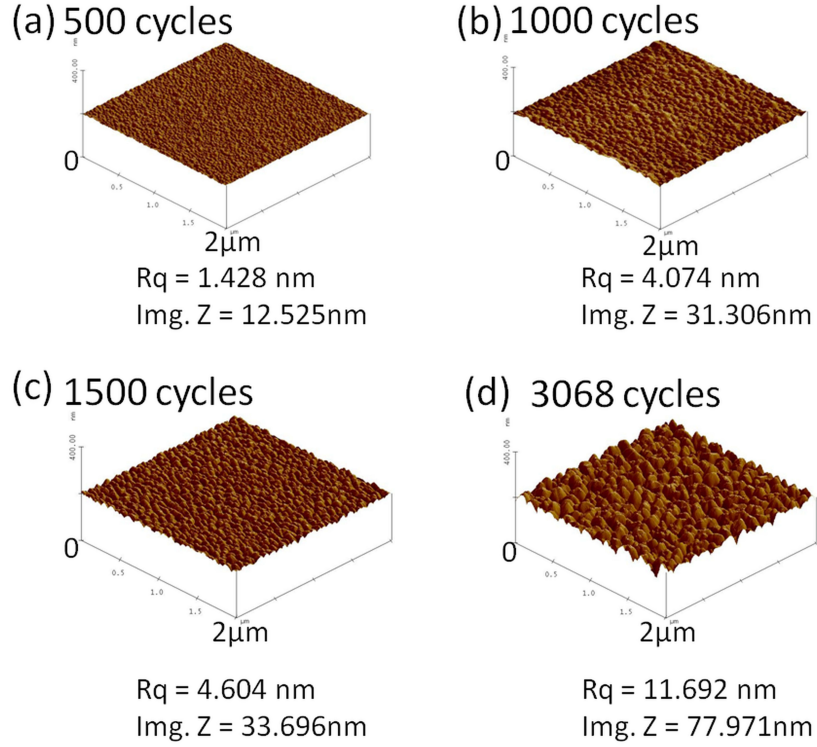


Figure 5.30: Morphology of PALD Ag films grown on TiN surface at 120 °C deposition temperature: (a) 500 PALD cycles, (b) 1000 PALD cycles, (c) 1500 PALD cycles, (d) 3068 PALD cycles

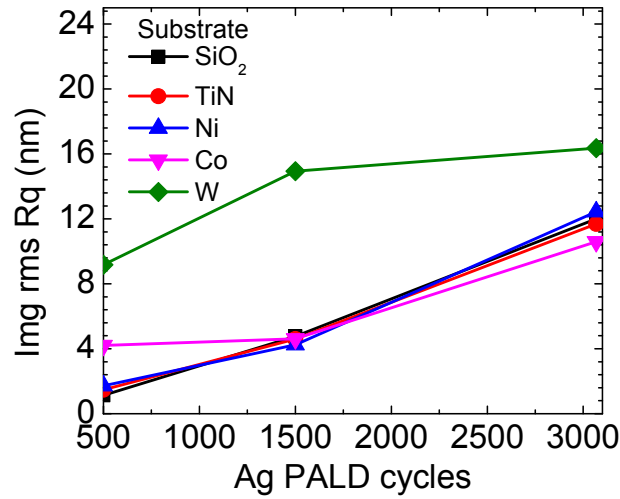


Figure 5.31: Surface roughness of PALD Ag films grown on different substrates at 120 °C deposition temperature for varying PALD cycles

$$\gamma_{oxide-metal} = \gamma_{oxide-v} - \gamma_{metal-v} \quad (5.1)$$

where  $\gamma_{oxide-metal}$  is the surface energy of the interfacial film between the oxide and the metal,  $\gamma_{oxide-v}$  is the pure surface energy of the oxide substrate in vacuum and  $\gamma_{metal-v}$  is the pure surface energy of the metal film in vacuum. Since oxides generally have a lower



vacuum surface energy than metals, wetting of metal film on oxide substrate may only be possible when the metal surface energy is lowered by minimizing its own surface area during growth [190], which explains why the growth of metal on oxide surface is usually from appearance of metal islands before continuous growth. It is obvious from equation 5.1 that a higher surface energy substrate than the deposited metal should in principle promote continuous growth of thin metal film. Baker et al. [191] used tungsten (surface energy of  $3.5 \text{ Jm}^{-2}$ ) as adhesion layer for the growth of ultra smooth platinum layers (surface energy of  $2.5 \text{ Jm}^{-2}$ ). Ag, Co, Ti and Ni have experimental surface energies of  $1.25 \text{ Jm}^{-2}$ ,  $2.55 \text{ Jm}^{-2}$ ,  $2.1 \text{ Jm}^{-2}$  and  $2.45 \text{ Jm}^{-2}$  respectively [192]. Therefore it is expected that W, Co, Ni and Ti substrate should allow smooth growth of Ag films faster than oxide or dielectric substrate. Results of particle sizes analysis correlates with the trend of metallic surface promoting faster island coalescence than TiN and  $\text{SiO}_2$  surface. However SEM images (Figures 5.32, 5.33, 5.34, 5.35 and 5.36) of the Ag films shows that Ag on W was quite rough compared to Ag on Ni, Co, TiN and  $\text{SiO}_2$  surface. Ag had better wetting and grew smoother on Co and Ni surface than on W surface. In addition, the Ag films appear more compact on Co and Ni than on  $\text{SiO}_2$  and TiN surfaces. After several cycles, Ag also grew smoothly on TiN and  $\text{SiO}_2$  surfaces as seen in the SEM images (Figures 5.35 and 5.36). However, SEM images (Figure 5.34) revealed that the silver layers might be flaking off during or after PALD growth on W surface. As a result, the Ag layer on W surface is less compact, rougher and contains voids in the film and near the substrate. One possible reason to explain this anomalous growth of Ag on W is that the surface of tungsten would have formed a native oxide in air with much lower surface energy (approximately  $0.35 \text{ Jm}^{-2}$  to  $1.62 \text{ Jm}^{-2}$  by simulation) [193]. Hydrogen plasma pre-treatment of 1500 W for 10s was necessary in the experiments of Baker et al., where it was suggested that tungsten native oxide may not be completely removed by hydrogen plasma [191]. The use of wet chemical etching before plasma dry etching could help to remove most of the native tungsten oxide which may possibly promote smooth growth of Ag on W, however this will require further investigations.

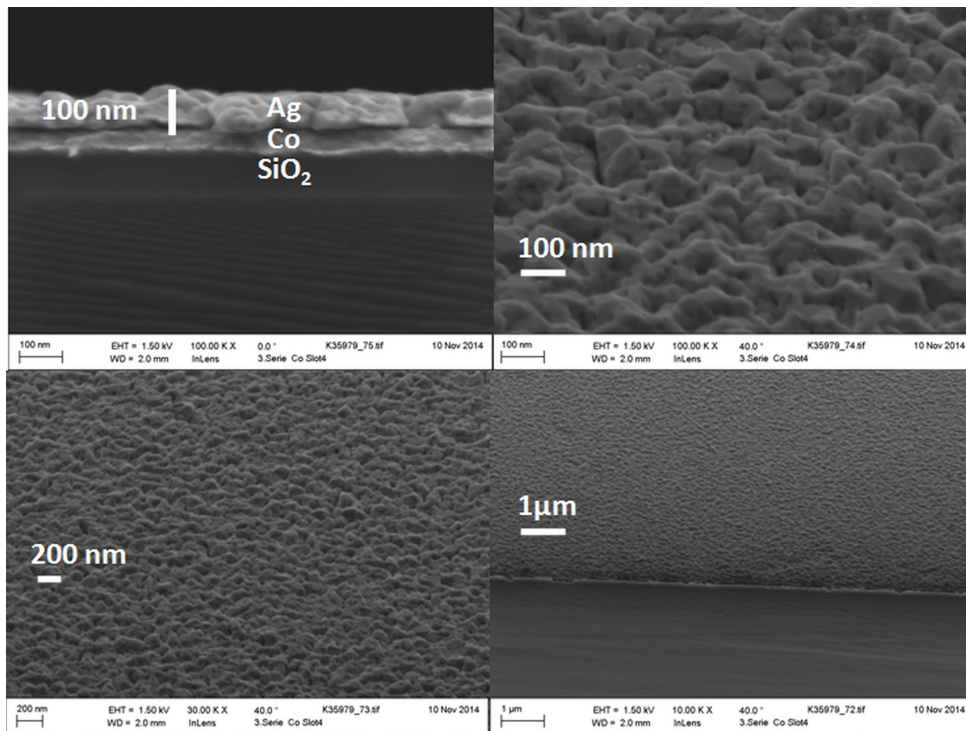


Figure 5.32: SEM morphology of PALD Ag films grown on Co surface at 120 °C deposition temperature for 3068 PALD cycles

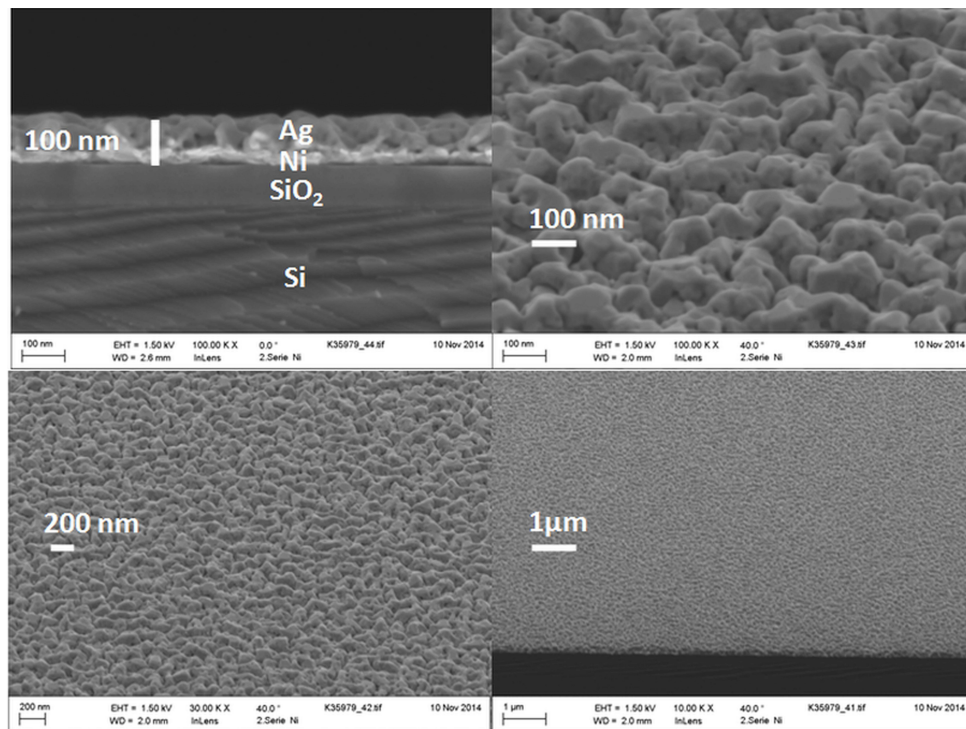


Figure 5.33: SEM morphology of PALD Ag films grown on Ni surface at 120 °C deposition temperature for 3068 PALD cycles

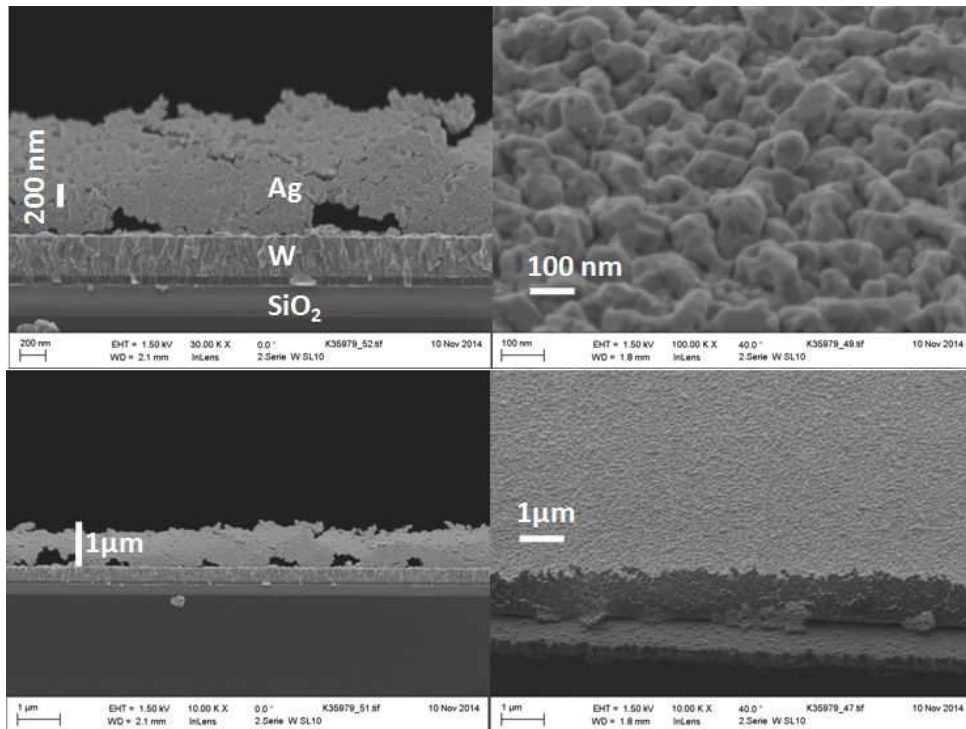


Figure 5.34: SEM morphology of PALD Ag films grown on W surface at 120 °C deposition temperature for 3068 PALD cycles

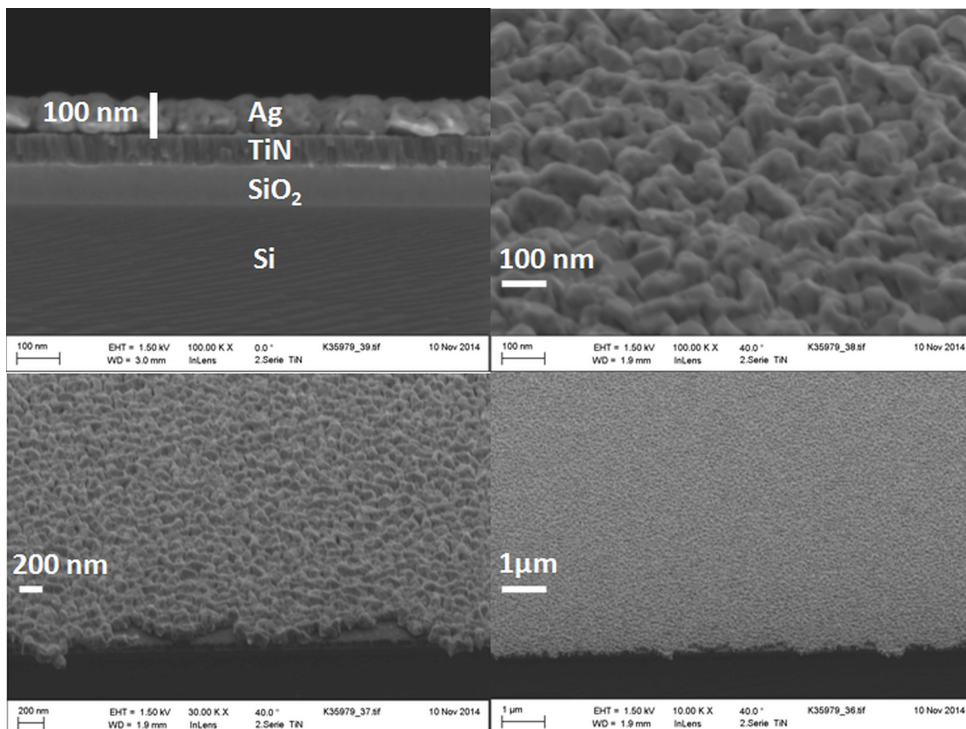


Figure 5.35: SEM morphology of PALD Ag films grown on TiN surface at 120 °C deposition temperature for 3068 PALD cycles

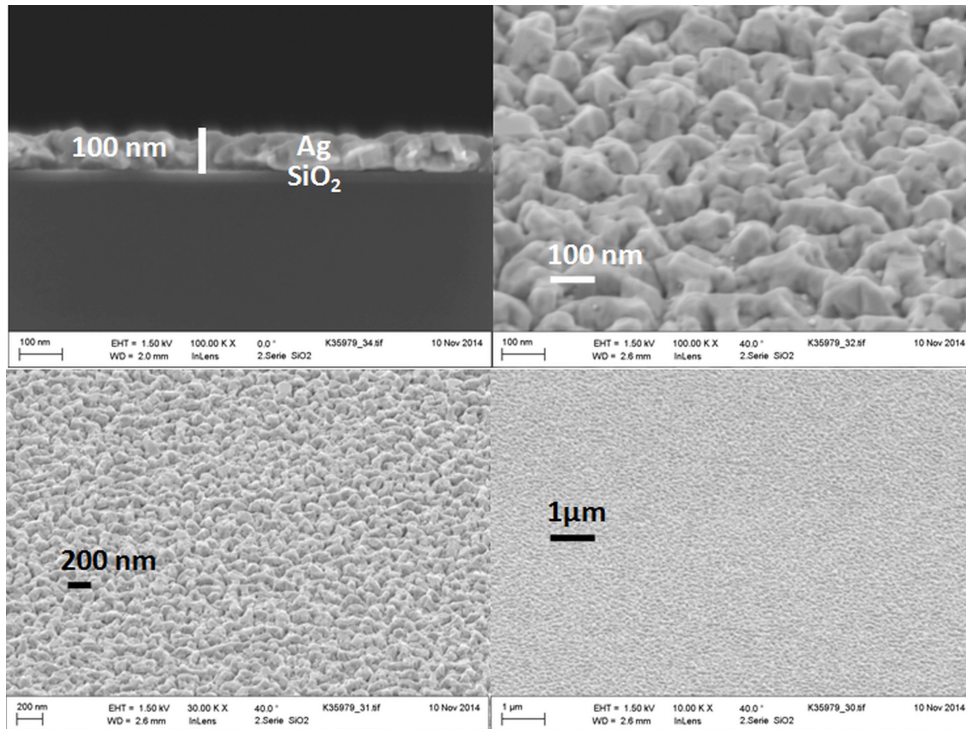


Figure 5.36: SEM morphology of PALD Ag films grown on  $\text{SiO}_2$  surface at  $120^\circ\text{C}$  deposition temperature for 3068 PALD cycles

Furthermore, results of Ag PALD deposition in trenches of silicon with  $2\ \mu\text{m}$  width and  $1\ \mu\text{m}$  depth (aspect ratio of 0.5) covered with thin Ti/TiN layers are shown in Figure 5.37.

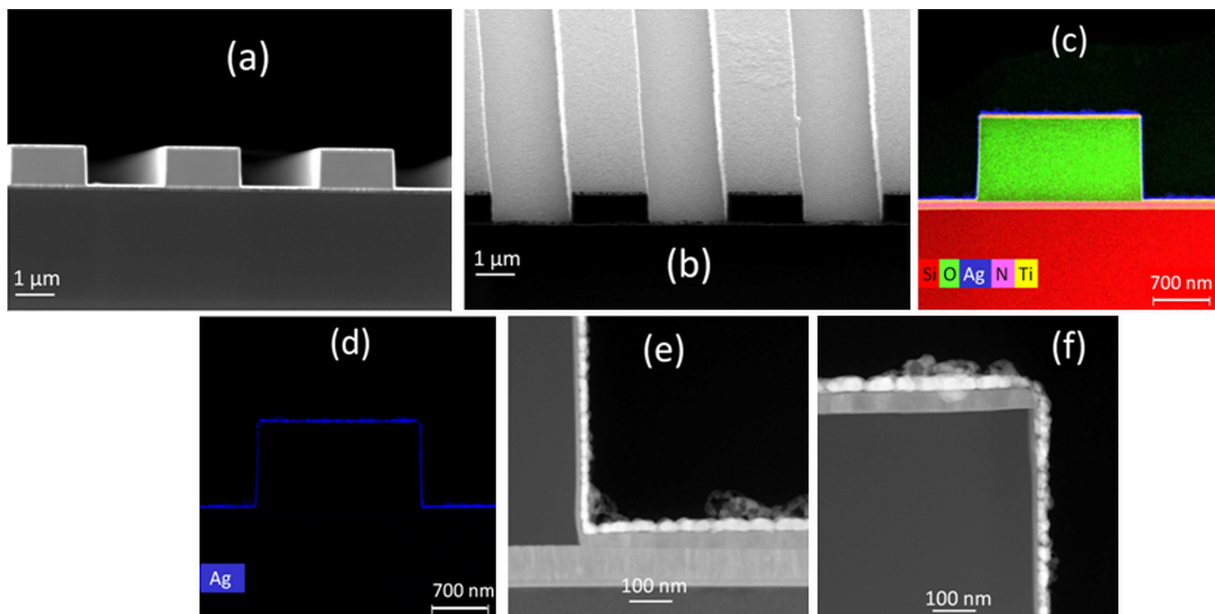
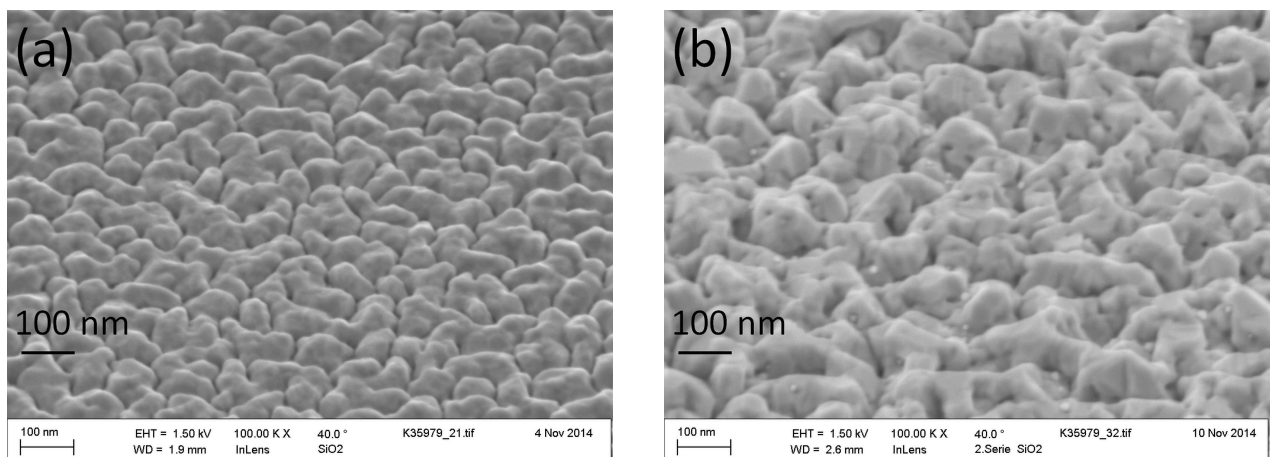


Figure 5.37: SEM and TEM cross sectional image of PALD Ag film deposited at  $120^\circ\text{C}$  on Ti/TiN/ $\text{SiO}_2$ /Si trenches of  $2\ \mu\text{m}$  width and  $1\ \mu\text{m}$  depth: (a) SEM trench cross section (b) SEM top view (c) TEM cross section showing film composition with EDX (d) TEM cross section showing Ag (e) bottom and side walls (TEM) (f) top and side walls (TEM)

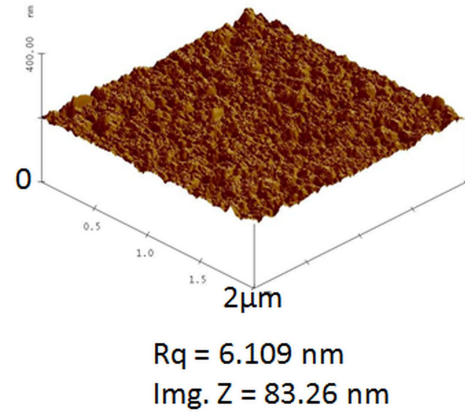
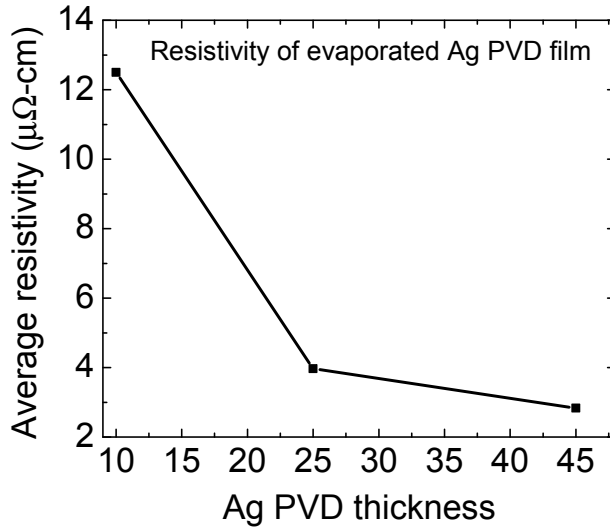
The silver deposition gave estimated step coverage of about 0.6 on this trench structures for about 40 nm Ag film thickness as measured with the SPIP imaging software. It can be observed that the Ti seed layers also had about 0.5 step coverage which might have made the growth of Ag layers to be slightly retarded on the side walls compare to the top and bottom of the trenches. Carbon and oxygen can also be seen on the surface of the film but not in the bulk silver as measured with EDX and also in agreement with XPS results. Generally, deposition in high aspect ratio structures by physical deposition technique such as evaporation and sputtering is limited to 0.2 step coverage [56]. Ag deposition has also been demonstrated by metal organic chemical vapor deposition with 0.8 step coverage on patterned SiO<sub>2</sub> substrate with 7:1 aspect ratio for about 70 nm Ag film [194] and by atomic layer deposition technique on patterned Si substrate with 8:1 aspect ratio for about 40 nm Ag film [89]. The results here show the possibility to also use an adhesion and barrier layer in the trenches such as Ti / TiN (Figure 5.37), Co or Ni during Ag plasma-assisted atomic layer deposition, which is necessary for real interconnects application in microelectronics. Metallic surface such as Co, Ni and Ti can act as adhesion layer for plasma-assisted atomic layer deposition of silver films. These barrier layers such as Co, Ni, Ti, TiN can be deposited by atomic layer deposition [29, 56] into the silicon trenches, preferably in-situ with silver deposition. Growth of silver layer seems to be rough on tungsten (W) with native oxide, and W should be deposited by ALD or MOCVD in-situ together with silver plasma-assisted ALD, in order to possibly obtain smooth growth of silver on tungsten surface.



(a) 1500 PALD cycles (approx. 47 nm film thickness, 9.4  $\Omega \cdot \text{cm}$ ) (b) 3068 PALD cycles (approx. 97 nm film thickness, 5.7  $\mu\Omega \cdot \text{cm}$ )

Figure 5.38: SEM images of conducting PALD Ag film on silicon oxide: (a) 1500 PALD cycles (approx. 47 nm film thickness, 9.4  $\Omega \cdot \text{cm}$ ) (b) 3068 PALD cycles (approx. 97 nm film thickness, 5.7  $\mu\Omega \cdot \text{cm}$ )

Resistivities were determined from sheet resistance measurements and thicknesses of Ag



(a) Change in resistivity of evaporated Ag PVD films with film thickness

(b) AFM morphology of approximately 45 - 50 nm evaporated PVD film

Figure 5.39: Resistivity and AFM morphology of evaporated Ag PVD films (a) Change in resistivity of evaporated Ag PVD films with film thickness (b) AFM morphology of approximately 45 - 50 nm evaporated PVD film

films deposited on SiO<sub>2</sub> using the relation:

$$\rho = R_s \times t \quad (5.2)$$

Where  $\rho$  is the resistivity in  $\Omega \cdot \text{cm}$ ,  $R_s$  is the measured sheet resistance in  $\Omega \cdot \text{sqr}^{-1}$  and  $t$  is the film thickness in cm.

Resistivity was above  $9.4 \Omega \cdot \text{cm}$  after 1500 cycles (about 47 nm Ag film). After 3068 PALD cycles, the film resistivity decreased sharply. A resistivity of  $5.7 \mu\Omega \cdot \text{cm}$  was obtained for approximately 97 nm thick PALD Ag film. The morphology of conducting PALD Ag films are shown in Figure 5.38. The thick 97 nm Ag layer had larger grains and therefore will have lower electron scattering at the surface as well as lower grain boundary scattering compared to 47 nm Ag layer. In other words, interconnected and large island size film will give better conductivity.

Resistivity of evaporated PVD Ag were measured for comparison which gave much lower resistivity with low thickness (Figure 5.39). The reason could be attributed to the fact that PVD layers were smoother as measured by AFM (Figure 5.39b) and contain even less film contamination.

Comparison of the resistivity obtained in this work with the previous Ag PALD reported is given in Table 5.7. The best resistivity of the deposited PALD Ag films in this work was obtained after thicker Ag films ( $5.7 \mu\Omega \cdot \text{cm}$  for 97 nm) compared with the work of Kariniemi et al. ( $6 - 8 \mu\Omega \cdot \text{cm}$  for 20 nm Ag films [13]). A higher plasma power (100 W) used in the work of Kariniemi could have produced denser hydrogen plasma which may have improved the resistivity compared to 50 W plasma power used in this work.

Table 5.7: Comparing the resistivity obtained with the previous Ag PALD reported

| Ag prec.  | other prec.<br>or gases | Dep. temp.<br>(°C) | GPC   | $\rho$ ( $\mu\Omega \cdot \text{cm}$ ),<br>film thickness | Substrates, Ref.<br>and year   |
|---|-------------------------|--------------------|---|---|--|
| Ag(fod)(PEt <sub>3</sub> )                              | H <sub>2</sub> plasma   | 70 - 200           | 0.03 nm/cycle<br>1 cycle=15 s,<br>0.12 nm/min | 5.7, 97 nm  | SiO <sub>2</sub> , TiN, Ti,<br>Co, Ni, W surfaces<br>this work, 2016 |
| Ag(fod)(PEt <sub>3</sub> )                              | H <sub>2</sub> plasma   | 100 - 120          | 0.8 nm/min                                    | 18, 50 nm   | SiO <sub>2</sub> (native)/Si<br>[12],2015                            |
| Ag(fod)(PEt <sub>3</sub> )                              | H <sub>2</sub> plasma   | 120 - 150          | 0.03 nm/cycle                                 | 6 - 8, 20 nm  | Si, glass<br>[13], 2011  |
| (hfac)Ag(1,5-COD)<br>in toluene                         | propanol                | 110 - 150          | -   | -   | glass, SiN<br>[88], 2010   |
| Ag(O <sub>2</sub> C <sup>t</sup> Bu)(PEt <sub>3</sub> ) | H radicals              | 140                | 0.12 nm/cycle                                 | 6, 40 nm  | Si, glass<br>[89], 2007  |

Besides, the film thickness in the work of Kariniemi was calculated from the bulk density of Ag, and it is believed that the actual Ag film thickness could be more than the Ag film thickness calculated from bulk density [13]. The resistivity obtained in this work is better than the one reported in a more recent work of van den Bruele et al. (18  $\mu\Omega \cdot \text{cm}$  for 50 nm Ag films [12]) using the same Ag precursor, but the Ag PALD process reported in the work of Bruele et al. was faster due to spatial-ALD configuration used [12]. Niskanen et al. [89] reported a resistivity of 6  $\mu\Omega \cdot \text{cm}$  for 40 nm Ag film using a different Ag precursor (Ag(O<sub>2</sub>C<sup>t</sup>Bu)(PEt<sub>3</sub>)) with a higher growth per cycle of 0.12 nm, however this precursor is not commercially available and may as well be less stable than the Ag precursor used in this work (Ag(fod)(PEt<sub>3</sub>)).

## 5.3 Plasma-assisted ALD of dielectric oxide and dopant layers

### 5.3.1 PALD of antimony oxide ( $\text{Sb}_2\text{O}_5$ ) film

Antimony oxide deposition was carried out with the ‘HFO’ chamber using the prototype CCP plasma source. The antimony precursor used was triethylantimony ( $(\text{C}_2\text{H}_5)_3\text{Sb}$ ), which belongs to metal alkyl of organometallic precursor class (refer to Figure 2.3a). The vapor pressure equation for triethylantimony can be extracted from the vapor pressure curve [166, 195] as :

$$\log \left[ \frac{P_{TESb}}{\text{mbar}} \right] = 8.0249 - \frac{2183 \text{ K}}{T} \quad (5.3)$$

where  $P_{TESb}$  is the vapor pressure measured in *mbar* and  $T$  is the temperature measured in  $K$  (Kelvin). Triethylantimony vapor pressure was stabilized at about 50 mbar by heating the precursor container to 70 °C. Precursor lines are usually maintained at 120 °C to prevent condensation in the lines. Oxygen radicals generated by the CCP plasma source are used as the oxidizing source.

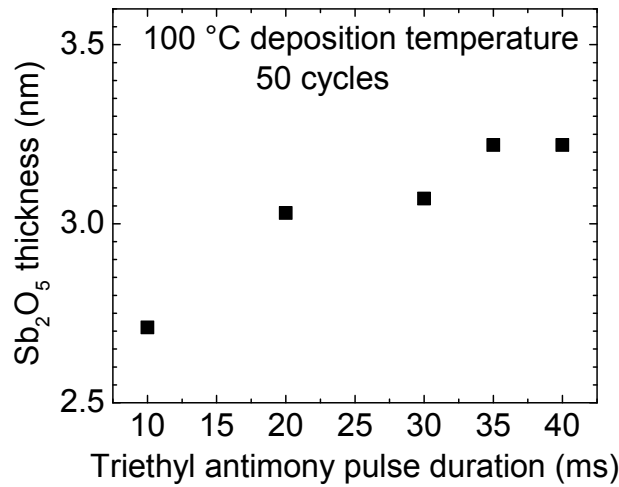


Figure 5.40: Investigation of Sb precursor saturation for  $\text{Sb}_2\text{O}_5$  PALD growth.

Parameters: 50 cycles, 100 °C deposition temperature, Sb Precursor (initial/pulse/exposure): 3 s / varied / 5 s,  $\text{O}_2$  plasma (initial/pulse/exposure): 1 s / 10 s / 1 s,  $\text{N}_2$  purge (Sb precursor and plasma purge): 1 s / 40 s, 100 sccm / 100 sccm / 100 sccm.

Depositions were carried out at 100 °C on Si samples (2 cm by 2 cm coupons) in order to investigate the self limiting behaviour of the process. All samples had native silicon oxide of about 2 to 2.5 nm as measured with spectroscopic ellipsometry. Sb precursor saturation (5.40) was observed between 20 ms to 30 ms pulse time and  $\text{O}_2$  plasma saturation (Figure 5.41) between 5 s to 7 s. Variation of purge times (Figure 5.42) also shows that 5 s purge is sufficient during both Sb precursor and  $\text{O}_2$  plasma subcycle step.



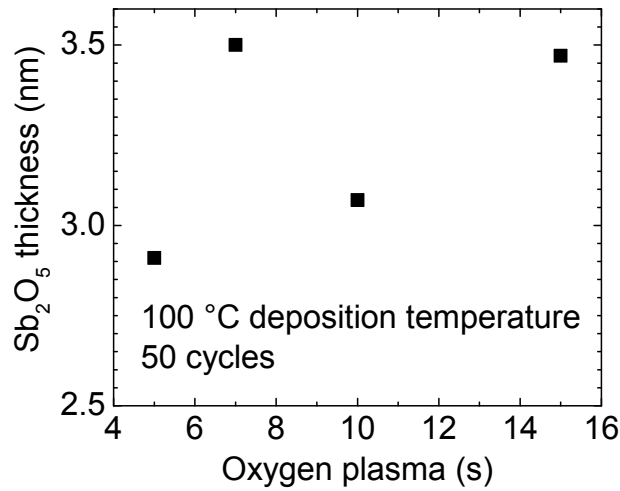


Figure 5.41: Investigation of O<sub>2</sub> plasma saturation for Sb<sub>2</sub>O<sub>5</sub> PALD growth.  
 Parameters: 50 cycles, 100 °C deposition temperature, Sb Precursor (initial/pulse/exposure): 3 s / 20 ms / 5 s, O<sub>2</sub> plasma (initial/pulse/exposure): 1 s / varied / 1 s, N<sub>2</sub> purge (Sb precursor and plasma purge): 1 s / 5 s, 100 sccm / 100 sccm / 100 sccm.

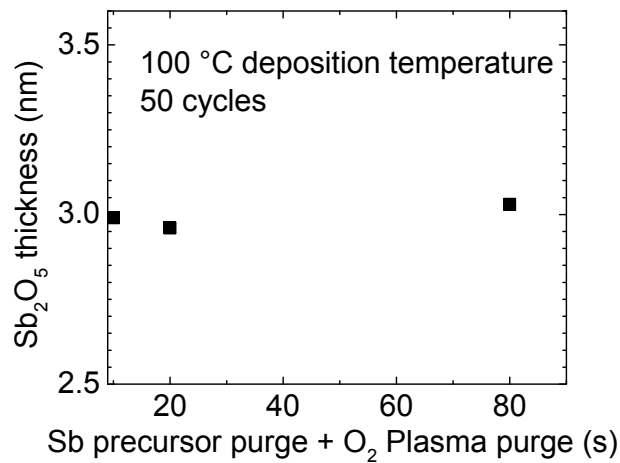


Figure 5.42: Variation of total purge times for Sb precursor and O<sub>2</sub> plasma.  
 The same purge time each is used during Sb precursor and O<sub>2</sub> plasma subcycle.  
 Parameters: 50 cycles, 100 °C deposition temperature, Sb Precursor (initial/pulse/exposure): 3 s / 20 ms / 5 s, O<sub>2</sub> plasma (initial/pulse/exposure): 1 s / 10 s / 1 s, N<sub>2</sub> purge (Sb precursor and plasma purge): 1 s / varied, 100 sccm / 100 sccm / 100 sccm.

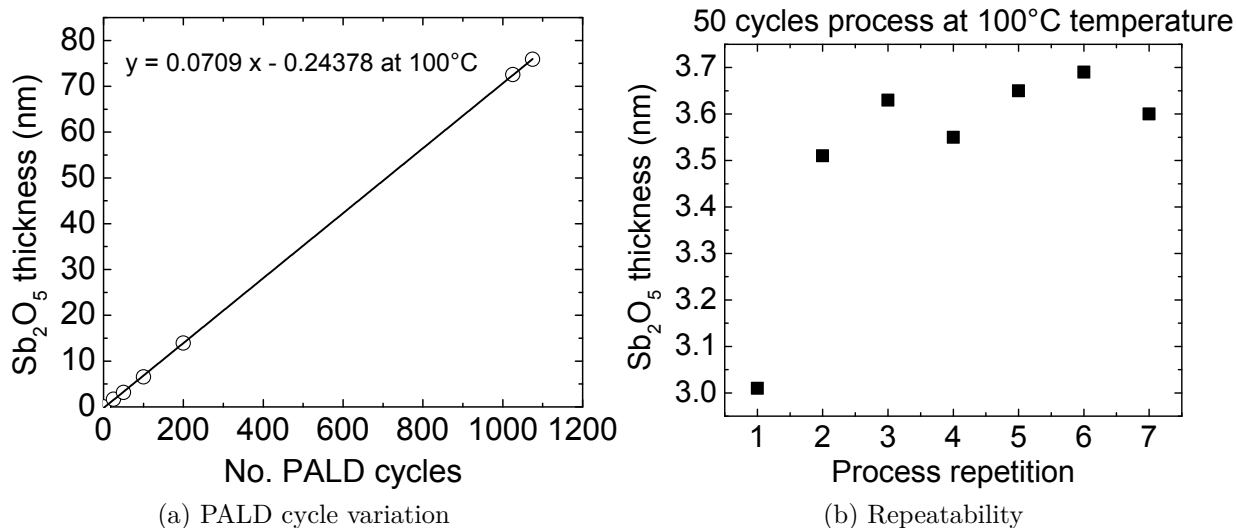


Figure 5.43: Variation of PALD cycles (a) and repeatability of the process (b) for  $\text{Sb}_2\text{O}_5$  PALD growth.

Parameters: 100 °C deposition temperature, Sb Precursor (initial/pulse/exposure): 3 s / 30 ms / 5 s,  $\text{O}_2$  plasma (initial/pulse/exposure): 1 s / 7 s / 1 s,  $\text{N}_2$  purge (Sb precursor and plasma purge): 1 s / 5 s, 100 sccm / 100 sccm / 100 sccm.

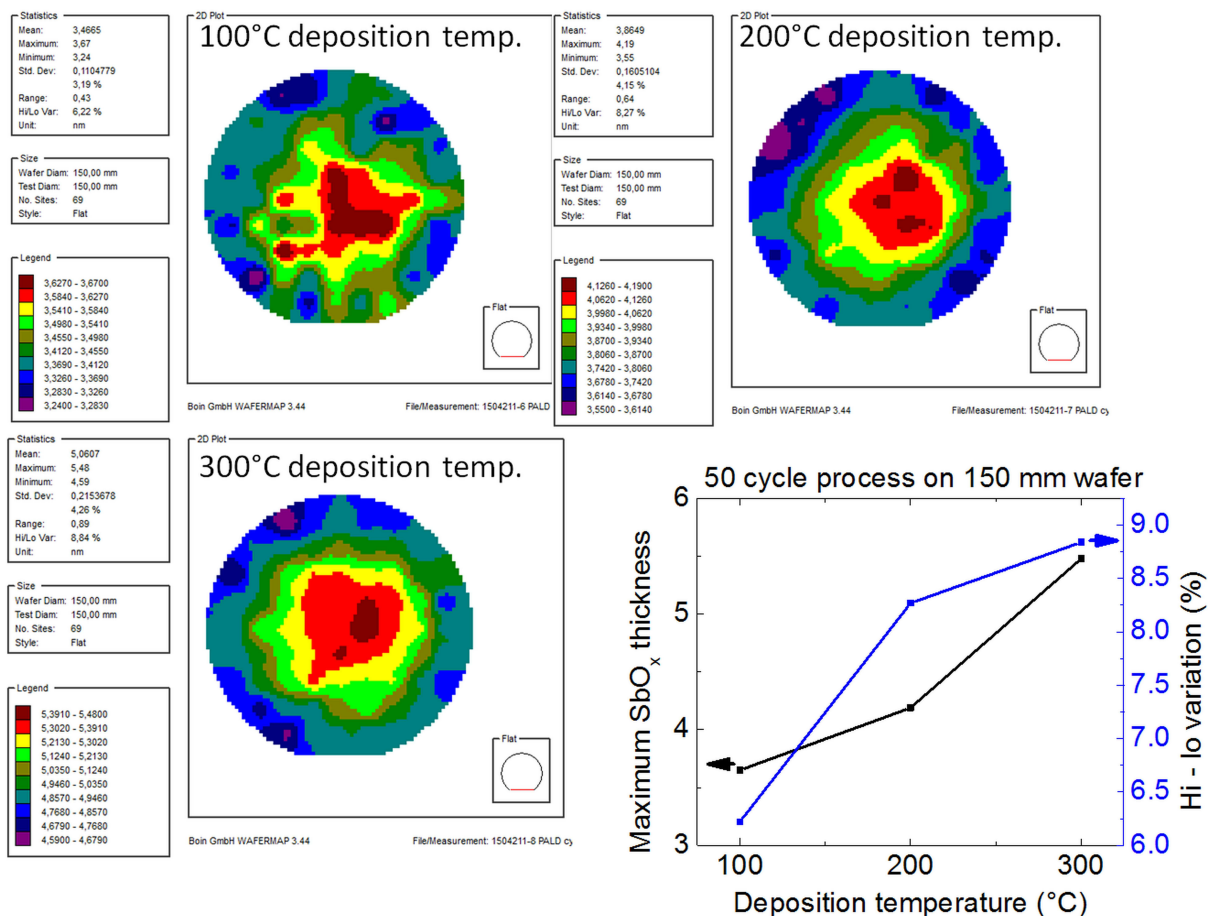
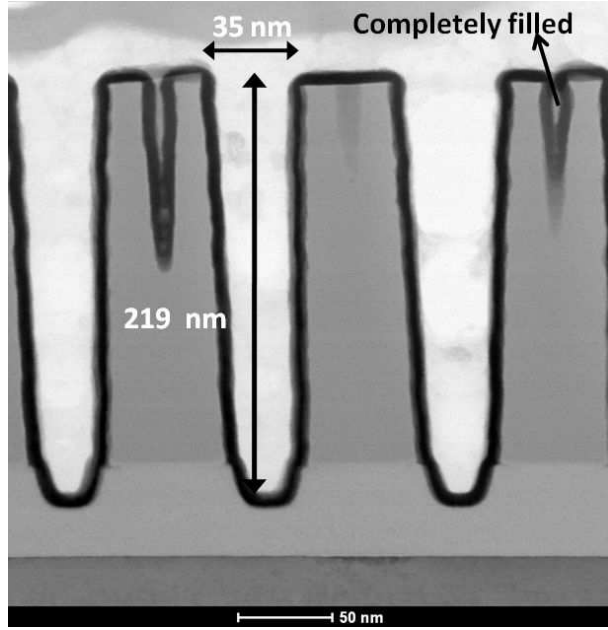


Figure 5.44: Variation of deposition temperatures for  $\text{Sb}_2\text{O}_5$  PALD growth. Other process parameters same as in Figure 5.43

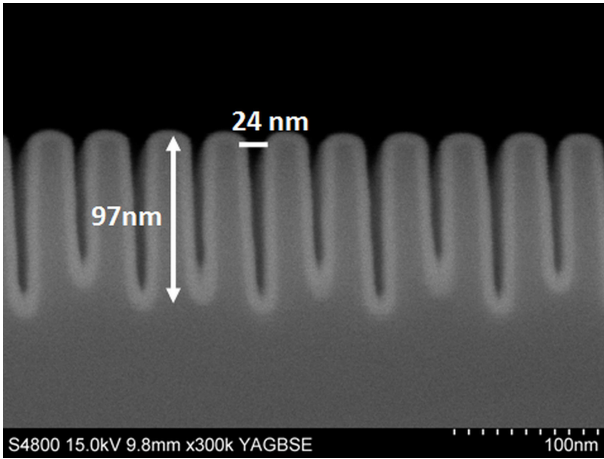
The antimony oxide film thickness also increases as the number of PALD cycles is increased with no incubation cycles (Figure 5.43a). A growth per cycle of approximately 0.07 nm was obtained at 100 °C deposition temperature. Processes were reproducible with maximum variation of  $\pm 0.5$  nm for a 50 cycle process (Figure 5.43b). Differences in  $\text{Sb}_2\text{O}_5$  thickness measured could be from ellipsometer measurement error and uncertainty in the  $\text{SiO}_2$  interfacial layer. Variation in deposition temperatures (Figure 5.44) shows a trend of increase in antimony oxide film thickness with deposition temperature. However, the hi-lo variation increases (uniformity decreases) as the deposition temperature is increased. The wafer map shows higher increase in film thickness in the region around the inlet of the plasma radicals on the wafer. Typical ALD process should have hi-lo variation less than 2 %. Elers et al. identified some possible sources of non-uniformity as overlapping precursor pulses, non-uniform precursor distribution, film reaction with gaseous by-products and thermal decomposition of precursor [196].  $(\text{C}_2\text{H}_5)_3\text{Sb}$  will only decompose at a temperature above 600 °C [197]. It is very unlikely that the  $\text{Sb}_2\text{O}_5$  film reacts with by-products because increasing Sb precursor and  $\text{O}_2$  plasma pulse times during saturation investigation did not lead to remarkably increased film thickness, since more by-products should be produced with more precursors. The best uniformity obtained for  $\text{Sb}_2\text{O}_5$  deposition on 150 mm Si wafer was approximately with hi-lo variation of 6 % at 100 °C, which could have been limited by the hardware design possibly due to some Sb precursor traps in the chamber present during the  $\text{O}_2$  plasma subcycle, leading to CVD type growth in the middle of the wafer. A source of precursor traps may be the cold chamber walls where precursors can likely condense. A higher deposition temperature should in principle promote better purge which should even improve the uniformity. But a plausible explanation for the opposite trend of uniformity with temperature may be possibly non-uniformity in substrate temperature, which may have resulted in lower film thickness at the wafer edges since the film thickness is also temperature dependent.

TEM and SEM results after antimony oxide PALD deposition on patterned Si high aspect ratio structures of approximately 6:1 and 4:1 are shown in Figures 5.45a and 5.45b. A step coverage of 100 % was obtained on these test structures. It can also be observed (figure 5.45a) that the PALD  $\text{Sb}_2\text{O}_5$  film could completely fill and block the narrow spaces in trenches when the film thickness is more than half of the width of the space. Surface roughness measured by AFM of about 73 nm PALD  $\text{Sb}_2\text{O}_5$  film deposited at 100 °C substrate temperature is shown in Figure 5.45c. The rms roughness obtained was 1.213 nm measured on 2 by 2  $\mu\text{m}^2$  area. Smoother antimony oxide films were grown by thermal atomic layer deposition at 250 °C using  $(\text{C}_2\text{H}_5)_3\text{Sb}$  and  $\text{O}_3$  with roughness of 0.159 nm on 2 by 2  $\mu\text{m}^2$  area [33]. PALD  $\text{Sb}_2\text{O}_5$  film optical properties were determined using the cauchy model for refractive index and extinction coefficient given as:

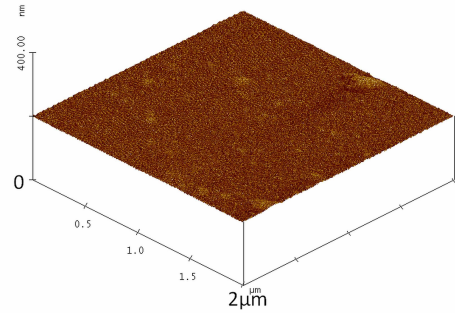
$$n(\lambda) = n_0 + \frac{10^2 \times n_1}{\lambda^2} + \frac{10^7 \times n_2}{\lambda^4} \quad (5.4)$$



(a) TEM after 100 cycles  $\text{Sb}_2\text{O}_5$  PALD deposition on high aspect ratio structure of approx. 6:1



(b) SEM after 100 cycles  $\text{Sb}_2\text{O}_5$  PALD deposition on high aspect ratio structure of approx. 4:1



$R_q = 1.213\text{nm}$ ,  $\text{Im}g. \text{Z range} = 15.169 \text{ nm}$   
(c) AFM measurement result of 1000 PALD cycles (73 nm)  $\text{Sb}_2\text{O}_5$  film

Figure 5.45: TEM (a) and SEM (b) after  $\text{Sb}_2\text{O}_5$  PALD deposition on high aspect ratio structures and AFM measurements of 73 nm  $\text{Sb}_2\text{O}_5$  film (c)

$$k(\lambda) = k_0 + \frac{10^2 \times k_1}{\lambda^2} + \frac{10^7 \times k_2}{\lambda^4} \quad (5.5)$$

Table 5.8: Cauchy dispersion coefficients of PALD  $\text{Sb}_2\text{O}_5$  film deposited at 100 °C temperature

| $n_0$ | $n_1$ | $n_2$ | $k_0$  | $k_1$  | $k_2$   |
|-------|-------|-------|--------|--------|---------|
| 1.892 | 99.2  | 179.3 | -0.035 | 212.38 | -265.02 |

where  $n$ ,  $k$ , and  $\lambda$  are refractive index, extinction coefficient and wavelength (in nm),

respectively. The coefficients  $n_0$ ,  $n_1$ ,  $n_2$ ,  $k_0$ ,  $k_1$  and  $k_2$  given in Table 5.8 (page 114) were determined from the ellipsometric fit of  $\Psi$  and  $\Delta$  in the wavelength range 300 nm to 800 nm obtained from 73 nm PALD  $\text{Sb}_2\text{O}_5$  film deposited at 100 °C temperature. The refractive index of  $\text{Sb}_2\text{O}_5$  film deposited at 100 °C was 1.928 at 633 nm wavelength.  $\text{Sb}_2\text{O}_5$  has refractive index of 2.087 in the cubic crystalline form and 2.35 in the orthorhombic form [198], therefore the  $\text{Sb}_2\text{O}_5$  film deposited at 100 °C might be amorphous.

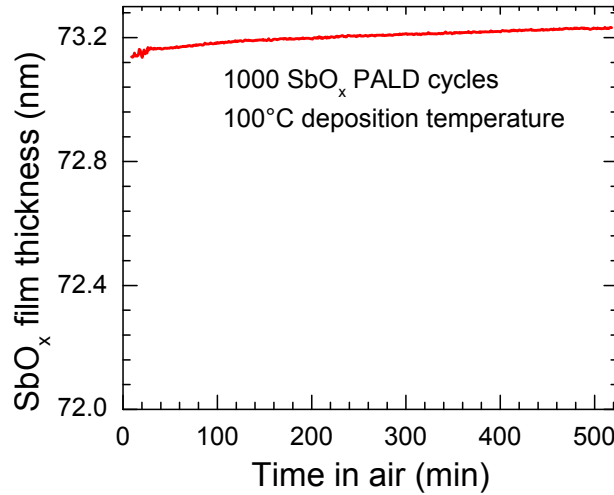


Figure 5.46: Stability of  $\text{Sb}_2\text{O}_5$  film: 1000 cycles plasma ALD of  $\text{Sb}_2\text{O}_5$  at 100 °C deposition temperature

Results of  $\text{Sb}_2\text{O}_5$  film thickness measurement depending on time exposed in air (Figure 5.46) shows that the film is quite stable in air. The film thickness only increased by 0.1 nm after approximately 500 minutes in air due to adsorption of air-borne molecules on the surface.  $\text{Sb}_2\text{O}_5$  film can, therefore, serve as a suitable dielectric material for passivating the Si surface as well as protecting other moisture sensitive material. Its high refractive index also makes it suitable as an optical coating.

### 5.3.2 PALD of boron oxide film

Boron oxide films were also deposited with ‘HFO’ chamber using the prototype CCP plasma source. The boron precursor used was tris(dimethylamino)borane (TDMAB or  $B(N(CH_3)_2)_3$ ) which belongs to the metal alkylamides class (Figure 2.5) of the metal-organic precursors. The vapor pressure of TDMAB is given as [199]:

$$\log \left[ \frac{P_{TDMAB}}{mbar} \right] = 5.94393 - \frac{2476 K}{T} + 1.75 \log \left[ \frac{T}{K} \right] - 0.0039086 \frac{T}{K} \quad (5.6)$$

where  $P_{TDMAB}$  is the vapor pressure measured in *mbar* and T is the temperature measured in *K* (Kelvin). TDMAB vapor pressure was stabilized at about 65 mbar by heating the precursor container to 70 °C. Ozone and oxygen radicals can be used as oxidizing source for  $B_2O_3$  deposition. Results of  $B_2O_3$  deposition using TDMAB with O radicals for the case of plasma ALD as well as TDMAB with ozone for the case of thermal ALD are shown in Figure 5.47.

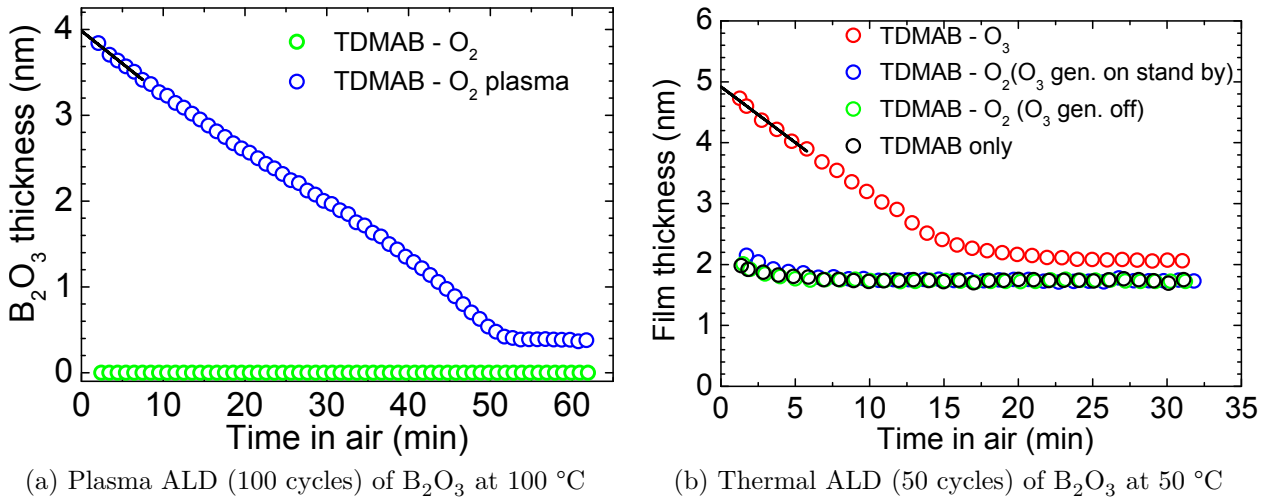


Figure 5.47: Investigation of  $B_2O_3$  deposition and film stability in air from tris-dimethyl-amido borane (TDMAB or  $B(N(CH_3)_2)_3$ ) with  $O_2$  plasma and  $O_3$  as oxidizing source

Time dependent ellipsometric measurements shows immediate evaporation of  $B_2O_3$  film in ambient air. This behaviour has been reported in literature [106,200] and the reason was attributed to moisture in the ambient air which transforms  $B_2O_3$  film into a volatile boric acid at room temperature [200]. One will reason that degradation of  $B_2O_3$  film due to its reaction with moisture may be much faster and noticeable under atmospheric pressure at room temperature than under vacuum at room temperature, because  $B_2O_3$  film appears to be stable in vacuum at room temperature. In addition, TDMAB does not react with oxygen gas alone (without plasma activation) at temperature from room temperature up to 100 °C.  $B_2O_3$  film thickness degradation is approximately linear with time and as a result extrapolation of linear fit of the data from first few measurements

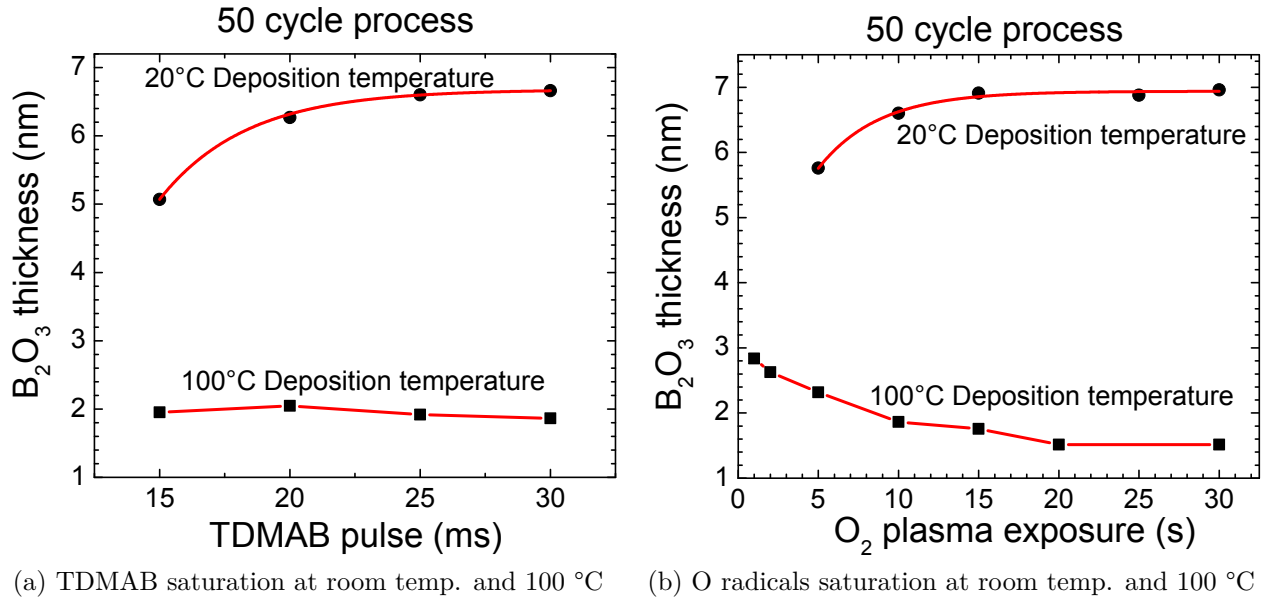


Figure 5.48: Investigation of saturation for TDMAB and O radicals at room temperature and 100 °C deposition: process parameters are given in Tables 5.9 and 5.10

(black lines in Figure 5.47) is done in order to determine starting  $B_2O_3$  film thickness.

Table 5.9: Deposition parameters for TDMAB saturation investigation

| Deposition Temp. (°C) | TDMAB (initial/pulse/exposure) | O radicals (initial/pulse/exposure) | Purge for both TDMAB and O                      |
|-----------------------|--------------------------------|-------------------------------------|---|
| 100                   | 3 s / varied / 5 s             | 1 s / 10 s / 1 s                    | 1 s / 5 s                                       |
| 20                    | 3 s / varied / 5 s             | 1 s / 10 s / 1 s                    | 1 s / 15 s<br>100 sccm / 100 sccm /<br>100 sccm |

Table 5.10: Deposition parameters for O radicals saturation investigation

| Deposition Temp. (°C) | TDMAB (initial/pulse/exposure) | O radicals (initial/pulse/exposure) | Purge for both TDMAB and O                      |
|-----------------------|--------------------------------|-------------------------------------|---|
| 100                   | 3 s / 30 ms / 5 s              | 1 s / varied / 1 s                  | 1 s / 5s  |
| 20                    | 3 s / 25 ms / 5 s              | 1 s / varied / 1 s                  | 1 s / 15 s<br>100 sccm / 100 sccm /<br>100 sccm |

Besides,  $B_2O_3$  film deposited with  $O_2$  plasma may be more stable in ambient air than  $B_2O_3$  film deposited with  $O_3$  in the experiments as also observed in [106]. Linear fits (black lines) in both graph in Figure 5.47 are  $y = -0.07594x + 3.98268$  for  $B_2O_3$  deposition with  $O_2$  plasma in Figure 5.47a and  $y = -0.1832x + 4.91899$  for  $B_2O_3$  deposition with  $O_3$  in Figure 5.47b. Thus initial vaporization rate in ambient air may be about 2 times faster

for  $B_2O_3$  film deposited with  $O_3$  than with  $O_2$  plasma, however the ambient conditions could not be controlled in the experiments.

Investigation of TDMAB saturation as well as O radicals saturation were carried out at 20 °C and 100 °C (Figure 5.48). Clear saturation was reached between 20 ms to 30 ms TDMAB pulse at 20 °C deposition temperature with  $B_2O_3$  film thickness remaining almost constant at saturation. However, film thickness decreased slightly as the TDMAB pulse is increased above 20 ms for deposition carried out at 100 °C substrate temperature. Also, saturation was reached at 15 s O radical exposure time with film thickness remaining fairly constant at saturation for deposition carried out at 20 °C substrate temperature, but the film thickness was higher with shorter  $O_2$  plasma exposure time for deposition carried out at 100 °C substrate temperature. This may be an indication that reaction by-products such as water may actually react with  $B_2O_3$  film at 100 °C thereby decreasing the film thickness (etching). Water is one of the reaction by-product observed with the in-situ mass spectrometer (Figure 5.49), and more TDMAB precursor and plasma time would mean more by-products produced (water). Thus,  $B_2O_3$  film thickness decreased with increase in TDMAB precursor and O plasma time at 100 °C deposition temperature.

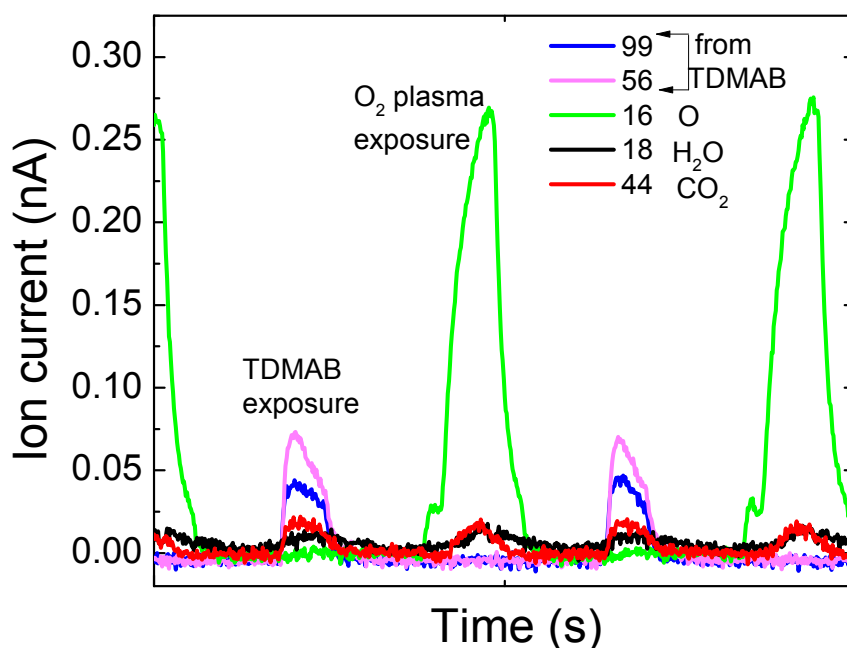


Figure 5.49: In-situ process monitoring with Quadrupole Mass Spectrometry using MID (multiple ion detection) scan of some specific masses

In addition,  $B_2O_3$  film thickness also decreased as the deposition temperature is increased (Figure 5.50), possibly due to increased precursor desorption at higher temperature or vaporization of  $B_2O_3$  film after reacting with water by-products and moisture traces in the chamber at higher temperatures.

Variation of PALD cycles at 20 °C and 100 °C deposition temperature (Figure 5.51) shows ALD type growth with no incubation cycles at both temperatures. An estimated



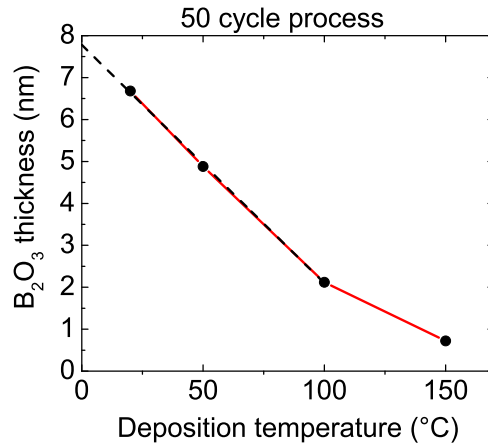


Figure 5.50: Investigation of B<sub>2</sub>O<sub>3</sub> growth depending on deposition temperature

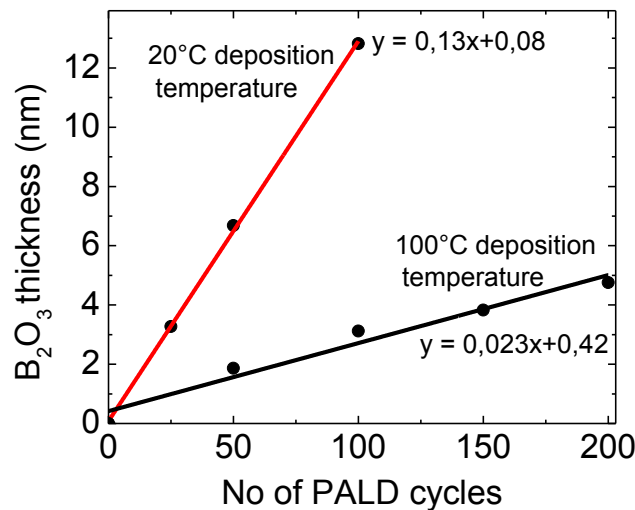


Figure 5.51: Variation of PALD cycles for B<sub>2</sub>O<sub>3</sub> PALD deposition at 20 °C and 100 °C deposition temperature.

20 °C deposition temperature parameters: TDMAB (initial/pulse/exposure): 3 s / 25 ms / 5 s, O<sub>2</sub> plasma (initial/pulse/exposure): 1 s / 10 s / 1 s, N<sub>2</sub> purge (TDMAB and plasma purge): 1 s / 15 s, 100 sccm / 100 sccm / 100 sccm.

100 °C deposition temperature parameters: TDMAB (initial/pulse/exposure): 3 s / 30 ms / 5 s, O<sub>2</sub> plasma (initial/pulse/exposure): 1 s / 10 s / 1 s, N<sub>2</sub> purge (TDMAB purge and plasma purge): 1 s / 5 s, 100 sccm / 100 sccm / 100 sccm.

growth per cycle of 0.13 nm was obtained at 20 °C deposition temperature. Growth per cycle varies between 0.02 - 0.05 nm depending on the O<sub>2</sub> plasma time for depositions made at 100 °C. Deposition parameters are given in Figure 5.51. B<sub>2</sub>O<sub>3</sub> film is quite unstable in air as earlier shown, and as a result, it should be protected with a stable film in order to

prevent it from vaporization. Stable films such as  $\text{Al}_2\text{O}_3$  or  $\text{Sb}_2\text{O}_5$  of sufficient thickness can be used as capping layers for  $\text{B}_2\text{O}_3$  to prevent it from evaporation.

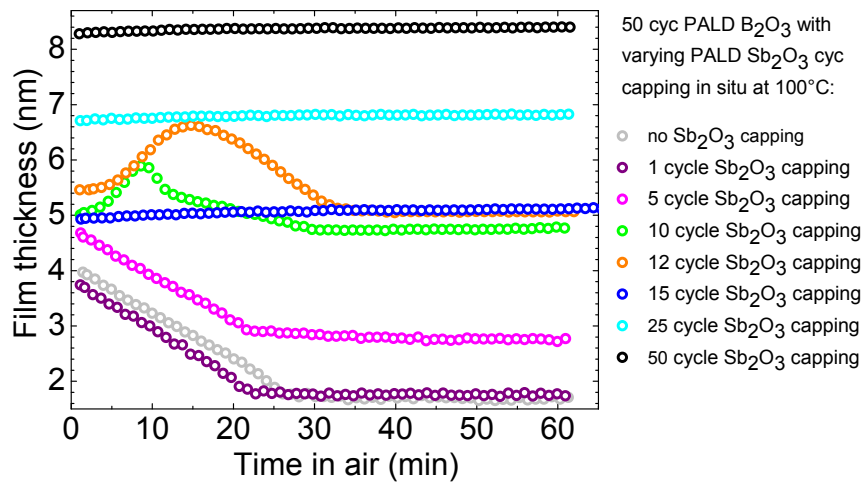


Figure 5.52: Stabilizing  $\text{B}_2\text{O}_3$  films with  $\text{Sb}_2\text{O}_5$  capping: Plasma ALD of  $\text{B}_2\text{O}_3$  at  $100\text{ }^\circ\text{C}$  (50 cycles of TDMAB and  $\text{O}_2$  plasma) followed by different in-situ plasma ALD cycles of TESb ( $\text{Sb}(\text{C}_2\text{H}_5)_3$ ) and  $\text{O}_2$  plasma at  $100\text{ }^\circ\text{C}$

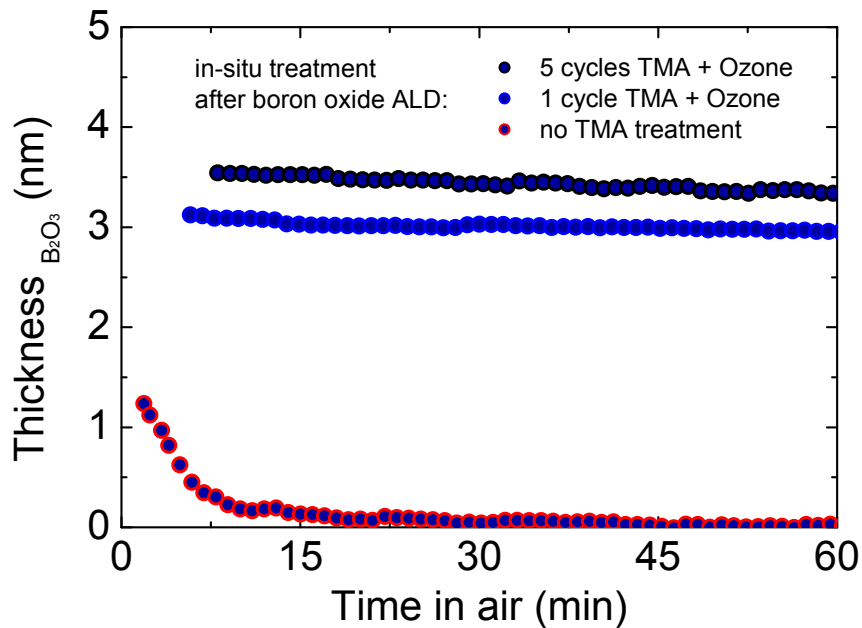


Figure 5.53: Stabilizing  $\text{B}_2\text{O}_3$  films with  $\text{Al}_2\text{O}_3$  capping: Thermal ALD of  $\text{B}_2\text{O}_3$  at  $50\text{ }^\circ\text{C}$  (50 cycles of TDMAB and ozone) followed by different in-situ ALD cycles of TMA and ozone at  $50\text{ }^\circ\text{C}$

From Figure 5.52, one can observe a rapid decrease in film thickness of  $\text{B}_2\text{O}_3$  layer without  $\text{Sb}_2\text{O}_5$  capping until 5 cycle  $\text{Sb}_2\text{O}_5$  capping (Figure 5.52), when the capping starts to protect the film. Furthermore, an initial swelling up before film degradation was observed for layers with 10 cycles and 12 cycles  $\text{Sb}_2\text{O}_5$  capping.  $\text{B}_2\text{O}_3$  film seems to be stable at least within one hour in air, beyond 15 cycle  $\text{Sb}_2\text{O}_5$  capping. Similarly, stability of  $\text{B}_2\text{O}_3$  layer capped with  $\text{Al}_2\text{O}_3$  film is shown in Figure 5.53.

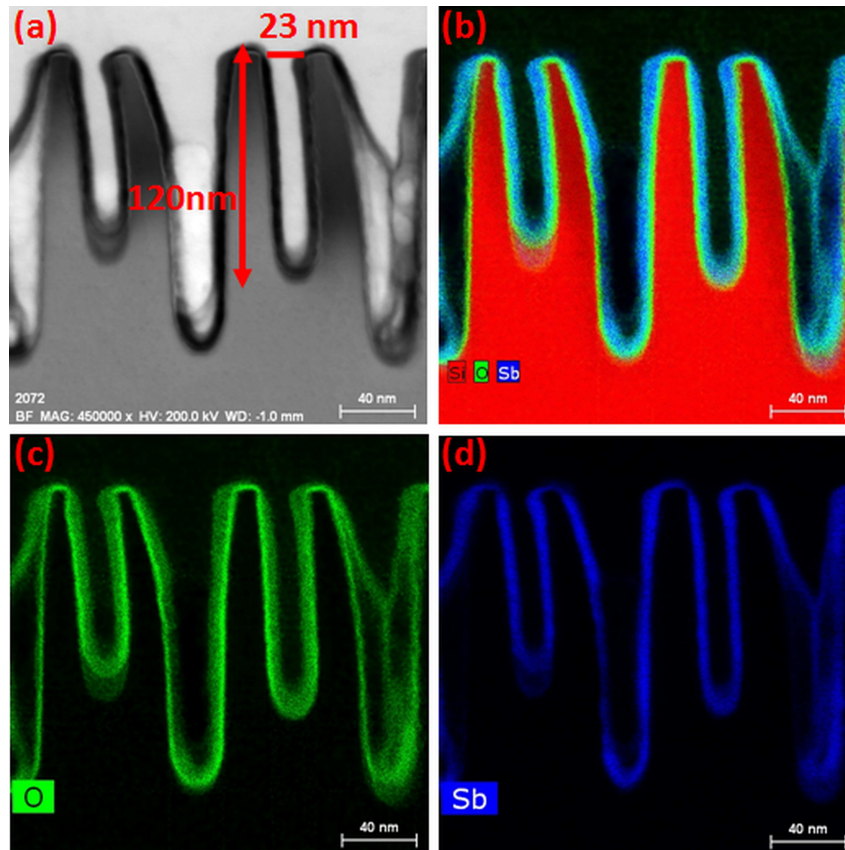


Figure 5.54:  $B_2O_3$  film (50 cycles) capped with in-situ  $Sb_2O_5$  film (50 cycles) at  $100\text{ }^\circ\text{C}$  on BHF cleaned patterned Si high aspect ratio structure. (a) TEM image (b) EDX showing Si, O and Sb (c) EDX showing O (d) EDX showing Sb

Deposition of  $B_2O_3$  film capped with in-situ  $Sb_2O_5$  film at  $100\text{ }^\circ\text{C}$  on BHF cleaned patterned Si high aspect ratio structure is shown in Figure 5.54. Highly conformal deposition was obtained on aspect ratio 6:1. EDX signals reveals Si, O and Sb but not boron. The  $Sb_2O_5$  capping might have been destroyed during TEM preparation which could have resulted in evaporation of  $B_2O_3$  film starting from the edges. Film delamination was also observed in the TEM images (Figure 5.54) which could be due to electron beam bombardment.

### 5.3.3 PALD of silicon oxide film

Silicon oxide deposition was carried out on the ‘SENTECH’ PALD system using the prototype ICP plasma source. The silicon precursor used was tris(dimethylamino)silane (TDMAS or  $\text{HSi}(\text{N}(\text{CH}_3)_2)_3$ ), which also belongs to the metal alkylamides class (Figure 2.5) of the metal-organic precursors. Its vapor pressure is given as [201]:

$$\log \left[ \frac{P_{TDMAS}}{\text{mbar}} \right] = 8.3449 - \frac{2210 \text{ K}}{T} \quad (5.7)$$

where  $P_{TDMAS}$  is the vapor pressure measured in *mbar* and T is the temperature measured in *K* (Kelvin).

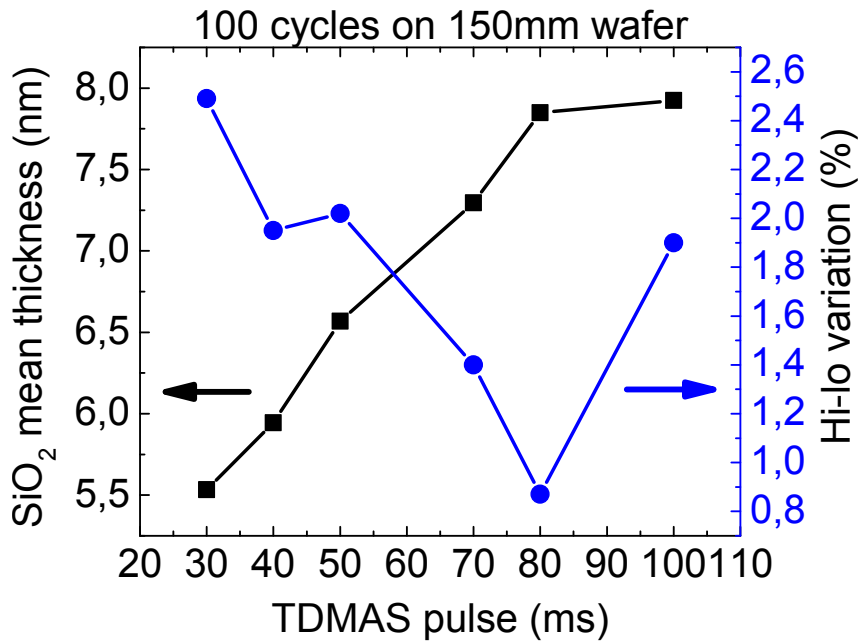


Figure 5.55: Investigation of saturation for TDMAS pulse:

TDMAS (pulse/purge): varied / 10 s, O<sub>2</sub> plasma (pulse/purge): 15 s / 10 s, O<sub>2</sub> flow into plasma head: 250 sccm, Number of PALD cycle: 100, Substrate temperature: 150 °C, N<sub>2</sub>Purge: 100 sccm, TDMAS bottle: room temp (heated up to 33 °C from lines), TDMAS line and chamber walls: 120 °C.

The precursor is pyrophoric with vapor pressure of about 13 *mbar* at 33 °C. As a result precursor bottle was kept at room temperature, while the precursor lines were maintained at 120 °C. Usually the precursor bottle can be heated up to 33 °C when the line temperature is maintained at 120 °C. For SiO<sub>2</sub> deposition, oxygen radicals generated by the ICP plasma source are used as the oxidizing source.

SiO<sub>2</sub> film was successfully deposited on 150 mm Si wafer at 150 °C substrate temperature. Investigation of saturation for TDMAS precursor (Figure 5.55) was carried out at 150 °C substrate temperature by varying TDMAS pulse time from 30 ms to 100 ms. This gives an increase in SiO<sub>2</sub> mean film thickness with TDMAS pulse times until saturation at 80 ms TDMAS pulse time. In addition, the wafer non-uniformity decreases as TDMAS pulse

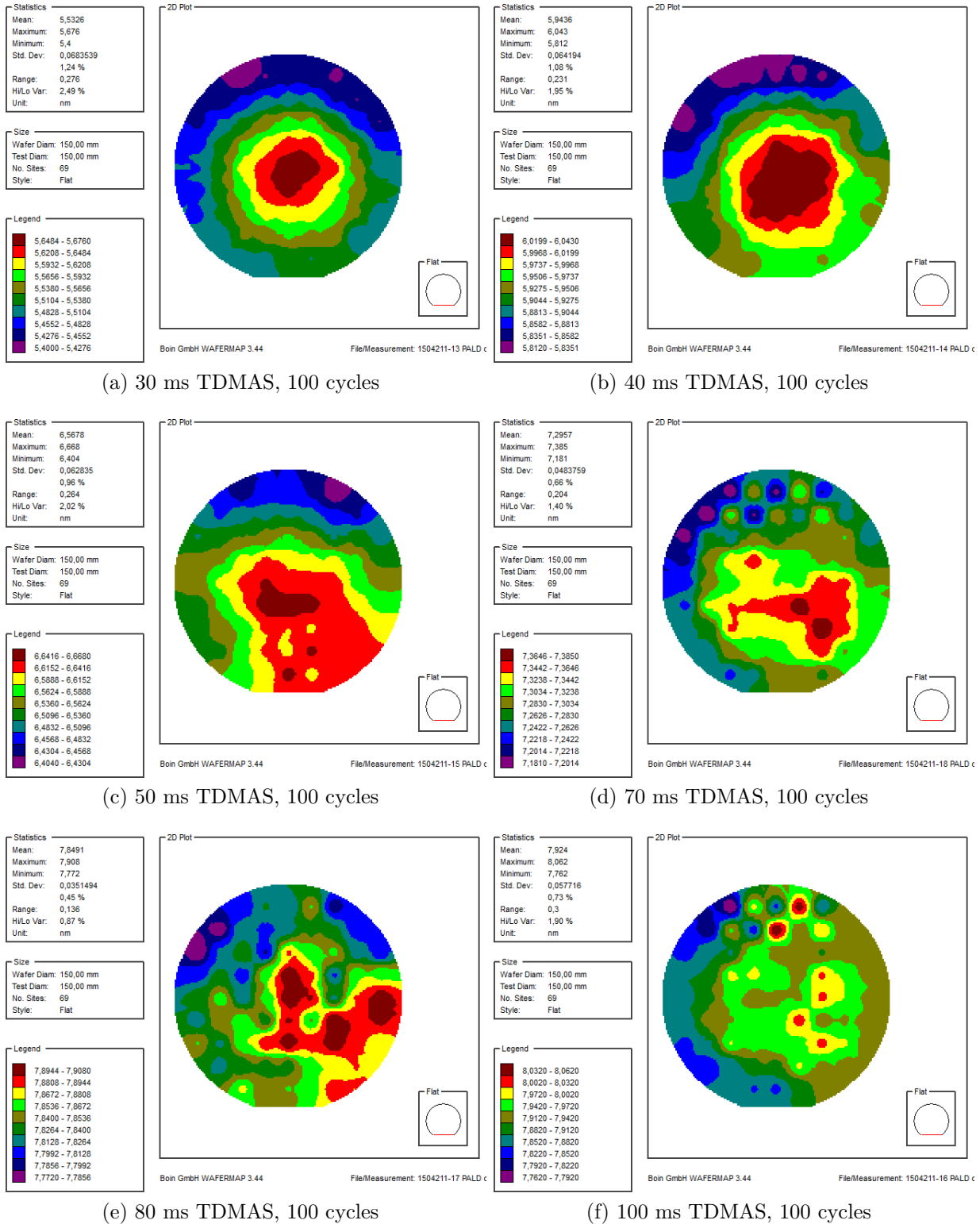


Figure 5.56: Wafer maps of PALD SiO<sub>2</sub> for varying TDMAS pulse times:  
 TDMAS pulse variation with 15 s O<sub>2</sub> plasma at 150 °C deposition temperature

times increases until 80 ms pulse. Depositions were highly conformal with non-uniformity of less than 1 % at saturation. Wafer maps of different TDMAS precursor pulses are shown in Figure 5.56. Uniformity may also be improved with a longer purge of 10 s.

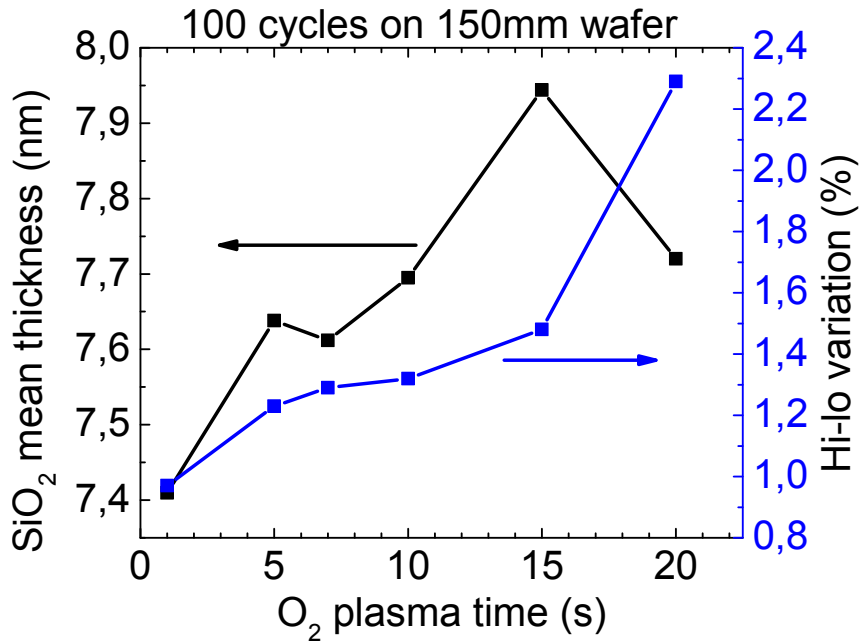


Figure 5.57: Investigation of O<sub>2</sub> plasma saturation for PALD SiO<sub>2</sub> growth: O<sub>2</sub> flow into plasma head: 250 sccm, TDMAS (pulse/purge): 80 ms / 5 s, O<sub>2</sub> plasma (pulse/purge): varied/2s, Number of PALD cycle: 100, Substrate temperature: 150 °C, N<sub>2</sub> purge: 100sccm, TDMAS bottle: room temp (heated up to 33 °C from lines), TDMAS line and chamber walls: 120 °C

Similarly, investigation of saturation for O radicals (Figure 5.57) was carried out at 150 °C substrate temperature by varying O<sub>2</sub> plasma time from 1 s to 20 s. Mean film thickness also increases as the plasma time is increased. However the non-uniformity increases with increase in plasma time. 5 s to 7 s plasma time will be sufficient for saturation on 150 mm wafer. Wafer map for 20 s plasma time (Figure 5.58) shows two peaks in the middle which indicates the outlet of the plasma tubes. Long plasma time might cause increased CVD deposition around the outlet of the plasma tubes on the wafer.

PALD cycle variation (Figure 5.59) gives linear SiO<sub>2</sub> film growth with number of PALD cycles and without incubation cycles. An average growth per cycle of 0.074 nm was obtained on Si wafer (native oxide approx. 1.7 nm) at 150 °C.

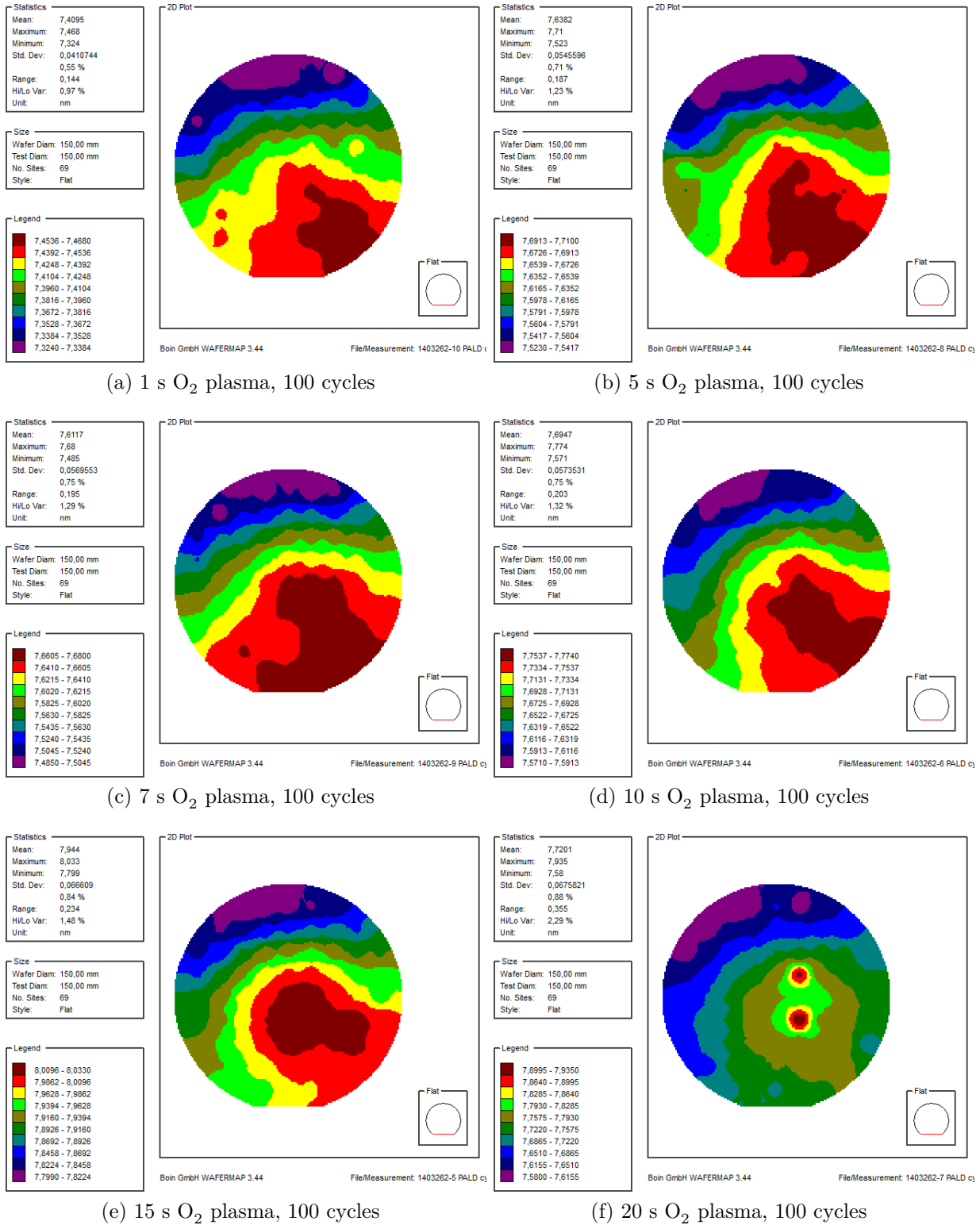


Figure 5.58: Wafer maps of PALD SiO<sub>2</sub> for varying O<sub>2</sub> plasma pulse times: Oxygen plasma variation with 80 ms TDMAS pulse at 150 °C deposition temperature

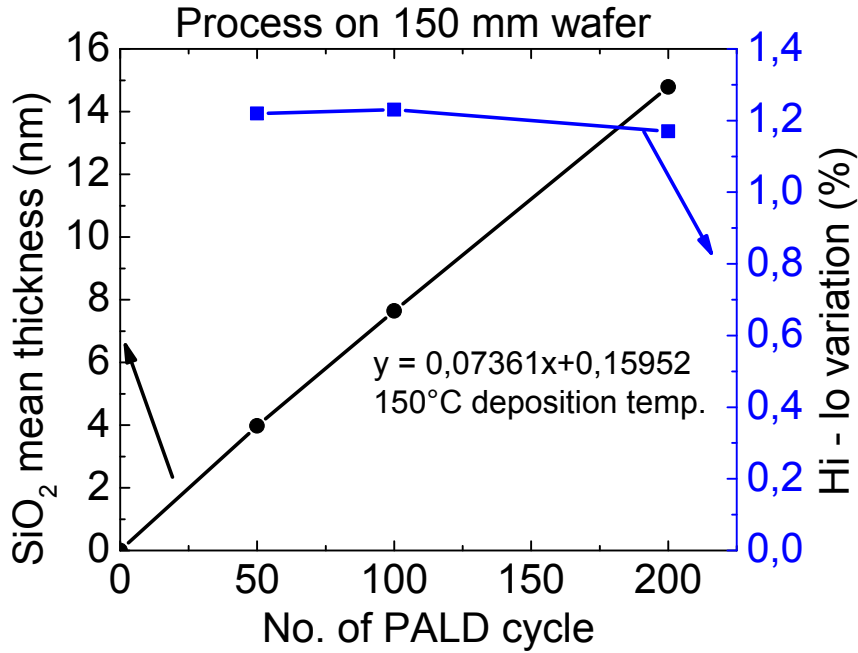


Figure 5.59: Investigation of PALD cycle variation for SiO<sub>2</sub> PALD deposition at 150 °C: TDMAS (pulse/purge): 80 ms / 5 s, O<sub>2</sub> plasma (pulse/purge): 5 s / 2 s, O<sub>2</sub> flow into plasma head: 250 sccm, Substrate temperature: 150 °C, N<sub>2</sub>Purge: 100 sccm, TDMAS bottle: room temp (heated up to 33 °C from lines), TDMAS line and chamber walls: 120 °C.

### 5.3.4 PALD of phosphorus containing oxide film

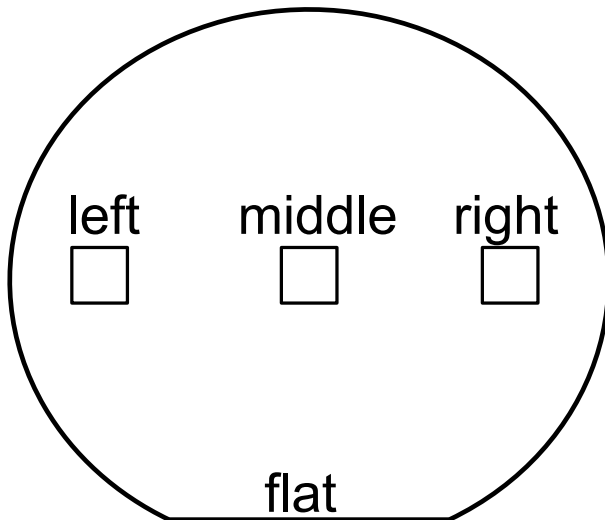
Oxide of phosphorus, PO<sub>x</sub> was deposited from triethyl phosphite (TEOP) and O radicals. Triethyl phosphite (TEOP) belongs to metal-alkoxide group of metal-organic precursors class (Figure 2.4). Depositions were also carried out on the 'SENTECH' PALD system.

The vapor pressure of triethyl phosphite (TEOP or C<sub>6</sub>H<sub>15</sub>O<sub>3</sub>P) was determined from the vapor pressure equation given as [202]:

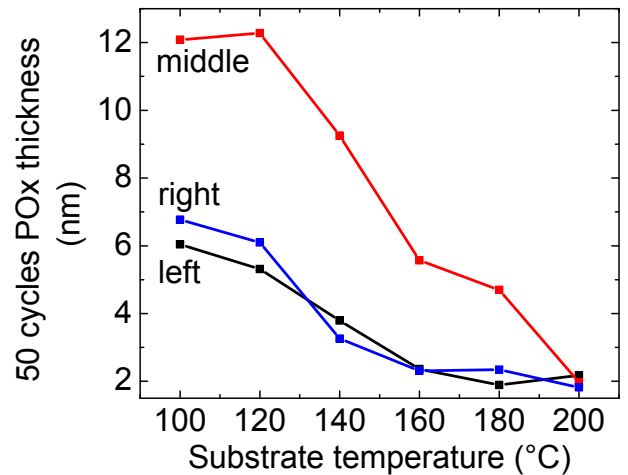
$$\log \left[ \frac{P_{TEOP}}{mbar} \right] = 7.324 - \frac{1683 K}{T - 43} \quad (5.8)$$

where  $P_{TEOP}$  is the vapor pressure measured in *mbar* and T is the temperature measured in K (Kelvin). As a result, the TEOP bottle temperature was maintained at 50 °C in order to obtain a vapor pressure of about 20 *mbar*. Usually, line temperatures were maintained at 120 °C. The PO<sub>x</sub> depositions were carried out on prepared samples of about 2 cm by 2 cm placed at different positions on a carrier wafer (Figure 5.60a) from 100 °C to 200 °C substrate temperature. Poor uniformity with exceptionally thick PO<sub>x</sub> layers were obtained at low temperature (Figure 5.60b). The deposited PO<sub>x</sub> film will not vaporize in ambient air at room temperature but the film thickness fluctuates in air due to moisture sensitivity of phosphorus as seen from the time dependent ellipsometric measurements in Figure 5.60c. XPS results of PALD PO<sub>x</sub> film in Figure 5.60d indicates the presence of phosphorus with carbon and nitrogen in the as-deposited film. The deposited phosphorus would be in form

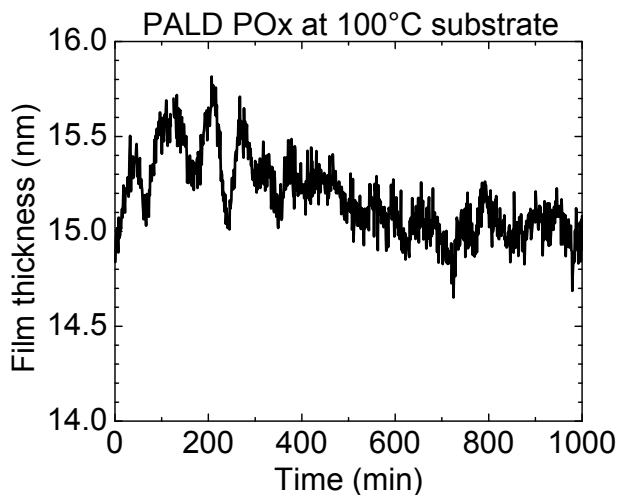




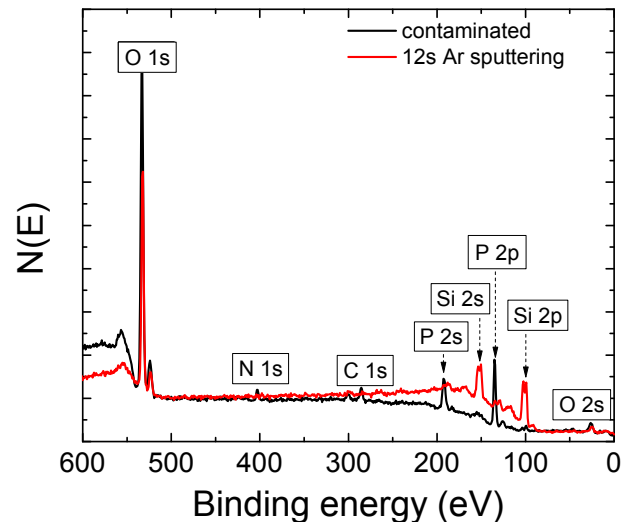
(a) Position of samples on the carrier wafer



(b) PO<sub>x</sub> film growth depending on deposition temperature



(c) Time dependent ellipsometric measurements of PO<sub>x</sub> film



(d) XPS of PALD PO<sub>x</sub> film

Figure 5.60: PO<sub>x</sub> PALD deposition from TEOP and O<sub>2</sub> plasma at different temperatures

of metaphosphate or some phosphorous acid corresponding to actual binding energy of 134 eV for P-2p.

Table 5.11: PALD cycle variation for PO<sub>x</sub> deposition at 200 °C

| PALD cycle | Maximum film thickness |
|------------|------------------------|
| 50 cycles  | 1.82 nm                |
| 400 cycles | 5.47 nm                |

For 50 cycle processes, PO<sub>x</sub> growth and range decreases with temperature (Figure 5.60b). Maximum growth is always in the middle until 200 °C when maximum is at the sides. This suggests that there may be condensation and or redeposition of byproducts at low

temperature and using higher deposition temperature may improve the uniformity of  $\text{PO}_x$  PALD film. However,  $\text{PO}_x$  PALD film deposition carried out at 200 °C (Table 5.12) shows that the growth per cycle may be quite low at this temperature because the film (phosphorous acid) decomposes and boils at 200 °C [203]. As a result,  $\text{PO}_x$  deposition did not appear to scale up properly with the number of cycles at 200 °C. One can conclude that optimal deposition temperature for conformal PALD  $\text{PO}_x$  film using triethyl phosphite and  $\text{O}_2$  plasma would be above 100 °C but less than 200 °C. One solution to increase the phosphorus concentration and film thickness with PALD cycles will be to mix  $\text{SiO}_2$  film and  $\text{PO}_x$  film in super cycles (Figure 5.61).

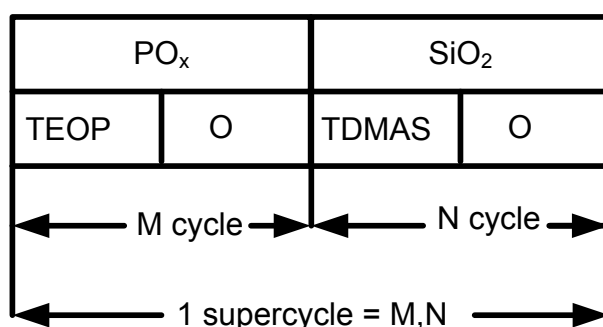


Figure 5.61: Illustration of PALD  $\text{PO}_x/\text{SiO}_2$  mixed oxide deposition

As a result, mixed  $\text{PO}_x/\text{SiO}_2$  oxide were deposited from super cycle of  $\text{PO}_x$  and  $\text{SiO}_2$  at 150 °C. Results of  $\text{PO}_x/\text{SiO}_2$  mixed oxide deposition on 150 mm Si wafer for 10 super cycles with  $M = 5$  and  $N = 1$  (see Figure 5.61) is shown in Figure 5.62. Wafer maps were taken by fitting the deposited film and  $\text{SiO}_2$  interface as a single layer.

Normally, pure  $\text{SiO}_2$  deposition would give about 0.74 nm film thickness for 10 cycles. The total film thickness obtained for  $\text{PO}_x/\text{SiO}_2$  mixed oxide and  $\text{SiO}_2$  native oxide was about 3.5 nm for 10 super cycles. Which means,  $\text{PO}_x/\text{SiO}_2$  mixed oxide thickness will be approximately 1.8 nm assuming 1.7 nm native  $\text{SiO}_2$ . Therefore, phosphorus was indeed incorporated into the  $\text{SiO}_2$  layer since the total  $\text{PO}_x/\text{SiO}_2$  mixed oxide thickness for 10 super cycles was greater than pure  $\text{SiO}_2$  film thickness for 10 cycles.  $\text{PO}_x/\text{SiO}_2$  mixed oxide deposition non-uniformity on 150 mm Si wafer was about 3 %. The ellipsometric measurements of uncapped and  $\text{SiO}_2$  capped  $\text{PO}_x/\text{SiO}_2$  mixed oxide film is shown in Figure 5.63. Increase and fluctuation of film thickness in air was observed for both capped and uncapped  $\text{PO}_x/\text{SiO}_2$  layer. In addition, one can also observe a fluctuation in mean squared error for the fit together with the film thickness, which shows that the film properties might also be changing in air. The capped film shows a slow and delayed thickness increase compared to the uncapped layer. The  $\text{PO}_x/\text{SiO}_2$  layer seems very sensitive to moisture even under thick  $\text{SiO}_2$  capping. The  $\text{PO}_x/\text{SiO}_2$  film itself did not evaporate in air but shows a rapid sensitivity to moisture. Moisture sensitivity may not be a limiting factor for the application of  $\text{PO}_x/\text{SiO}_2$  layer as a dopant source since the P dopant itself did not evaporate in air. In addition, results of ellipsometric measurements for layers in Figure

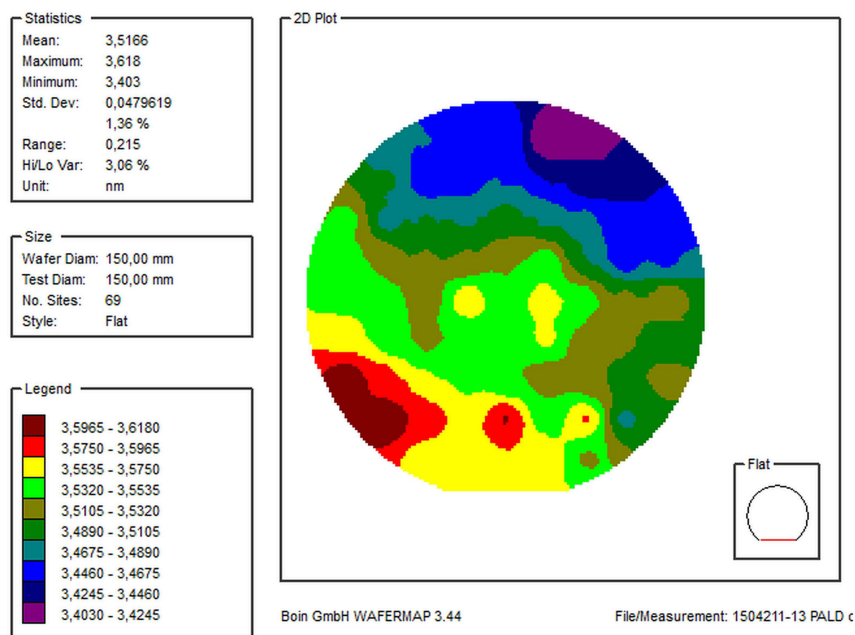


Figure 5.62: Deposition of  $\text{PO}_x/\text{SiO}_2$  mixed oxide by PALD:

$\text{O}_2$  flow into plasma head: 250 sccm, TEOP (pulse/purge): 50 ms / 10 s, TDMAS (pulse/purge): 80 ms / 10 s,  $\text{O}_2$  plasma (pulse/purge): 15 / 10 s, Number of PALD super cycles: 10 with (M=5,N=1), Substrate temperature: 150 °C,  $\text{N}_2$  purge: 100 sccm, TDMAS bottle: room temp (heated up to 33 °C from lines), TEOP bottle: 50 °C, TDMAS line, TEOP line and chamber walls: 120 °C

5.64 shows that  $\text{PO}_x/\text{SiO}_2$  layer capped with  $\text{Sb}_2\text{O}_5$  layer of about 7 nm could possibly stabilize the  $\text{PO}_x/\text{SiO}_2$  layer for about 1 day. The  $\text{Sb}_2\text{O}_5$  capping were prepared ex-situ after  $\text{PO}_x/\text{SiO}_2$  layer deposition.  $\text{Sb}_2\text{O}_5$  capping of  $\text{PO}_x/\text{SiO}_2$  layer (Figure 5.64) seems to be quite effective in comparison to  $\text{SiO}_2$  capping (Figure 5.63). Therefore,  $\text{Sb}_2\text{O}_5$  layer may be used to protect  $\text{PO}_x/\text{SiO}_2$  layer for long time handling in air. In addition, Sb and P will give doping of the same type (n) in Si or Ge, which may additionally increase the n-type doping level.

The variation of PALD super cycles for  $\text{PO}_x/\text{SiO}_2$  deposition is shown in Table 5.12. Clearly, the film thickness increases as the number of PALD super cycles is increased. One can also increase the phosphorus contents by increasing the number of  $\text{PO}_x$  sub-cycles, that is increasing M, (see Figure 5.61).

Figure 5.65 shows the cross section of a film stack after the deposition of  $\text{PO}_x/\text{SiO}_2$  mixed oxide film capped with in-situ  $\text{SiO}_2$  film at 150 °C on BHF cleaned patterned Si high aspect ratio structure. Highly conformal film deposition was obtained on the structures with aspect ratio of 6. EDX signals reveals conformal P deposition inside the trenches with no carbon contamination in the film. Carbon was only found on the surface of the Si trenches which could be from organic absorption during TEM preparation. Conformal deposition of P in the trenches will allow uniform n-type doping of Si from P diffusion.

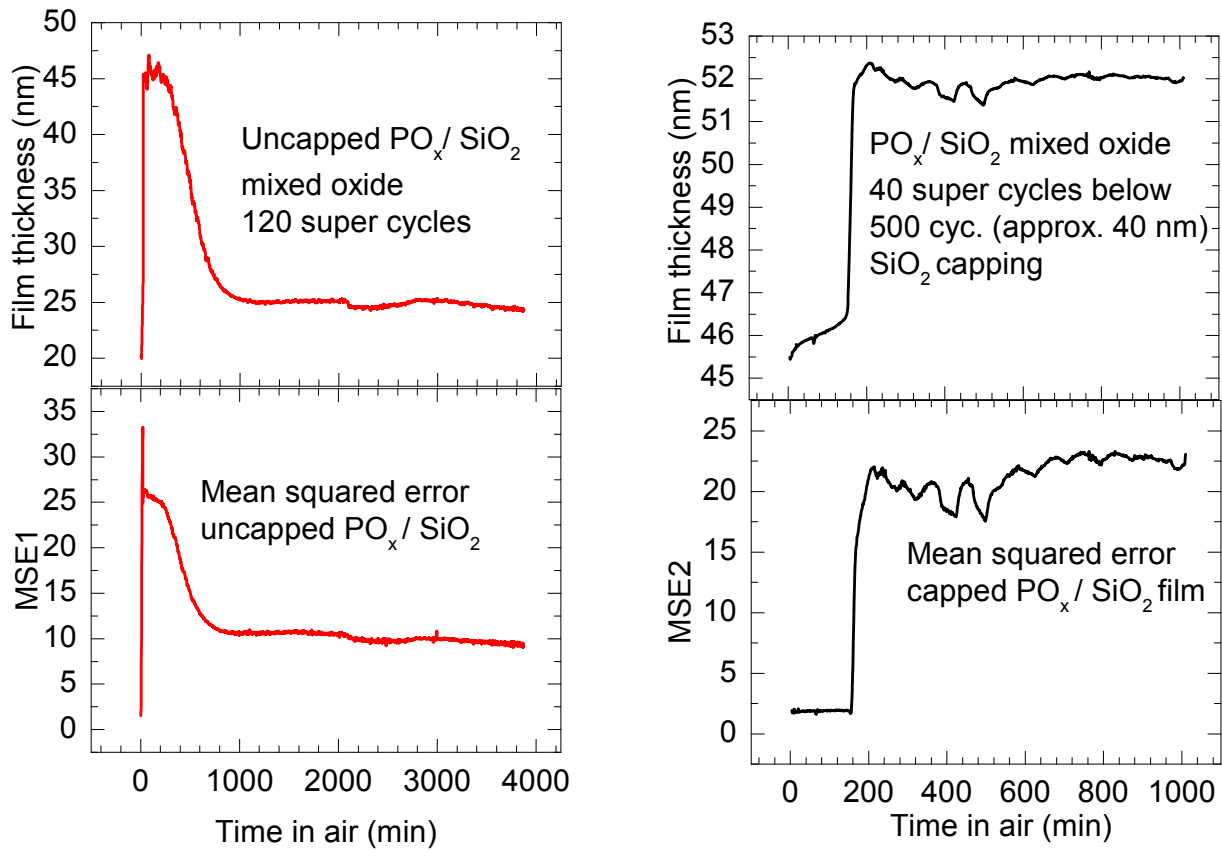


Figure 5.63: Stability of uncapped  $\text{PO}_x/\text{SiO}_2$  mixed oxide film compared with  $\text{PO}_x/\text{SiO}_2$  capped with  $\text{SiO}_2$  layer in-situ

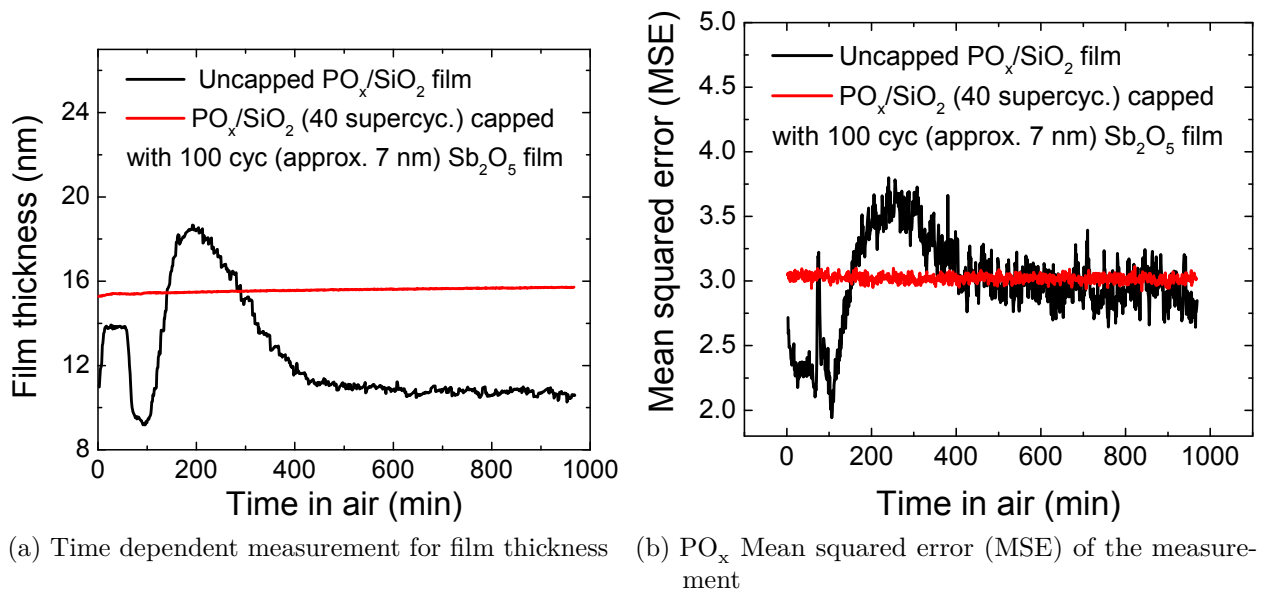


Figure 5.64: Stability of uncapped  $\text{PO}_x/\text{SiO}_2$  mixed oxide film compared with  $\text{PO}_x/\text{SiO}_2$  capped with  $\text{Sb}_2\text{O}_5$  layer ex-situ

Results of TEM cross section of a film stack after the deposition of  $\text{PO}_x/\text{SiO}_2$  mixed oxide film at  $150^\circ\text{C}$  capped ex-situ with 100 cycles PALD  $\text{Sb}_2\text{O}_5$  film at  $100^\circ\text{C}$  on BHF cleaned

Table 5.12: PALD super cycle variation for  $\text{PO}_x/\text{SiO}_2$  ( $M=5, N=1$ ) mixed oxide deposition at  $150^\circ\text{C}$

| Sample number | Super cycle<br>( $M=5, N=1$ ) | Total film thickness<br>+ $\text{SiO}_2$ interface | $\text{SiO}_2$ interface | Estimated $\text{PO}_x/\text{SiO}_2$<br>thickness |
|---------------|-------------------------------|--|--------------------------|---|
| 1504211-W13   | 10 super cycles               | 3.5 nm   | 1.7 nm                   | 1.8 nm  |
| MLY146-20-s48 | 40 super cycles               | 9.95 nm  | 2 nm                     | 7.95 nm   |
| MLY146-20-s50 | 80 super cycles               | 15.69 nm   | 2 nm                     | 13.69 nm  |
| MLY146-20-s52 | 120 super cycles              | 20.1 nm  | 2 nm                     | 18.1 nm   |
|               | ( $M=10, N=1$ )               |  |                          |   |
| SLZ007-1-s35  | 40 super cycles               | 19.2 nm  | 2 nm                     | 17.2 nm   |

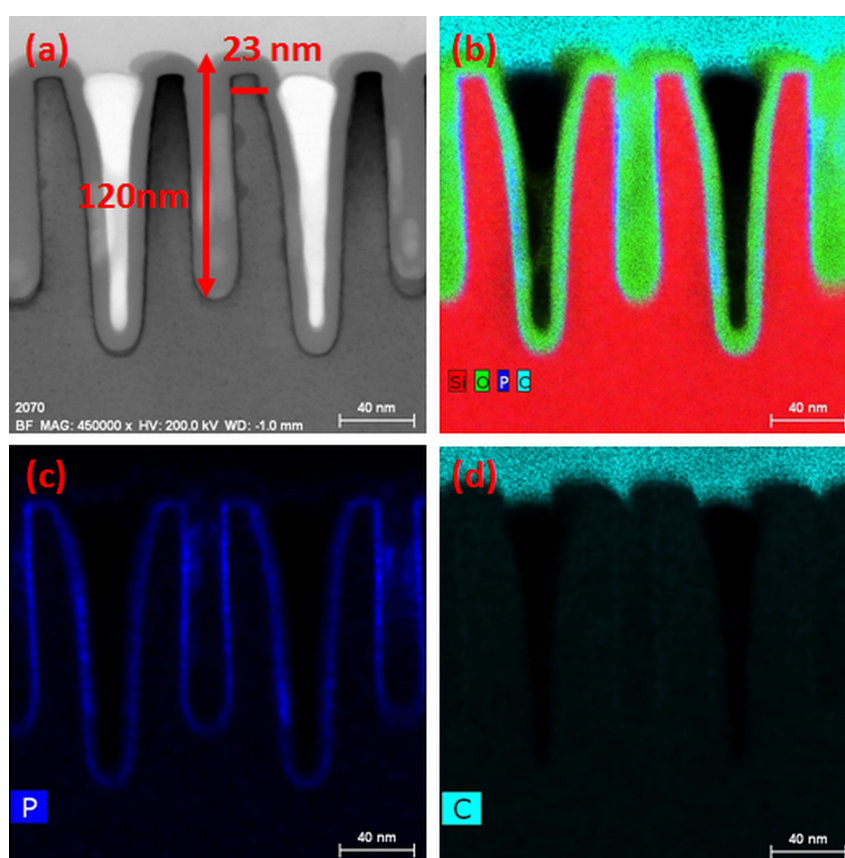


Figure 5.65: TEM / EDX results after deposition of  $\text{PO}_x/\text{SiO}_2$  mixed oxide film (20 super cycles, ( $M=5, N=1$ )) capped with in-situ  $\text{SiO}_2$  film (100 cycles) at  $150^\circ\text{C}$  on BHF cleaned patterned Si high aspect ratio structure. (a) TEM image (b) EDX showing Si, O, P and C (c) EDX showing P (d) EDX showing C

patterned Si high aspect ratio structure are shown in Figure 5.66. A dark film region (Figure 5.66a) can be seen on top of bright film region in the stack, which indicate  $\text{Sb}_2\text{O}_5$  film on top of  $\text{PO}_x/\text{SiO}_2$  mixed oxide film. Si, O, P, C, N and Sb can be detected from the EDX signal (Figure 5.66b). C contamination was mostly found on the surface. Little N contamination detected could be from the unremoved silicon precursor ligand in this

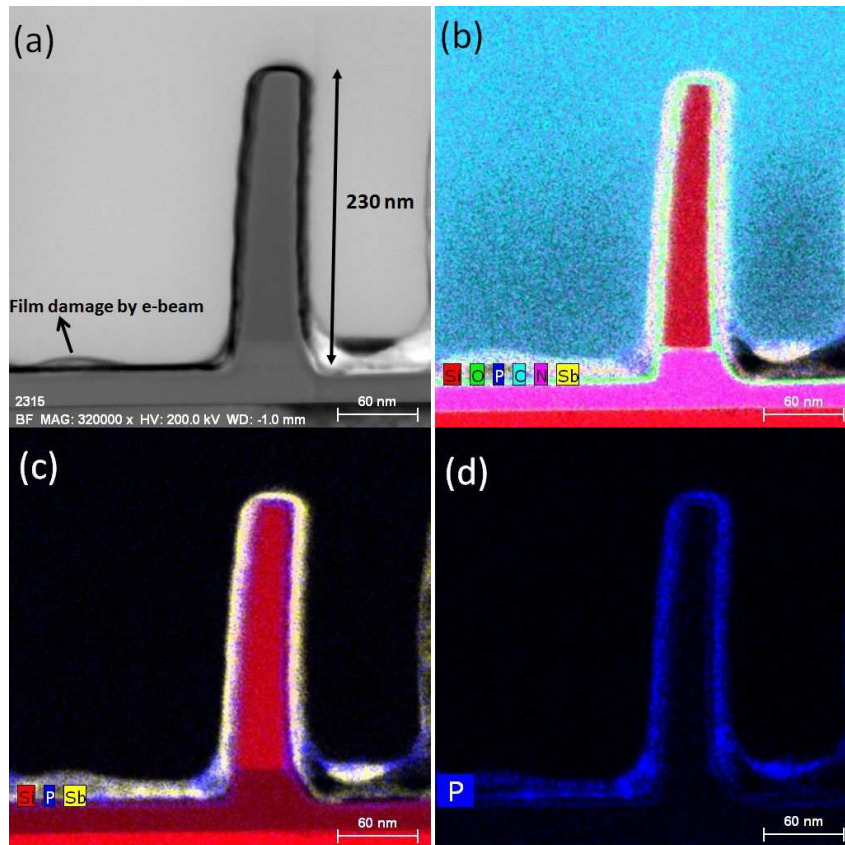


Figure 5.66: TEM / EDX results after deposition of  $\text{PO}_x/\text{SiO}_2$  mixed oxide film (40 super cycles,  $(M=5, N=1)$ ) at  $150^\circ\text{C}$  capped ex-situ with  $\text{Sb}_2\text{O}_5$  film (100 cycles) at  $100^\circ\text{C}$  on BHF cleaned patterned Si high aspect ratio structure. (a) TEM image (b) EDX showing Si, O, P, C, N and Sb (c) EDX showing Si, P and Sb (d) EDX showing P

case. In addition, EDX signal (Figure 5.66c) reveals Sb on top of P. The film can be easily damaged by electron beam bombardment and the image quality degrades after repeated TEM measurements on same spot. P deposition in the trench structure (Figure 5.66d) (aspect ratio of approximately 6) was also conformal.

## 5.4 Doping from PALD source layer

Doping of silicon and germanium can be achieved through diffusion of dopants from solid phase atomic layer pre-deposited source layer. As illustrated in Figure 5.67, dopant layers such as oxides of boron, antimony and phosphorus are deposited on top of silicon or germanium substrates and, then, these dopants can diffuse into the crystal lattice through thermal processing techniques such as rapid thermal annealing (RTA), flash lamp annealing (FLA) or laser annealing (LA).

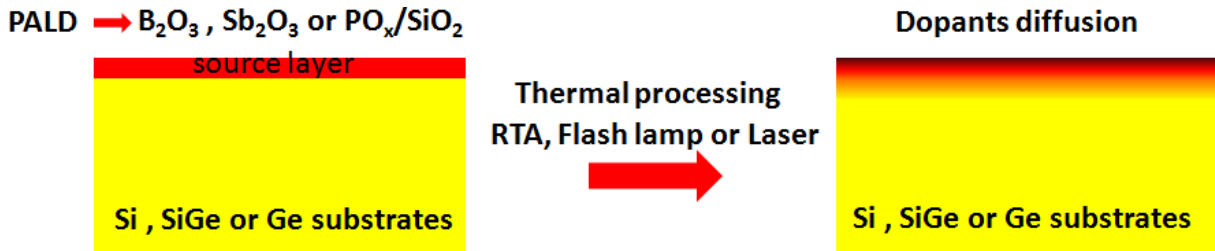
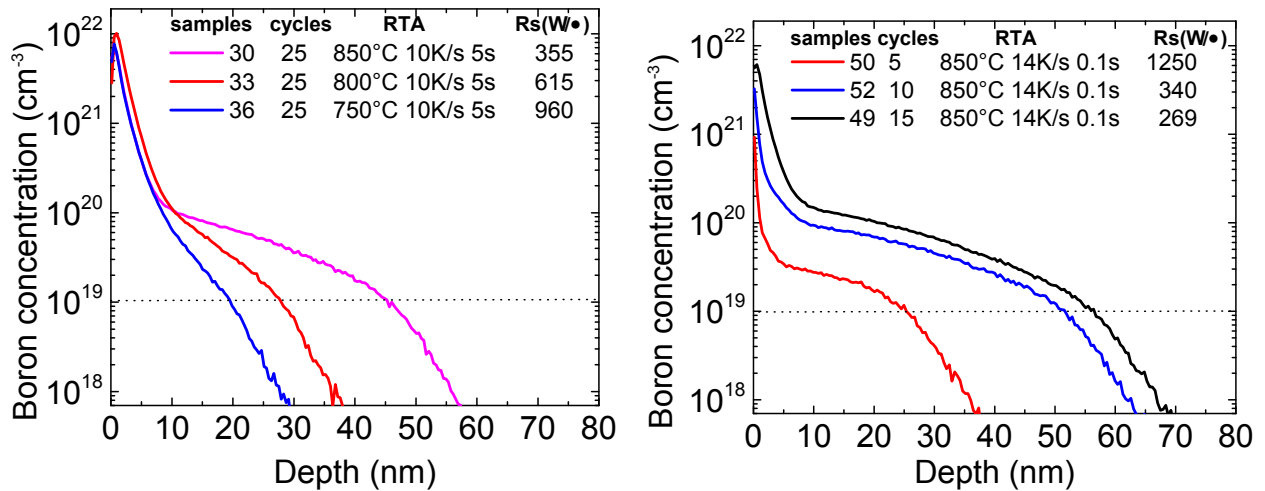


Figure 5.67: Illustration of diffusion doping process from PALD source layers

### 5.4.1 Silicon (Si) doping

#### $B_2O_3$ source layer without capping



(a) Samples with the same ( $\approx 3.3$  nm)  $B_2O_3$  layer thickness but different RTA conditions

(b) Samples with the same RTA conditions but different PALD  $B_2O_3$  layer thickness

Figure 5.68: SIMS measured boron concentration profiles in silicon of different samples with PALD  $B_2O_3$  source layers after rapid thermal annealing (RTA) treatments

Figure 5.68 shows result of boron diffusion into silicon lattice from PALD  $B_2O_3$  source layer deposited at room temperature after rapid thermal annealing process. In this case, the RTA system and PALD system were in a cluster tool, hence the samples were directly transferred from PALD system to RTA system, that is the  $B_2O_3$  layers were not exposed to

ambient air. There is an increase in diffusion of boron in Si samples with same  $B_2O_3$  source layer thickness, as the maximum annealing temperature is increased (Figure 5.68a with ramp rate of 10 K/s and hold time 5 s). Diffusion of boron into silicon also increases as the  $B_2O_3$  source layer thickness increases up to about saturation at same annealing conditions (Figure 5.68b with 14 K/s ramp, 0.1s hold time and 850 °C maximum temperature).

### $B_2O_3$ source layer with $Sb_2O_5$ capping

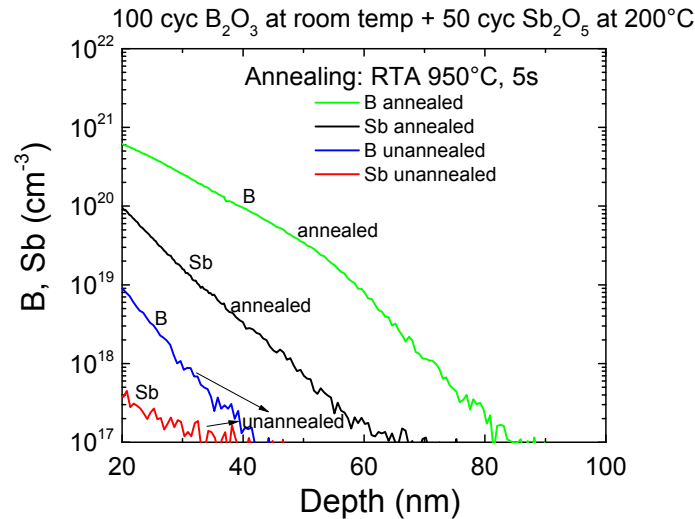


Figure 5.69: Comparison of SIMS measured B and Sb profiles in silicon for rapid thermal annealed and unannealed samples with same thickness of PALD  $B_2O_3$  capped with  $Sb_2O_5$  source layers

Figure 5.69 shows result of boron (B) and antimony (Sb) diffusion into silicon (Si) lattice from PALD  $B_2O_3$  deposited at room temperature capped with 50 cycles  $Sb_2O_5$  deposited at 200 °C. The RTA system was not in a cluster tool with the PALD system in this case, and the samples were shipped to the location of the annealing experiments. The SIMS profile (Figure 5.69) of B and Sb in Si for annealed and unannealed samples shows that, both B and Sb, diffused inside Si after RTA treatments. Sb diffusion may have been promoted by B diffusion after RTA. Comparison of SIMS profiles (Figure 5.70) of samples with only PALD  $Sb_2O_5$  source layer with samples of PALD  $B_2O_3$  capped with  $Sb_2O_5$  after the same flash annealing treatment shows that Sb diffusion is lower with pure  $Sb_2O_5$  source, which implies that Sb diffusion may be enhanced when co-doped with another dopant. The B signal found in the SIMS profile (Figure 5.70) for pure  $Sb_2O_5$  source layer is the background (p-type) B doping. In addition, the B signal is lower than Sb signal in the SIMS profile, after flash annealing of samples with 100 cycles  $B_2O_3$  capped with 50 cycles  $Sb_2O_5$  in Figure 5.70 because of low  $B_2O_3$  deposition at high temperature (100 °C).

It may be beneficial to grow  $B_2O_3$  layer and  $Sb_2O_5$  capping at the same temperature, however it is necessary to grow  $B_2O_3$  at room temperature to obtain the highest growth per cycle and possibly deposit the capping material at room temperature.  $SiN_x$  was reported



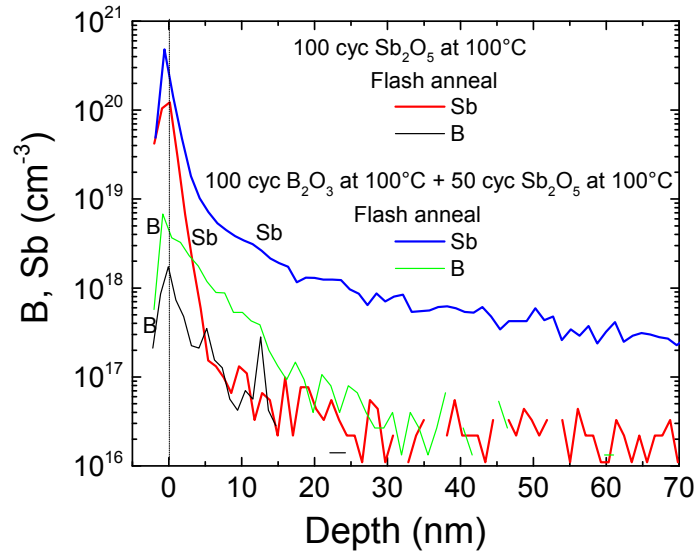


Figure 5.70: Comparison of SIMS measured B and Sb profiles in silicon for sample with only PALD  $\text{Sb}_2\text{O}_5$  source layer and sample with PALD  $\text{B}_2\text{O}_3$  capped with  $\text{Sb}_2\text{O}_5$  source layer after same flash annealing conditions

to grow at room temperature by plasma-assisted ALD [204], which can as well be used for PALD  $\text{B}_2\text{O}_3$  capping in future work.

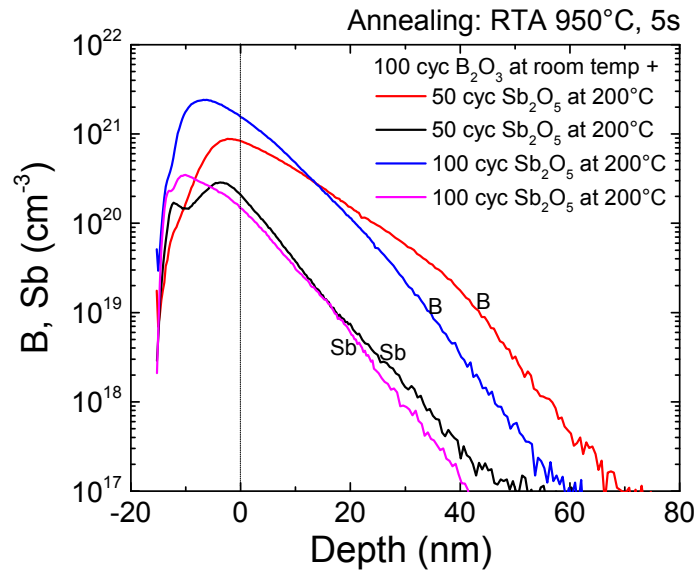


Figure 5.71: Comparison of SIMS measured B and Sb profiles in silicon for samples with same PALD  $\text{B}_2\text{O}_3$  thickness but different PALD  $\text{Sb}_2\text{O}_5$  capping (50 cycles and 100 cycles capping) after same rapid thermal annealing conditions

SIMS profiles of B and Sb in Si after rapid thermal annealing of samples of about same  $\text{B}_2\text{O}_3$  source thickness but different  $\text{Sb}_2\text{O}_5$  capping cycles (Figure 5.71) show that there was slightly higher  $\text{B}_2\text{O}_3$  source left close to the Si surface under thicker (100 cycles)  $\text{Sb}_2\text{O}_5$  capping. However, diffusion of B was slightly deeper for samples with thinner (50 cycles)  $\text{Sb}_2\text{O}_5$  capping. The junction depth in Figure 5.71 at the level of  $5 \times 10^{18} \text{ cm}^{-3}$  is

approximately 40 nm for 100 cycles capping and 50 nm for 50 cycles capping.

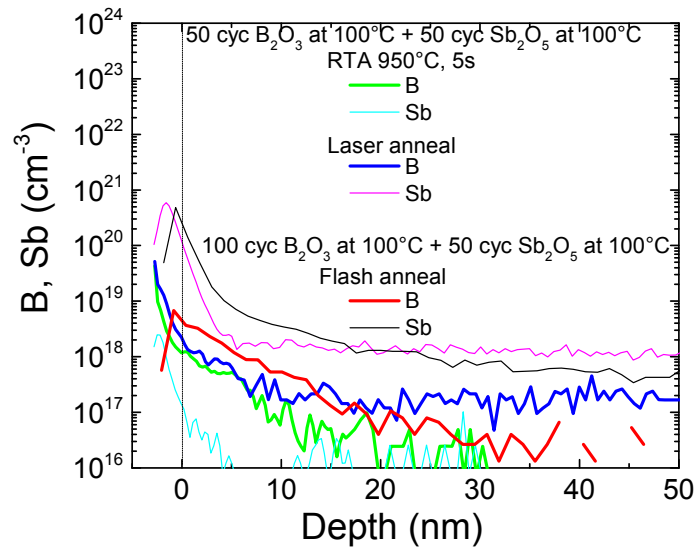


Figure 5.72: Comparison of SIMS measured B and Sb profiles in silicon for samples with different types of annealing treatment

The B dopant profile in Si for samples with different types of annealing treatment (RTA, flash and laser annealing) (Figure 5.72) is approximately identical (less than 20 nm junction depth), possibly because  $B_2O_3$  source is too low due to higher deposition temperature (100 °C) of  $B_2O_3$ . It can be observed that the Sb level was higher for samples that were treated with laser anneal or flash anneal which could possibly mean that Sb diffusion is also enhanced by ultra-short high-temperature annealing.

### Phosphorus containing source layer

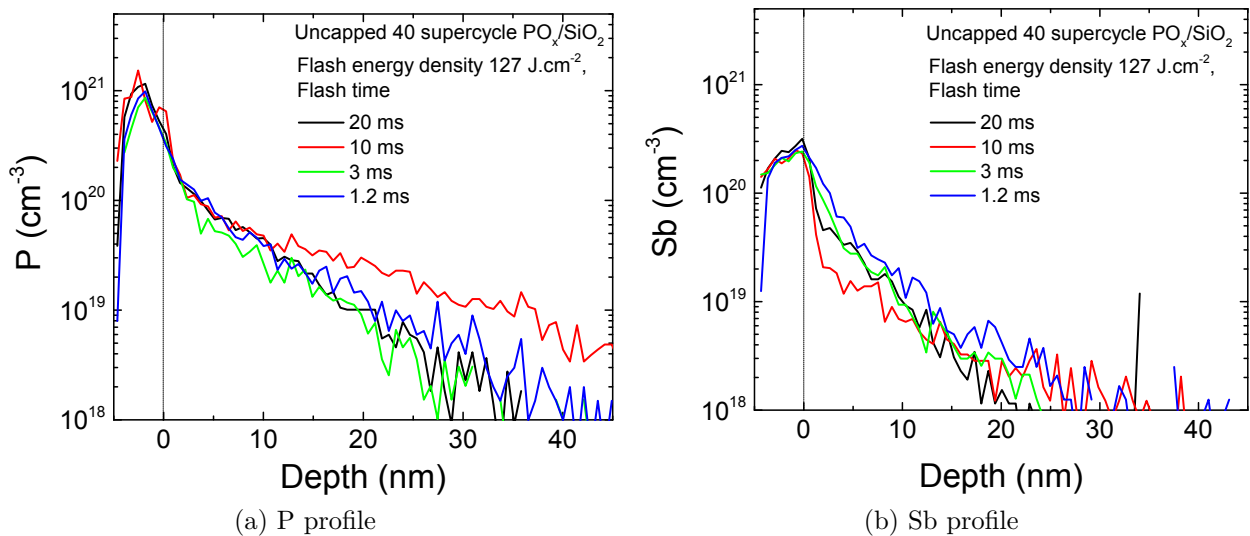


Figure 5.73: Comparison of SIMS measured P and Sb profiles in Si for uncapped  $PO_x/SiO_2$  source layers after varying flash anneal treatment time

SIMS profiles of phosphorus (P) diffusion into Si from uncapped  $\text{PO}_x/\text{SiO}_2$  source layer after several flash annealing variations are shown in Figures 5.73, 5.74 and 5.75. It can be observed that there was also Sb diffusion in all the annealed samples without Sb source which is due to cross contamination in the flash tool. The SIMS results appear to be almost the same for diffusion of P from uncapped  $\text{PO}_x/\text{SiO}_2$  source after variation in flash time (Figure 5.73), flash energy density (Figure 5.74) and flash pre-heat temperature (Figure 5.75).

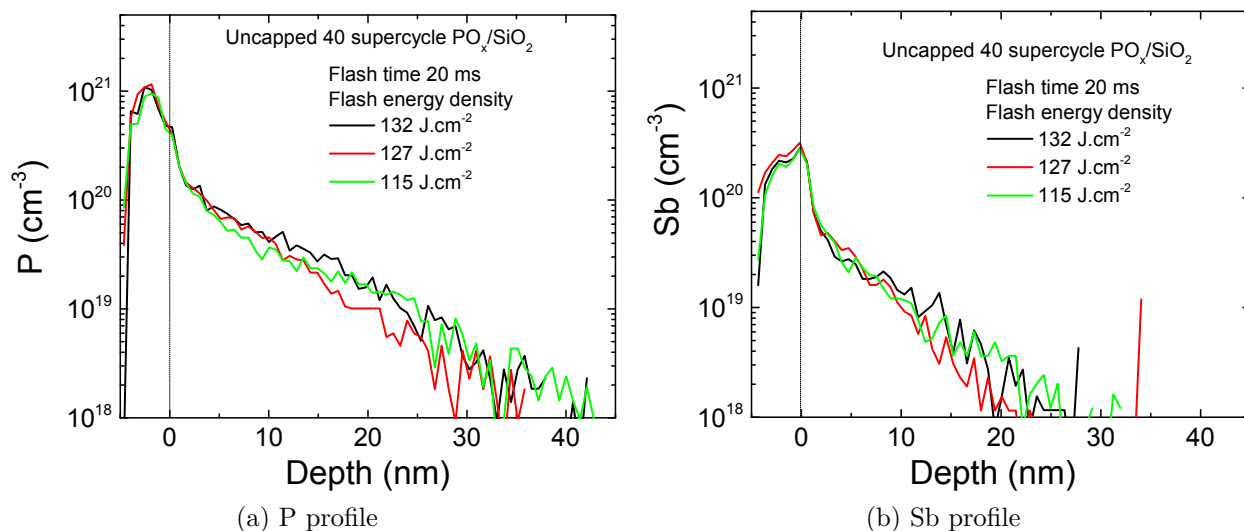


Figure 5.74: Comparison of SIMS measured P and Sb profiles in Si for uncapped  $\text{PO}_x/\text{SiO}_2$  source layer after varying flash anneal energy density

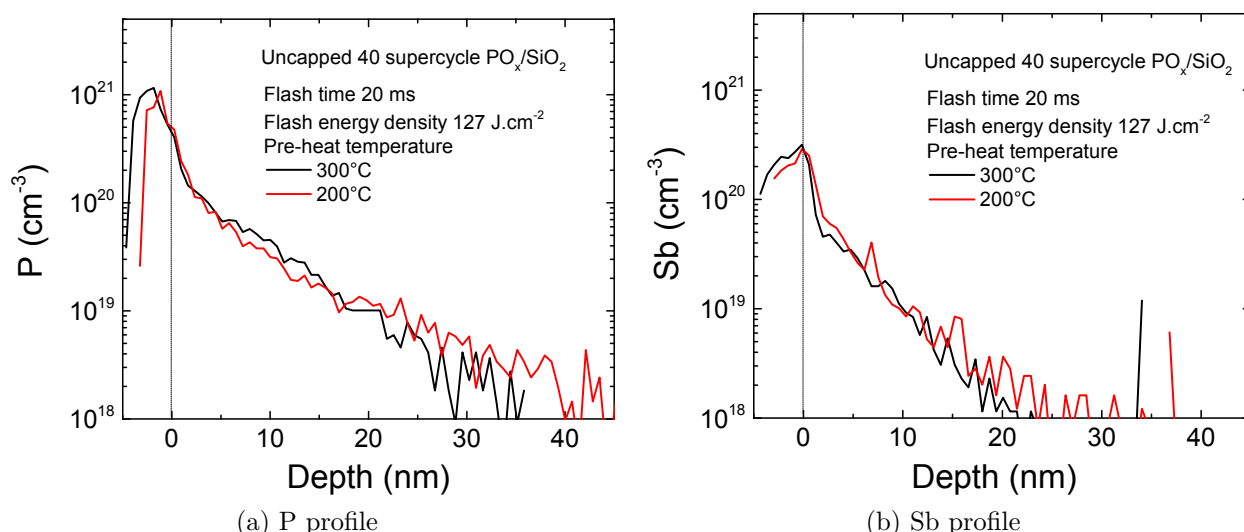


Figure 5.75: Comparison of SIMS measured P and Sb profiles in Si for uncapped  $\text{PO}_x/\text{SiO}_2$  source layer after varying flash anneal pre-heat temperature

All the samples were packaged and shipped to the location of the flash experiments, however the uncapped  $\text{PO}_x/\text{SiO}_2$  source is still quite sensitive to moisture as already shown

in Figure 5.64. As a result, the  $\text{PO}_x/\text{SiO}_2$  source may not be reproducible for long time handling in air and will need  $\text{Sb}_2\text{O}_5$  capping to keep the phosphorus source constant for the flash variations. This gives an explanation to almost the same SIMS profiles obtained for all the flash variations for diffusion from uncapped  $\text{PO}_x/\text{SiO}_2$  sources.

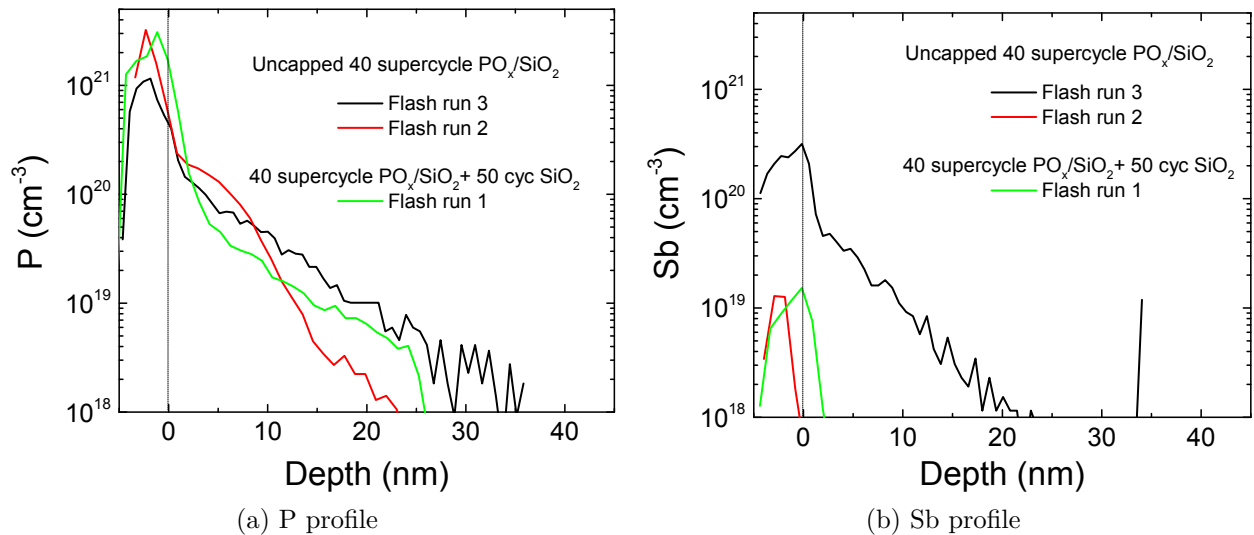


Figure 5.76: Comparison of SIMS measured P and Sb profiles in Si for uncapped  $\text{PO}_x/\text{SiO}_2$  and  $\text{SiO}_2$  capped  $\text{PO}_x/\text{SiO}_2$  source layer after increasing flash anneal runs

There was always Sb contamination detected in the SIMS profile even without Sb source, and one would notice a remarkable increase in Sb level (Figure 5.76) as the number of flash runs increases. There were annealings of some other samples with  $\text{Sb}_2\text{O}_5$  layer which are considered to be the source of Sb contamination in the flash tool. Therefore, Sb diffusion level in Si increased as the number of flash runs was increased for the uncapped  $\text{PO}_x/\text{SiO}_2$  source layer.

Moreover, SIMS profile result after same the flash annealing condition of Si samples having  $\text{PO}_x/\text{SiO}_2$  source layer capped with different material layers is shown in Figure 5.77. It can be observed that  $\text{SiO}_2$  capping for  $\text{PO}_x/\text{SiO}_2$  source is also ineffective, since the diffusion profile of P in Si appears close to that of the uncapped  $\text{PO}_x/\text{SiO}_2$  source. However, there is a higher P concentration in the bulk of Si as well as close to the Si surface for  $\text{PO}_x/\text{SiO}_2$  source capped with a  $\text{Sb}_2\text{O}_5$  layer, which means  $\text{Sb}_2\text{O}_5$  capping for  $\text{PO}_x/\text{SiO}_2$  is the most effective; this also correlates to the result of ellipsometric measurements shown in Figure 5.64.

SIMS results after flash anneal of Si having  $\text{PO}_x/\text{SiO}_2$  (40 super cycles) capped with  $\text{Sb}_2\text{O}_5$  (100 cycles) source layer are shown in Figure 5.78. One would strikingly observe the possibility of co-diffusion of Sb and P in Si, especially with 20 ms flash time as it was also obtained earlier with B promoting Sb diffusion in Si. It can possibly be concluded here that P promotes Sb diffusion in Si and vice versa, which means they may actually be co-diffusing and promoting each other. Sb and P belong to the same n-type dopant

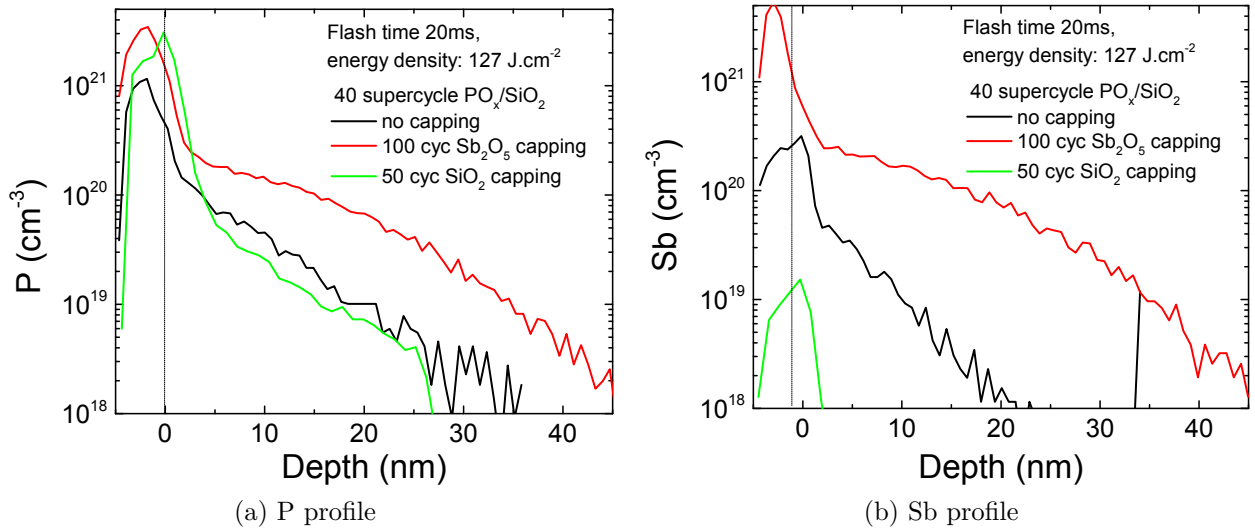


Figure 5.77: Comparison of SIMS measured P and Sb profiles in Si for  $\text{PO}_x/\text{SiO}_2$  source layer capped with different material layers after similar flash anneal treatment

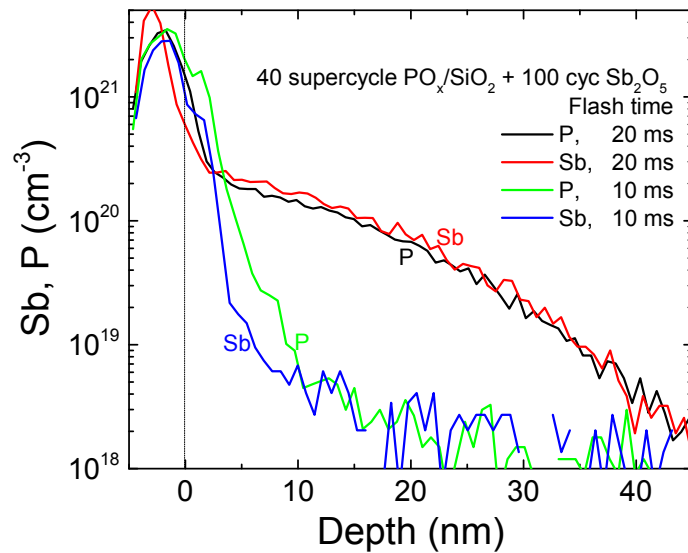


Figure 5.78: Comparison of SIMS measured P and Sb profiles in Si for  $\text{PO}_x/\text{SiO}_2$  capped with  $\text{Sb}_2\text{O}_5$  source layer after 10 ms and 20 ms flash times

class and this can possibly boost n-type doping suppose both P and Sb are activated in Si. However, investigation of Sb and P dopants activation in Si will be required in future work. Moreover, one can clearly see a decreased diffusion of P and Sb with shorter (10 ms) flash time in this case (Figure 5.78) and with the possibility to tune the junction depth below 10 nm.

## 5.4.2 Germanium (Ge) doping

### Phosphorus containing source layer

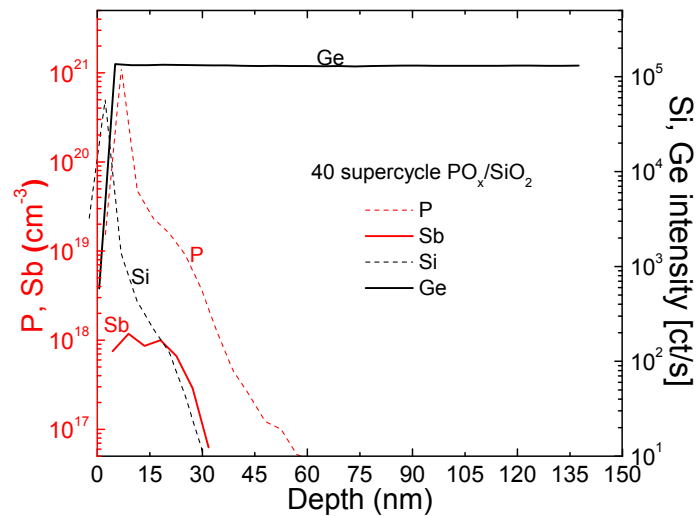


Figure 5.79: SIMS profile in epitaxial Ge ( $1\mu\text{m}$ ) for uncapped  $\text{PO}_x/\text{SiO}_2$  source layer after flash anneal

The P depth close to the surface in the diffusion profile (Figure 5.79) of P in Ge from uncapped  $\text{PO}_x/\text{SiO}_2$  source layer is similar to P diffusion in Si from uncapped  $\text{PO}_x/\text{SiO}_2$  source layer.  $\text{PO}_x/\text{SiO}_2$  may also be suitable as source layer for P doping in Ge.

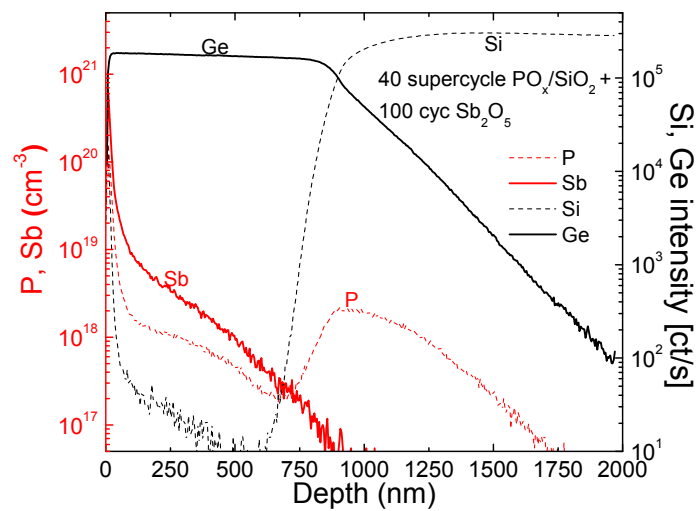


Figure 5.80: SIMS profile in epitaxial Ge ( $1\mu\text{m}$ ) for  $\text{PO}_x/\text{SiO}_2$  capped with  $\text{Sb}_2\text{O}_5$  source layer after flash anneal

Besides, there is deep diffusion of P and Sb in Ge (Figure 5.80) after flash anneal from  $\text{PO}_x/\text{SiO}_2$  capped with  $\text{Sb}_2\text{O}_5$  source layer. Sb could also diffuse in Ge which might have enhanced P diffusion in Ge. The flash parameters were same for the SIMS profiles in Figures 5.79, 5.80 and, 5.81. N-type doping level may be increased from Sb and P co-diffusion in Ge when both Sb and P are activated after diffusion in Ge. A shorter flash

time can be used to obtain a shallow junction when  $\text{PO}_x/\text{SiO}_2$  capped with  $\text{Sb}_2\text{O}_5$  is used as source layer for Ge.

### $\text{Sb}_2\text{O}_5$ source layer

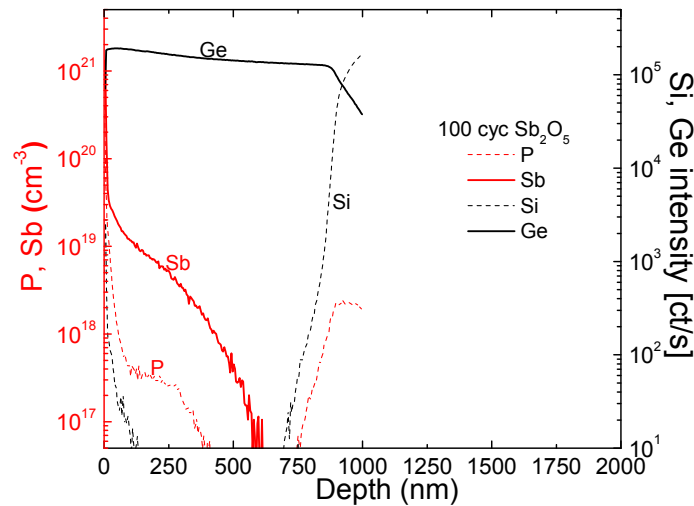


Figure 5.81: SIMS profile in epitaxial Ge ( $1\mu\text{m}$ ) for  $\text{Sb}_2\text{O}_5$  source layer after flash anneal

Diffusion of Sb in Ge seems feasible after flash anneal of  $\text{Sb}_2\text{O}_5$  source layer (Figure 5.81). There is also a phosphorus cross contamination in the SIMS profile (Figure 5.81), but Sb diffusion profile appears gaussian-like and less deep in Ge compared to Sb and P co-diffusion with higher phosphorus content (Figure 5.80) in the source layer.  $\text{Sb}_2\text{O}_5$  film alone may be suitable as source layer for Ge.

## 5.4.3 Silicon-Germanium (Si-Ge) doping

### Phosphorus containing source layer

Diffusion of P in SiGe matrix from uncapped  $\text{PO}_x/\text{SiO}_2$  source layer was obtained after flash anneal (Figure 5.82).  $\text{PO}_x/\text{SiO}_2$  source layer can be used for SiGe doping.

Co-diffusion of P and Sb and deep profile (Figure 5.83) was obtained in SiGe after flash anneal of  $\text{PO}_x/\text{SiO}_2$  capped with  $\text{Sb}_2\text{O}_5$  source layer.  $\text{PO}_x/\text{SiO}_2$  capped with  $\text{Sb}_2\text{O}_5$  source layer may also be used for SiGe n-type doping, but the flash conditions should be controlled to obtain shallow junctions.

### $\text{Sb}_2\text{O}_5$ source layer

There is limited diffusion of Sb in SiGe from  $\text{Sb}_2\text{O}_5$  source layer after flash anneal (Figure 5.84).

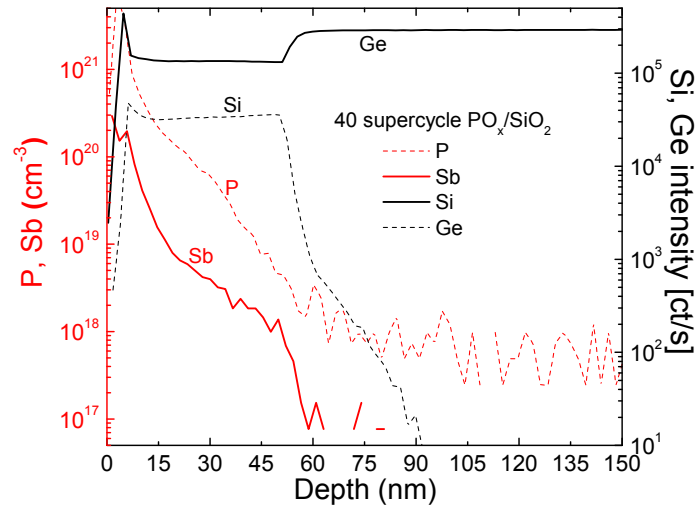


Figure 5.82: SIMS profile in epitaxial SiGe (50 nm) for uncapped  $\text{PO}_x/\text{SiO}_2$  source layer after flash anneal

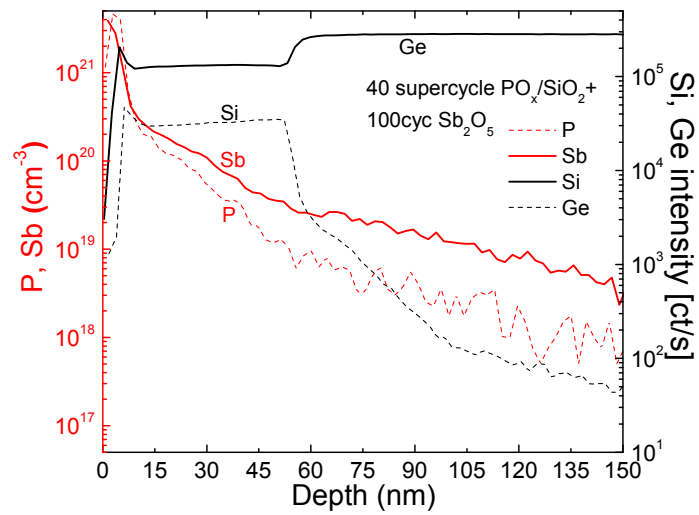


Figure 5.83: SIMS profile in epitaxial SiGe (50 nm) for  $\text{PO}_x/\text{SiO}_2$  capped with  $\text{Sb}_2\text{O}_5$  source layer after flash anneal

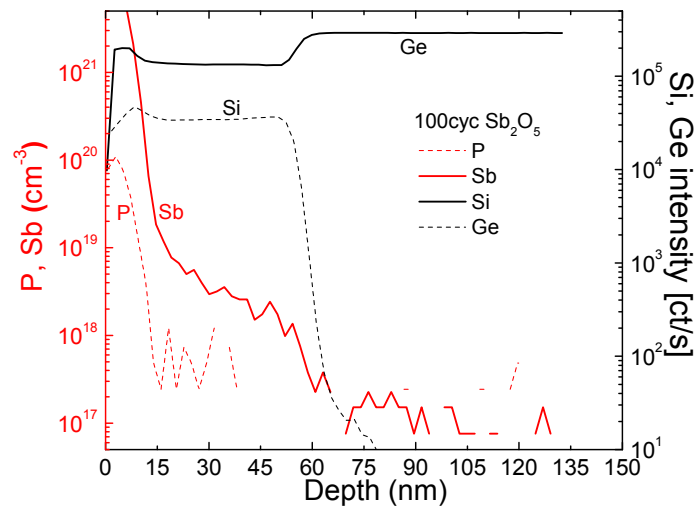


Figure 5.84: SIMS profile in epitaxial SiGe (50 nm) for  $\text{Sb}_2\text{O}_5$  source layer after flash anneal



# Conclusion and Future Prospects

## 6.1 Summary and conclusion

Plasma-assisted atomic layer deposition is a viable method for highly conformal thin film deposition especially on three-dimensional structures. Silver is a future interconnect material in integrated circuits. In addition, fabrication of oxide dopants by atomic layer deposition can help to produce ultra-shallow junctions which will pave way to production of advanced transistors such as FinFETs. The following conclusions can be made from various sections of the experiments:

### 6.1.1 Plasma monitoring

Silver coated wafer can be used to monitor distribution of plasma radicals which may help in hardware optimization of the plasma source. A valve between the plasma source and the chamber may be required for metal ALD process to prevent contamination of the plasma source.

### 6.1.2 Silver layers plasma-assisted ALD

Pure silver films were obtained with low carbon and oxygen contamination at 120 °C and 200 °C using the improved inductively coupled plasma (ICP) source. The deposited Ag PALD layers were polycrystalline cubic. The Ag precursor and its reaction products were less volatile and needed higher wall temperatures for efficient purge. For better Ag conductivity, deposition temperature should be high enough that the hydrogen plasma completely removes the Ag precursor ligand. More than 3000 PALD cycles were needed to obtain a resistivity of  $5.7 \mu\Omega \cdot \text{cm}$  for 97 nm Ag layer at 120 °C deposition temperature. In this work, high surface energies metal substrates such as nickel, cobalt and titanium have been shown to be good adhesion layers for the deposition of Ag films by plasma-assisted ALD. Tungsten substrate on the other hand appears to be a poor adhesion layer for Ag deposition by plasma-assisted ALD, possibly due to low surface energy of native oxide of tungsten. Besides, Ag PVD layers were more conductive and smoother in comparison to the Ag PALD layers. The choice of deposition method may depend on some factors such as the required film thickness, the topography and surface area of the substrate, Ag deposition by plasma-assisted ALD method is preferred on high aspect ratio structures.

### 6.1.3 Oxide dopant layers plasma-assisted ALD

- Stable antimony oxide layers ( $\text{Sb}_2\text{O}_5$ ) were deposited by plasma-assisted atomic layer deposition technique on flat and patterned silicon substrates from triethyl antimony and oxygen radicals at 100 °C growth temperature. Depositions were carried out on the HFO PALD system. Saturation behaviour was observed at 30 ms pulse time for antimony precursor, and from 5s to 7 s pulse time for oxygen radicals. A growth per cycle of approximately 0.071 nm was obtained at 100 °C deposition temperature. Uniformity of  $\text{Sb}_2\text{O}_5$  films deposited on 150 mm silicon wafer degraded as the deposition temperature was increased. In addition,  $\text{Sb}_2\text{O}_5$  film thickness increased as the growth temperature was increased. Almost 100 % step coverage was obtained for depositions of  $\text{Sb}_2\text{O}_5$  films at 100 °C on patterned silicon substrates with an aspect ratio of approximately 6:1.
- Plasma-assisted atomic layer deposition of boron oxide ( $\text{B}_2\text{O}_3$ ) films was carried out on the HFO system using tris(dimethylamino)borane as precursor and oxygen radicals as the oxidizing source. Depositions were carried out at room temperature up to 100 °C growth temperature. The deposited  $\text{B}_2\text{O}_3$  film was highly volatile in ambient air as shown in the ellipsometric measurements, and could be protected by depositing a stable film such as  $\text{Sb}_2\text{O}_5$  or  $\text{Al}_2\text{O}_3$  on top of it.  $\text{Sb}_2\text{O}_5$  or  $\text{Al}_2\text{O}_3$  film of sufficient thickness can protect volatile  $\text{B}_2\text{O}_3$  layers in ambient air. Clear saturation behaviour was observed at room growth temperature for boron precursor at 30 ms pulse time, as well as between 10 s to 15 s pulse time for oxygen radicals. However, at 100 °C growth temperature, the film thickness decreased slightly as the boron precursor pulse and oxygen radical pulse times were increased. In addition,  $\text{B}_2\text{O}_3$  film thickness decreased as the deposition temperature was increased. An estimated growth per cycle of 0.13 nm was obtained at room temperature while the growth per cycle was between 0.02 nm to 0.05 nm at 100 °C growth temperature. Depositions of  $\text{B}_2\text{O}_3$  film capped with in-situ  $\text{Sb}_2\text{O}_5$  film on patterned silicon samples with a high aspect ratio of 6:1 was also conformal, but shows delamination of the underneath  $\text{B}_2\text{O}_3$  film in the SEM/TEM images.
- Plasma-assisted atomic layer deposition of silicon oxide ( $\text{SiO}_2$ ) films were carried out on the SENTECH system. The depositions were carried out at 150 °C growth temperature using tris(dimethylamino)silane as precursor and oxygen radical as the oxidizing source. Highly conformal silicon oxide (less than 1 % uniformity) was obtained on 150 mm wafer. In addition, the PALD process shows saturation at 80 ms pulse time for the silicon precursor and 10 s pulse time for oxygen radicals. An average growth per cycle of approximately 0.074 nm was obtained on 150 mm wafer at 150 °C deposition temperature.

- Oxide of phosphorus ( $\text{PO}_x$ ) was grown using triethyl phosphite and oxygen radicals. The depositions were carried out on the SENTECH system. The phosphorus oxide ( $\text{PO}_x$ ) film thickness decreased as deposition temperature was increased, while the uniformity improved with increased deposition temperature. Depositions were carried out at 150 °C growth temperature to improve the uniformity but gave low film growth. In order to increase the film thickness, a novel plasma-assisted atomic layer deposition process of phosphorus containing films from mixing of  $\text{PO}_x/\text{SiO}_2$  in supercycles was designed. Mixed oxide of  $\text{PO}_x/\text{SiO}_2$  grown on 150 mm silicon substrate gave approximately 3 % non-uniformity. In addition, the growth of  $\text{PO}_x/\text{SiO}_2$  mixed oxide on silicon high aspect ratio of about 6:1 gave almost 100 % step coverage as revealed in the TEM images. Ellipsometric measurement revealed that  $\text{PO}_x/\text{SiO}_2$  mixed oxide were sensitive to ambient air but the phosphorus content might not be lowered. Besides,  $\text{PO}_x/\text{SiO}_2$  film capped with an approximately 40 nm thick  $\text{SiO}_2$  film could be protected from ambient air only for a short time (typically for 1 hour) while capping of  $\text{PO}_x/\text{SiO}_2$  was more effective using a  $\text{Sb}_2\text{O}_5$  film. About 7 nm thick  $\text{Sb}_2\text{O}_5$  film could protect a  $\text{PO}_x/\text{SiO}_2$  layer from ambient air for at least 1 day. Sensitivity of  $\text{PO}_x/\text{SiO}_2$  film to ambient air might not be a limiting factor to its application as a dopant layer because the phosphorus content was not volatile at room temperature.

#### 6.1.4 Doping from plasma-assisted ALD source layer

- Less than 20 nm ultra-shallow junctions could be produced on silicon substrate from PALD source layer of  $\text{B}_2\text{O}_3$  and  $\text{PO}_x/\text{SiO}_2$  using appropriate flash annealing, laser annealing or rapid thermal annealing conditions.
- $\text{B}_2\text{O}_3$  source layer could be used for p-type doping on silicon substrate.
- $\text{PO}_x/\text{SiO}_2$  film could be used as source layer for n-type doping on silicon, germanium and silicon-germanium substrates.
- $\text{Sb}_2\text{O}_5$  could be used as source layer for n-type doping on silicon-germanium and germanium substrates.

## 6.2 Future work and recommendation

### 6.2.1 Silver layers plasma-assisted ALD

- In-situ ellipsometric monitoring can help in faster process optimization and should be integrated into the existing PALD systems.

- In-situ plasma-assisted atomic layer deposition of high surface energy metals such as nickel and cobalt as substrates together with silver layers may be investigated to check whether unoxidized high surface energy substrates promote smooth thin silver layer growth.
- Plasma-assisted atomic layer deposition of silver layers on wet chemical cleaned tungsten surface as substrate should be investigated to check whether complete removal of native tungsten oxide promote smooth silver growth.

### **6.2.2 Oxide dopant layers plasma-assisted ALD**

- It would be useful to grow boron oxide and suitable capping at the same deposition temperature. Boron oxide is best grown at room temperature and it would be interesting to grow a suitable capping also at room temperature. Protective cappings for boron oxide such as antimony oxide, aluminum oxide and silicon nitride may be grown by PALD preferably at room temperature.
- Phosphorus oxide may also be grown using other suitable precursors for example phosphorus precursor of alkylamide type. In addition, it may be useful to grow mixed oxides of  $\text{PO}_x/\text{SbO}_x$  by plasma-assisted ALD.

### **6.2.3 Doping from plasma-assisted ALD source layer**

Diffusion doping from plasma-assisted atomic layer deposited dopant sources on different substrates using several annealing conditions needs to be further investigated. Specifically, measurement of sheet resistances and determination of activated dopant levels (dose) from sheet resistances and SIMS profiles are necessary.

# Appendices

## A.1 Snell's law

Snell's law,

$$n_i \sin \theta_i = n \sin \theta_t \quad (7.9)$$

where  $n$  is the complex index of refraction of the sample to be measured and  $n_i$  is the index of refraction of the surrounding medium, in general case,  $n_i = 1$ , if the surrounding medium is air. Therefore,

$$\sin \theta_i = n \sin \theta_t \quad (7.10)$$

But,

$$\sin^2 \theta_t + \cos^2 \theta_t = 1 \quad \cos^2 \theta_t = 1 - \sin^2 \theta_t \quad \cos \theta_t = \sqrt{1 - \sin^2 \theta_t} \quad (7.11)$$

By substituting for  $\sin \theta_t$  from snell's law, we obtain  $\cos \theta_t$  in terms of  $\theta_i$  as:

$$\cos \theta_t = \sqrt{1 - \frac{1}{n^2} \sin^2 \theta_i} \quad (7.12)$$

## A.2 Figure of merit for ellipsometric fit

There are two figures of merit that defines the goodness of the spectroscopic ellipsometric fit; the mean squared error (MSE) and the reduced chi squared error ( $\chi^2$ ). The mean squared error and the reduced chi squared error are defined by [164]:

$$MSE = \frac{1}{N - m - 1} \sum_{j=1}^N [\rho_{exp}(\lambda_j) - \rho_{calc}(\lambda_j, z)]^2 \quad (7.13)$$

$$\chi^2 = \frac{1}{N - m - 1} \sum_{j=1}^N \frac{[\rho_{exp}(\lambda_j) - \rho_{calc}(\lambda_j, z)]^2}{\sigma(\lambda_j)^2} \quad (7.14)$$

where  $\rho_{exp}$  and  $\rho_{calc}$  are experimental and calculated values of the quantities to be fitted, in this case  $\Psi$  and  $\Delta$ .  $N$  is the number of wavelength points,  $z$  is a vector of the fitted parameters in the model and  $m$  is the dimensionality of  $z$ . One could notice that

$\chi^2$  expression has an extra term  $\sigma$ , which is the pointwise experimental errors of the measurement itself. MSE assumed that all experimental error are immeasurable and equal for all points. In general,  $\chi^2$  figure of merit is more accurate.

### A.3 Calculation of sheet resistance in four point probe measurement

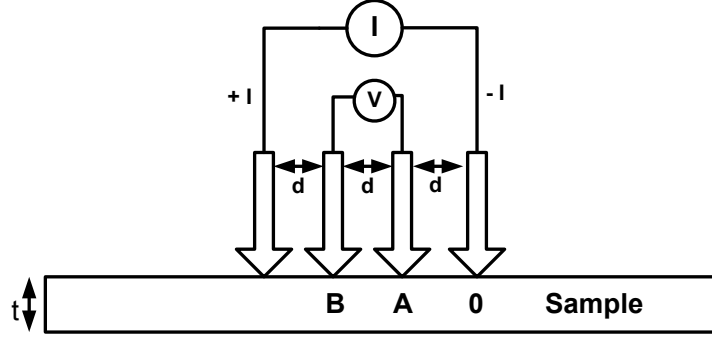


Figure A.1: Four point probe measurement.

Assuming a uniform probe spacing,

Change in resistance

$$dR = \frac{\rho dx}{S} \quad (7.15)$$

where R is the resistance and S is the surface area, x is the length.

$$R = \int_A^B \frac{\rho dx}{S} \quad (7.16)$$

For bulk sample,  $t \gg d$ , surface area  $S = 2\pi x^2$

$$R = \int_d^{2d} \frac{\rho dx}{2\pi x^2} \quad (7.17)$$

$$R = \left[ \frac{\rho}{-2\pi x} \right]_d^{2d} \quad (7.18)$$

$$R = \frac{\rho}{2\pi} \left[ \frac{1}{d} - \frac{1}{2d} \right] \quad (7.19)$$

$$R = \frac{\rho}{4\pi d} \quad (7.20)$$

Due to current superposition from the two outer tips, resistance  $R = \frac{V}{2I}$ , this implies,

$$R = \frac{\rho}{4\pi d} = \frac{V}{2I} \quad (7.21)$$

$$\rho = 2\pi d \left( \frac{V}{I} \right) \quad (7.22)$$

Sheet resistance,

$$R_s = \frac{\rho}{t} \quad (7.23)$$

Therefore, for bulk material  $t \gg d$ , sheet resistance is given as;

$$R_s = \frac{2\pi d}{t} \left( \frac{V}{I} \right) (\Omega/\text{square}) \quad (7.24)$$

where  $d$  is the adjacent probe separation and  $t$  is the sample thickness

On the other hand, for thin layers,  $t \ll d$ , surface area  $S = 2\pi xt$

$$R = \int_d^{2d} \frac{\rho dx}{2\pi xt} \quad (7.25)$$

$$R = \left[ \frac{\rho}{2\pi t} \ln x \right]_d^{2d} \quad (7.26)$$

$$R = \frac{\rho}{2\pi t} (\ln(2d) - \ln(d)) = \frac{\rho}{2\pi t} \ln \left( \frac{2d}{d} \right) = \frac{\rho}{2\pi t} \ln(2) \quad (7.27)$$

$$R = \frac{\rho}{2\pi t} \ln(2) = \frac{V}{2I} \quad (7.28)$$

$$R_s = \frac{\rho}{t} = \frac{\pi}{\ln 2} \left( \frac{V}{I} \right) (\Omega/\text{square}) \quad (7.29)$$

Therefore, for thin layers  $t \ll d$ , sheet resistance is given as;

$$R_s = 4.534 \left( \frac{V}{I} \right) (\Omega/\text{square}) \quad (7.30)$$

# A.4 Periodic table of the elements

|                                 |                                 |                                |                                     |                                 |                                  |                                  |                                 |                                  |                                    | Atomic Number                     |                                   |                                    |                                 |                                      |                                   |                                      |                                     |                                  |                                | Symbol                              |                                  |                                   |                                  |                                  |                                  |                                  |                                    |                                  |                                 | Name                              |                                  |                                  |  |  |  |  |  |  |  | Atomic Mass |  |  |  |  |  |  |  |  |  |
|---------------------------------|---------------------------------|--------------------------------|-------------------------------------|---------------------------------|----------------------------------|----------------------------------|---------------------------------|----------------------------------|------------------------------------|-----------------------------------|-----------------------------------|------------------------------------|---------------------------------|--------------------------------------|-----------------------------------|--------------------------------------|-------------------------------------|----------------------------------|--------------------------------|-------------------------------------|----------------------------------|-----------------------------------|----------------------------------|----------------------------------|----------------------------------|----------------------------------|------------------------------------|----------------------------------|---------------------------------|-----------------------------------|----------------------------------|----------------------------------|--|--|--|--|--|--|--|-------------|--|--|--|--|--|--|--|--|--|
| 1<br>IA<br>1A                   |                                 |                                |                                     |                                 |                                  |                                  |                                 |                                  |                                    |                                   |                                   |                                    |                                 |                                      |                                   |                                      |                                     | 18<br>VIIIA<br>8A                |                                |                                     |                                  |                                   |                                  |                                  |                                  |                                  |                                    |                                  |                                 |                                   |                                  |                                  |  |  |  |  |  |  |  |             |  |  |  |  |  |  |  |  |  |
| 1<br>H<br>Hydrogen<br>1.008     |                                 |                                |                                     |                                 |                                  |                                  |                                 |                                  |                                    |                                   |                                   |                                    |                                 |                                      |                                   |                                      |                                     | 2<br>He<br>Helium<br>4.003       |                                |                                     |                                  |                                   |                                  |                                  |                                  |                                  |                                    |                                  |                                 |                                   |                                  |                                  |  |  |  |  |  |  |  |             |  |  |  |  |  |  |  |  |  |
| 3<br>Li<br>Lithium<br>6.941     | 4<br>Be<br>Beryllium<br>9.012   |                                |                                     |                                 |                                  |                                  |                                 |                                  |                                    |                                   |                                   |                                    |                                 |                                      |                                   |                                      |                                     | 5<br>B<br>Boron<br>10.811        | 6<br>C<br>Carbon<br>12.011     | 7<br>N<br>Nitrogen<br>14.007        | 8<br>O<br>Oxygen<br>15.999       | 9<br>F<br>Fluorine<br>18.998      | 10<br>Ne<br>Neon<br>20.180       |                                  |                                  |                                  |                                    |                                  |                                 |                                   |                                  |                                  |  |  |  |  |  |  |  |             |  |  |  |  |  |  |  |  |  |
| 11<br>Na<br>Sodium<br>22.990    | 12<br>Mg<br>Magnesium<br>24.305 | 3<br>IIIB<br>3B                | 4<br>IVB<br>4B                      | 5<br>VB<br>5B                   | 6<br>VIB<br>6B                   | 7<br>VIIB<br>7B                  | 8<br>VIII<br>8                  | 9<br>VIII<br>9                   | 10<br>VIII<br>10                   | 11<br>IB<br>1B                    | 12<br>IIB<br>2B                   | 13<br>IIIA<br>3A                   | 14<br>IVA<br>4A                 | 15<br>VA<br>5A                       | 16<br>VIA<br>6A                   | 17<br>VIIA<br>7A                     | 18<br>VIIIA<br>8A                   |                                  |                                |                                     |                                  |                                   |                                  |                                  |                                  |                                  |                                    |                                  |                                 |                                   |                                  |                                  |  |  |  |  |  |  |  |             |  |  |  |  |  |  |  |  |  |
| 19<br>K<br>Potassium<br>39.098  | 20<br>Ca<br>Calcium<br>40.078   | 21<br>Sc<br>Scandium<br>44.956 | 22<br>Ti<br>Titanium<br>47.867      | 23<br>V<br>Vanadium<br>50.942   | 24<br>Cr<br>Chromium<br>51.996   | 25<br>Mn<br>Manganese<br>54.938  | 26<br>Fe<br>Iron<br>55.845      | 27<br>Co<br>Cobalt<br>58.933     | 28<br>Ni<br>Nickel<br>58.693       | 29<br>Cu<br>Copper<br>63.546      | 30<br>Zn<br>Zinc<br>65.38         | 31<br>Ga<br>Gallium<br>69.723      | 32<br>Ge<br>Germanium<br>72.631 | 33<br>As<br>Arsenic<br>74.922        | 34<br>Se<br>Selenium<br>78.972    | 35<br>Br<br>Bromine<br>79.904        | 36<br>Kr<br>Krypton<br>84.798       |                                  |                                |                                     |                                  |                                   |                                  |                                  |                                  |                                  |                                    |                                  |                                 |                                   |                                  |                                  |  |  |  |  |  |  |  |             |  |  |  |  |  |  |  |  |  |
| 37<br>Rb<br>Rubidium<br>85.468  | 38<br>Sr<br>Strontium<br>87.62  | 39<br>Y<br>Yttrium<br>88.906   | 40<br>Zr<br>Zirconium<br>91.224     | 41<br>Nb<br>Niobium<br>92.906   | 42<br>Mo<br>Molybdenum<br>95.95  | 43<br>Tc<br>Technetium<br>98.907 | 44<br>Ru<br>Ruthenium<br>101.07 | 45<br>Rh<br>Rhodium<br>102.906   | 46<br>Pd<br>Palladium<br>106.42    | 47<br>Ag<br>Silver<br>107.868     | 48<br>Cd<br>Cadmium<br>112.411    | 49<br>In<br>Indium<br>114.818      | 50<br>Sn<br>Tin<br>118.711      | 51<br>Sb<br>Antimony<br>121.760      | 52<br>Te<br>Tellurium<br>127.6    | 53<br>I<br>Iodine<br>126.904         | 54<br>Xe<br>Xenon<br>131.294        |                                  |                                |                                     |                                  |                                   |                                  |                                  |                                  |                                  |                                    |                                  |                                 |                                   |                                  |                                  |  |  |  |  |  |  |  |             |  |  |  |  |  |  |  |  |  |
| 55<br>Cs<br>Cesium<br>132.905   | 56<br>Ba<br>Barium<br>137.328   | 57-71<br>Lanthanide Series     | 72<br>Hf<br>Hafnium<br>178.49       | 73<br>Ta<br>Tantalum<br>180.948 | 74<br>W<br>Tungsten<br>183.84    | 75<br>Re<br>Rhenium<br>186.207   | 76<br>Os<br>Osmium<br>190.23    | 77<br>Ir<br>Iridium<br>192.217   | 78<br>Pt<br>Platinum<br>195.085    | 79<br>Au<br>Gold<br>196.967       | 80<br>Hg<br>Mercury<br>200.592    | 81<br>Tl<br>Thallium<br>204.383    | 82<br>Pb<br>Lead<br>207.2       | 83<br>Bi<br>Bismuth<br>208.980       | 84<br>Po<br>Polonium<br>[208.982] | 85<br>At<br>Astatine<br>209.987      | 86<br>Rn<br>Radon<br>222.018        |                                  |                                |                                     |                                  |                                   |                                  |                                  |                                  |                                  |                                    |                                  |                                 |                                   |                                  |                                  |  |  |  |  |  |  |  |             |  |  |  |  |  |  |  |  |  |
| 87<br>Fr<br>Francium<br>223.020 | 88<br>Ra<br>Radium<br>226.025   | 89-103<br>Actinide Series      | 104<br>Rf<br>Rutherfordium<br>[261] | 105<br>Db<br>Dubnium<br>[262]   | 106<br>Sg<br>Seaborgium<br>[266] | 107<br>Bh<br>Bohrium<br>[264]    | 108<br>Hs<br>Hassium<br>[269]   | 109<br>Mt<br>Meitnerium<br>[268] | 110<br>Ds<br>Darmstadtium<br>[269] | 111<br>Rg<br>Roentgenium<br>[272] | 112<br>Cn<br>Copernicium<br>[277] | 113<br>Uut<br>Ununtrium<br>unknown | 114<br>Fl<br>Flerovium<br>[289] | 115<br>Uup<br>Ununpentium<br>unknown | 116<br>Lv<br>Livermorium<br>[293] | 117<br>Uus<br>Ununseptium<br>unknown | 118<br>Uuo<br>Ununoctium<br>unknown |                                  |                                |                                     |                                  |                                   |                                  |                                  |                                  |                                  |                                    |                                  |                                 |                                   |                                  |                                  |  |  |  |  |  |  |  |             |  |  |  |  |  |  |  |  |  |
|                                 |                                 |                                |                                     |                                 |                                  |                                  |                                 |                                  |                                    |                                   |                                   |                                    |                                 |                                      |                                   |                                      |                                     | 57<br>La<br>Lanthanum<br>138.905 | 58<br>Ce<br>Cerium<br>140.116  | 59<br>Pr<br>Praseodymium<br>140.908 | 60<br>Nd<br>Neodymium<br>144.242 | 61<br>Pm<br>Promethium<br>144.913 | 62<br>Sm<br>Samarium<br>150.36   | 63<br>Eu<br>Europium<br>151.964  | 64<br>Gd<br>Gadolinium<br>157.25 | 65<br>Tb<br>Terbium<br>158.925   | 66<br>Dy<br>Dysprosium<br>162.500  | 67<br>Ho<br>Holmium<br>164.930   | 68<br>Er<br>Erbium<br>167.259   | 69<br>Tm<br>Thulium<br>168.934    | 70<br>Yb<br>Ytterbium<br>173.055 | 71<br>Lu<br>Lutetium<br>174.967  |  |  |  |  |  |  |  |             |  |  |  |  |  |  |  |  |  |
|                                 |                                 |                                |                                     |                                 |                                  |                                  |                                 |                                  |                                    |                                   |                                   |                                    |                                 |                                      |                                   |                                      |                                     | 89<br>Ac<br>Actinium<br>227.028  | 90<br>Th<br>Thorium<br>232.038 | 91<br>Pa<br>Protactinium<br>231.036 | 92<br>U<br>Uranium<br>238.029    | 93<br>Np<br>Neptunium<br>237.048  | 94<br>Pu<br>Plutonium<br>244.064 | 95<br>Am<br>Americium<br>243.061 | 96<br>Cm<br>Curium<br>247.070    | 97<br>Bk<br>Berkelium<br>247.070 | 98<br>Cf<br>Californium<br>251.080 | 99<br>Es<br>Einsteinium<br>[254] | 100<br>Fm<br>Fermium<br>257.095 | 101<br>Md<br>Mendelevium<br>258.1 | 102<br>No<br>Nobelium<br>259.101 | 103<br>Lr<br>Lawrencium<br>[262] |  |  |  |  |  |  |  |             |  |  |  |  |  |  |  |  |  |

|              |                |                  |             |           |          |         |           |            |          |
|--------------|----------------|------------------|-------------|-----------|----------|---------|-----------|------------|----------|
| Alkali Metal | Alkaline Earth | Transition Metal | Basic Metal | Semimetal | Nonmetal | Halogen | Noble Gas | Lanthanide | Actinide |
|--------------|----------------|------------------|-------------|-----------|----------|---------|-----------|------------|----------|



# Resume

## Personal Data

Name: Akinwumi Abimbola AMUSAN  
Date of Birth: 02.10.1984  
Place of Birth: Ibadan, Nigeria  
Email address: akinwummy@yahoo.com, akinwumi.amusan@ovgu.de

## Education

2010 - 2012: KTH, Royal Institute of Technology, Sweden.  
**Master of Science (MSc)** in Photonics  
MSc thesis: Simulation of Traveling Wave Electroabsorption Modulators  
Suitable for 100Gbps

2009 - 2010: Ghent University, Belgium.  
**Erasmus Mundus Master of Science** in Photonics

2001 - 2006: Ladoke Akintola University of Technology, Ogbomosho, Nigeria.  
**Bachelor of Technology (B. Tech)**  
Electronic and Electrical Engineering  
B. Tech project: Power Control in WCDMA Mobile  
Communications System

May - June 2000: **WASSCE** West African Secondary School Certificate Examination

## Work Experience

2012 - 2016: Institute for Micro and Sensor System (IMOS),  
Otto-von-Guericke Universitat Magdeburg, Germany.  
**PhD research student**

2008 - 2009: ICT, University of Ibadan, Nigeria.  
**Network/Telecom Administrator**

2007 - 2008: Akwa Ibom State Polytechnic, Ikot Osurua, Nigeria.  
**National Youth Service Corps**

## Award and Scholarship

2009 - 2011: Erasmus Mundus Scholarship from European Commission.  
01/2016 - 08/2016: Research stipendiat, IMOS, Magdeburg

## Related Publications

- [1] Akinwumi A Amusan, Bodo Kalkofen, Hassan Gargouri, Klaus Wandel, Cay Pinnow, Marco Lisker, and Edmund P Burte. Ag films grown by remote plasma enhanced atomic layer deposition on different substrates. *Journal of Vacuum Science and Technology A*, 34(1):01A126, 2016.
- [2] Bodo Kalkofen, Akinwumi A Amusan, Muhammad S K Bukhari, Bernd Garke, Marco Lisker, Hassan Gargouri, and Edmund P Burte. Use of B<sub>2</sub>O<sub>3</sub> films grown by plasma-assisted atomic layer deposition for shallow boron doping in silicon. *Journal of Vacuum Science and Technology A*, 33(3):031512, 2015.
- [3] Bodo Kalkofen, Akinwumi A Amusan, Marco Lisker, and Edmund P Burte. Application of atomic layer deposited dopant sources for ultra-shallow doping of silicon. *Physica Status Solidi (C)*, 11(1):41–45, 2014.
- [4] Bodo Kalkofen, Akinwumi A Amusan, Marco Lisker, and Edmund P Burte. Investigation of oxide thin films deposited by atomic layer deposition as dopant source for ultra-shallow doping of silicon. *Microelectronic Engineering*, 109:113–116, 2013.

# References

- [1] R J Baker. *CMOS: circuit design, layout, and simulation*, volume 1. John Wiley & Sons, New Jersey, USA, 2008.
- [2] Y Zhao, C Zhou, X Zhang, P Zhang, Y Dou, W Wang, X Cao, B Wang, Y Tang, and S Zhou. Passivation mechanism of thermal atomic layer-deposited  $\text{Al}_2\text{O}_3$  films on silicon at different annealing temperatures. *Nanoscale research letters*, 8(1):1–7, 2013.
- [3] B Kalkofen and E P Burte. Atomic layer deposition of boron oxide as dopant source for shallow doping of silicon. In *Meeting Abstracts*, number 17, pages 943–943. The Electrochemical Society, 2010.
- [4] A Szeghalmi, M Helgert, R Brunner, F Heyroth, U Gösele, and M Knez. Atomic layer deposition of  $\text{Al}_2\text{O}_3$  and  $\text{TiO}_2$  multilayers for applications as bandpass filters and antireflection coatings. *Applied optics*, 48(9):1727–1732, 2009.
- [5] J Jur, W J Sweet, C J Oldham, and G N Parsons. Atomic layer deposition of conductive coatings on cotton, paper, and synthetic fibers: Conductivity analysis and functional chemical sensing using all-fiber capacitors. *Advanced Functional Materials*, 21(11):1993–2002, 2011.
- [6] <http://www-mtl.mit.edu/researchgroups/Metrology/PAPERS/SemiInternationalOct2000/>. 2000.
- [7] R Manepalli, F Stepniak, S A Bidstrup-Allen, and P A Kohl. Silver metallization for advanced interconnects. *Advanced Packaging, IEEE Transactions on*, 22(1):4–8, 1999.
- [8] M Hauder, J Gstöttner, W Hansch, and D Schmitt-Landsiedel. Scaling properties and electromigration resistance of sputtered ag metallization lines. *Applied Physics Letters*, 78(6):838–840, 2001.
- [9] J-M Seo, S K Cho, H-C Koo, S-K Kim, O J Kwon, and J J Kim. Thin film silver deposition by electroplating for ulsi interconnect applications. *Korean Journal of Chemical Engineering*, 26(1):265–268, 2009.
- [10] N Marechal, E Quesnel, and Y Pauleau. Silver thin films deposited by magnetron sputtering. *Thin Solid Films*, 241(1):34–38, 1994.

- [11] M Lisca, B Kalkofen, M Lisker, E P Burte, I Szymańska, and E Szłyk. Silver films deposited by liquid-delivery mocvd using (tertbutylcarboxylate)(triethylphosphine) silver with toluene as the solvent. *ECS Transactions*, 25(8):1039–1046, 2009.
- [12] F J van den Bruele, M Smets, A Illiberi, Y Creyghton, P Buskens, F Roozeboom, and P Poodt. Atmospheric pressure plasma enhanced spatial ald of silver. *Journal of Vacuum Science & Technology A*, 33(1):01A131, 2015.
- [13] M Kariniemi, J Niinistö, T Hatanpää, M Kemell, T Sajavaara, M Ritala, and M Leskelä. Plasma-enhanced atomic layer deposition of silver thin films. *Chemistry of Materials*, 23(11):2901–2907, 2011.
- [14] Y S Chauhan, D D Lu, V Sriramkumar, S Khandelwal, J P Duarte, N Paydavosi, A Niknejad, and C Hu. *FinFET Modeling for IC Simulation and Design*. Academic Press, Cambridge, Massachusetts, USA, 2015.
- [15] C Hu. *Modern semiconductor devices for integrated circuits*. Prentice Hall, New Jersey, USA, 2010.
- [16] R Surdeanu, Y V Ponomarev, R Cerutti, B J Pawlak, L K Nanver, I Hoflijk, P A Stolk, C J J Dachs, M A Verheijen, M Kaiser, M J P Hopstaken, J G M van Berkum, F Roozeboom, L K Nanver, and R Lindsay. Laser annealing for ultra-shallow junction formation in advanced CMOS. In *Rapid Thermal and Other Short-time Processing Technologies III: Proceedings of the International Symposium*, volume 2002, page 413. The Electrochemical Society, 2002.
- [17] K Tsutsui, T Matsuda, M Watanabe, C-G Jin, Y Sasaki, B Mizuno, E Ikenaga, K Kakushima, P Ahmet, T Maruizumi, H Nohira, T Hattori, and H Iwai. Activated boron and its concentration profiles in heavily doped Si studied by soft x-ray photoelectron spectroscopy and hall measurements. *Journal of Applied Physics*, 104(9):093709, 2008.
- [18] S Ingole, P Aella, P Manandhar, S B Chikkannanavar, E A Akhadov, D J Smith, and S T Picraux. Ex situ doping of silicon nanowires with boron. *Journal of Applied Physics*, 103(10):104302, 2008.
- [19] B Kalkofen, M Lisker, and E P Burte. Phosphorus diffusion into silicon after vapor phase surface adsorption of phosphine. *Materials Science and Engineering: B*, 124:288–292, 2005.
- [20] Y Yamamoto, R Kurps, C Mai, I Costina, J Murota, and B Tillack. Phosphorus atomic layer doping in Ge using RPCVD. *Solid-State Electronics*, 83:25–29, 2013.

- [21] J C Ho, R Yerushalmi, Z A Jacobson, Z Fan, R L Alley, and A Javey. Controlled nanoscale doping of semiconductors via molecular monolayers. *Nature Materials*, 7(1):62–67, 2008.
- [22] T Kääriäinen, D Cameron, M-L Kääriäinen, and A Sherman. *Atomic Layer Deposition: Principles, Characteristics, and Nanotechnology Applications*. John Wiley & Sons, New Jersey, USA, 2013.
- [23] J Antson and T Suntola. Method for producing compound thin films, November 15 1977.
- [24] T Suntola. Atomic layer epitaxy. *Thin Solid Films*, 216(1):84–89, 1992.
- [25] International Technology Roadmap for Semiconductors. [www.itrs.net](http://www.itrs.net). 2013.
- [26] S M George. Atomic layer deposition: an overview. *Chemical reviews*, 110(1):111–131, 2009.
- [27] H S Nalwa. *Handbook of thin film materials*. Academic Press, Cambridge, Massachusetts, USA, 2002.
- [28] R L Puurunen. Surface chemistry of atomic layer deposition: A case study for the trimethylaluminum/water process. *Journal of Applied Physics*, 97(12):121301, 2005.
- [29] B S Lim, A Rahtu, and R G Gordon. Atomic layer deposition of transition metals. *Nature materials*, 2(11):749–754, 2003.
- [30] T Aaltonen, P Alén, M Ritala, and M Leskelä. Ruthenium thin films grown by atomic layer deposition. *Chemical Vapor Deposition*, 9(1):45–49, 2003.
- [31] T Aaltonen, M Ritala, V Sammelselg, and M Leskelä. Atomic layer deposition of iridium thin films. *Journal of the Electrochemical Society*, 151(8):G489–G492, 2004.
- [32] R B Yang, J Bachmann, M Reiche, J W Gerlach, U Gösele, and K Nielsch. Atomic layer deposition of antimony oxide and antimony sulfide. *Chemistry of materials*, 21(13):2586–2588, 2009.
- [33] B Kalkofen, V M Mothukuru, M Klingsporn, and E P Burte. Investigation of antimony oxide films deposited by atomic layer deposition. *ECS Transactions*, 45(3):461–473, 2012.
- [34] A C Jones and M L Hitchman. *Chemical vapour deposition: precursors, processes and applications*. RSC Publishing, Piccadilly, London, UK, 2009.

- [35] S M Rossnagel, A Sherman, and F Turner. Plasma-enhanced atomic layer deposition of Ta and Ti for interconnect diffusion barriers. *Journal of Vacuum Science & Technology B*, 18(4):2016–2020, 2000.
- [36] P Tägtström, P Maårtensson, U Jansson, and J-O Carlsson. Atomic layer epitaxy of tungsten oxide films using oxyfluorides as metal precursors. *Journal of the Electrochemical Society*, 146(8):3139–3143, 1999.
- [37] J Niinistö, M Putkonen, L Niinistö, S L Stoll, K Kukli, T Sajavaara, M Ritala, and M Leskelä. Controlled growth of HfO<sub>2</sub> thin films by atomic layer deposition from cyclopentadienyl-type precursor and water. *Journal of Materials Chemistry*, 15(23):2271–2275, 2005.
- [38] M Putkonen and L Niinistö. Zirconia thin films by atomic layer epitaxy. a comparative study on the use of novel precursors with ozone. *Journal of Materials Chemistry*, 11(12):3141–3147, 2001.
- [39] V Pore, A Rahtu, M Leskelä, M Ritala, T Sajavaara, and J Keinonen. Atomic layer deposition of photocatalytic TiO<sub>2</sub> thin films from titanium tetramethoxide and water. *Chemical Vapor Deposition*, 10(3):143–148, 2004.
- [40] V Miikkulainen, M Leskelä, M Ritala, and R L Puurunen. Crystallinity of inorganic films grown by atomic layer deposition: Overview and general trends. *Journal of Applied Physics*, 113(2):021301, 2013.
- [41] L Hiltunen, H Kattelus, M Leskelä, M Mäkelä, L Niinistö, E Nykänen, P Soininen, and M Tiittad. Growth and characterization of aluminium oxide thin films deposited from various source materials by atomic layer epitaxy and chemical vapor deposition processes. *Materials chemistry and physics*, 28(4):379–388, 1991.
- [42] J W Lim, S J Yun, and J H Lee. Characteristics of aluminum silicate films grown by plasma-enhanced atomic layer deposition. *Electrochemical and Solid-State Letters*, 8(9):F25–F28, 2005.
- [43] M Tiitta and L Niinistö. Volatile metal  $\beta$ -diketonates: Ale and cvd precursors for electroluminescent device thin films. *Chemical Vapor Deposition*, 3(4):167–182, 1997.
- [44] O Nilsen, R Balasundaraprabhu, E V Monakhov, N Muthukumarasamy, H Fjellvåg, and B G Svensson. Thin films of In<sub>2</sub>O<sub>3</sub> by atomic layer deposition using In(acac)<sub>3</sub>. *Thin Solid Films*, 517(23):6320–6322, 2009.
- [45] E Nykänen, J Laine-Ylijoki, P Soininen, L Niinistö, M Leskelä, and L G Hubert-Pfalzgraf. Growth of PbS thin films from novel precursors by atomic layer epitaxy. *Journal of Materials Chemistry*, 4(9):1409–1412, 1994.

- [46] V Pore, T Hatanpaa, M Ritala, and M Leskelä. Atomic layer deposition of metal tellurides and selenides using alkylsilyl compounds of tellurium and selenium. *Journal of the American Chemical Society*, 131(10):3478–3480, 2009.
- [47] M Juppo, M Vehkamäki, M Ritala, and M Leskelä. Deposition of molybdenum thin films by an alternate supply of  $\text{MoCl}_5$  and Zn. *Journal of Vacuum Science & Technology A*, 16(5):2845–2850, 1998.
- [48] J W Elam, C E Nelson, R K Grubbs, and S M George. Kinetics of the  $\text{WF}_6$  and  $\text{Si}_2\text{H}_6$  surface reactions during tungsten atomic layer deposition. *Surface Science*, 479(1):121–135, 2001.
- [49] P Alen, M Juppo, M Ritala, T Sajavaara, J Keinonen, and M Leskelä. Atomic layer deposition of Ta(Al)N(C) thin films using trimethylaluminum as a reducing agent. *Journal of the Electrochemical Society*, 148(10):G566–G571, 2001.
- [50] S-H Kim, J-K Kim, N Kwak, H Sohn, J Kim, S-H Jung, M-R Hong, S H Lee, and J Collins. Atomic layer deposition of low-resistivity and high-density tungsten nitride thin films using  $\text{B}_2\text{H}_6$ ,  $\text{WF}_6$  and  $\text{NH}_3$ . *Electrochemical and Solid-State Letters*, 9(3):C54–C57, 2006.
- [51] N Pinna and M Knez. *Atomic layer deposition of nanostructured materials*. John Wiley & Sons, New Jersey, USA, 2012.
- [52] E Guziewicz, M Godlewski, K Kopalko, E Łusakowska, E Dynowska, M Guziewicz, M M Godlewski, and M Phillips. Atomic layer deposition of thin films of ZnSe structural and optical characterization. *Thin Solid Films*, 446(2):172–177, 2004.
- [53] J R Bakke, J S King, H J Jung, R Sinclair, and S F Bent. Atomic layer deposition of ZnS via in situ production of  $\text{H}_2\text{S}$ . *Thin Solid Films*, 518(19):5400–5408, 2010.
- [54] W-S Jeon, S Yang, C-S Lee, and S-W Kang. Atomic layer deposition of  $\text{Al}_2\text{O}_3$  thin films using trimethylaluminum and isopropyl alcohol. *Journal of The Electrochemical Society*, 149(6):C306–C310, 2002.
- [55] M Ritala, M Leskelä, J-P Dekker, C Mutsaers, P J Soininen, and J Skarp. Perfectly conformal TiN and  $\text{Al}_2\text{O}_3$  films deposited by atomic layer deposition. *Chemical Vapor Deposition*, 5(1):7–9, 1999.
- [56] H Kim. Atomic layer deposition of metal and nitride thin films: Current research efforts and applications for semiconductor device processing. *Journal of Vacuum Science & Technology B*, 21(6):2231–2261, 2003.

- [57] F B Oruc, L E Aygun, I Donmez, N Biyikli, A K Okyay, and H Y Yu. Low temperature atomic layer deposited ZnO photo thin film transistors. *Journal of Vacuum Science & Technology A*, 33(1):01A105, 2015.
- [58] C Ozgit-Akgun, E Goldenberg, S Bolat, B Tekcan, F Kayaci, T Uyar, A K Okyay, and N Biyikli. Low-temperature hollow cathode plasma-assisted atomic layer deposition of crystalline iii-nitride thin films and nanostructures. *Physica Status Solidi (C)*, 12(4-5):394–398, 2015.
- [59] B Kalkofen, V M Mothukuru, M Lisker, and E P Burte. P-type doping of silicon suitable for structures with high aspect ratios by using a dopant source of boron oxide grown by atomic layer deposition. *ECS Transactions*, 45(6):55–67, 2012.
- [60] <http://www.pv-magazine.com>. 2015.
- [61] T G Allen and A Cuevas. Plasma enhanced atomic layer deposition of gallium oxide on crystalline silicon: demonstration of surface passivation and negative interfacial charge. *Physica Status Solidi (RRL)-Rapid Research Letters*, 9999, 2015.
- [62] D Kim, T Nam, J Park, J Gatineau, and H Kim. Growth characteristics and properties of indium oxide and indium-doped zinc oxide by atomic layer deposition. *Thin Solid Films*, 587:83–87, 2015.
- [63] J R Bakke, H J Jung, J T Tanskanen, R Sinclair, and S F Bent. Atomic layer deposition of CdS films. *Chemistry of Materials*, 22(16):4669–4678, 2010.
- [64] [https://en.wikipedia.org/wiki/Hard\\_disk\\_drive](https://en.wikipedia.org/wiki/Hard_disk_drive). 2013.
- [65] A Paranjpe, S Gopinath, T Omstead, and R Bubber. Atomic layer deposition of  $\text{AlO}_x$  for thin film head gap applications. *Journal of the Electrochemical Society*, 148(9):G465–G471, 2001.
- [66] <http://www.indiana.edu/~hightech/fpd/papers/ELDs.html>. 1999.
- [67] F H Fabreguette, R A Wind, and S M George. Ultrahigh x-ray reflectivity from  $\text{W}/\text{Al}_2\text{O}_3$  multilayers fabricated using atomic layer deposition. *Applied Physics Letters*, 88(1):013116, 2006.
- [68] M Ishii, S Iwai, H Kawata, T Ueki, and Y Aoyagi. Atomic layer epitaxy of AlP and its application to x-ray multilayer mirror. *Journal of Crystal Growth*, 180(1):15–21, 1997.
- [69] H Kumagai, K Toyoda, K Kobayashi, M Obara, and Y Iimura. Titanium oxide/aluminum oxide multilayer reflectors for water-window wavelengths. *Applied Physics Letters*, 70(18):2338–2340, 1997.



- [70] D Riihelä, M Ritala, R Matero, and M Leskelä. Introducing atomic layer epitaxy for the deposition of optical thin films. *Thin Solid Films*, 289(1):250–255, 1996.
- [71] B J O'Neill, D H K Jackson, J Lee, C Canlas, P C Stair, C L Marshall, J W Elam, T F Kuech, J A Dumesic, and G W Huber. Catalyst design with atomic layer deposition. *ACS Catalysis*, 5(3):1804–1825, 2015.
- [72] T M Mayer, J W Elam, S M George, P G Kotula, and R S Goeke. Atomic-layer deposition of wear-resistant coatings for microelectromechanical devices. *Applied Physics Letters*, 82(17):2883–2885, 2003.
- [73] N D Hoivik, J W Elam, R J Linderman, V M Bright, S M George, and Y C Lee. Atomic layer deposited protective coatings for micro-electromechanical systems. *Sensors and Actuators A: Physical*, 103(1):100–108, 2003.
- [74] T W Scharf, S V Prasad, M T Dugger, P G Kotula, R S Goeke, and R K Grubbs. Growth, structure, and tribological behavior of atomic layer-deposited tungsten disulphide solid lubricant coatings with applications to MEMS. *Acta materialia*, 54(18):4731–4743, 2006.
- [75] C F Herrmann, F W DelRio, D C Miller, S M George, V M Bright, J L Ebel, R E Strawser, R Cortez, and K D Leedy. Alternative dielectric films for rf mems capacitive switches deposited using atomic layer deposited  $\text{Al}_2\text{O}_3/\text{ZnO}$  alloys. *Sensors and Actuators A: Physical*, 135(1):262–272, 2007.
- [76] J Kim, K Chakrabarti, J Lee, K-Y Oh, and C Lee. Effects of ozone as an oxygen source on the properties of the  $\text{Al}_2\text{O}_3$  thin films prepared by atomic layer deposition. *Materials Chemistry and Physics*, 78(3):733–738, 2003.
- [77] H Tiznado, D Domínguez, F Muñoz-Muñoz, J Romo-Herrera, R Machorro, O E Contreras, and G Soto. Pulsed-bed atomic layer deposition setup for powder coating. *Powder Technology*, 267:201–207, 2014.
- [78] Strem Chemicals. [www.strem.com](http://www.strem.com).
- [79] H B Profijt, S E Potts, M C M Van De Sanden, and W M M Kessels. Plasma-assisted atomic layer deposition: Basics, opportunities, and challenges. *Journal of Vacuum Science and Technology A*, 29(5):050801, 2011.
- [80] S M Rossnagel, J J Cuomo, and W D Westwood. *Handbook of plasma processing technology: fundamentals, etching, deposition, and surface interactions*. William Andrew, New York, USA, 1990.
- [81] H Conrads and M Schmidt. Plasma generation and plasma sources. *Plasma Sources Science and Technology*, 9(4):441, 2000.

- [82] T Takagi. Ion–surface interactions during thin film deposition. *Journal of Vacuum Science & Technology A*, 2(2):382–388, 1984.
- [83] E R Cleveland, O Glembocki, and S M Prokes. Plasma enhanced atomic layer deposition of silver thin films for applications in plasmonics and surface enhanced raman scattering. In *SPIE NanoScience+ Engineering*, pages 84670H–84670H. International Society for Optics and Photonics, 2012.
- [84] M Boccas, T Vucina, C Araya, E Vera, and C Ahhee. Protected-silver coatings for the 8-m gemini telescope mirrors. *Thin Solid Films*, 502(1):275–280, 2006.
- [85] A P Piedade, M T Vieira, A Martins, and F Silva. In vitro behaviour of nanocrystalline silver-sputtered thin films. *Nanotechnology*, 18(10):105103, 2007.
- [86] M A Butler and A J Ricco. Chemisorption-induced reflectivity changes in optically thin silver films. *Applied physics letters*, 53(16):1471–1473, 1988.
- [87] A J Nagy, G Mestl, and R Schögl. The role of subsurface oxygen in the silver-catalyzed, oxidative coupling of methane. *Journal of Catalysis*, 188(1):58–68, 1999.
- [88] P R Chalker, S Romani, P A Marshall, M J Rosseinsky, S Rushworth, and P A Williams. Liquid injection atomic layer deposition of silver nanoparticles. *Nanotechnology*, 21(40):405602, 2010.
- [89] A Niskanen, T Hatanpää, K Arstila, M Leskelä, and M Ritala. Radical-enhanced atomic layer deposition of silver thin films using phosphine-adducted silver carboxylates. *Chemical Vapor Deposition*, 13(8):408–413, 2007.
- [90] L Gao, P Härter, C H Linsmeier, A Wiltner, R Emling, and D Schmitt-Landsiedel. Silver metal organic chemical vapor deposition for advanced silver metallization. *Microelectronic engineering*, 82(3):296–300, 2005.
- [91] H-K Kim, H-C Jeong, K S Kim, S H Yoon, S S Lee, K W Seo, and I-W Shim. Preparation of silver thin films using liquid-phase precursors by metal organic chemical vapor deposition and their conversion to silver selenide films by selenium vapor deposition. *Thin Solid Films*, 478(1):72–76, 2005.
- [92] K-M Chi and Y-H Lu. MOCVD of silver thin films from the (1, 1, 1, 5, 5, 5-hexafluoro-2, 4-pentanedionato)-silver [bis (trimethylsilyl) acetylene] complex. *Chemical Vapor Deposition*, 7(3):117–120, 2001.
- [93] Z Yuan, N H Dryden, J J Vittal, and R J Puddephatt. Chemical vapor deposition of silver. *Chemistry of materials*, 7(9):1696–1702, 1995.

- [94] R Arsat, S J Tan, W Wlodarski, and K Kalantar-Zadeh. Hydrogen gas sensor based on  $\text{Sb}_x\text{O}_y$  nanostructures with a langasite substrate. *Sensor Letters*, 4(4):419–425, 2006.
- [95] R Binions, C J Carmalt, and I P Parkin. Antimony oxide thin films from the atmospheric pressure chemical vapour deposition reaction of antimony pentachloride and ethyl acetate. *Polyhedron*, 25(15):3032–3038, 2006.
- [96] P W Haycock, G A Horley, K C Molloy, C P Myers, S A Rushworth, and L M Smith. MOCVD of antimony oxides for gas sensor applications. *Le Journal de Physique IV*, 11(PR3):Pr3–1045, 2001.
- [97] N Tigau, V Ciupina, and G Prodan. Structural, optical and electrical properties of  $\text{Sb}_2\text{O}_3$  thin films with different thickness. *Journal of Optoelectronics and Advanced Materials*, 8(1):37, 2006.
- [98] B Pillep, P Behrens, U-A Schubert, J Spengler, and H Knözinger. Mechanical and thermal spreading of antimony oxides on the  $\text{TiO}_2$  surface: dispersion and properties of surface antimony oxide species. *The Journal of Physical Chemistry B*, 103(44):9595–9603, 1999.
- [99] K Matsuzawa, T Shido, and Y Iwasawa. Reversible structure transformation of antimony oxides on  $\text{SiO}_2$  relevant to selective catalytic oxidation of ethanol. *Langmuir*, 19(7):2756–2762, 2003.
- [100] S C Grund, K Hanusch, H J Breunig, and H U Wolf. Antimony and antimony compounds. *Ullmann 's Encyclopedia of Industrial Chemistry*, 2006.
- [101] M Nalin, Y Messaddeq, S J L Ribeiro, M Poulain, and V Briois. Photosensitivity in antimony based glasses. *Journal of Optoelectronics and Advanced Materials*, 3(2):553–558, 2001.
- [102] B Kalkofen, S Matichyn, and E Burte. Atomic layer deposition of antimony oxide on hydrogen-terminated silicon substrates. *ECS Transactions*, 19(1):105–114, 2009.
- [103] H Virola and L Niinistö. Controlled growth of antimony-doped tin dioxide thin films by atomic layer epitaxy. *Thin Solid Films*, 251(2):127–135, 1994.
- [104] M Putkonen and L Niinistö. Atomic layer deposition of  $\text{B}_2\text{O}_3$  thin films at room temperature. *Thin Solid Films*, 514(1):145–149, 2006.
- [105] X Ma, W N Unertl, and A Erdemir. The boron oxide–boric acid system: Nanoscale mechanical and wear properties. *Journal of materials research*, 14(08):3455–3466, 1999.

- [106] W H Kim, I-K Oh, M-K Kim, W J Maneng, C-W Lee, G Lee, C Lansalot-Matras, W Noh, D Thompson, D Chu, and H Kim. Atomic layer deposition of  $B_2O_3/SiO_2$  thin films and their application in an efficient diffusion doping process. *Journal of Materials Chemistry C*, 2(29):5805–5811, 2014.
- [107] H-C Yuan, J Oh, Y Zhang, O A Kuznetsov, D J Flood, and H M Branz. Antireflection and  $SiO_2$  surface passivation by liquid-phase chemistry for efficient black silicon solar cells. In *Photovoltaic Specialists Conference (PVSC), 2012 38th IEEE*, pages 000686–000689. IEEE, 2012.
- [108] K-D Kim, H-K Shin, and S-M Chang. Thin film passivation characteristics in OLED using in-situ passivation. *Transactions on Electrical and Electronic Materials*, 13(2):93–97, 2012.
- [109] S Day, M F Grant, R Bellerby, S A Rosser, G J Cannell, J P Stagg, D A H Buckley, and I Wilson. Silica on silicon components for passive optical networks. In *Advanced Networks and Services*, pages 130–139. International Society for Optics and Photonics, 1995.
- [110] H Subbaraman, X Xu, A Hosseini, X Zhang, Y Zhang, D Kwong, and R T Chen. Recent advances in silicon-based passive and active optical interconnects. *Optics express*, 23(3):2487–2511, 2015.
- [111] J D Ferguson, A W Weimer, and S M George. Atomic layer deposition of  $Al_2O_3$  and  $SiO_2$  on BN particles using sequential surface reactions. *Applied Surface Science*, 162:280–292, 2000.
- [112] J W Klaus, O Sneh, A W Ott, and S M George. Atomic layer deposition of  $SiO_2$  using catalyzed and uncatalyzed self-limiting surface reactions. *Surface Review and Letters*, 6(03n04):435–448, 1999.
- [113] M A Cameron, I P Gartland, J A Smith, S F Diaz, and S M George. Atomic layer deposition of  $SiO_2$  and  $TiO_2$  in alumina tubular membranes: pore reduction and effect of surface species on gas transport. *Langmuir*, 16(19):7435–7444, 2000.
- [114] Y Fedorenko, J Swerts, J W Maes, E Tois, S Haukka, C-G Wang, G Wilk, A Delabie, W Deweerdt, and S De Gendt. Atomic layer deposition of hafnium silicate from  $HfCl_4$ ,  $SiCl_4$ , and  $H_2O$ . *Electrochemical and Solid-State Letters*, 10(5):H149–H152, 2007.
- [115] J W Klaus and S M George. Atomic layer deposition of  $SiO_2$  at room temperature using  $NH_3$ -catalyzed sequential surface reactions. *Surface Science*, 447(1):81–90, 2000.

- [116] B A McCool and W J Desisto. Self-limited pore size reduction of mesoporous silica membranes via pyridine-catalyzed silicon dioxide ald. *Chemical Vapor Deposition*, 10(4):190–194, 2004.
- [117] Y Du, X Du, and S M George. SiO<sub>2</sub> film growth at low temperatures by catalyzed atomic layer deposition in a viscous flow reactor. *Thin Solid Films*, 491(1):43–53, 2005.
- [118] L K Tan, A S M Chong, X S E Tang, and H Gao. Combining atomic layer deposition with a template-assisted approach to fabricate size-reduced nanowire arrays on substrates and their electrochemical characterization. *The Journal of Physical Chemistry C*, 111(13):4964–4968, 2007.
- [119] Y Du, X Du, and S M George. Mechanism of pyridine-catalyzed SiO<sub>2</sub> atomic layer deposition studied by fourier transform infrared spectroscopy. *The Journal of Physical Chemistry C*, 111(1):219–226, 2007.
- [120] S I Kol'tsov. Oxidation of polyhydrosiloxane prepared by molecular layering. *Russian Journal of General Chemistry*, 71(10):1531–1535, 2001.
- [121] S-W Lee, K Park, B Han, S-H Son, S-K Rha, C-O Park, and W-J Lee. Atomic layer deposition of silicon oxide thin films by alternating exposures to Si<sub>2</sub>Cl<sub>6</sub> and O<sub>3</sub>. *Electrochemical and Solid-State Letters*, 11(7):G23–G26, 2008.
- [122] J-H Lee, U-J Kim, C-H Han, S-K Rha, W-J Lee, and C-O Park. Investigation of silicon oxide thin films prepared by atomic layer deposition using SiH<sub>2</sub>Cl<sub>2</sub> and O<sub>3</sub> as the precursors. *Japanese Journal of Applied Physics*, 43(3A):L328, 2004.
- [123] W-J Lee, C-H Han, J-K Park, Y-S Lee, and S-K Rha. Atomic layer deposition and properties of silicon oxide thin films using alternating exposures to SiH<sub>2</sub>Cl<sub>2</sub> and O<sub>3</sub>. *Japanese Journal of Applied Physics*, 49(7R):071504, 2010.
- [124] J D Ferguson, E R Smith, A W Weimer, and S M George. Ald of SiO<sub>2</sub> at room temperature using TEOS and H<sub>2</sub>O with NH<sub>3</sub> as the catalyst. *Journal of the Electrochemical Society*, 151(8):G528–G535, 2004.
- [125] T Murata, Y Miyagawa, Y Nishida, Y Yamamoto, T Yamashita, M Matsuura, K Asai, and H Miyatake. Low-temperature silicon oxide offset spacer using plasma-enhanced atomic layer deposition for high-k/metal gate transistor. *Japanese Journal of Applied Physics*, 49(4S):04DB11, 2010.
- [126] Z Ma, S Brown, J Y Howe, S H Overbury, and S Dai. Surface modification of Au/TiO<sub>2</sub> catalysts by SiO<sub>2</sub> via atomic layer deposition. *The Journal of Physical Chemistry C*, 112(25):9448–9457, 2008.

- [127] B Hatton, V Kitaev, D Perovic, G Ozin, and J Aizenberg. Low-temperature synthesis of nanoscale silica multilayers—atomic layer deposition in a test tube. *Journal of Materials Chemistry*, 20(29):6009–6013, 2010.
- [128] Y K Jeong, H-J Kim, H G Kim, and B-H Choi. Luminescent properties of BaMgAl<sub>10</sub>O<sub>17</sub>:Eu<sup>2+</sup> blue phosphor grown with SiO<sub>2</sub> using atomic layer deposition. *Current Applied Physics*, 9(3):S249–S251, 2009.
- [129] Y-B Jiang, N Liu, H Gerung, J L Cecchi, and C J Brinker. Nanometer-thick conformal pore sealing of self-assembled mesoporous silica by plasma-assisted atomic layer deposition. *Journal of the American Chemical Society*, 128(34):11018–11019, 2006.
- [130] J W Lim, S J Yun, and J H Kim. Optical and electrical properties of Ti<sub>x</sub>Si<sub>1-x</sub>O<sub>y</sub> films. *ETRI journal*, 31(6):675–679, 2009.
- [131] Y Qin, Y Kim, L Zhang, S-M Lee, R B Yang, A Pan, K Mathwig, M Alexe, U Gösele, and M Knez. Preparation and elastic properties of helical nanotubes obtained by atomic layer deposition with carbon nanocoils as templates. *Small*, 6(8):910–914, 2010.
- [132] J Bachmann, R Zierold, Y T Chong, R Hauert, C Sturm, R Schmidt-Grund, B Rheinländer, M Grundmann, U Gösele, and K Nielsch. A practical, self-catalytic, atomic layer deposition of silicon dioxide. *Angewandte Chemie International Edition*, 47(33):6177–6179, 2008.
- [133] K Pitzschel, J M M Moreno, J Escrig, O Albrecht, K Nielsch, and J Bachmann. Controlled introduction of diameter modulations in arrayed magnetic iron oxide nanotubes. *ACS nano*, 3(11):3463–3468, 2009.
- [134] J Lee, S Farhangfar, R Yang, R Scholz, M Alexe, U Gösele, J Lee, and K Nielsch. A novel approach for fabrication of bismuth-silicon dioxide core-shell structures by atomic layer deposition. *Journal of Materials Chemistry*, 19(38):7050–7054, 2009.
- [135] D Hiller, R Zierold, J Bachmann, M Alexe, Y Yang, J W Gerlach, A Stesmans, M Jivanescu, U Müller, J Vogt, H Hilmer, P Löper, M Künle, F Munnik, K Nielsch, and M Zacharias. Low temperature silicon dioxide by thermal atomic layer deposition: Investigation of material properties. *Journal of Applied Physics*, 107(6):064314, 2010.
- [136] O Albrecht, R Zierold, C Patzig, J Bachmann, C Sturm, B Rheinländer, M Grundmann, D Görnitz, B Rauschenbach, and K Nielsch. Tubular magnetic nanostructures based on glancing angle deposited templates and atomic layer deposition. *Physica Status Solidi (B)*, 247(6):1365–1371, 2010.

- [137] B B Burton, M P Boleslawski, A T Desombre, and S M George. Rapid SiO<sub>2</sub> atomic layer deposition using tris(tert-pentoxo)silanol. *Chemistry of Materials*, 20(22):7031–7043, 2008.
- [138] X Liang, K S Barrett, Y-B Jiang, and A W Weimer. Rapid silica atomic layer deposition on large quantities of cohesive nanoparticles. *ACS Applied Materials & Interfaces*, 2(8):2248–2253, 2010.
- [139] M Lindblad and A Root. Atomically controlled preparation of silica on alumina. *Studies in Surface Science and Catalysis*, 118:817–826, 1998.
- [140] S Kamiyama, T Miura, and Y Nara. Comparison between Hf-silicate films deposited by ALD with BDMAS (SiH<sub>2</sub>[N(CH<sub>3</sub>)<sub>2</sub>]<sub>2</sub>) and TDMAS (SiH[N(CH<sub>3</sub>)<sub>2</sub>]<sub>3</sub>) precursors. *Electrochemical and Solid-State Letters*, 8(10):F37–F39, 2005.
- [141] S Kamiyama, T Miura, and Y Nara. Comparison between SiO<sub>2</sub> films deposited by atomic layer deposition with SiH<sub>2</sub>[N(CH<sub>3</sub>)<sub>2</sub>]<sub>2</sub> and SiH[N(CH<sub>3</sub>)<sub>2</sub>]<sub>3</sub> precursors. *Thin Solid Films*, 515(4):1517–1521, 2006.
- [142] P S Waggoner, C P Tan, and H G Craighead. Atomic layer deposited silicon dioxide films on nanomechanical silicon nitride resonators. *Journal of Applied Physics*, 107(11):114505, 2010.
- [143] S-J Won, S Suh, M S Huh, and H J Kim. High-quality low-temperature silicon oxide by plasma-enhanced atomic layer deposition using a metal–organic silicon precursor and oxygen radical. *Electron Device Letters, IEEE*, 31(8):857–859, 2010.
- [144] H Jung, W-H Kim, I-K Oh, C-W Lee, C Lansalot-Matras, S J Lee, J-M Myoung, H-B-R Lee, and H Kim. Growth characteristics and electrical properties of SiO<sub>2</sub> thin films prepared using plasma-enhanced atomic layer deposition and chemical vapor deposition with an aminosilane precursor. *Journal of Materials Science*, 51(11):5082–5091, 2016.
- [145] T Hirvikorpi, M Vähä-Nissi, A Harlin, J Marles, V Miikkulainen, and M Karppinen. Effect of corona pre-treatment on the performance of gas barrier layers applied by atomic layer deposition onto polymer-coated paperboard. *Applied Surface Science*, 257(3):736–740, 2010.
- [146] S Kamiyama, T Miura, Y Nara, and T Arikado. Atomic layer deposition of hafnium silicate gate dielectric films using Hf[N(CH<sub>3</sub>)(C<sub>2</sub>H<sub>5</sub>)]<sub>4</sub> and SiH[N(CH<sub>3</sub>)<sub>2</sub>]<sub>3</sub> precursors. *Electrochemical and Solid-State Letters*, 8(8):G215–G217, 2005.
- [147] Y Kinoshita, F Hirose, H Miya, K Hirahara, Y Kimura, and M Niwano. Infrared study of tris(dimethylamino)silane adsorption and ozone irradiation on Si (100) surfaces for ALD of SiO<sub>2</sub>. *Electrochemical and Solid-State Letters*, 10(10):G80–G83, 2007.

- [148] F Hirose, Y Kinoshita, S Shibuya, Y Narita, Y Takahashi, H Miya, K Hirahara, Y Kimura, and M Niwano. Atomic layer deposition of SiO<sub>2</sub> from tris(dimethylamino)silane and ozone by using temperature-controlled water vapor treatment. *Thin Solid Films*, 519(1):270–275, 2010.
- [149] K-M Jeon, J-S Shin, J-Y Yun, S J Lee, and S-W Kang. Plasma-enhanced atomic layer deposition of silicon dioxide films using plasma-activated triisopropylsilane as a precursor. *Journal of Vacuum Science & Technology A*, 32(3):031511, 2014.
- [150] M Putkonen, M Bosund, O M E Ylivaara, R L Puurunen, L Kilpi, H Ronkainen, S Sintonen, S Ali, H Lipsanen, X Liu, E Haimi, S-P Hannula, T Sajavaara, T Buchanan, E Karwacki, and M Vähä-Nissi. Thermal and plasma enhanced atomic layer deposition of SiO<sub>2</sub> using commercial silicon precursors. *Thin Solid Films*, 558:93–98, 2014.
- [151] B B Burton, S W Kang, S W Rhee, and S M George. SiO<sub>2</sub> atomic layer deposition using tris(dimethylamino)silane and hydrogen peroxide studied by insitu transmission ftir spectroscopy. *The Journal of Physical Chemistry C*, 113(19):8249–8257, 2009.
- [152] D M King, X Liang, B B Burton, M K Akhtar, and A W Weimer. Passivation of pigment-grade TiO<sub>2</sub> particles by nanothick atomic layer deposited SiO<sub>2</sub> films. *Nanotechnology*, 19(25):255604, 2008.
- [153] W Gasser, Y Uchida, and M Matsumura. Quasi-monolayer deposition of silicon dioxide. *Thin Solid Films*, 250(1):213–218, 1994.
- [154] K Yamaguchi, S Imai, N Ishitobi, M Takemoto, H Miki, and M Matsumura. Atomic-layer chemical-vapor-deposition of silicon dioxide films with an extremely low hydrogen content. *Applied Surface Science*, 130:202–207, 1998.
- [155] S Morishita, Y Uchida, and M Matsumura. Atomic-layer chemical-vapor-deposition of SiO<sub>2</sub> by cyclic exposures of CH<sub>3</sub>OSi(NCO)<sub>3</sub> and H<sub>2</sub>O<sub>2</sub>. *Japanese Journal of Applied Physics*, 34(10R):5738, 1995.
- [156] S Morishita, W Gasser, K Usami, and M Matsumura. New substances for atomic-layer deposition of silicon dioxide. *Journal of Non-Crystalline Solids*, 187:66–69, 1995.
- [157] G W Rehm. *Understanding phosphorus fertilizers*. Minnesota Extension Service, University of Minnesota, USA, 1997.
- [158] A Marklund, B Andersson, and P Haglund. Organophosphorus flame retardants and plasticizers in swedish sewage treatment plants. *Environmental Science & Technology*, 39(19):7423–7429, 2005.
- [159] W Gleason. An introduction to phosphorus: history, production, and application. *The Journal of the Minerals, Metals & Materials Society (TMS)*, 59(6):17–19, 2007.



- [160] B Lucheva, T S Tsonev, and R Petkov. Method for obtaining of copper-phosphorus alloys. *Journal of the University of Chemical Technology and Metallurgy*, 40:235–8, 2005.
- [161] G Hanrahan, T M Salmassi, C S Khachikian, and K L Foster. Reduced inorganic phosphorus in the natural environment: significance, speciation and determination. *Talanta*, 66(2):435–444, 2005.
- [162] S A Trifonov, V A Lapikov, and A A Malygin. Reactivity of phenol-formaldehyde microspheres toward  $\text{PCl}_3$ ,  $\text{VOCl}_3$ , and  $\text{CrO}_2\text{Cl}_2$  vapors. *Russian Journal of Applied Chemistry*, 75(6):969–973, 2002.
- [163] V V Brei, V A Kaspersky, and N U Gulyanitskaya. Synthesis and study of boron phosphate and titanium silicate compounds on silica surface. *Reaction Kinetics and Catalysis Letters*, 50(1):415–421, 1993.
- [164] H G Tompkins and E A Irene. *Handbook of ellipsometry*. William Andrew, New York, USA, 2005.
- [165] M Born and E Wolf. *Principle of Optics*. Pergamon, Oxford, UK, 7th edition, 1999.
- [166] V M Mothukuru. *Atomic layer deposition of dopant containing oxide layers on silicon: MSc Thesis*. Otto-von-Guericke Universität, Magdeburg, Germany, 2012.
- [167] P S Hauge and F H Dill. A rotating-compensator fourier ellipsometer. *Optics Communications*, 14(4):431–437, 1975.
- [168] O Acher, E Bigan, and B Drevillon. Improvements of phase-modulated ellipsometry. *Review of scientific instruments*, 60(1):65–77, 1989.
- [169] D K Schroder. *Semiconductor material and device characterization*. John Wiley & Sons, New Jersey, USA, 2006.
- [170] ASTM. Standard test method for sheet resistance uniformity evaluation by in-line four-point probe with the dual-configuration procedure, 1997.
- [171] J Thornton et al. Scanning probe microscopy training notebook, 2000.
- [172] D Briggs and J T Grant. *Surface analysis by Auger and X-ray photoelectron spectroscopy*. IM Publications, West Sussex, UK, 2003.
- [173] H R Verma. *Atomic and nuclear analytical methods*. Springer, Berlin Heidelberg, 2007.
- [174] <https://www.purdue.edu/ehrs/rem/rs/sem.htm>. 2014.

- [175] <http://www.dsimagingllc.com/courses/>. 2013.
- [176] <http://www.eag.com/mc/sims-ion-beam-sputtering.html#next>. 2015.
- [177] *EPILOGOS-ICP Mikrowellenplasmaquelle für PEALD*. SENTECH Instruments.
- [178] A De Rooij. The oxidation of silver by atomic oxygen. *EsA Journal*, 13:363–382, 1989.
- [179] M L Zheludkevich, A G Gusakov, A G Voropaev, A A Vecher, E N Kozyrski, and S A Raspopov. Oxidation of silver by atomic oxygen. *Oxidation of metals*, 61(1-2):39–48, 2004.
- [180] A A Bergh. Atomic hydrogen as a reducing agent. *Bell System Technical Journal*, 44(2):261–271, 1965.
- [181] D Jelić, J Penavin-Škundrić, D Majstorović, and S Mentus. The thermogravimetric study of silver (i) oxide reduction by hydrogen. *Thermochimica Acta*, 526(1):252–256, 2011.
- [182] J F Moulder, W F Stickle, P E Sobol, K D Bomben, J Chastain, and R C King. *Handbook of X-ray photoelectron spectroscopy: a reference book of standard spectra for identification and interpretation of XPS data*. Physical Electronics, Inc, Minnesota, USA, 1995.
- [183] M G Blaber, M D Arnold, and M J Ford. Search for the ideal plasmonic nanoshell: the effects of surface scattering and alternatives to gold and silver. *The Journal of Physical Chemistry C*, 113(8):3041–3045, 2009.
- [184] T W H Oates, H Wormeester, and H Arwin. Characterization of plasmonic effects in thin films and metamaterials using spectroscopic ellipsometry. *Progress in Surface Science*, 86(11):328–376, 2011.
- [185] S Babar and J H Weaver. Optical constants of Cu, Ag, and Au revisited. *Applied Optics*, 54(3):477–481, 2015.
- [186] A D Rakić, A B Djurišić, J M Elazar, and M L Majewski. Optical properties of metallic films for vertical-cavity optoelectronic devices. *Applied Optics*, 37(22):5271–5283, 1998.
- [187] T W H Oates and A Mücklich. Evolution of plasmon resonances during plasma deposition of silver nanoparticles. *Nanotechnology*, 16(11):2606, 2005.
- [188] S Marsillac, S A Little, and R W Collins. A broadband analysis of the optical properties of silver nanoparticle films by in situ real time spectroscopic ellipsometry. *Thin Solid Films*, 519(9):2936–2940, 2011.

- [189] C T Campbell. Ultrathin metal films and particles on oxide surfaces: structural, electronic and chemisorptive properties. *Surface science reports*, 27(1):1–111, 1997.
- [190] J W Clancey, A S Cavanagh, R S Kukreja, A Kongkanand, and S M George. Atomic layer deposition of ultrathin platinum films on tungsten atomic layer deposition adhesion layers: Application to high surface area substrates. *Journal of Vacuum Science & Technology A*, 33(1):01A130, 2015.
- [191] L Baker, A S Cavanagh, J Yin, S M George, A Kongkanand, and F T Wagner. Growth of continuous and ultrathin platinum films on tungsten adhesion layers using atomic layer deposition techniques. *Applied Physics Letters*, 101(11):111601, 2012.
- [192] L Vitos, A V Ruban, H L Skriver, and J Kollar. The surface energy of metals. *Surface Science*, 411(1):186–202, 1998.
- [193] I N Yakovkin and M Gutowski. Driving force for the  $\text{WO}_3$  (001) surface relaxation. *Surface Science*, 601(6):1481–1488, 2007.
- [194] E T Eisenbraun, A Klaver, Z Patel, G Nuesca, and A E Kaloyeros. Low temperature metalorganic chemical vapor deposition of conformal silver coatings for applications in high aspect ratio structures. *Journal of Vacuum Science & Technology B*, 19(2):585–588, 2001.
- [195] J L Zilko. Metal organic chemical vapor deposition: technology and equipment. *Handbook of thin film deposition processes and techniques*, page 151, 2002.
- [196] K-E Elers, T Blomberg, M Peussa, B Aitchison, S Haukka, and S Marcus. Film uniformity in atomic layer deposition. *Chemical Vapor Deposition*, 12(1):13–24, 2006.
- [197] L M Fraas, P S McLeod, L D Partain, and J A Cape. Gasb films grown by vacuum chemical epitaxy using triethyl antimony and triethyl gallium sources. *Journal of applied physics*, 61(8):2861–2865, 1987.
- [198] [https://en.wikipedia.org/wiki/Antimony\\_trioxide#Properties](https://en.wikipedia.org/wiki/Antimony_trioxide#Properties). 2015.
- [199] E Wiberg and K Schuster. Zur kenntnis der verbindungsreihe  $\text{BCl}_{3-n}[\text{N}(\text{CH}_3)_2]_n$ . (über dimethylamino-substituierte borchloride). *Zeitschrift für anorganische und allgemeine Chemie*, 213(1-2):77–88, 1933.
- [200] M Putkonen and L Niinistö. Atomic layer deposition of  $\text{B}_2\text{O}_3$  thin films at room temperature. *Thin Solid Films*, 514(1):145–149, 2006.
- [201] Background statement for semi draft document # 5329 new standard: Guide for tris(dimethylamino) silane (3DMAS). 2012.

- [202] [https://commons.wikimedia.org/wiki/File:Vapour\\_pressure\\_triethyl\\_phosphite.svg](https://commons.wikimedia.org/wiki/File:Vapour_pressure_triethyl_phosphite.svg). 2015.
- [203] [https://en.wikipedia.org/wiki/Phosphorous\\_acid](https://en.wikipedia.org/wiki/Phosphorous_acid). 2015.
- [204] H C M Knoops, E M J Braeken, K de Peuter, S E Potts, S Haukka, V Pore, and W M M Kessels. Atomic layer deposition of silicon nitride from bis (tert-butylamino) silane and N<sub>2</sub> plasma. *ACS applied materials & interfaces*, 7(35):19857–19862, 2015.